TRANSPORT PHENOMENON IN JET IMPINGEMENT BAKING

by

NITIN NITIN

A Dissertation submitted to the

Graduate School-New Brunswick

Rutgers, The State University of New Jersey

in partial fulfillment of the requirements

for the degree of

Doctor of Philosophy

Graduate Program in Food Science

written under the direction of

Professor Mukund V. Karwe

and approved by

_____

_____

_____

_____

New Brunswick, New Jersey

January, 2009

ABSTRACT OF THE DISSERTATION

TRANSPORT PHENOMENON IN JET IMPINGEMENT BAKING

By NITIN NITIN

Dissertation Director:

Professor Mukund V. Karwe

In food industry, hot air jet impingement ovens are used to bake pizza shells, crackers, cookies, and to toast ready-to-eat cereals. Despite its significant applications and advantages (faster processing and better quality products) in food processing industry, there is a very limited understanding of detailed transport processes (heat and mass transport) involved in jet impingement baking.

To develop quantitative understanding of transport processes during jet impingement baking, we have modeled the flow field and its associated thermal transport phenomenon for a cookie shaped and a hot dog geometry using numerical simulation and have validated it using experimental data. To predict temperature and moisture distribution during baking, we have developed four different baking models based on coupled heat and mass transfer. These models

differ based on coupling of heat and mass transport terms, vapor transport, thermodiffusion and stages of a baking process.

Results of flow field and its associated thermal transport studies demonstrated that numerical simulation approach can be used to predict both flow field and thermal transport during jet impingement baking. The results highlight that local and average surface heat transfer coefficient values are a function of nozzle to plate spacing, jet inlet velocity and geometry of target product. Comparison of temperature and moisture profiles among the models show significant differences in temperature and moisture profile. Based on comparison of these models, we established that vapor transport process is important for modeling of a baking process, while thermo-diffusion process does not make a significant contribution to moisture transport. The results also demonstrate that introduction of stages in baking based on empirical approaches can introduce artificial steps in temperature-time profile. Comparison of numerically predicted center point temperature with experimental measurements in a potato disk shows that modified model II (with vapor transport and a single stage baking process) provides the best match with the experimentally measured data. In summary, we have modeled the complete transport process during jet impingement baking, which can predict the baking time, crust thickness, temperature and moisture distributions within the food for a given jet velocity and air temperature.

This work would not have been completed without love, patience and support of my family. I would like to thank my wife Dr. Madhu Sharma, my parents (Sh. N.K. Sharma and Sudesh Sharma) and my younger brother (Dr. Ashish Sharma) for their unconditional love and support.

Table of Contents

List of Tables

List of Illustrations

CHAPTER 1

Introduction

Baking, drying and freezing operations are the key process-engineering components of many food processing operations. The underlying engineering principles for these processes are based on thermal and mass transport. For several years extensive research efforts have been directed to understand the complex nature of these processes in different food processing operations. In addition to improved understanding of existing technologies, researchers have also explored new options for a given process. The underlying theme of these studies has been to develop faster, economical, versatile, easily scalable processes and achieve desired product characteristics. An example of this is a jet impingement technology. Jet impingement is a process in which a jet of air or fluid impinges on the surface of a food material. The principal applications of jet impingement have been focused in areas of baking, drying and freezing.

Jet impingement technology is used to heat or cool products because of higher and uniform rates of heat transfer. In food industry, hot air jet impingement ovens are used to bake pizza shells, crackers, cookies, and to toast ready-to-eat cereals (Li and Walker, 1996). Despite its significant applications and advantages (faster processing and better quality products) in food processing industry, there is a very limited understanding of detailed transport processes (heat and mass transport) involved in jet impingement baking. In this study we have aimed at developing a quantitative understanding of flow field, thermal and mass transport

processes during jet impingement baking. To develop this understanding, we have used combination of numerical modeling and experimental approaches to quantify transport processes involved during jet impingement baking. The key focus of this research lies in developing an integrated understanding of flow field, surface thermal transport processes and thermal and mass transport processes within a food matrix during jet impingement processing. It is our anticipation that this integration of quantitative knowledge for various transport processes in jet impingement baking will provide a comprehensive understanding for design of optimized jet impingement systems for food applications. The results of the study can be easily extended to drying applications and with few modifications to freezing applications.

To mathematically model transport processes during baking, we need to develop a predictive model for surface transport processes (heat and mass transfer rates) and transport processes (heat conduction, diffusion, vapor evaporation etc.) inside a food matrix during baking. For jet impingement system, surface transport processes are in turn closely coupled with flow field of a turbulent impinging jet. In the first part of this research, we developed a numerical simulation approach to model turbulent jet impingement flow field and predict associated surface heat transfer coefficient. This model was developed for two model geometries - cookie shaped geometry and cylindrical geometry. Numerical simulation results for the flow field and the surface heat transfer coefficient were validated by comparison with experimental measurements. In the second part, we developed a model to predict the baking processes in a food

matrix. Results from numerical prediction of average surface heat transfer coefficient were used for defining boundary conditions for a baking process. Mathematical models for a baking process were based on coupled heat and mass transfer processes. These models were used to predict temperature-moisture profiles within a food matrix during a baking process. The first model considered in this study was proposed by Zanoni et al, (1994), the other two models were developed to improve coupling of heat and mass transport terms during baking and highlight significance of moisture transport models (vapor transport models) in predicting temperature and moisture profiles.

Comparison of numerical simulation results for flow field and surface heat transfer coefficient indicated good agreement with respective experimental measurements. These comparisons were carried out for both cookie disk shaped and cylindrical hot dog geometry. Numerical simulation also confirmed that surface heat transfer coefficient was independent of thermo-physical properties of food material and local heat transfer coefficient was highest at the stagnation point in impinging jet. Based on a conjugate thermal transport model, the predicted center point temperature was compared with experimentally measured temperature-time data in a cylindrical hot dog. Comparison of these results highlights the significance of mass transport during a baking process.

For the second part, we modeled coupled heat and mass transfer process during baking of a cylindrical disc. The models were developed in two stages. First, a 1-d model of baking was considered for a cylindrical disc, which was modified to model the cylindrical disc as a 2-d axisymmetric geometry. The

results of these models provide a quantitative prediction of temperature and moisture distribution in a baked product as a function of time. The numerically predicted temperature- time and moisture-time profiles were compared among three baking models. In addition the results of predicted-temperature-time were also compared with the experimental measurements. Comparison of numerically predicted results highlight significance of various transport rates in a baking process and provides a fundamental insight into a baking process. Comparison of numerically predicted results with experimental measurements validates the models.

Developing a quantitative predictive approach based on mathematical modeling of different stages of jet impingement baking processes will provide a key to understand transport phenomenon associated with this technology. This understanding is critical for not only optimizing existing baking processes but also to develop hybrid-baking technologies and novel product development operations.

Background & Literature Review

In this section, a brief introduction to oven system is provided, followed by literature review for jet impingement for food applications. In the next section, we review various experimental studies for understanding flow field and thermal transport phenomena during jet impingement processing. In the last section of this chapter, review of mathematical modeling of jet impingement flow field, surface thermal transport and mathematical modeling of a baking process is presented.

Introduction to Ovens

Ovens are used in several food processing operations such as toasting, baking and drying in household cooking as well as in industry. Today's ovens have advanced from earlier simple devices to sophisticated microchip controlled devices. Ovens can be classified into three categories according to the energy transfer mode: 1) Convection, 2) Infrared Radiation, and 3) Microwave.

1) Convection oven: In convection ovens, heat transfer to the product is by the movement of hot air surrounding the product. In standard household ovens, air is heated either by an electric coil or gas burner and heat transfer occurs by natural convection of hot air. In swirl ovens, a fan or a blower controls the movement of air. This leads to higher heat and mass transfer rates as compared to natural convection ovens (Walker, 1987; Walker and Sparman, 1989). Ovens with swirl

mode of processing have gained a significant part of food processing market due to relatively faster operations and an opportunity to create a crust, color and texture of the processed foods. These types of ovens are used by cereal, pizza, bakery, food service and pet food industries.

Jet impingement ovens represent a special class of forced convection ovens. Such ovens were first designed by Donald Smith (1975). He designed an oven system in which high velocity hot air jets impinged perpendicularly on a food product (U.S. Patent Number 3884213). Since then food industry has used the jet impingement technology for many applications in baking and freezing. In these ovens, high velocity (up to 50 m/s or ~100 mph) jets of hot air impinge on a food product for faster processing rates or smaller cooking times. A schematic diagram of a jet impingement oven is shown in **Figure 1.1,** which shows multiple jets impinging on a food product. **Figure 1.2 (a) and 1.2 (b)** shows examples of commercial jet impingement oven systems. Figure 1.2 (a) is an example of a jet impingement oven used for food service industry and Figure 1.2 (b) illustrates an industrial size jet impingement oven for food manufacturing industry.
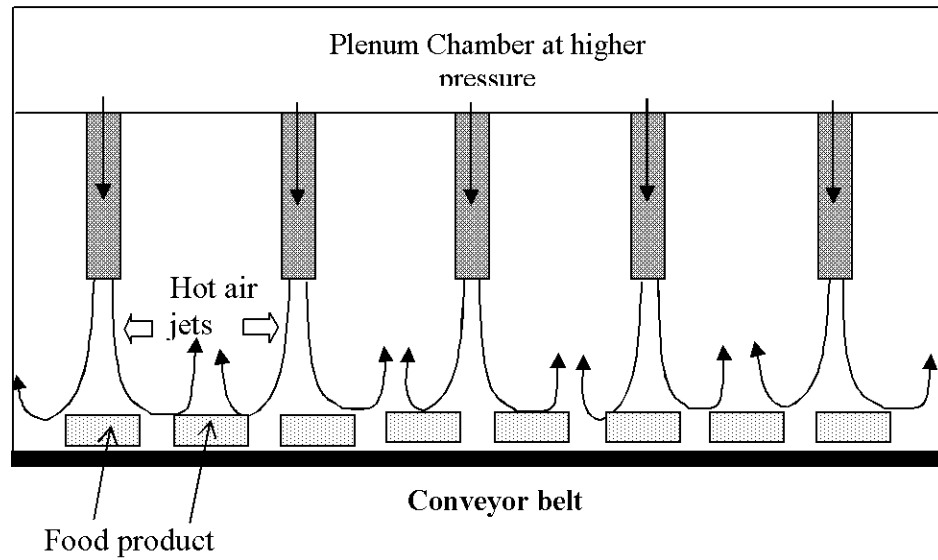
Figure 1.1

Schematic diagram of a jet impingement oven with food placed on a conveyor belt

Figure 1.2(a)
Example of a jet impingement oven used by pizza service industry
Source: Donyon Inc.
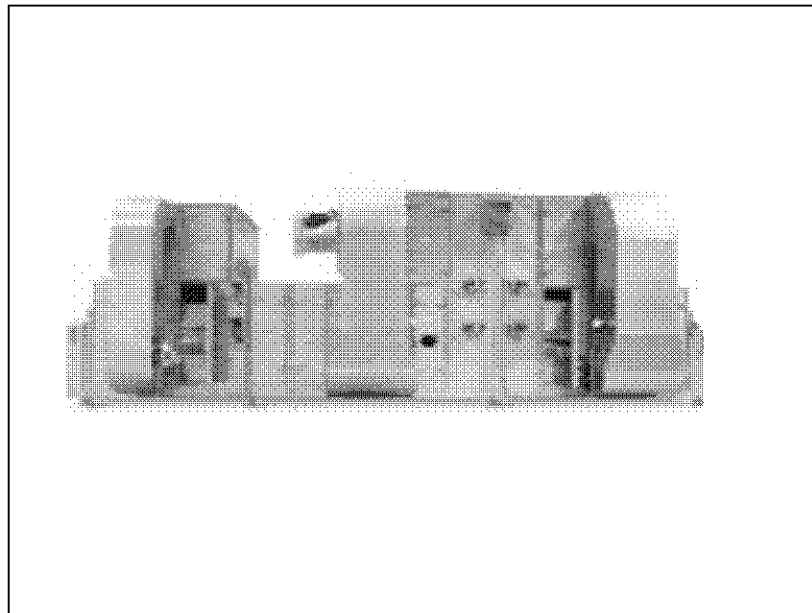
Figure 1.2(b)

Example of a jet impingement oven used by food manufacturing
industry, Source: Wolverine Corp.

2) Infrared Oven: In an infrared oven, heat is transferred to the product by radiation from an electric coil or hot surface heated by gas fired burners. Infrared radiation ovens are used more in industrial applications with limited household applications. The ovens or chambers that use only infrared heat source are usually used in food service industry to keep products warm. Since radiation heat transfer depends upon the shape factor between the heat source and the product, and also because the radiant heat flux decreases with square of distance between the heat source and the product, design of a radiation heat transfer oven is product specific so as to keep efficiency of heat transfer high. Generally radiation is combined with convection mode of heat transfer to improve the efficiency of processing.

3) Microwave Oven: In microwave ovens, electromagnetic energy is transferred from a magnetron to the food product. This microwave energy is converted to heat by molecular absorption of energy, mainly by water and fat molecules in the food product.

Microwave ovens have become an essential part of household over the past decade with some industrial applications. The success of microwave technology at home front is linked to its fast and clean food processing along with the success of frozen food market. Today, microwave ovens are mainly used to cook, reheat or thaw a food product. Even though baking (heating) operation in a microwave oven requires considerably less time as compared to a conventional convection oven, lack of crust and lack of desirable color formation are its main

limitations. Microwave processed products such as breads have been found to have tough and rubbery characteristics (Icoz et al., 2004; Sumnu et al., 2005). However, microwave ovens are being used successfully in industrial drying applications. Since the focus of this research was jet impingement, the rest of the background and discussion will focus on jet impingement.

Jet Impingement for food applications

Air impingement systems have been developed as a promising thermal processing technique for industrial food processing operations with a considerable reduction in process times and also a good quality product in terms of better moisture retention (Li and Walker, 1996; Ovadia and Walker, 1998; Wahlby and others, 2000). Several studies have been done to investigate the effect of hot air impingement on the difference in quality of baked foods as compared to those baked in natural convection ovens (Walker and Sparman, 1989; Li and Walker, 1996; Yin and Walker, 1995). They found that breads baked in an impingement oven had higher compressibility and better shelf life compared to those baked in a conventional oven. The results are shown in **Figures 1.3 and 1.4.** Since the rate of surface moisture removal is higher under hot air jet impingement, it results in a quick crust formation. Since the crust has lower moisture diffusivity, the product retained more moisture inside, making it more compressible. This also increased the production yield. In addition, higher moisture retention in baked products can enhance the perceived quality of the processed food (Walker, 1987) including retention of some key health promoting

nutraceutical compounds such as Omega-3 fatty acids (Borquez et al., 1999). In the study by Borquez et al., (1999), improved stability of omega –3 was attributed to reduced processing time and lower processing temperature as compared to comventional operations. The detailed list of food processing applications based on jet impingement is listed in **Table 1.1.**
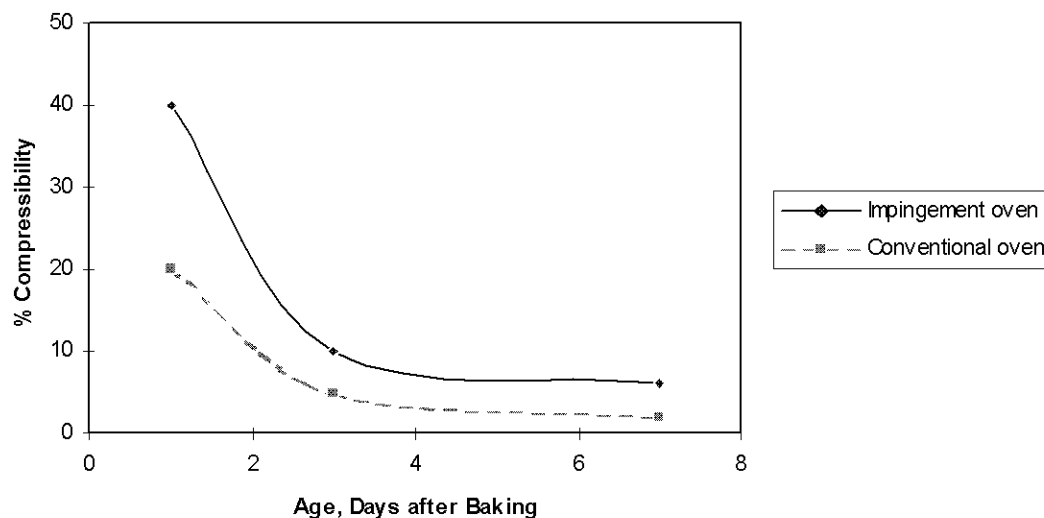
Figure 1.3

Compressibility of dinner rolls baked by impingement and conventional ovens (Redrawn from Walker, 1989 b)
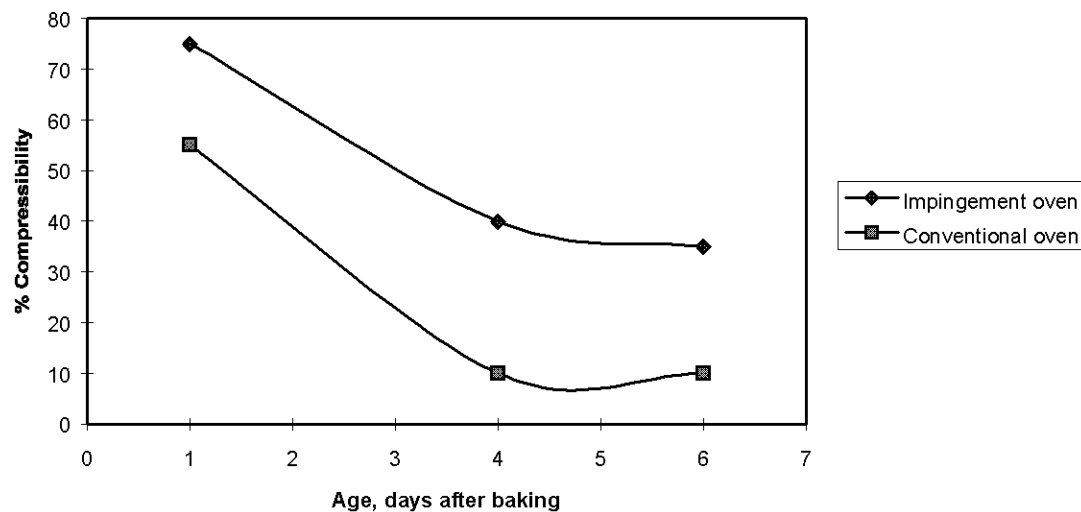
Figure 1.4

Compressibility of hamburger buns baked by impingement and conventional ovens (Redrawn from Walker, 1989 b)

Table 1.1

Applications of jet impingement oven

Food products processed in jet impingement oven	Type of processing
Pizzas	Baking
Sausage	Browning
Cocoa beans	Roasting
Peanuts	Roasting
Dinner rolls	Baking
Quiche	Baking
Fruit pies	Baking
Cookies	Baking
Muffins	Baking
Ready to eat cereals	Toasting

Jet Impingement- Flow Field and Heat Transfer Studies

Several researchers have experimentally investigated the flow field and heat transfer phenomena associated with impinging jets especially in the mechanical engineering discipline. Gardon and Cobonpue (1962), Gardon and Akfirat (1965), Martin (1977), Polat and others (1989), Goldstein and Timmers (1982), Goldstein and Seoul (1991), Viskanta and Huber (1994 a, b), and Colucci and Viskanta (1996) have carried out some of the most comprehensive studies in the field of jet impingement. There have been few studies focused on mass transfer related to jet impingement system (Martin, 1977; Sparrow and Lovell, 1980 and Angioletti et al, 2003). Most of the mass transfer results for jet impingement in drying applications are derived from empirical correlation between heat and mass transfer coefficient's (Martin, 1977).

In this section, review of literature in the area of jet impingement research is presented. Although, most of the studies in this area are focused on non –food applications they do provide a key insight into jet impingement processing. In the following sections, we discuss briefly the characterization of jets, review of flow field studies of impinging turbulent jets, measurement and modeling studies for heat transfer rates for jet impingement application, mass transfer studies, challenges in numerical modeling for jet impingement systems and potential future research areas with focus on food applications.

Introduction to Jets

A jet is a directed stream of fluid coming out of an orifice, tube or a nozzle. Jets can be broadly classified as submerged or non-submerged jets. When the medium of the jet is same as the surrounding medium it is classified as a submerged jet. Submerged jets can be divided into two categories, i.e., free jets and impinging jets. Majority of industrial applications involve impinging jets. In impinging jets we have a jet of liquid or gas coming from a nozzle or a tube and impinging on a desired surface, while in case of free jets we do not have a target surface for impingement. Jets can further be classified as based on Reynolds number, i.e., laminar or turbulent. Further, impinging jets can also be classified as confined and unconfined jets depending on the exit conditions. This review and discussion will focus on submerged turbulent air jets as these jets are mainly used in food applications such as baking, thawing, etc. Extensive research efforts have been directed to develop complete understanding of flow field of impinging jets both in case of a single jet and for multiple jets. The major motivation for these efforts has been to characterize flow field and effect of its associated turbulence on thermal and mass transport processes.

Flow Field in a Single jet

Free jet:

Based on the pioneering work by Gardon and Akfirat, (1965), flow field of an impinging jet has been classified into three regions i.e. free jet region, stagnation region and lateral spread region. Free jet region is further classified

into three sub regions: potential core region, developing flow region and developed flow region. Potential core region is a part of a jet flow where no vorticity is introduced in the flow due to free shear between an impinging jet and a stagnant air. Nozzle edges cause development of a mixing boundary layer on the periphery of a jet resulting in reduction of the potential core region and significant energy dissipation from the jet. Rate of dissipation of energy and length of the potential core region are largely dependent on shape and configuration of the nozzle (Jambunathan et al., 1992). This region of mixing is called the developing flow region, which eventually leads to the developed flow region **(Figure 1.5)**.

Mixing of surrounding air with jet air generates turbulence in the free jet (Gardon and Akfirat, 1964; 1965). As shown in **Figure 1.6,** turbulence level increases with an increase in the jet length. Turbulence peaks shifts from an outer region of a jet to a center of a jet with downstream distance. Figure 1.6 shows that width of the mixing region also increases with an increase in downstream distance from the nozzle. Characteristics of turbulence in a free jet region are effected by various factors including nozzle geometry, exit velocity, length of nozzle and sharpness at nozzle exit (Martin, 1977; Polat et al., 1989). Turbulence in a free jet region and its associated dissipation of energy are important factors contributing to efficient heat transfer in a jet impingement process.

Potential Core

Developing
Region

Fully Developed
Turbulent Flow
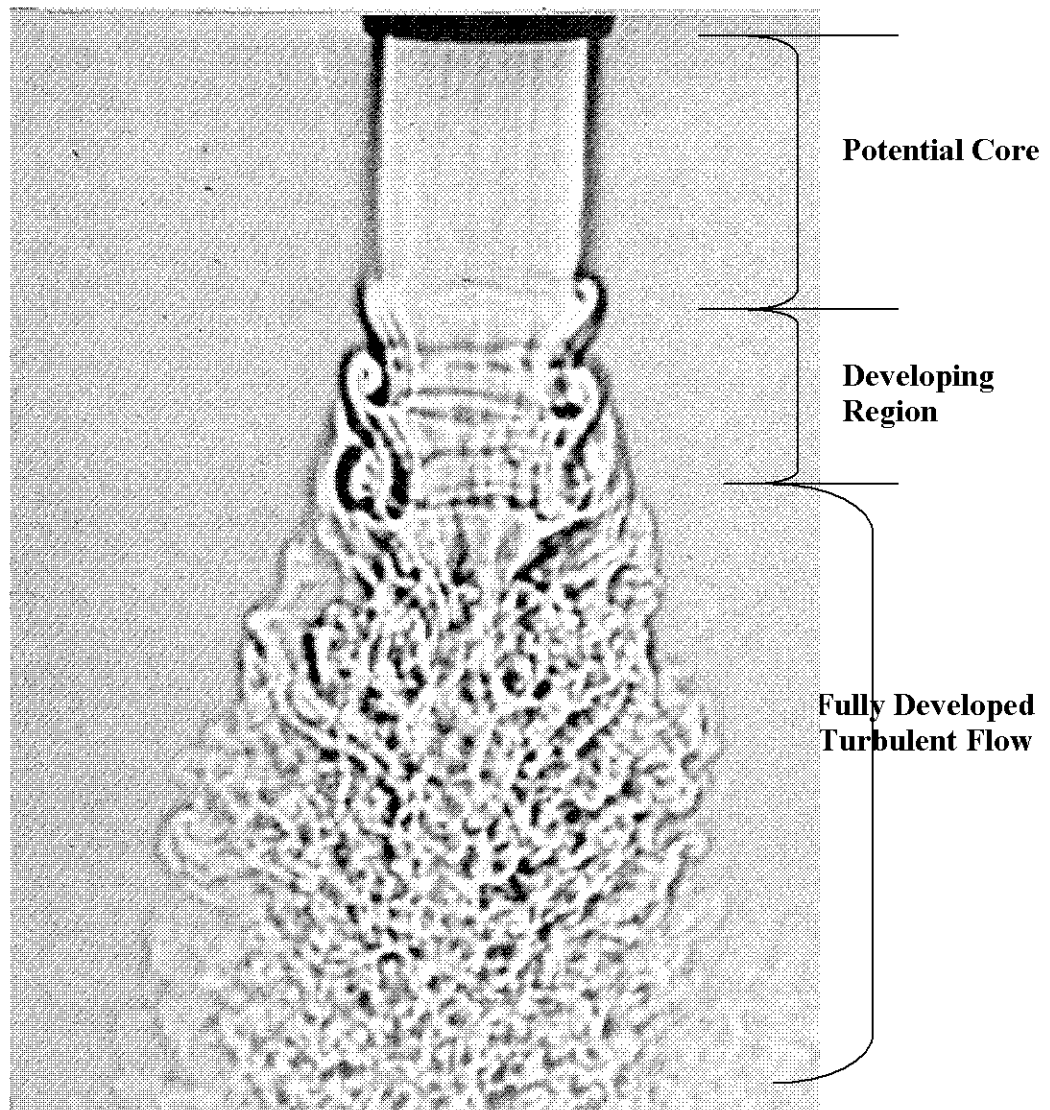
Figure 1.5

**Diagram illustrating the transition from laminar region
to a turbulent region in a round submerged jet of air (Reynolds
number~30,000 based on nozzle diameter)
(Fred Landis and Asher, 1962)**
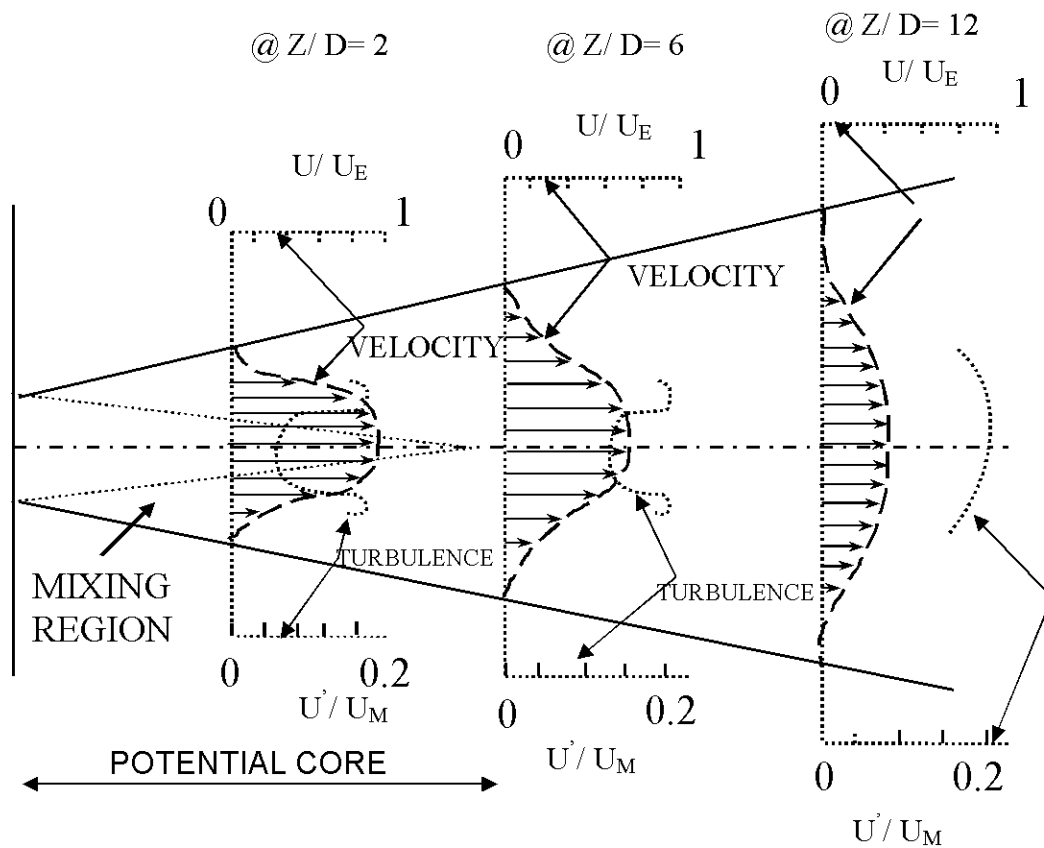
NOTATION:
U= Jet velocity
U_E= Jet exit velocity
U_M= Centerline velocity of jet
U'= R.m.s. value of fluctuating
    component of velocity
Z/D = Ratio of axial distance to nozzle
    diameter

FIGURE 1.6

Schematic distribution of velocity and turbulence intensity in an axis-symmetric jet
(Adapted From Gardon and Akfirat, 1965)

Impinging Jet:

Figure 1.7 shows three regions (Free jet, Stagnation zone, and Lateral spread region) in a single jet impinging on a flat surface. In a free jet region, the flow field is same as discussed above for a free submerged turbulent jet. An impinging jet behaves as a free jet up to a distance of about 1-1.5 nozzle diameters from an impinging surface (Gardon and Akfirat, 1965). After this distance, deceleration of an impinging jet begins as a jet enters into a stagnation region. In the stagnation region there is impingement and deflection of the jet. In this region, jet axial velocity decreases rapidly to zero and the static pressure rises. In a lateral spread region, negative pressure gradient causes a rapid increase in radial velocity near the stagnation region and the velocity drops as the jet spreads in a radial direction. This drop in velocity is due to a wider area available for the same mass of material to flow and also due to viscous drag at the wall (Marcroft and Karwe, 1999).

To characterize flow field of a single impinging jet both quantitative and qualitative approaches have been adopted. Qualitative approach is based on a flow pattern visualization using the smoke wire method (Popiel and Trass, 1991 and Viskanta, 1993) for a jet impinging on a flat surface. In addition to this similar approach has been adopted by Cornaro et al, (1999) to study the flow pattern of a circular impinging jet impinging on concave and convex surface geometries. Results of these studies provide flow visualization to characterize various processes, e.g., vortex initiation, fluid entrainment etc. in an impinging jet.
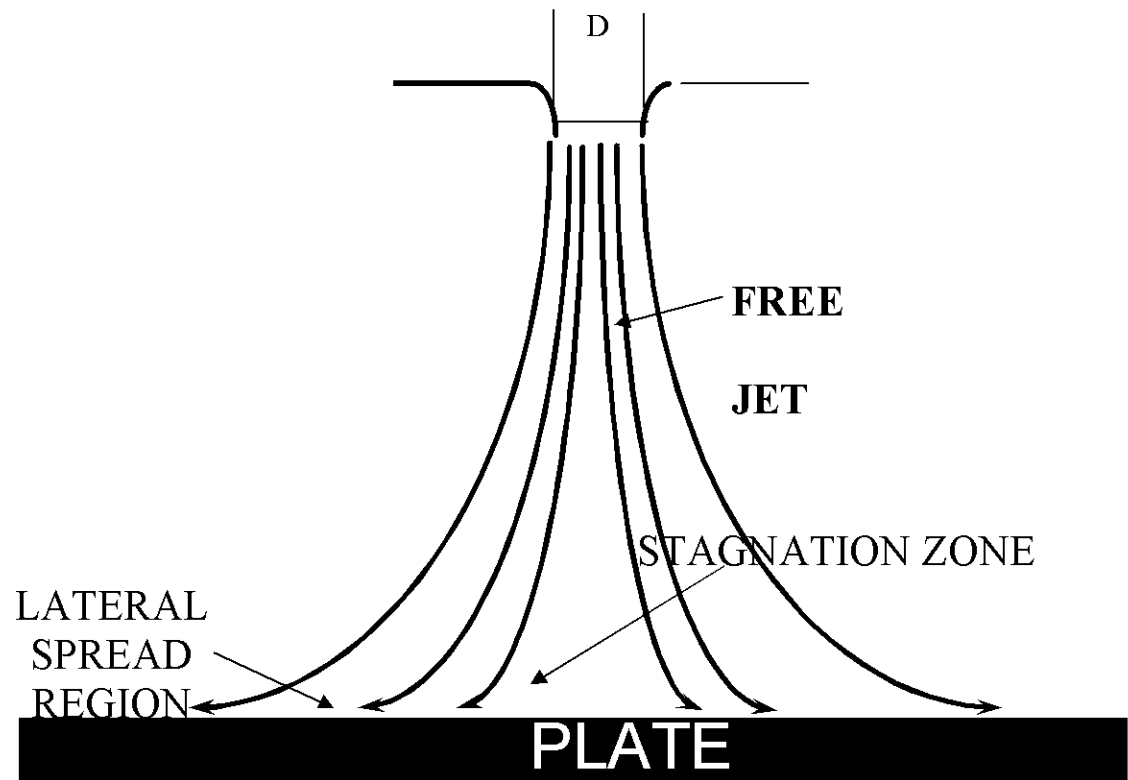
Figure 1.7

Schematic diagram of three zones in a single impinging jet

One of the quantitative approaches to characterize flow field of a single jet impinging jet is based on hot wire anemometry (Gardon and Akfirat, 1965, Sugiyama and Usami, 1979). Hot wire anemometry measurements provide a point velocity of an impinging jet at discrete observational points. Similar measurements of point velocities in a flow field of an impinging jet have been made using Pitot tube (Stoy and Ben- Hain, 1973). Both Pitot tube and hot wire anemometry are invasive techniques and are likely to induce changes in the flow field. Non-invasive velocity measurement approaches based on LDA (Laser Doppler Anemometry- Durst, 1981) or PIV (Particle Imaging Velocimetry - Adrian, 1991) have also been developed to quantitatively measure the flow field of an impinging jet. PIV technique allows the study of an entire flow field if suitable tracer particles and light sources are available as compared to point measurement with the LDA systems. Marcoft and Karwe (1999) have measured the flow field of a single jet impinging on a flat surface upto Z/D= 5. The typical flow field of an impinging jet at 10 mm from the target plate is shown in **Figure 1.8.** In addition PIV techniques have been applied to free and wall bounded jet flows (Nakabe et al.,, 2001; Hsiao and Sheu, 1996; Gogineni et al., 1999).
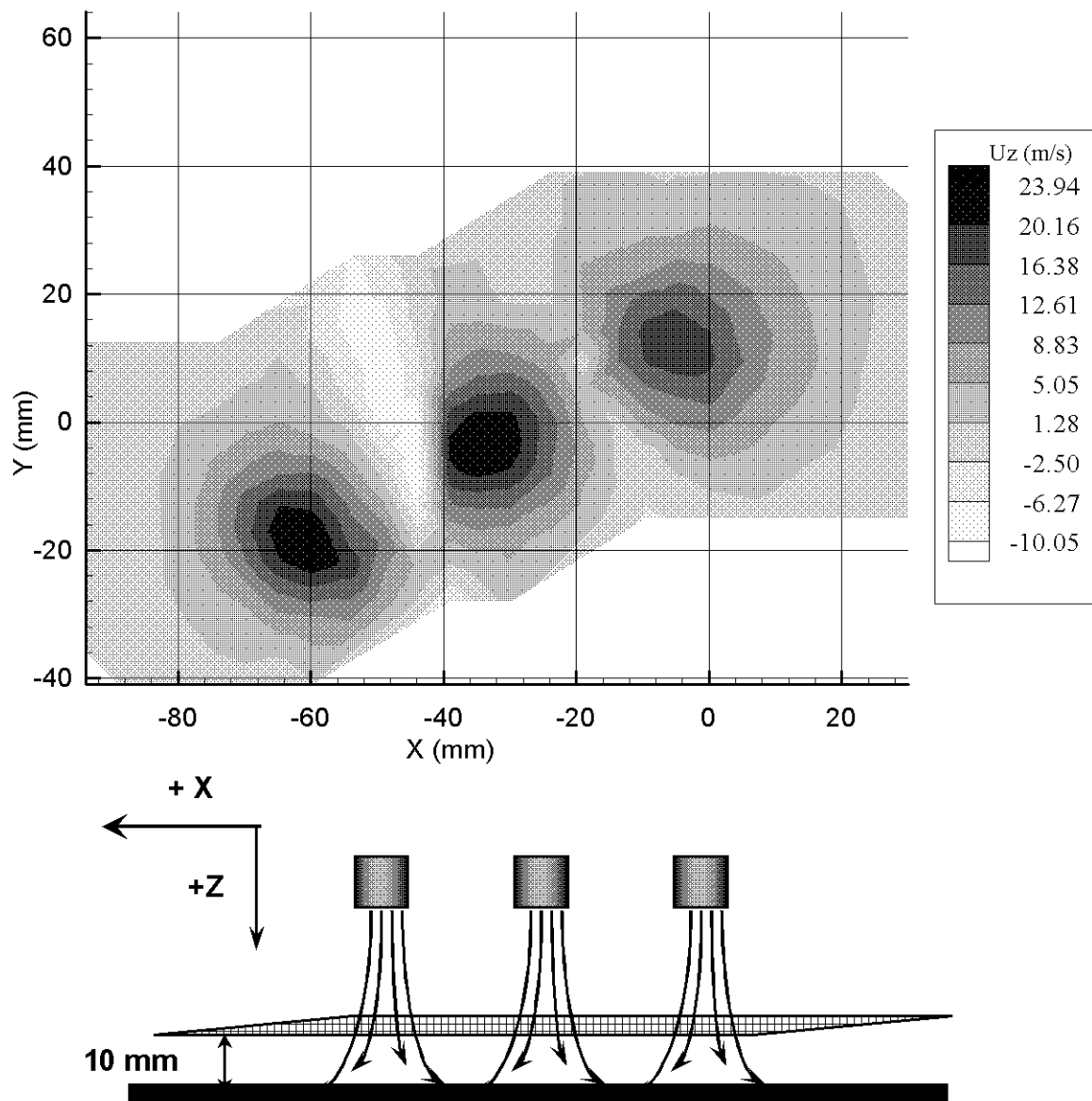
Figure 1.8

Contours of constant axial (U_z) velocity for three jets impinging on a flat plate. Measurements made in a plane 10 mm from flat plate

Flow Field in Turbulent Multiple Submerged Jets

Although the flow field in multiple impinging jets has similar characteristics i.e. free jet region, stagnation and lateral spread region as described for the single impinging jets, yet there are significant differences in the flow field of multiple jets as compared to a single jet. These differences are due to possible interactions between neighboring jets, which are characteristics of multiple jet configuration only. Firstly, there can be interaction between surrounding jets in the mixing domain prior to impingement. The possibility of this interaction will depend on nozzle-to- nozzle spacing. In addition there can be interaction in a lateral spread region of two jets. This interaction can occur in two forms and depends on the exit conditions in an oven. In case of lateral exit in ovens, we can have a cross flow based interactions. **Figure 1.9** shows a schematic of a cross flow based jet interaction in multiple jets. In such cases a jet flow, can sweep against its surrounding jets in a lateral spread region, while moving towards lateral exit. This interaction will disrupt the stagnation region of adjacent jets and will reduce the rates of heat transfer. The cross flow effect is controlled by the location of exit ports in multiple jet impingement system. In second case of closed recirculatory system interaction between the lateral jets can lead to strong up flows or "upward jet fountains" as described by Viskanta and Huber, (1994a;) Saripalli, (1983). These upward fountains can create high level of turbulence in lateral spread region and can enhance the rate of heat transfer.

Exit

Wall Jet Interaction
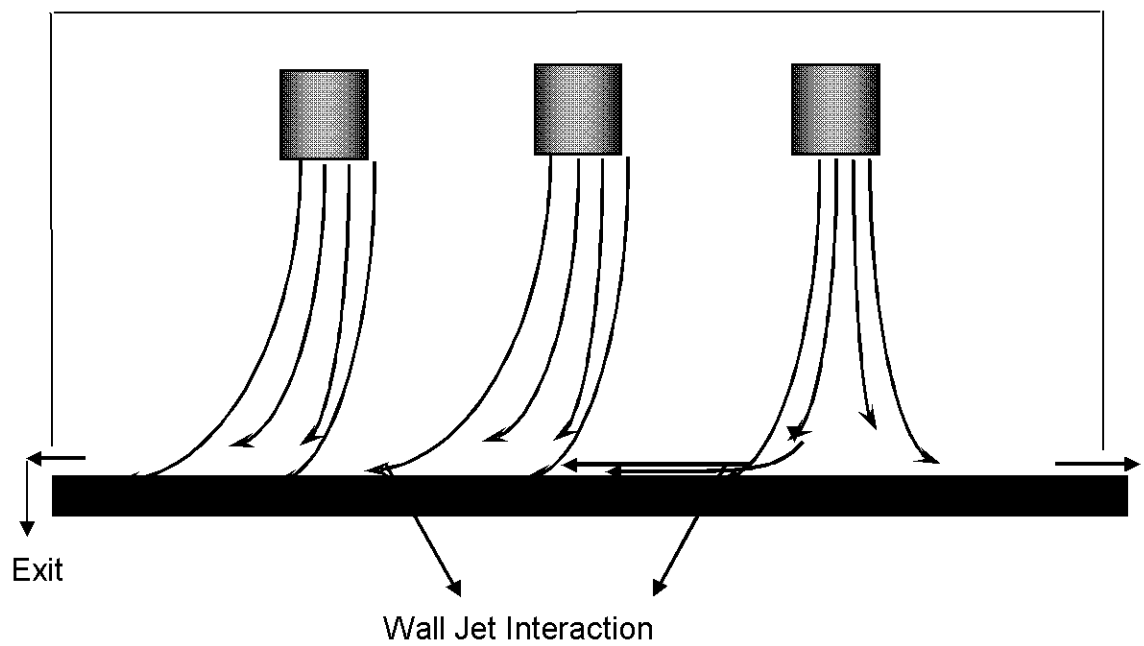
Figure 1.9

Schematic diagram of wall jet interaction during cross flow in multiple jet configurations

To understand the flow characteristics of multiple impinging jets, several experimental studies of flow field have been carried out. The majority of studies in the flow field of multiple jets geometry for turbulent regime (Re~25000) have been done using non-submerged water jets (Viskanta and Huber, 1994a; Saripalli, 1983, Barata et. al, 1992). Most of these studies are based on using water as a jet medium. Selection of water for flow visualization definitely reduces the challenges of seeding airflow with tracer particles, but this approach provides a limited understanding of air jets due to significant differences in interaction of water with surrounding air as compared to air jets.

Only few quantitative studies on flow field have been reported using submerged air jet system. One of the major flow field studies (Marcoft and Karwe, 1999) using submerged air multiple jets configuration has been done using the technique of LDA (Laser Doppler Anemometry). It was used to map the velocity field for three and four jets configuration. **Figures 1.8** and **1.10** show details of velocity contours at a distance of 10 mm from the impingement plate for three and four jets configuration, respectively.

The results showed (Marcoft et al., 1999) that the axial velocity contours for multiple submerged air jets configuration show similar trend in the free mixing and the stagnation region as discussed for single jet configuration. The measured velocity profiles also showed negative (upward) velocity regions in the lateral flow regime. These negative velocity regions occur because of interaction between adjacent jets, which causes flow reversal in the lateral flow regime of multiple impinging jets. These negative velocity regions are important in

describing the heat transfer characteristics of multiple jets (Marcoft et al., 1999) due to increased levels of turbulence in the lateral flow regime. For velocity measurements made close to an impinging plate, the magnitude of maximum negative velocity in these regions was almost 50% of the maximum jet velocity measured near the nozzle exit. The magnitude of negative velocity will depend on nozzle to nozzle spacing, inlet velocity of impinging jets and nozzle to plate spacing. Similar results of jet interaction resulting in a reverse flow have been shown (Viskanta and Huber, 1994a; Saripalli, 1983) using water jets. Both these studies have shown a formation of an "interaction fountain", i.e., the reverse flow region in lateral flow regime. **Figure 1.11** shows the schematic representation of the reverse flow in form of interaction fountain between the adjacent jets. Most of the above studies for flow field have been mainly based on flat target plate geometry except few qualitative studies for cylindrical geometries (Cornaro et al., 1999). Very little quantitative and predictive approaches have been developed to study the interaction of impinging jets with different surface geometries and presence of multiple objects under different jets, which is common in food processing operations. Understanding of these factors and their effect of flow field will help us design better processing equipment based on jet impingement for food industry.
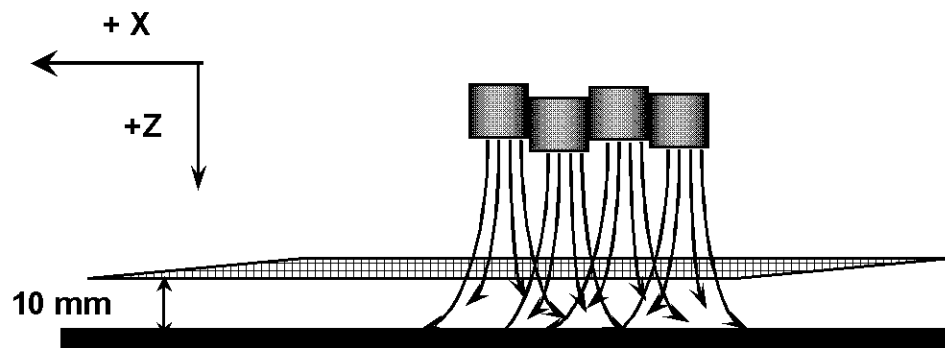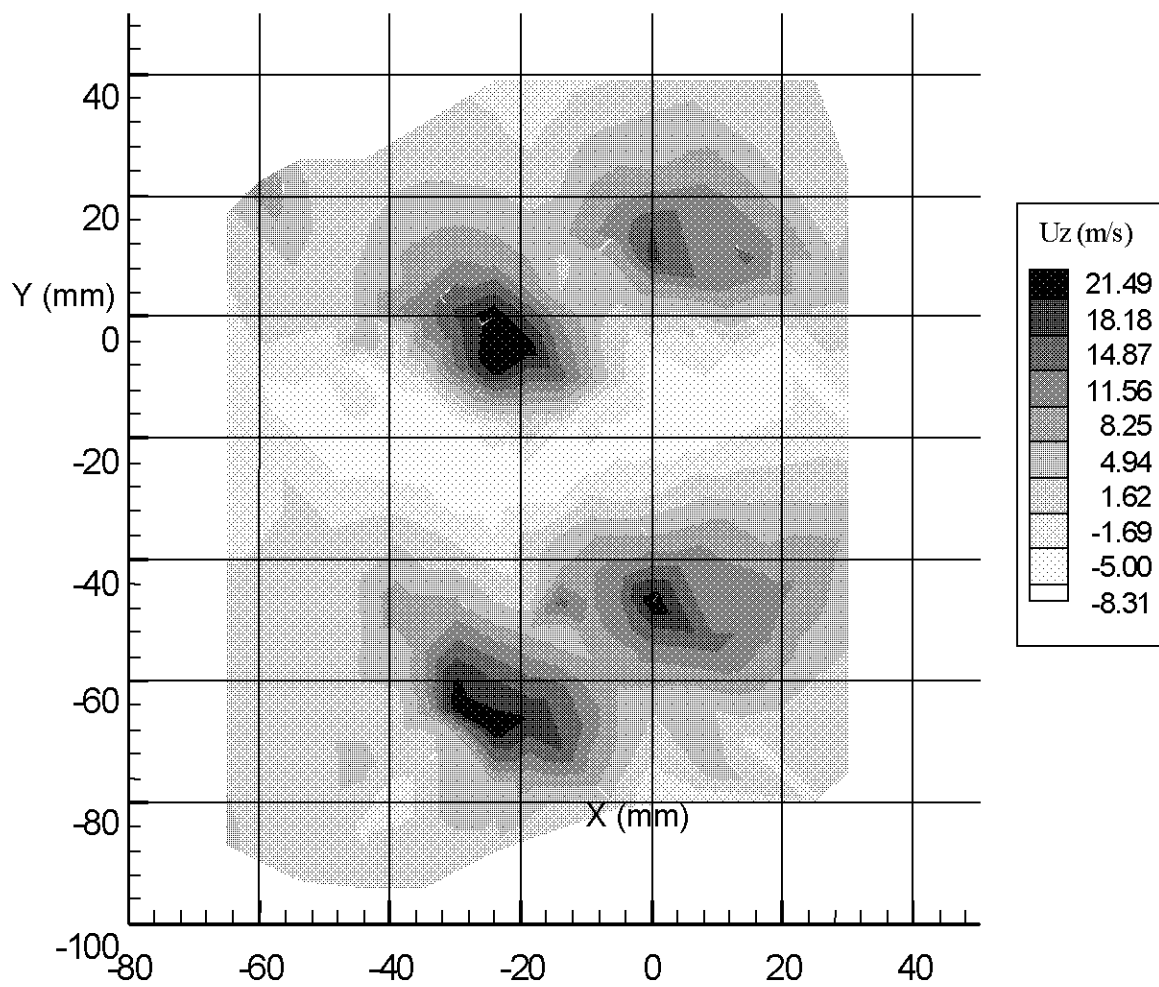
Figure 1.10

Contours of constant axial (U_z) velocity for four jets impinging on a flat plate. Measurements made in a plane 10 mm from flat plate

INTERACTION
FOUNTAIN

INTERACTION
FOUNTAIN
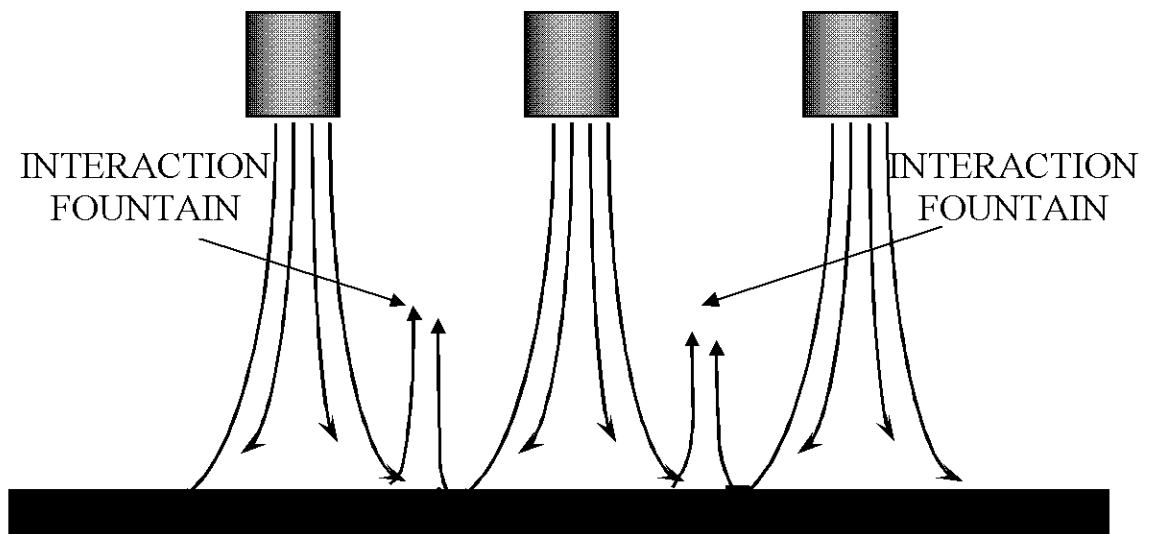
Figure 1.11

**Schematic diagram of reverse flow ("Interaction Fountain") in
multiple jet configurations**

Heat Transfer Characteristics of Impinging Turbulent Submerged Jets

Single Jet

Heat transfer characteristics for a single jet impinging on a flat surface show a maximum in the magnitude of heat transfer coefficient in the stagnation region of a jet. In the stagnation region, strong velocity gradient combined with fluctuations in velocity due to turbulence results in a local heat transfer maximum. The magnitude of this maximum is shown to be a function of the Reynolds number and a nozzle to plate spacing (Gardon and Akfirat, 1965; Martin, 1977). With an increase in the Reynolds number or a nozzle to plate spacing up to 3-5 nozzle diameters or both, the magnitude of this maxima in heat transfer coefficient increases (Gardon and Akfirat, 1965).

Figure 1.12 shows a variation of heat transfer coefficient for a jet impinging on a flat plate at different nozzle to plate spacing. Increase in magnitude of heat transfer coefficient with an increase in nozzle to plate spacing up to 6 nozzle diameter is due to an increase in level of turbulence developed due to mixing of an impinging jet air with a surrounding air while for this range of nozzle to plate spacing the centerline velocity is nearly constant (Gardon and Akfirat, 1965). For nozzle to plate spacing greater than 7 nozzle diameters, a decrease in the magnitude of maxima for heat transfer coefficient around stagnation region is observed. This decrease is due to decline in the centerline jet velocity with not appreciable increase in the turbulence level. This clearly shows that the magnitude of the maxima in heat transfer coefficient in the

stagnation region is a function of two parameters, namely turbulence and the jet velocity, i.e., to get maximum heat transfer, both turbulence level and velocity need to be maximum.

To understand the role of turbulence in jet impingement systems, several experimental studies have been carried out. Studies (Donaldson et al., 1971; Khan et al., 1982) have shown that heat flux associated with turbulent impinging jet is significantly higher than those associated with laminar impinging jet for the same pressure distribution. Kataoka et al., (1987) has conducted a detailed study focused on effects of turbulence on surface heat transfer coefficient for two-dimensional jets. The study has highlighted the role of large-scale eddy structures in enhancement of stagnation point heat transfer coefficient in a turbulent flow. Penetration of eddies in an impinging boundary layer will result in improved heat transfer rates. This study also indicates the unsteady nature of heat transfer process associated with impingement systems. Further presence of eddies may also cause oscillation in location of jet impingement center.

Studies for small nozzle to plate spacing, i.e., between 0.25-1 nozzle diameters, have shown great potential of impinging jets for the cooling applications in electronic packaging industry (Viskanta and Huber, 1994b). **Figure 1.13** shows a variation of local heat transfer coefficient for small nozzle to plate spacing. The study has shown that at large Reynolds number (Re ~15,000) and small nozzle to plate spacing (0.25-1 nozzle diameters) the maxima in surface heat transfer coefficient is not observed right at the stagnation point in contrast with studies for a large nozzle to plate spacing (5-6 nozzle diameters),

but at a distance away from the center. The existence of secondary maxima in the local heat transfer has also been indicated for small nozzle to plate spacing. For nozzle to plate spacing of less than 1 nozzle diameter, there is sharp increase in the magnitude of the secondary heat transfer coefficient maxima in the lateral jet region as compared to the case of nozzle to jet spacing of 2-5 nozzle diameters (Gardon and Cobonpue, 1961; Gardon and Akfirat, 1965; Martin, 1977). The locations of these secondary maxima have been found to be a function of the Reynolds number and a plate to jet spacing. Similar trend were also observed Lytle and Webb (1994).

This difference in the variation of heat transfer coefficient at a small nozzle to plate spacing (less than 1 nozzle diameter) is due to differences in the jet flow field. For small nozzle to plate spacing the shear layer does not develop, as an impinging jet does not get a chance to mix with a surrounding air. Existence of local maxima near the center of a jet has been attributed to a sudden acceleration of a jet fluid after impinging on the plate (Viskanta and Huber, 1994b). Small nozzle to plate spacings (less than 1 nozzle diameter) can provide higher average heat transfer rates as compared with large nozzle to plate spacing (~3-6 nozzle diameter), but the extent of variation in surface heat transfer coefficient along the lateral surface (radial axis) is significantly higher for small nozzle to plate spacing. This can result in non-uniform heating or cooling of the product with dimensions larger than the jet diameter.
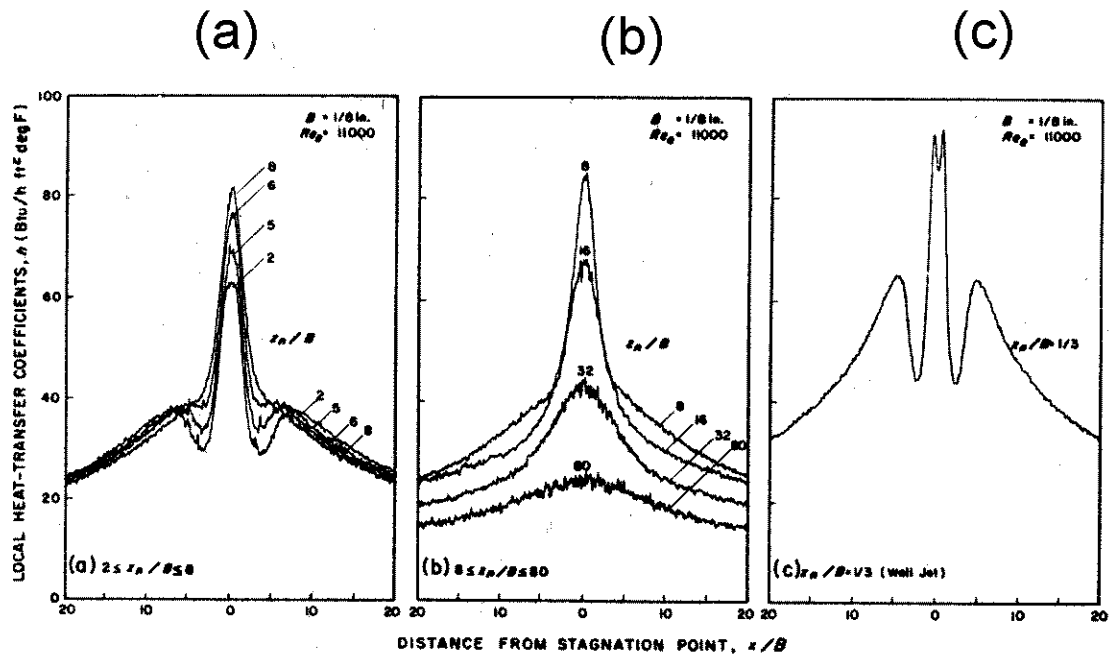
Figure 1.12

Lateral variation of local heat transfer coefficients between a plate and
an impinging two dimensional air jet at different nozzle to plate distances
(Taken from Gardon et. al, 1965)
(B=Nozzle Diameter, z_n=Nozzle to plate spacing (axial distance)

(a) $2 \leq \dfrac{z_n}{B} \leq 8$

(b) $8 \leq \dfrac{z_n}{B} \leq 80$

(c) $\dfrac{z_n}{B} < 1$

(a)

(b)
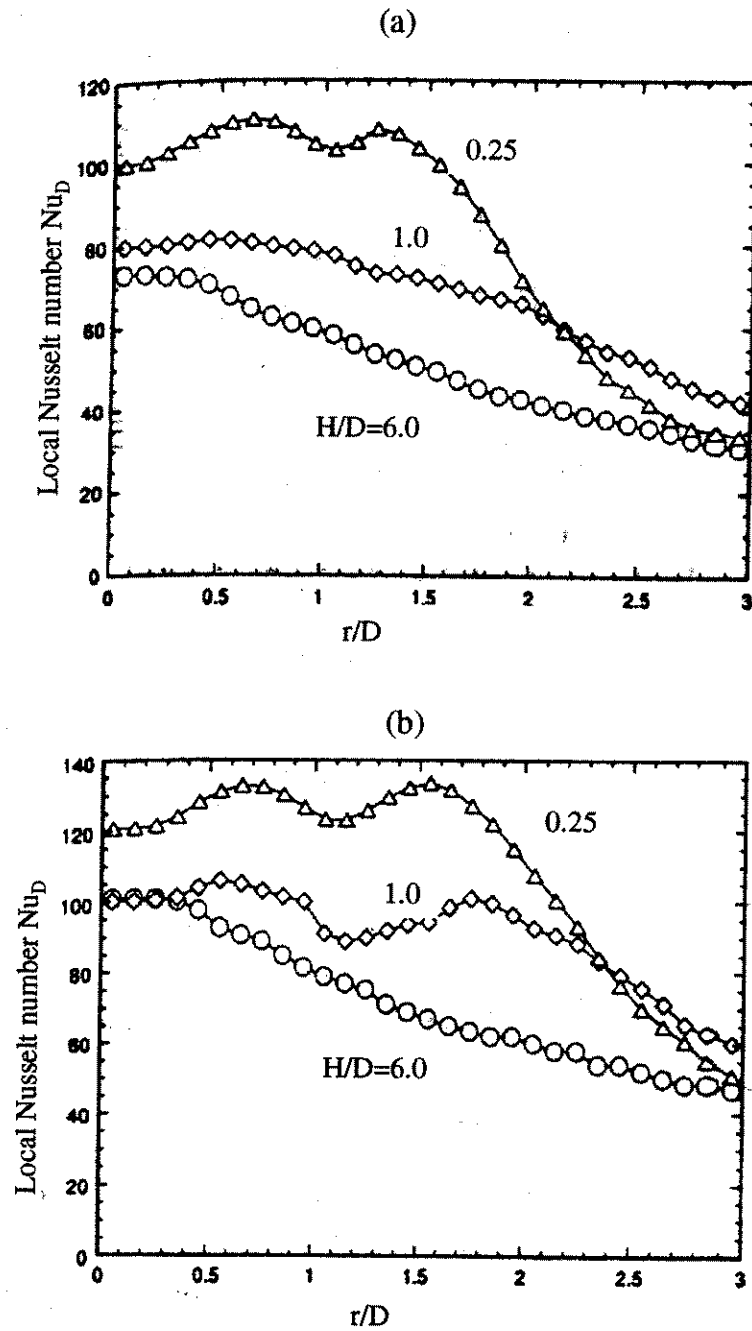
Figure 1.13

Effect of separation distance (H/D)-(Nozzle to plate/ Diameter of jet) on local Nusselt Number distributions for Reynolds number (a) 10,300 and (b) 17,100 (Taken from Viskanta et al., 1994 a)

In addition to above-discussed factors, nozzle geometry and jet outlet conditions have also been shown to affect surface heat transfer coefficient associated with jet impingement. Several researchers (Colucci and Viskanta, 1996, Hollworth and Berry, 1978) have directed their efforts to characterize the differences in heat transfer rates for different nozzle geometries. Colucci and Viskanta, (1996) have studied the effect of orifice and nozzle jet geometries on local heat transfer coefficient in a jet impingement system. In case of orifice geometry, typically there is a slot through which a jet is ejected from the plenum chamber, while in case of nozzle geometry, typically there is a long cylindrical tube which extends out from the plenum chamber into the oven. Results of both studies have shown higher rates of heat transfer for circular nozzle jet geometry as compared to orifice jets at the stagnation point. This difference in rate of heat transfer has been attributed to differences in a jet velocity profile for orifice and nozzle geometry. In nozzle geometry, the cylindrical tube allows the jet flow to develop as compared to an orifice jet outlet.

Multiple Jets

Heat transfer coefficient for an array of multiple jets is affected by several additional factors such as jet-jet mixing, wall jet interactions, cross flow, nozzle spacing and arrangement of jet nozzles in array etc., in addition to those described earlier for a single jet. Heat transfer characteristics of multiple jets are more complex as compared to single jet.

Wall jet interactions as discussed in the flow field studies of multiple jets can cause an increase in local turbulence due to mixing and in some cases can cause a formation of upward fountain resulting in formation of secondary maxima between the jets. The study by Goldstein and Trimmers (1982) has mapped the surface heat transfer coefficient from an array of circular impinging jets using liquid crystals. The study demonstrated the existence of secondary maxima in surface heat transfer in between the impinging jets (along the radial axis). Similar results on secondary maxima in between the jets have been shown by Viskanta and Huber (1994). In another study Goldstein and Behbahani (1982), have shown that the formation of secondary peaks in heat transfer is reduced with an increase in a distance between a nozzle and an impingement plate. In addition to the effect of wall jet interactions, crossflow has also been shown to effect the heat transfer uniformity and its magnitude. It has been shown by several researchers (Metzger and Korstad, 1972; Flourscheutz et al, 1981) that crossflow has detrimental effect on both magnitude and uniformity of heat transfer rates. Thus systems with minimum crossflow are recommended for heat transfer applications based on jet impingement.

In addition to all these factors, nozzle array geometry also has influence on heat transfer rates by affecting the flow field. LDA based flow field studies by Marcoft and Karwe (1999) illustrated the variation in the flow field in two different jet array geometries, i.e., triangular or rectangular configuration of multiple jets. Differences in a flow field of these nozzle configurations are expected to effect heat transfer rates, although the authors did not carry out heat transfer studies. In

addition to nozzle array configuration, jet- jet spacing can also affect the uniformity of the heat transfer rates (Viskanta and Huber, 1994b). Jet-Jet spacing can also influence the flow field of adjacent jets by interference (effect on turbulence) and crossflow interactions.

Experimental Approaches for Heat Transfer Measurements

Experimental approaches have dominated the research efforts on thermal transport processes during jet impingement. Various research methodologies have been used to measure and characterize the spatial variation of heat transfer rates. In this review, we provide a brief discussion on approaches used to measure and characterize the heat transfer rates for impingement systems.

Traditionally, the lumped capacitance technique has been used to determine average convective heat transfer coefficients for a given product geometry. In this technique a transducer representing the product geometry is made of high thermal conductivity material and a temperature sensor is placed at its center to determine the change in temperature. The detail discussion on this approach is presented in Chapter 3. In this approach heat transfer coefficient is evaluated based on slope of a temperature- time curve. This technique has been applied to impingement baking systems (Nitin and Karwe, 2001). This method provides us a quantitative measure of average heat transfer coefficient as a function of jet flow conditions. This technique combined with local heat flux measurements can help provide accurate estimation of surface heat flux for jet impingement applications. Using this combination approach we have measured

both the local and average heat transfer coefficient for various model food geometries. The details regarding this approach are discussed in Chapter 3.

Use of liquid crystals provides a way of studying spatial variation of heat transfer coefficients under impinging jets (Goldstein and Trimmers, 1982; Baughn, 1995; Mesbah et al., 1996, Lee and Lee, 2000). However liquid crystals work only in temperature range of –10°C to 110°C. This makes it difficult to apply liquid crystals to freezing or baking applications as freezing temperatures can go to as low as –40°C and baking temperatures as high as 250°C. Also, for such a wide temperature range, the resolution of liquid crystal systems is low.

The method of using micro-calorimeters (Westknemper, 1961; Donaldson et al., 1971) has been applied to various heat transfer applications. Donaldson et al., (1971) developed a method for studying heat transfer under heated impinging jets consisting of calorimeter disks (micro-calorimeters). This approach is similar to a lumped capacitance method, with a difference of smaller lumped units (disks which are flushed mounted on polyurethane foam insulation) to detect spatial variation. The disadvantage of this method is that it cannot be used to study the effect of object geometry on heat transfer rates. This poses a serious drawback for most food applications, as the geometry of food product is a critical factor affecting the flow field and heat transfer rates. The other limitation of this approach is the limited spatial resolution (defined by size constraint of calorimeter disk) as compared to liquid crystals. This technique has been applied for heat transfer measurements in air impingement applications in the freeze-thaw range (Sarkar, 2002; Sarkar and Singh, 2003).

In addition to these techniques a heat flux gage can be used to measure the local heat transfer coefficient. A heat flux gage measures the heat flux and the surface temperature of the impinging air. Based on heat flux data the local heat transfer coefficient can be calculated. This technique can be used to measure the heat flux over small areas and thus can provide measure for local heat transfer coefficient. Heat flux gages can be used for different geometric shapes without much interference to the flow field of an impinging jet. The accuracy of the heat flux gage measurement is affected by the conductivity difference between a flux gage and a substrate. For larger difference in conductivity between gage and substrates (> 100) the measurement of local heat flux can have error in the range of 20% (Deo and Karwe, 1999). This error results because large differences in conductivity can significantly effect the proportion of thermal energy conducted through a gage as compared to a substrate. This can in-turn effect the true measurement of heat transfer rate.

Another very useful approach to measure the spatial variation of heat transfer is to use naphthalene film on the surface of model object. Due to mass transfer the naphthalene film is sublimated from the target surface from which surface mass transfer coefficient can be estimated. Using a well-known heat/mass transfer analogy, local convective heat transfer rates can be calculated. This technique has been used by Sparrow and Lovell, (1980) and Angioletti et al, (2003). This technique has an advantage as it helps in reducing the conduction errors associated with thermal measurements and also provides a

direct experimental evidence of surface mass transfer rates, which could be important for food processing applications.

In conclusion, none of the heat transfer measurement techniques are perfect and all of them have their own limitations. But with careful experimental design they can be applied with sufficient accuracy to determine surface heat transfer coefficients.

Very limited efforts have been directed to measure heat transfer results for different product geometries, for multiple jets and multiple products being processed simultaneously in a typical food-processing environment etc. In addition to empirical correlations to predict the heat transfer rates for jet impingement system, efforts need to be focused on numerical simulations strategies to develop more rigorous predictive abilities to predict the heat transfer rates. The challenge in modeling lies in developing comprehensive solutions for turbulent flow field and its associated conjugate heat transfer problem. In addition to these challenges, to model the jet impingement problem for food applications, significant efforts need to be focused on measurements of mass transfer rates in addition to heat transfer studies. Combined heat and mass transfer measurements and simulations will help in developing comprehensive predictive strategies for food applications based on jet impingement processing.

Mathematical Modeling of Flow field and Heat transfer in Turbulent Jet Impingement System

Flow field and heat transfer associated with jet impingement has been the subject of investigation for approximately 50 years. In addition to experimental approaches to study the flow field and heat transfer associated with jet impingement systems, some research groups (Patankar et. al, 1977; Morris et. al, 1996; Catalano et. al, 1989; Polat et al., 1991; Craft et. al, 2008; Seyedein et. al, 1994; Behrouzi and McGuirk, 1998; Behnia et. al, 1999 and Park and Sung, 2001) have employed numerical approaches to study the complex flow field and heat transfer associated with turbulent jet impingement.

Numerical approach of most of the above studies has been based on standard k-ε model to model the system. Patankar et al, (1977) modeled the flow field of a turbulent impinging jet using two-equation standard k-ε model. This model uses two additional parameters k, turbulent kinetic energy and ε, dissipative rate to model the turbulent flow field. Results of this study indicated a good agreement with the earlier reported experimental data (Goldstein et. al, 1971). Similarly Morris et. al, (1996), and Catalano et. al, (1989) have used a similar approach to model the flow field for a two dimensional jet in a confined cross flow system. Polat et al., (1991) have used k-ε model to compute the flow field and heat transfer for a single two-dimensional jet impingement on a flat plate. In addition to standard k-ε model, several variants of k-ε model have been proposed to improve the prediction of wall heat transfer for turbulent flows. Some of these modifications include near wall treatment for turbulent jets as proposed

by Launder and Spalding (1972). Others include variants such as low Reynolds number k-ε model. Accurately predicting surface heat transfer for turbulent flows has been a significant challenge as different variants and different models results in significantly different predictions. Some of the models tend to over predict (e.g. low- Reynolds number k-ε model) the surface heat transfer coefficient and some tend to under predict the surface heat transfer rates as compared to experimental measurements. The challenges in accurate prediction of surface heat transfer coefficient have been due to limitations of the turbulent models in accurately modeling turbulent length scales and anisotropy associated with turbulence. To address this challenge various research groups and commercial companies (CFD companies) are working to develop better models to predict near wall turbulence and accurately predict the anisotropy in turbulence structures.

Most of the above studies have been limited to 2-d turbulent impinging jets on a flat surface. For most food applications (including baking, drying and thawing), we are interested in measurement and prediction of flow field and conjugate heat transfer for a defined geometry object as compared to flat surfaces. No study has reported the modeling of flow field and conjugate heat transfer for an object placed under a turbulent jet. Ability to model and predict flow field and surface heat transfer rates for different geometrical shapes will provide key information on surface variation of heat flux.

Mathematical Modeling of Heat and Mass transfer during Baking

Baking is a complex process, which involves many physical, chemical and biochemical changes in a food matrix. Heating of a food matrix, evaporation and

drying of water, crust formation, structural and volumetric changes are the key physical processes involved during baking. Browning reactions, gelatinization of starch, and denaturation of proteins are some of the key biochemical processes involved in baking. The physical processes are controlled mainly by heat and mass transfer processes and nature of food matrix. It is important to note the interrelationship between the physical and the chemical processes during baking. Physical processes are affected by the chemical structure of a food material, which in turn is affected by the thermal and mass transport processes (physical processes). Closed loop relationship between two these processes provides a big challenge in effectively modeling the baking processes. Despite the lack of effective models to predict the ultra structure of baked products combined with chemical and other physical changes, modeling of the baking processes has proven to be a useful tool in optimizing the baking process to meet desired product quality, evaluation of novel baking processes and its impact on baked food characteristics and optimization of energy consumption.

With these motivations, several research groups have proposed different mathematical approaches to model a baking process. Some of these models are based on overall energy balance calculation during the baking process to predict only average temperature and moisture content of the baked product (Kaiser et. al 1974; Savoye et. al 1992). Using such models, baking of thin products is considered as a drying process with constant rate in early stages of baking followed by falling rate of drying in later stages. These models (lumped approach) do not take into account the temperature and moisture gradients

within the products. Using the above approach, Broyart and Trystram (2002) developed a simplified model for heat and mass transfer during continuous baking of thin biscuits, taking into account the effects of oven design, and heat transfer by radiation, conduction and convection. The predictions of their model were in good agreement with experimental data from continuous, indirect, gas fired, pilot plant oven. The focus of such models is to help optimize the energy consumption during baking processes, and prediction of average properties of baked products. These models have a great potential for industrial applications and optimization of baking processes but provides a limited understanding of resulting food characteristics e.g. crust formation.

The second category of models is based on translating a phenomenological approach during baking process into a mathematical model. Most of these models are based on simultaneous heat and mass transfer processes within a food matrix (De Viers et al, 1989, 1995; Zanoni et al, 1993, 1994). These models differ in mathematical details involved in translating a phenomenological model.

De Viers et al, (1989) has proposed a mathematical model of heat and water transfer in crumb region of the baked product. The model places emphasis on movement of air bubbles in a dough/crumb to influence the heat and water transfer in a product. The water transport was modeled as a evaporation – condensation process in a gaseous domain and a diffusion process in a liquid domain. The significant limitation of this model is lack of prediction of crust behavior or kinetics of crust formation in a given baking system. This model has

limitation in modeling the water transport, as there is very limited evaporation in the crumb region (approximately constant water concentration) of most food products, hence the water transport is limited to diffusion only. The other major limitation of De Viers model is difficulty in modeling air movement inside a heterogeneous food matrix.

Zanoni et al. (1993, 1994), have proposed a different mathematical model in which baking is divided into two domains – Crust and Crumb. Crust is defined, as a region of advancing evaporation front inside the product while crumb is a region, where the temperature asymptotically approaches that of the evaporation front. During a baking process evaporation front advances into the product and develops a crust on top of the product. The top surface temperature of a product asymptotically approaches the air temperature in a oven. Mathematical model based on this approach was used to predict rate of crust development in baking of bread. Zanoni et al (1995), have experimentally modeled the kinetics of starch gelatinization and surface browning of bread. Thus, using the combination of a physical model based on heat and mass transport with experimental/ empirical models for chemical changes can provide a useful strategy in modeling baking processes.

In addition to baking models, similar approach based on combined heat and mass transport has been developed for drying applications. The one major difference in drying applications is that the dryer temperatures are not sufficiently high in most cases to move the evaporation front inside the product, thus most of the drying takes place at the surface of a product.

Mathematical Modeling of Flow Field and Transport Phenomenon (heat and mass transfer processes) During Baking

Most of the studies in area of mathematical modeling of baking processes are generally focused on transport processes inside a baked product or are focused on drying approaches to model baking processes. Very limited emphasis has been placed on combined modeling of flow field, conjugate heat transfer and detailed transport processes inside a baked product. To develop novel baking technologies, to compare uniformity of baking under set of process conditions and to model effect of flow field on external heat and mass transport processes during baking it is important to combine the process of mathematical modeling of internal transport processes in the baked product with detailed modeling of flow field and conjugate heat and mass transport processes in the oven. This approach becomes extremely useful when standard correlations to determine surface heat and mass transfer coefficients are not directly applicable for a particular type of oven system e.g. Jet impingement oven or such correlations cannot reliably predict the surface transport coefficients for a given geometry of baked product.

The above approach can also improve the prediction of the baking process as detailed local surface transport (heat and mass transfer) coefficients can only be predicted using computational modeling or direct experimental approaches. Computational modeling of combined flow field and external & internal transport processes during baking can provide an excellent opportunity to optimize the baking process both from process engineering and product

development approaches. With this objective, in recent years few research groups have developed computational fluid dynamics approach to model the external flow field in different food processes. Studies by Hu and Sun (2000 ; 2001), Verboven et al,(2000a and b), and Mirade et al., (2002) have used the standard k-ε model for solving problems related to meat chilling, blast freezing and convection ovens using various computational fluid dynamics (CFD) packages.

Conclusion Based on Literature Review

Based on the literature review in this chapter, it is clear that there is a need to quantitatively understand the fluid flow and transport processes (at the surface and inside the food matrix) during baking in a jet impingement system. This understanding will provide quantitative insight on effect of jet impingement process variables (jet velocity and air temperature) on uniformity of baking and kinetics of crust formation. This formed the basis and rationale for our research. Understanding from this study can be extended to freezing, thawing and drying operations using jet impingement systems.

CHAPTER 2

Specific Objectives

Overall objective of this dissertation was to numerically simulate transport phenomena during jet impingement baking.   Specific objectives of this research are:

Objective 1

To carry out numerical simulation of conjugate thermal transport during jet impingement baking and validate it using experimental data

This objective was subdivided into two sub-objectives, which are as follows:

 Objective 1a: To numerically simulate the flow field for a single jet impinging with or without a model food object and its experimental validation

Here, the aim was numerically predict the flow field of an axisymmetric turbulent impinging jet on a flat surface and on a surface of a model food object. The results of numerical simulation were compared with experimental flow measurement data obtained by Marcoft et al, (1999).

Objective 1b: To numerically predict the conjugate heat transfer between a turbulent hot air jet and a model food object and its experimental validation

The aim was to model conjugate thermal transport process to numerically predict the surface heat transfer coefficient for a model food object. Numerical simulation predicted both the flow field and the surface heat transfer coefficient for an impinging jet on a model food object. Two different geometries i.e., disk

and cylindrical were selected for simulation of cookie and hot dog shaped objects. Using numerical simulation, the effect of oven geometry and jet air velocity on surface heat transfer coefficient was evaluated. The numerical predicted (both local and average heat transfer coefficient) values were validated using experimentally measured local and average heat transfer coefficient for the above selected model geometries.

Objective 2

To develop mathematical models to numerically simulate the coupled heat and mass transport in a food product during baking and to validate them experimentally

This aim was further sub-divided into two sub-objectives, which are as follows:

Objective 2a: To model coupled heat and mass transport process in a 1-d model geometry based on three different phenomenological models to simulate baking process and to compare the results with experimental measurements:

In this aim, the baking process was numerically simulated based on three different phenomenological baking models. The initial studies were carried based on a baking model proposed by Zanoni et al., (1994). This model was modified to create two new baking models to simulate a baking process. These new proposed models were different from Zanoni's model based on coupling of heat and mass transport equations during baking and modeling vapor transport process during baking. Based on these models, the temperature-time and moisture-time profile within a food matrix were predicted and compared among

different baking models. Further the results of these models were compared with the experimental measurements in a potato disk.

Objective 2b: To model transport processes within a food matrix during baking of a 2-d axisymmetric model of a food and compare numerical predictions with the experimental measurements:

In this objective, the three baking models were extended to model the 2-d axisymmetric geometry of a cylindrical disc. In parallel with 1-d simulations, the numerically predicted temperature and moisture contours were compared across the three baking models and further the results were compared with experimental measurements. The results of this study have provided a comprehensive numerical toolbox to simulate baking processes. Further the discussion on various phenomenological models and their respective mathematical formulation has enhanced our understanding of physical processes during baking.

CHAPTER 3

Research Methods

This chapter describes the details of research methods including experimental and numerical approaches to study the heat and mass transport processes during jet impingement baking. The first part of this chapter describes various experimental approaches for measurement of thermal transport properties for jet impingement baking and the second part of this chapter is focused on theoretical and numerical approaches to model jet impingement baking. In this study, experimental studies were conducted to characterize the experimental system e.g., jet inlet velocity and air temperature in a pilot scale oven. These measurements were used as input values for numerical simulation of conjugate thermal transport in an impinging jet. In addition experimental measurements were made to estimate heat transfer rates for comparison with numerical predictions.

Experimental Studies

Jet Impingement Oven

Jet impingement (Jetzone dryer) oven used in the study was a pilot plant scale batch unit provided by Wolverine Corporation, MA. The detailed photograph of front part of the oven is shown in **Figure 3.1**. It shows jet tubes, turntable and the control panel to control and maintain the jet velocity or plenum

pressure, jet air temperature, and turntable rotation speed. This panel also controls the start up and shut down procedures of the oven. **Figure 3.2** shows the schematic representation of the jet impingement oven. In the oven there were thirteen jet tubes through which heated air came out and impinged on the surface of a product. Each tube had an outside diameter 18.6 mm and inside diameter of 17.4 mm. Spacing between the centers of adjacent jet tubes was 54 mm and is constant in the entire set up. There was an aluminum bowl, which could be placed on a turntable. The maximum speed of rotation of turntable was 60 rpm.

Figure 3.1

Front view of the oven (JetZone, Wolverine Corp., Ma)

Glass
Canopy

Plenum Chamber

420
mm

Jet
Tubes
(13)

Turntable

Rubber
Bushing

Aluminu
m
Bowl

Top View

5

2   6   10

54 mm

1   3   7   11   13

18.6
mm

4   8   12

9
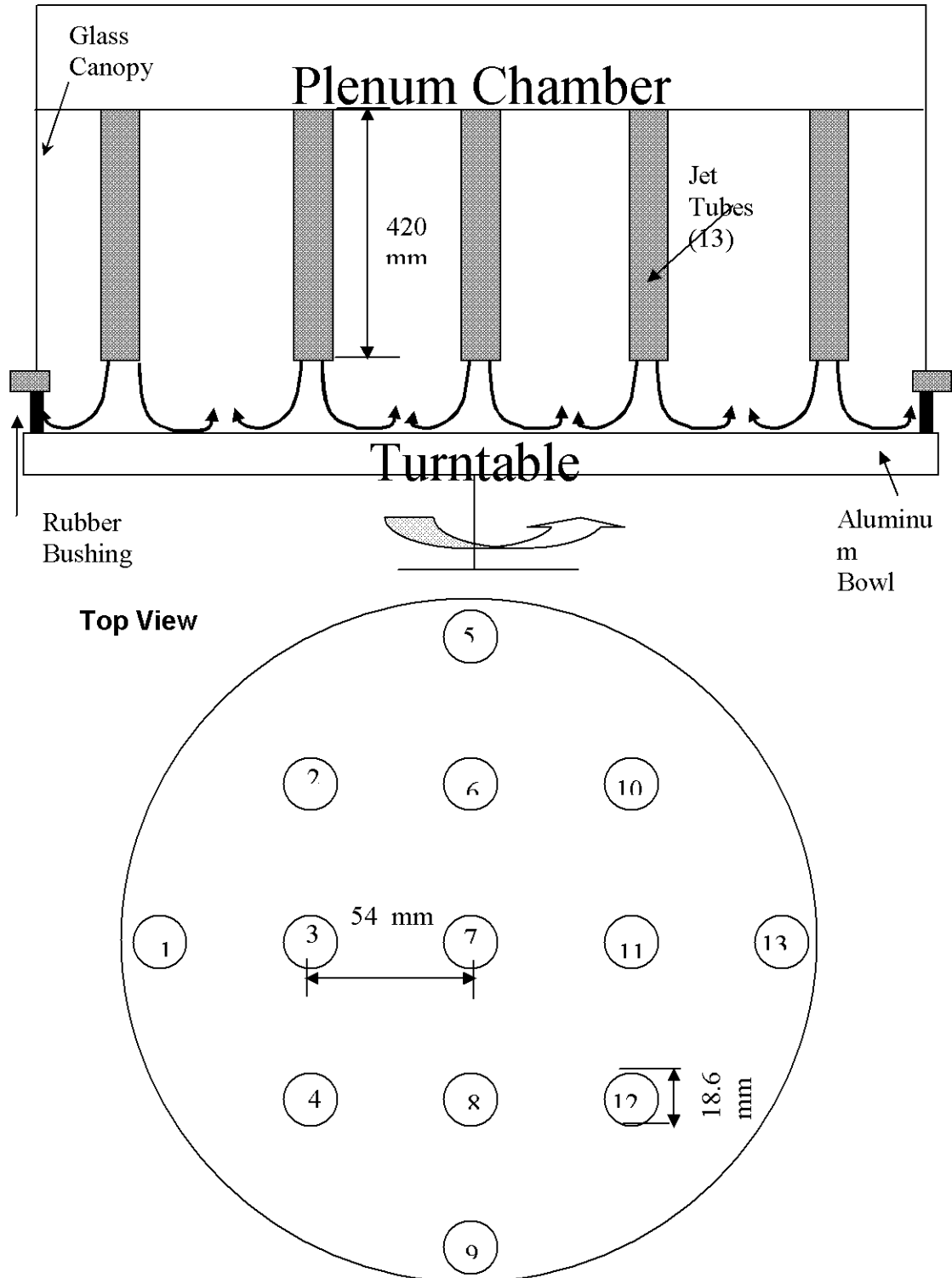
Figure 3.2

**Schematic diagram the Jet Zone of oven chamber, showing position and
spacing of jet tubes**

Working Description of the Oven

During operational mode, outside ambient air was drawn by a fan and filtered by passing through a wire mesh. This filtered air was driven by a fan through electric heaters and after being heated to the required temperature it entered the plenum chamber of the oven. The airflow path is shown in **Figure 3.3**. The fan speed controlled the air velocity or the plenum pressure in the oven. A controlled temperature electric duct heated the process air in a heater unit (as shown in a Figure 3.3), which had a total output of 54 kW. The filtered, heated air was made to impinge on the surface of a product placed on an aluminum bowl. After treating the product the air was exhausted to the atmosphere. In the plenum chamber we had an interconnected dampers, which directed the heated air either for impingement when the bowl was in up position or to the exhaust when the unit was not in operational mode (i.e., when the bowl was in down position). When the unit was in operational mode, the turntable with aluminum bowl on top lifted up automatically to seal the glass canopy, which surrounded the jet tubes. The maximum pressure, which can be obtained in the plenum chamber, was 5.5" W.C. (water column), which corresponds to 1370 Pa, with the maximum temperature of 400 °F (250 °C).
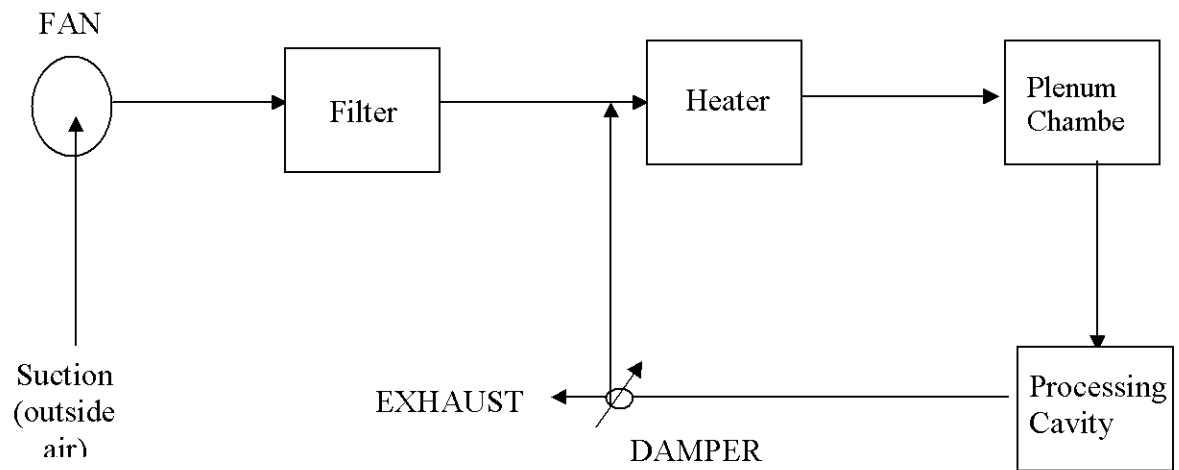
Figure 3.3

Air flow path in a Jetzone oven

Temperature Measurement

Temperature measurements were carried out using T- type thermocouples. Temperature measurements were made to measure the hot air temperature (under the jet nozzle exit) and model food objects center temperature (center of cylindrical cookie shaped object). Air temperature values during experiments ranged from room temperature to 150 °C. As reported in (Omega Temperature Handbook, Omega Corp., CT), T- type thermocouples are used for the temperature range of 0-350 °C. The estimation of error in measurement of temperature in the above reported range is 1 °C for every 100 °C temperature range (Omega Temperature Handbook, Omega Corp., CT). In our experiment we used a 30-gauge wire (0.254 mm diameter) for making the thermocouples. The T-type thermocouple was made by fusing two wires (Cu and Constantan) of thermocouple cable to form a junction. Then T- type thermocouple was inserted inside a stainless steel tubing (SS-316) of outside diameter 1.58 mm and inside diameter 1.37 mm. The length of the tubing was so selected so it could reach half the height of the aluminum model cookie. These dimensions of height of thermocouple were selected to measure the center temperature of the model cookie. The thermocouple wire was glued using an epoxy resin to the top of the tubing with thermocouple junction exposed out of the tubing. The thermocouple was inserted inside the cookie (aluminum metal) and to ensure good contact between the metal tubing and the aluminum cookie the gap was filled with a relatively high conductivity (16 (BTU.in)/(hr.ft^2. °F) = 0.71

(W/(m K))) omega-therm paste. **Figure 3.4** shows the schematic representation of thermocouple inside a cookie.
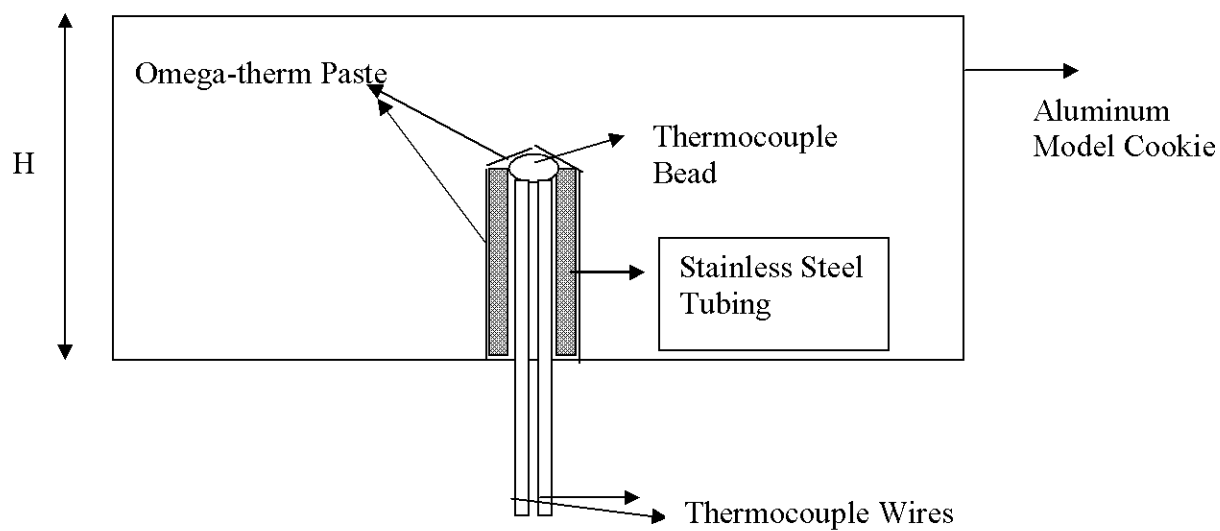
Figure 3.4

Schematic representation of thermocouple arrangement inside the model cookie

Velocity Measurement

To determine the flow characteristics in the oven cavity, i.e., whether laminar or turbulent, we needed to estimate the range of Reynolds number. To calculate the Reynolds number we were required to measure the velocity values of the jets. We also needed to calculate the Reynolds number to establish the correlations between the dimensionless Nusselt number (Nu) and the dimensionless Reynolds number (Re).

The velocity measurement was carried out using a pitot tube. A pitot tube is a simple device, which helps estimate the point velocity in any flow system provided the direction of flow of the fluid, is known. The pitot tube was acquired from Airflow Technical, Netcong, NJ. The pitot tube consisted of two concentric tubes with an end turned through right angle. The tip of the tube, which faces the flow direction, measures the total impact pressure (P_t) of the flow. The static pressure (P_s) is measured by the radial holes in the pitot tube. The difference in total impact pressure and the static pressure gives us the pressure associated with the velocity of the flow. The pitot tube was connected to a U tube manometer, which provided us the differential pressure (difference between the total pressure and the static pressure). This differential pressure was converted to the velocity value using the formula (Beckwith et al, 1993).

$$U = \frac{\sqrt{2(P_t - P_s)}}{\sqrt{\rho}} = \frac{\sqrt{2(\Delta P)}}{\sqrt{\rho}}$$

(3.1)

This above formula assumes that the flow in the system is incompressible. Flow is considered to be incompressible for mach number less than or equal to 0.2. This assumption was verified by comparing the calculated velocity values based on incompressible flow calculations and compressible flow calculations using equation (3) (**Figure 3.5**).

For Compressible Flows:

$$U = \sqrt{2\frac{k(P_s)}{(k-1)(\rho)} * \left[\left(1+\frac{\Delta P}{P_S}\right)^{(k-1)/k} - 1\right]}$$

(3.2)

k= Ratio of specific heats= c_p/c_v

ΔP= P_t-P_s

The result of the analysis showed that there was no significant difference in the velocity values obtained with both the above equations. This fact proved that the effect of compressibility factor on fluid flow in a system was negligible. The velocity values were measured at different conditions of temperature, plenum pressure and under different nozzles. Based on the measured maximum velocity (right under the nozzle exit) values we calculated the Reynolds number.
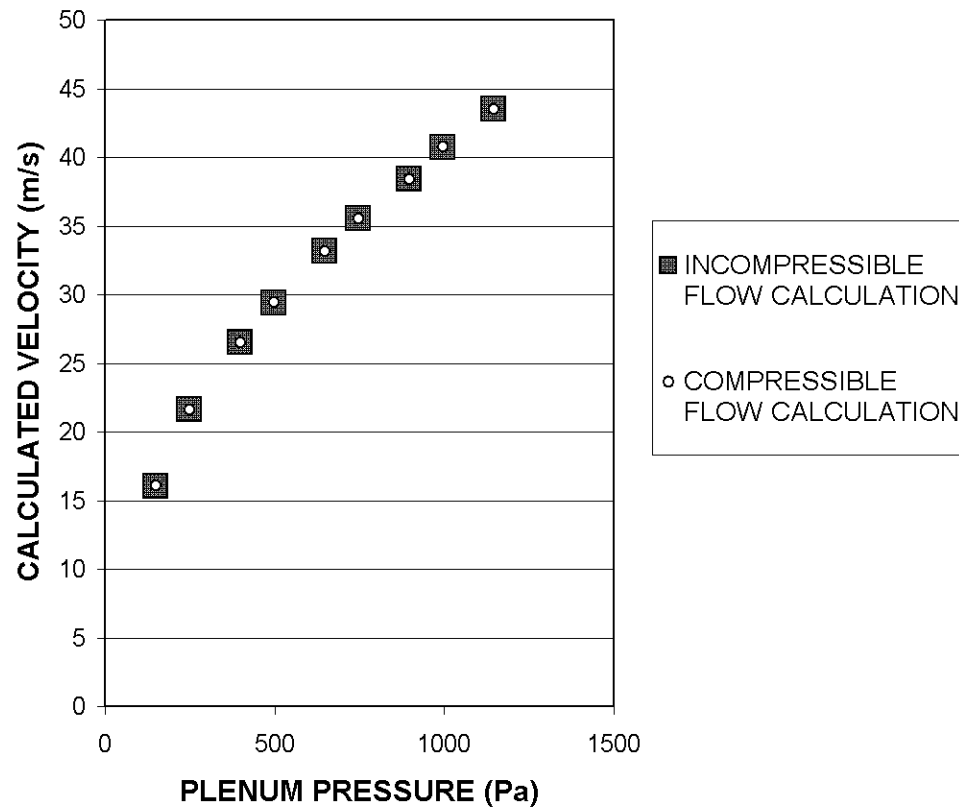
Figure 3.5

**Comparison of the velocity values for the compressible flow calculations
with incompressible flow calculations for jet #7 at 65 $^{\circ}$C**

Data Acquisition System

To record temperature versus time data of a thermocouple, we used Keithley Matrabyte (Cleveland, OH) hardware (DAS-TC board) and their TestPoint software in our experimental set up. This software was programmed to record the temperature of T –type thermocouple at a frequency of 10 Hz. The Keithley data acquisition board used in the study had a capability to record the temperature from six channels simultaneously. This feature of the data acquisition board was used to record the temperature of multiple cookies placed simultaneously in the system. To record the temperature of hot air in the oven, a T- type thermocouples was placed under the center of jet tube # 9 at a distance of 20 mm from the end of the tube. In addition to this arrangement, the oven control system had in built thermocouple to record the temperature of the hot air in the plenum chamber. A good agreement (i.e. maximum difference of 1 °C) was observed between the temperatures recorded by the in built thermocouple and the external thermocouple (under jet # 9).

To record the heat flux value for the measurement of local heat transfer coefficient in a jet impingement system the DAS 1800- HR board also provided by Keithley instruments was used (Chapter 3, Section 3.5). The heat flux signal was in milli-volts. This signal was amplified 100 times using voltage amplifier and the amplified signal was supplied to the DAS 1800-HR, which was calibrated to read the voltage output in the range of 0-10 V. This voltage output was later converted to heat flux value using the standard calibration data provided by the

manufacturer of the heat flux gage (RdF Corporation, MA). The details of this approach for the measurement of heat flux are described in the design of experiments for the local maximum in the heat transfer coefficient (Chapter 4).

Model Cookies

Model cookies made of aluminum metal were used in the study of heat transfer characteristics in a hot air jet impingement oven. Each model cookie had a small hole at its base from which the thermocouple was inserted. The diameter of the hole in each disk was 1.58 mm and the height of the hole was always chosen as half the height of the cookie shaped disk. Thus temperature response at the center was monitored in all the model cookies. The selection of material and dimensions of the model cookie was based on the requirements of the approach of lumped mass analysis (the details of this analysis are discussed in the chapter 2). For lumped mass analysis approaches the Biot number defined, as $Bi = h \ H/k_s$ should be less than 0.1. This requirement had to be verified because value of heat transfer coefficient was not known before experiments were carried out. The other considerations in the selection of the size of the cookie was to select model cookie dimensions close to the actual cookie size so that we can obtain a realistic estimation of heat transfer coefficient in jet impingement oven system, which can be used for the real food baking system in such ovens.

Heat Flux Gauge

To measure a maximum in the local heat transfer coefficient for model cookies in jet impingement oven, a heat flux gage was used. Several studies (Gardon, and Akfirat, 1965; Martin, 1977) have shown the existence of this maximum right under the center of the jet. In their studies, a flat electrically heated plate was used to measure the local heat transfer coefficient. The details of this arrangement are given by Martin, (1977). Most of these studies focus on cooling applications of high-speed jets. In our study we had cylindrical geometry objects (cookie shaped object) placed under hot air jets and to measure the local heat transfer coefficient a heat flux gage was mounted at the center of the top surface of the model cookie. The heat flux gage works on the principle of generation of voltage signal based on the temperature difference across two thin parallel plates filled with a material of known conductivity. The heat flux gage also measures the surface temperature of the heat flux gage. The equation for estimation of the local heat transfer coefficient from the data of heat flux (q) and the surface (T_s) and the air temperature (T_a) is given below:

$$ h = C_f * \frac{q}{(T_s - T_a)} \qquad (3.3) $$

Where q is the heat flux (W/m^2)

The heat flux gage used in experiments was acquired from RdF Corporation, MA. The calibration voltage output for the heat flux gage at 70 ºF was 2.65

microvolts/Btu/ft^2.hr. Voltage correction factor, C_f (output multiplication factor vs. receiving surface temperature) in the measurements of the heat flux based on 70 °F as a base value (C_f = 1 at 70 °F) for gage # 20472-3 is shown in **Figure 3.6** (provided by the manufacturer). In the experimental set up the heat flux gage was mounted on top of a metal cookie surface using permanent bond cement (AP cement) also provided by RdF Corporation, MA. Cement was applied to the surface of the model cookie and gage was pressed against the surface using 30 kg of weight over a period of three hours. The use of the permanent bond cement ensured good contact between the heat flux gage and the cookie surface, thus reducing any loose contact errors between two surfaces.

$$y = 1.0336e^{-0.0021x}$$
$$R^2 = 0.9932$$
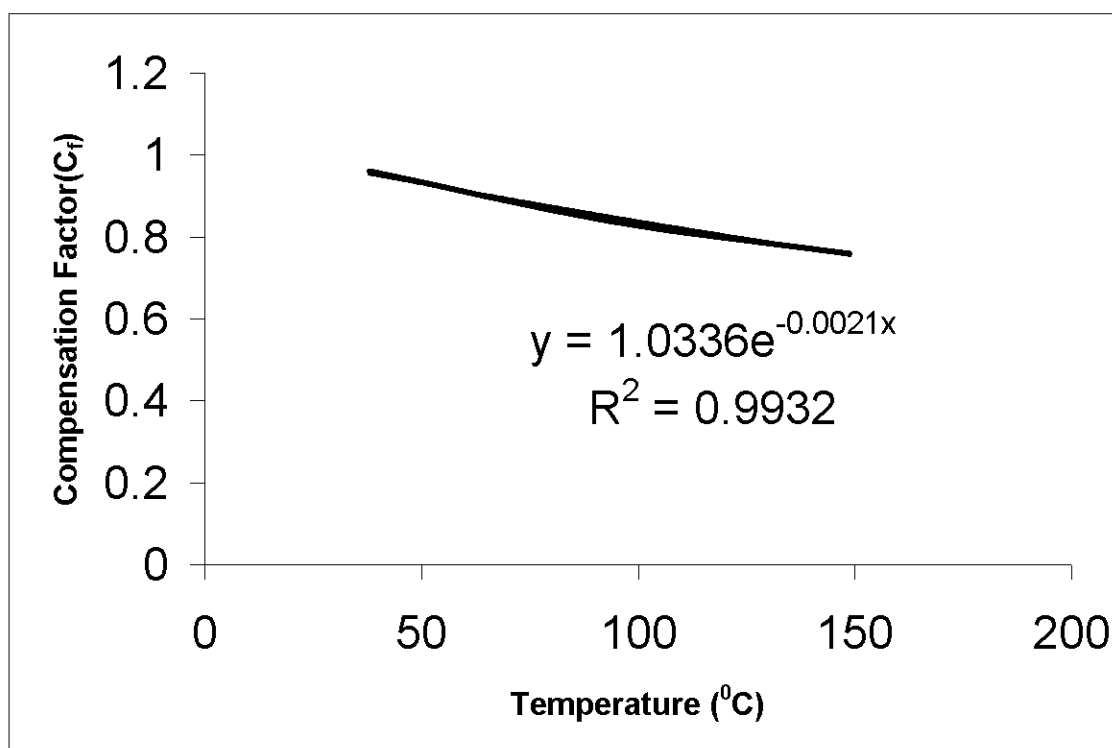
Figure 3.6

Plot of voltage correction factor for RdF heat flux gage # 20472-3
(Output correction factor vs. surface temperature)

Experimental Measurement of Heat Transfer Coefficient

The experiments for the measurement of heat transfer coefficient in a hot air jet impingement oven were designed for the following two objectives:

1. Measurement of top surface average heat transfer coefficient
2. Measurement of local heat transfer coefficient

In all the above experiments the base of the aluminum bowl was insulated with a thin wooden plate. This was done to minimize conduction heat transfer from the base of the aluminum bowl to the model cookie. The thermocouples were inserted into the base of the model cookies/ model hot dogs through a hole drilled in the wooden plate. The diameter of this hole was just enough to allow the thermocouple tubing to pass through it.

Measurement of the average top surface heat transfer coefficient for model cookies:

Measurement of Average Heat Transfer Coefficient

For the measurement of average heat transfer coefficient, experiments were carried in a pilot scale jet impingement oven (JetZone, Wolverine Corporation, Merrimac, MA). The pilot scale oven had 13 jet tubes with inter tube spacing of 53.4 mm and tube diameter of 18.6 mm. Details of the oven geometry are described in (Nitin and Karwe, 2001). During processing, hot air was

directed downward from the plenum chamber through a series of 13 jet tubes to impinge on the product in the bowl, which was placed on a turntable. Since we were interested in flow field and heat transfer characteristics of a single jet, the model cookie shaped was placed in a well in a wooden plate. Schematic drawing of the set up is shown in **Figure 3.7**. Thus only the top surface area of the model cookie was exposed to the hot air jet. Lumped mass approach (for Biot number < 0.1) was used to calculate the average heat transfer coefficient based on temperature- time data for the model cookie.

To experimentally determine the average heat transfer coefficient for a single impinging jet, temperature vs. time response of a model cookie of 50 mm diameter and 10 mm thickness placed on a wooden plate was recorded. To prevent any conduction from the bottom of the bowl, the bottom side of the cookie was insulated using wooden piece. Air Temperature was varied at two levels (65 °C and 150°C). The experiments were carried out at two jet velocities namely 22 and 42 m/s.

Jet

Thermocouple

Wooden block

Model cookie with
only top surface
exposed to Jet
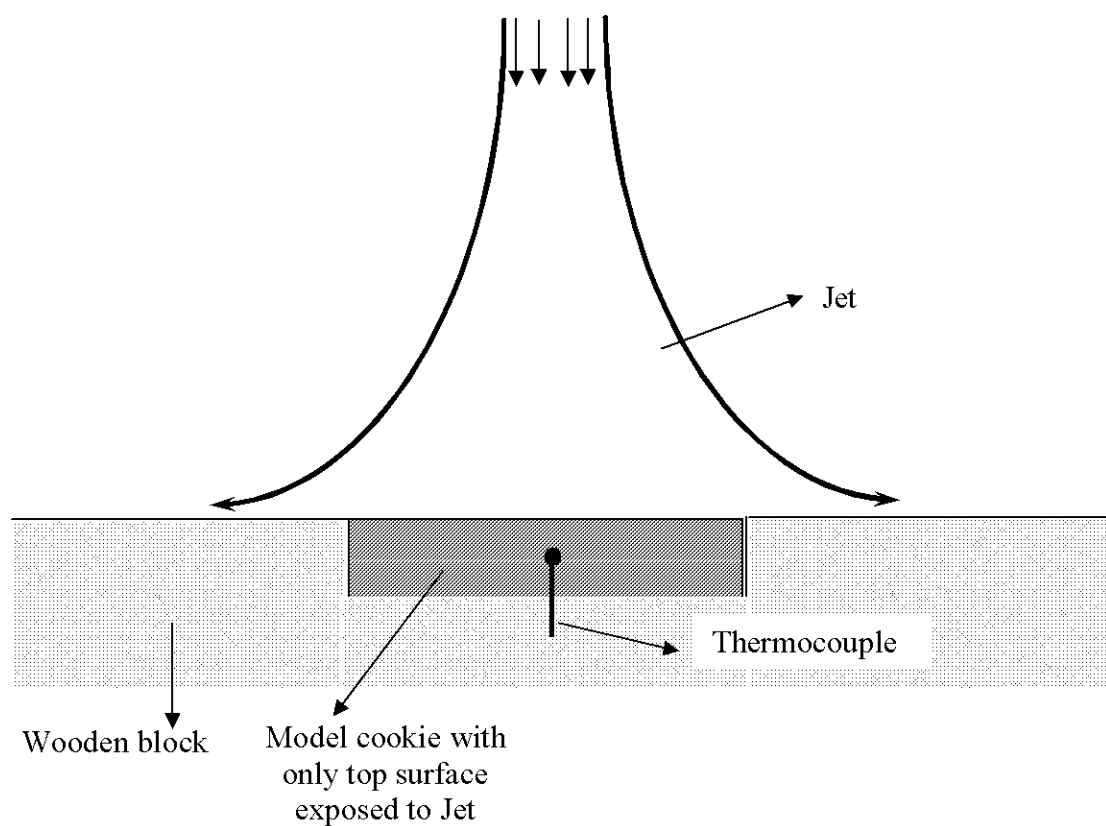
Figure 3.7

**Schematic representation of jet impinging on a model cookie with
only top surface area exposed**

Measurement of Local Heat Transfer Coefficient

The objective of this experimental set up was to determine the local maxima in heat transfer coefficient in a jet impingement system. The local maximum in heat transfer coefficient have been shown to exist right under the jet (Gardon and Akfirat, 1965; Martin, 1977). Local heat transfer measurements were carried out using a heat flux gage attached on top a model cookie of 50 mm diameter. The heat flux gage was attached at the center of the top surface of the model cookie using the permanent binding cement (AP- cement, provided by RdF Corporation). Arrangement of the heat flux gage on model cookie surface is shown in **Figure 3.8**.

The model cookie with heat flux gage attached at the center was placed under jet # 7, the center jet. Experiments were carried out at four conditions of plenum pressure (250, 500, 750, 1050 Pa) and two conditions of temperature (65 °C, 149 °C). The surface temperature of the cookie and the hot air temperature of the jets were recorded. The output of heat flux generated by the heat flux sensor was in the range of millivolt values. The output voltage value was converted to heat flux value by using the conversion factor provided by the manufacturer, which was 2.65 (μV/(BTU/ft^2 hr)) at 70 °F for the particular gage (gage #20472-3). The correction factor for this conversion factor at any other temperature was obtained from the curve provided by the manufacturer. The curve for the output correction factor was shown in **Figure 3.6**. A trend line was fitted to the curve to

get the desired equation and based on the equation the output multiplication factors were calculated at different surface temperatures. The simultaneous recording of the heat flux value, surface temperature and the hot air temperature allowed us to calculate the heat transfer coefficient value as described in formula given by equation (4.4).

$$h_{max} = C_f * q / (T_0 - T_S) \tag{3.4}$$

where,

q= Heat flux (W/m^2)

T_0 = Jet air temperature ($^\circ C$)

T_S = Heat flux gage surface temperature ($^\circ C$)
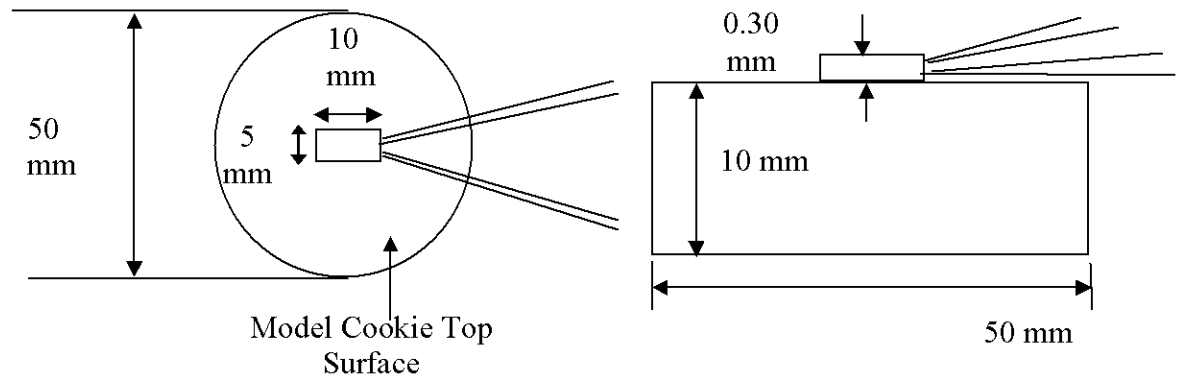
Figure 3.8

**Schematic representation of top view of model cookie with 50 mm diameter with
heat flux gage attached to the top surface of the cookie**

Theoretical Analysis

In this section, discussion will be focused on theoretical basis of experimental and numerical studies conducted as outlined in the previous section. Theoretical basis will be discussed for the following:

1) Experimental approach to measure surface heat transfer coefficient

2) Flow field simulation (details of turbulence model)

3) Mathematical model for baking (details of transport processes)

Measurement of Average Surface Heat Transfer Coefficient

During baking or cooking in a jet impingement oven, simultaneous heat and mass transfer occurs. The resistance to heat transfer in actual baking operation lies both in a hot air and a food material. Since our goal was to determine only the surface heat transfer characteristics, we chose a lumped mass approach. In this approach the resistance offered by the material to heat transfer was kept negligible by ensuring that the Biot number for model cookies was less than 0.1 (Ozisik, 1993).

By choosing the material of model cookies as aluminum, which has high thermal conductivity (200 W/mK), the Biot number (hH/k_s) based on thickness of these model cookies, where h is the average surface heat transfer coefficient, k_s is the conductivity of the solid, H is the thickness of the disk (10 mm) was expected to be much less than 0.1 if the surface heat transfer coefficient is less than 2000 W/m^{2}K. This value of heat transfer coefficient is approximately 10

times higher than the value reported in the literature (Martin, 1977). This requirement was later verified from the experimental results. It is important to note that during jet impingement, we have forced convection heat transfer and in forced heat convection the h value depends only on the shape of the object and not on the thermophysical properties of the object. Selection of this lumped mass approach based on aluminum model cookies also eliminated the mass transfer process during heating of the model cookies. So from the transient heat transfer response of the system to step change in ambient temperature, h can be calculated from the response time τ of the system, using the following equation.

For Bi < 0.1, the variation of temperature of the cookies with time for a step change in the surrounding temperature is given by

$$(T_o\text{-}T_t)/(T_o\text{-}T_i) = e^{-t/\tau} \qquad\qquad (3.5)$$

where

T_t= Temperature at the center of the cookie at any time t

T_i =Initial temperature of the cookie

T_o = Temperature of the heating medium

t = Time

τ = Time constant of the cookie =m c_p / h A.

where

m= Mass of the cookie

c_p= Heat capacity

h= Average surface heat transfer coefficient

A= Surface area of the cookie.

Slope of the plot of ln $(T_o\text{-}T_t)$ /$(T_o\text{-}T_i)$ vs. time (t) will be $-1/\tau$ from which h can be calculated. **Figure 3.9** shows the above representative plot between the dimensionless temperature ratio and time from which "h" was obtained by calculating the slope of the plot.

$\ln\left((T_o\text{-}T_t)/(T_o\text{-}T_i)\right)$

$Slope = -hA/mc_p$

Time (t)
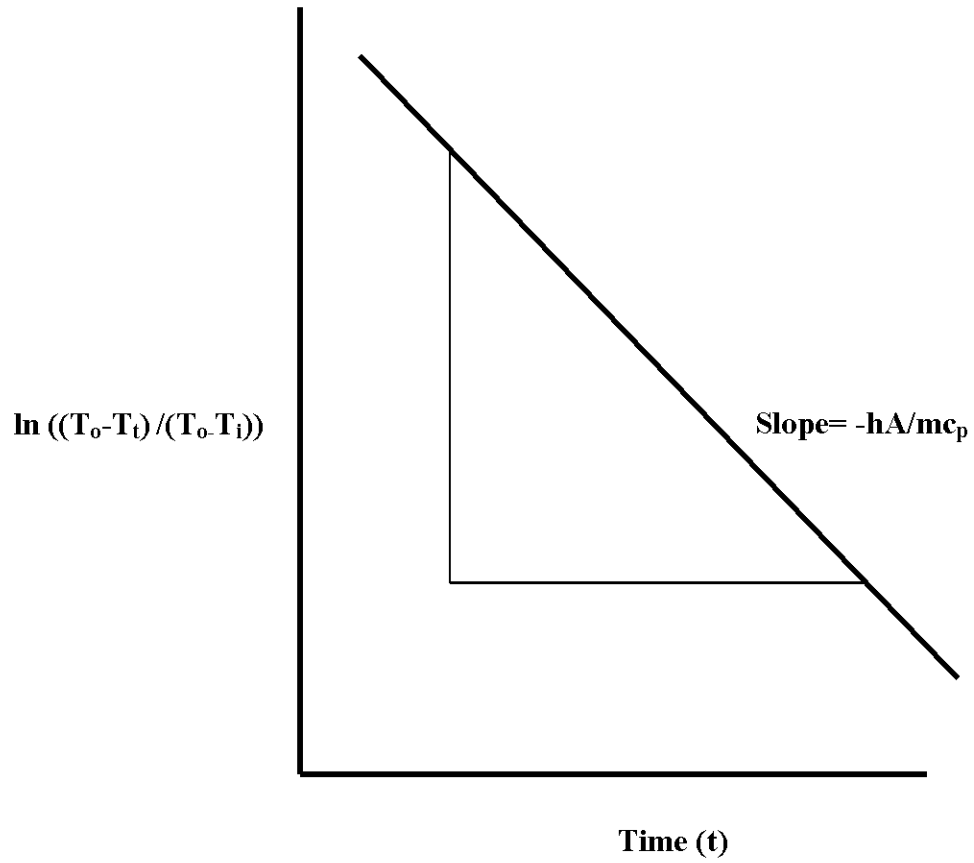
Figure 3.9

Method to calculate average heat transfer coefficient

Mathematical Modeling of Flow Field Simulation

Figure 3.10 describes the schematic outline of an impinging jet on a flat

surface. The schematic shows a circular jet in a chamber with a wall on top and

bottom surfaces. The sides of the chamber are open to the environment. The

turbulent circular jet enters through a nozzle opening on top of the chamber and

impinges on a bottom wall.

Jet Inlet
V=Inlet Velocity

Top (wall), u= 0; v=0

d

r

z

Specified Velocity Profile

z

Exit
P= Patm

Jet

Bottom, (wall), u= 0; v=0

u= Axial velocity, m/s
v=Radial velocity, m/s
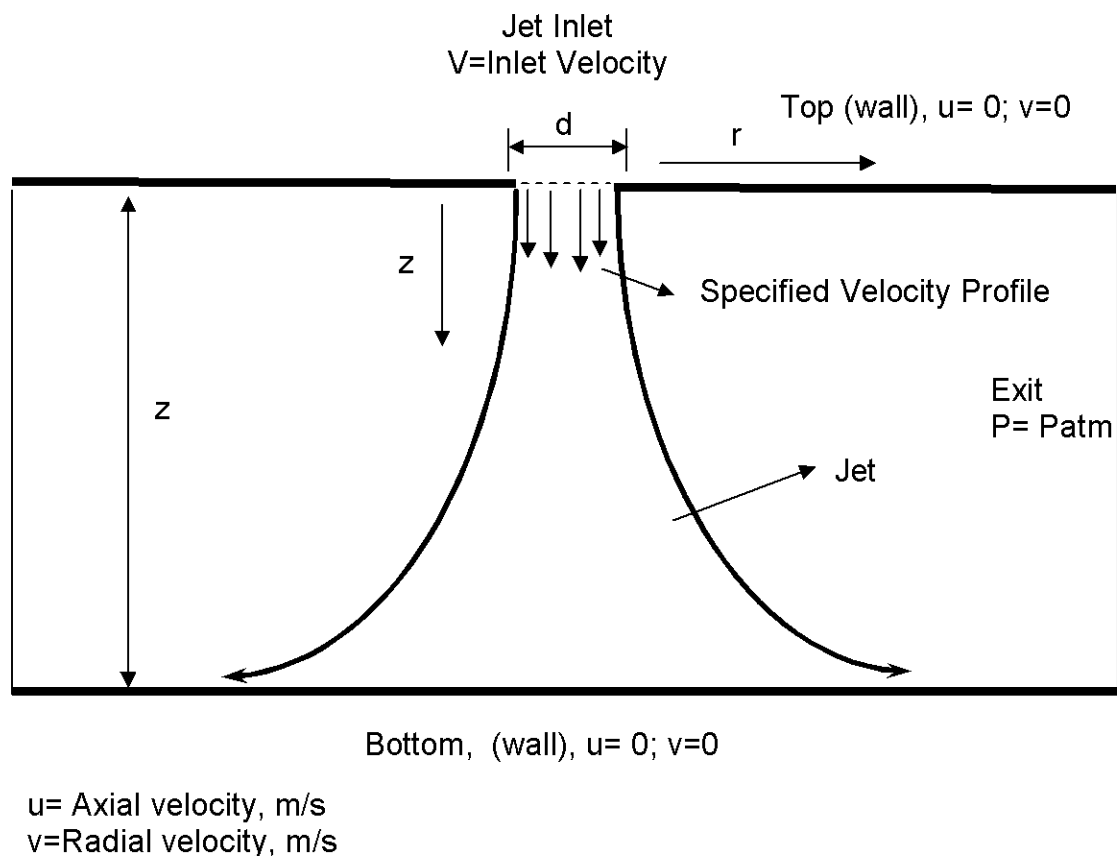
To numerically simulate flow field of a turbulent single impinging jet as

shown in Figure 3.10, two-equation turbulent model was used. In this model,

transport equations were formulated both for the velocity and the length scale or

alternative pair that make up eddy viscosity. For all two-equation models, kinetic

energy equations (k) are used for the velocity scale and for modeling length scale dissipation rates (ϵ) are most widely used. The combination of these approaches led to the development of k-ϵ model for turbulence. In this study, we had chosen to use two-equation model for numerical simulations because of its established reliability in prediction of large variety of turbulent flow fields and relative ease of formulation (discussed in literature review, Chapter 1). This k-ϵ model was developed by Jones and Launder (1972). This model like other two-equation models is based on standard Boussinesq hypothesis for estimation of Reynolds stress (Hallback et al, 1996), transport equations for kinetic energy (k) and an auxiliary term for length scale (which in case of k- ϵ model is ϵ). There are other variants of two-equation models e.g. k-ω model. The standard equations for k- ϵ model are described below:

Mean flow equation based on Boussinesq hypothesis:

$$\frac{DU_i}{Dt} = \frac{\partial}{\partial x_j}\left[-\left(\frac{P}{\rho}+\frac{2K}{3}\right)\delta_{ij} + 2(v+v_T)S_{ij}\right] \qquad (3.6)$$

Transport equation for kinetic energy:

$$\frac{DK}{Dt} = 2v_T S_{ij} S_{ij} - \varepsilon + \frac{\partial}{\partial x_i}\left[\left(v+\frac{v_T}{\sigma_k}\right)\frac{\partial K}{\partial x_i}\right] \qquad (3.7)$$

ϵ-equation:

$$\frac{D\varepsilon}{Dt} == C_{\varepsilon 1}\frac{\varepsilon}{K}2v_T S_{ij}S_{ij} - C_{\varepsilon 2}\frac{\varepsilon^2}{K} + \frac{\partial}{\partial x_i}\left[\left(v+\frac{v_T}{\sigma_\varepsilon}\right)\frac{\partial\varepsilon}{\partial x_i}\right] \qquad (3.8)$$

and the eddy viscosity relation

$$v_T = C_\mu \frac{K^2}{\varepsilon} \qquad (3.9)$$

where:

U= Mean velocity

S_{ij}= Mean strain rate tensor

K= Turbulent kinetic energy per unit mass

P= Mean pressure

ε =Dissipation rate (Homogeneous)

v =Kinematic molecular viscosity

v_T = Kinematic eddy viscosity

$C_{\varepsilon 1}$, $C_{\varepsilon 2}$, σ_ε and σ_k are model parameters in standard k- ε model whose values

are 1.44, 1.92,1.3 and 1.0 respectively.

Numerical Simulation of Flow Field for a Single Impinging Jet:

To numerically simulate flow field on an impinging jet, governing mass and momentum equations were solved using a commercial computational fluid dynamics (CFD) code Fluent (Version 6.0, Fluent, Inc., Lebanon, NH). The jet impingement system was modeled as a 2-D axi-symmetric turbulent jet impinging on a flat surface. Because of axial symmetry, numerical simulations were carried out in a radial slice of the system. Computational mesh was generated using commercial mesh generating software (Gambit, Lebanon, NH.). For all flow field simulations structured uniform face mesh of quadrilateral geometry was used to discretize the computational domain. The details of the geometry, boundary conditions for nozzle to plate spacing (z/d) of 5 are shown in **Figure 3.10.** In this study nozzle to plate spacing (z/d) ratio was used as a parameter for simulation of flow field. Steady state flow field of an impinging jet was modeled using

standard k-ε model. Flow field for a turbulent impinging jet on a model cookie was solved using the standard k-ε model (Arpaci and Larsen, 1984; Jaluria and Torrance, 1986) to simulate turbulence. Flow field simulation was carried under isothermal conditions, thus energy equation was not solved along with momentum and mass conservation equations for this case. Velocity boundary condition at air inlet was set using a user-defined function (UDF) to generate an inlet velocity profile based on the turbulent flow characteristics of a circular pipe. Equation (3.10) represents the inlet velocity profile used to model the inlet velocity boundary condition.

$$u = u_{max}*(1-r/R)^{1/7}$$ (3.10)

where,

u = axial (z) component of velocity

R = radius of the jet inlet

r = radial distance from the jet axis

u_{max} = maximum center line velocity

Simulated flow field of an isothermal impinging jet was compared with the experimental velocity measurements carried by Marcoft et al, (1999) using LDA system. To directly compare simulation results with experimental data, the computational geometry was created to directly match the z/d spacing (nozzle to plate spacing) of the experimental system i.e. z/d =5. Maximum jet inlet velocity and hot air temperature were also matched with the velocity and temperature conditions for the experimental system.

Jet Inlet
V=Inlet Velocity

R

Top (wall), no slip, u= 0; v=0

Z

Specified Velocity
Profile

Axis of
Symmetry

$\dfrac{\partial u}{\partial r} = 0$

Exit
P= Patm

Bottom, (wall), no slip, u= 0; v=0

Figure 3.10

Details of geometry and boundary conditions for numerical simulations of a single jet impinging on a flat plate at z/d =5

Numerical Simulations of Single Jet Impinging on a Model Cookie

Governing mass, momentum and energy conservation equations in the computational domain were solved using a commercial computational fluid dynamics (CFD) code Fluent (Version 6.0, Fluent, Inc., Lebanon, NH). To numerically simulate the thermal transport for a single impinging jet on a model cookie, the conjugate heat transfer problem was solved, i.e., conduction heat transfer inside the cookie was coupled with the convection heat transfer in the air at the surface of the model cookie. For the purpose of numerical simulation in Fluent, two continuum domains (fluid and solid) were created to model the conjugate heat transfer between the impinging jet and the model cookie. The surfaces of solid domain were coupled with the fluid domain by defining a common edge between the fluid and solid geometry. One side of the edge had the thermophysical properties of model cookie and the other side had the thermophysical properties of air. Using this the boundary condition at the common edge was determined based on solution of conjugate heat transport problem.

The jet impingement system was modeled as a 2-d axisymmetric turbulent jet impinging on a cylindrical model cookie. Because of axial symmetry, numerical simulations were carried out in a radial slice of the system. The details of the geometry, boundary conditions and the computational mesh for nozzle to plate spacing (z/d) of 3 are shown in **Figure 3.11**. When we wanted to focus on the heat transfer only from the top surface, the arrangement in **Figure 3.11** was

modified such that side surface of the cookie was covered with a wooden insulation as shown in **Figure 3.7**.

Jet inlet
u= u(r), turbulent
u = u_{max}, T=T_{jet}

Top surface
u=0, v =0, $\dfrac{\partial T}{\partial z} = 0$

r

Computational
domain: radial slice

$\dfrac{\partial u}{\partial r} = 0$ d = 20 mm

z = 60 mm

$\dfrac{\partial T}{\partial r} = 0$

100 mm

Exit
P=P_{atm}
T=T_{jet}

t = 10 mm

25 mm

Axis of symmetry

z

Bottom surface
u=0, v =0, $\dfrac{\partial T}{\partial z} = 0$
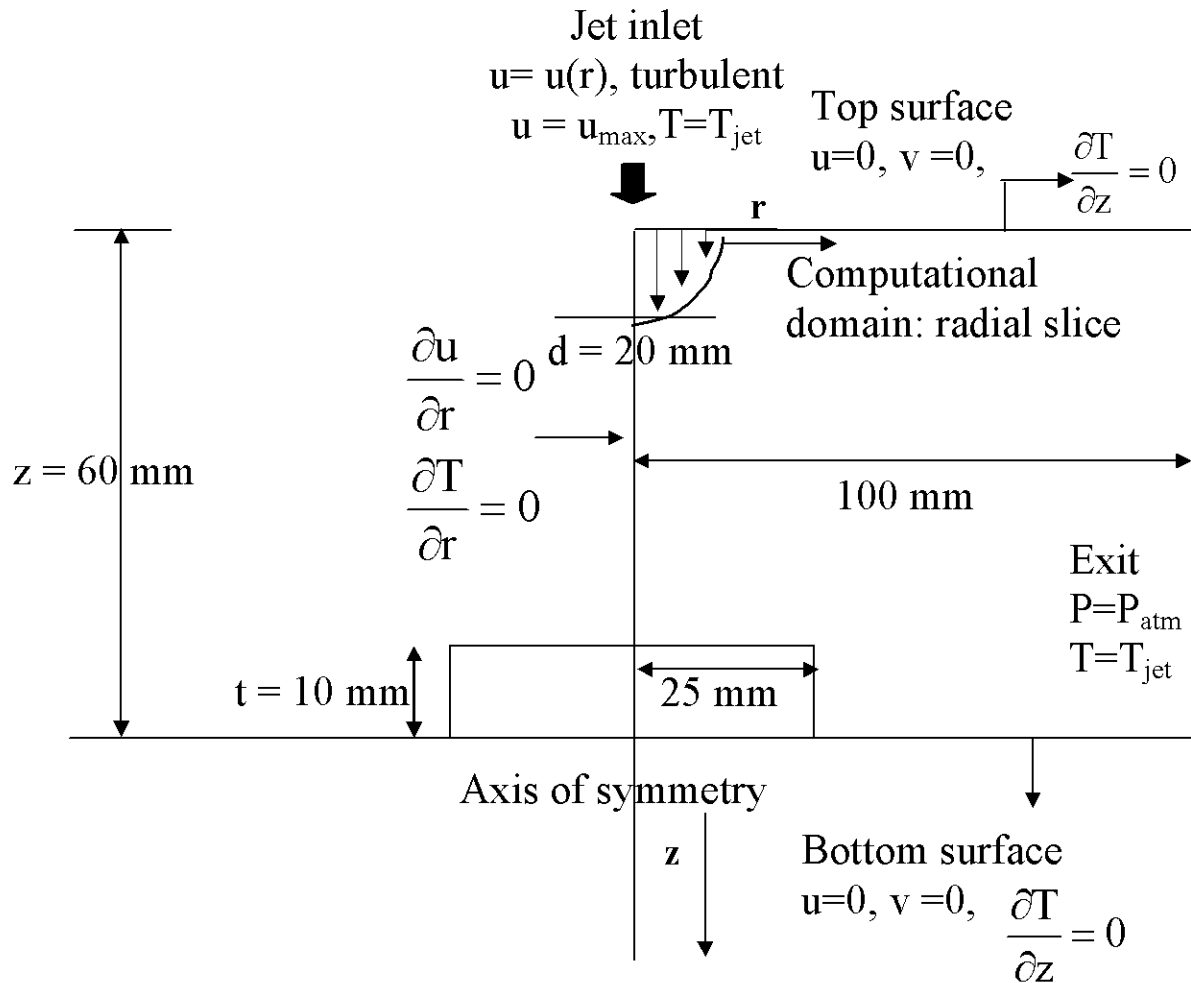
Figure 3.11

Details of geometry and boundary conditions for numerical simulations of a single jet impinging on a model cookie (axisymmetric model) at z/d =3

To measure local heat flux, we used a heat flux gage in the experiments, which was bonded at the center of the top surface of the cookie as shown in **Figure 3.8**. Therefore, the numerical simulations were carried out with and without a heat flux gage to investigate how much interference was caused by the heat flux gage. Thus, the effect of thermophysical properties of heat flux gage on the surface heat flux measurement was simulated (for more discussion on this, see Deo and Karwe, 1998). In the case of numerical simulation with the heat flux gage attached, three continuum domains were created (fluid domain, solid domain for heat flux gage, and another solid domain for model cookie). The solid domain of the heat flux gage was coupled with the fluid domain at the top and the solid domain of the cookie at the bottom. This coupling is achieved by having a common boundary condition at the interface of the heat flux gage with air and with solid cookie at top and bottom surfaces of heat flux gage respectively.

The computational grids for all numerical simulations were generated using a commercial grid generator Gambit (Fluent Inc, Lebanon, NH). For all cases in the numerical simulation, structured uniform face mesh of quadrilateral geometry was used to discretize the computational domain. The computational grid with model cookie for nozzle to plate spacing (z/d =5) of 5 is shown in **Figure 3.12**. The computational mesh was successively refined at three levels to check for grid independence of the numerical solutions. No significant improvements were observed in the numerical predictions of temperature and velocity distributions when the mesh interval size was 0.1 units (0.8 mm) of grid spacing or less for the computational domain. Hence it was used in all the subsequent

computations. Details of the number of quadrilateral elements and node points for mesh interval size of 0.8 mm for nozzle-to-plate spacing (z/d) of 2, 3 and 5 are shown in **Table 3.1.**

In the numerical simulation, first we solved for the flow field of a turbulent impinging jet on the surface of model cookie without any thermal transport, i.e., isothermal conditions at 298 K. After the steady flow field solution was obtained, thermal transport was turned on (energy equation was solved) and then the combined flow field and thermal transport in the air and the model cookie was solved as an unsteady state problem. The steady state flow field solution in the first step provides the initial condition for time evolution of unsteady state solution for the thermal problem. This step approach was possible because temperature and velocity solutions were not coupled in this problem.

r

z

Axis of
Symmetry

Exit

**Coupled Boundary
Condition**

Model
Cookie

Bottom surface

$$u=0, \quad v=0, \quad \frac{\partial T}{\partial z} = 0$$
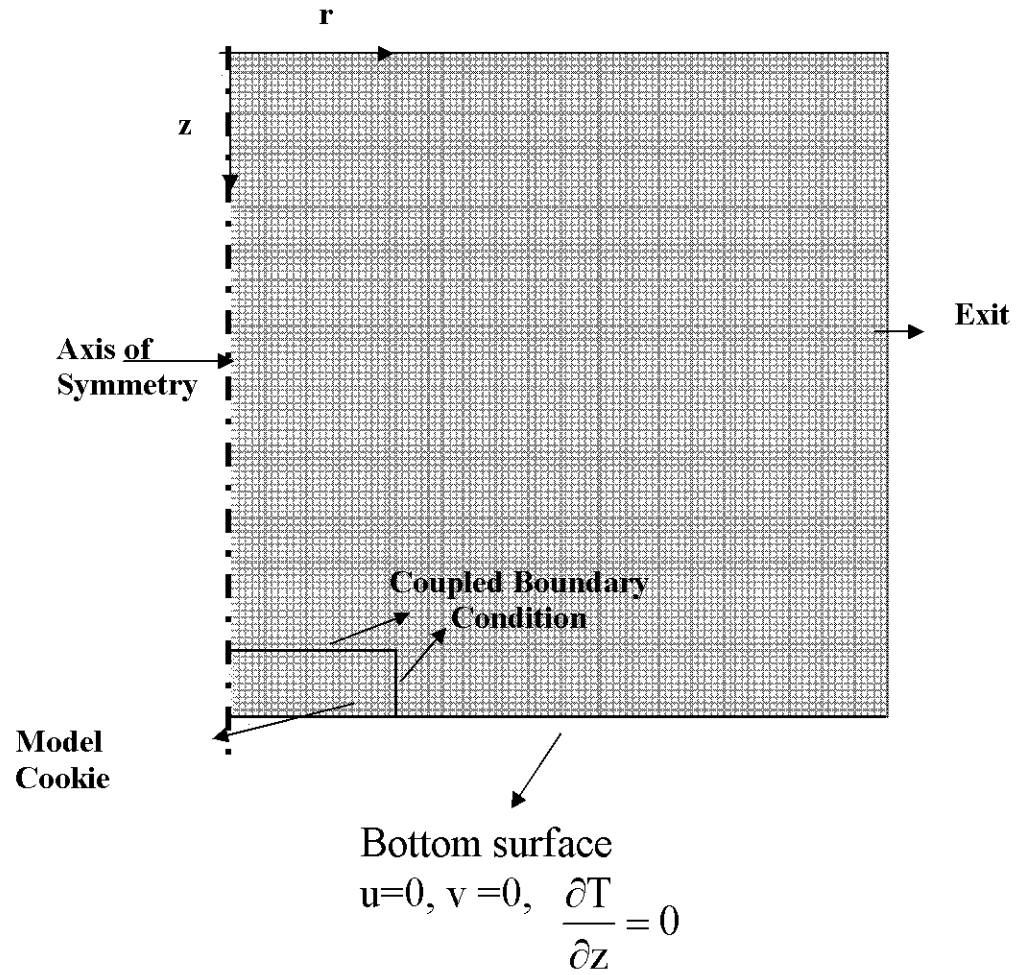
Figure 3.12

**Computational grid for numerical simulations of a single jet impinging on
a flat plate at z/d =5**

Table 3.1 Details of grid and geometry for numerical simulations

Property	z/d=5	z/d=3	z/d=2
# Nodes	10234	6150	4250
# Quadrilateral Cells	9750	5842	3808
z (mm)	100	60	40
d (mm)	20	20	20

Coupled thermal boundary conditions between air, the top and side surfaces were defined (edges of the cookie exposed to air) by a mesh design in which both the continuum domains (air and model cookie) were coupled by common edge (as shown in Figure 3.12). In addition, adiabatic thermal boundary conditions at the bottom edge of the model cookie and the top and the bottom walls of oven were used in all the simulations. The insulating boundary condition at the bottom surface of the cookie was used to simulate the conditions for a cookie placed on a wooden board in our experiments. All numerical simulations were carried out at hot air jet inlet temperature of 450 K.

From the numerical solution of temperature field, heat flux at the surface of cookie was calculated as

$$q = -k_{air} \left[\frac{\partial T}{\partial z} \right]_{air} \text{ at } z = 10 \text{ mm (top surface)} \tag{3.11}$$

The local surface heat transfer coefficient (h) was calculated as

$$h = q/(T_s - T_{jet}) \tag{3.12}$$

T_{jet} = jet air inlet temperature (°K)

T_s = surface temperature (°K)

k_{air} = thermal conductivity of air (W/mK)

To obtain the average heat transfer coefficient, the local heat transfer coefficient values were averaged over the surface area. Simulations were carried out at three different values of z/d spacing (jet nozzle to oven bottom wall spacing), i.e., 2, 3 and 5 for four different values of maximum jet centerline velocity (U_{max}), i.e., 10, 20, 30 and 40 m/s. Results for the average and local heat

transfer coefficient obtained from the numerical simulations were compared with the experimental results based on a study carried out in a pilot scale jet impingement oven for a case of z/d =3. In the experiment we could not vary the value of z/d. For z/d= 3, numerical simulations were also carried out for U_{max} = 22, 29, 36, and 42 m/s, to exactly match the experimental conditions in a pilot scale oven.

Numerical Simulation for Cylindrical Shaped Object

To numerically simulate the thermal transport for a single impinging jet on a curved cylinder, we selected model hot dog geometry. Similar approach as discussed in previous section (numerical simulation of cookie shaped object) was carried out to develop the computational mesh, boundary condition and CFD set up for the cylindrical hot dog shaped geometry. The conjugate heat transfer problem was solved, i.e., conduction heat transfer inside the cylinder was coupled with the convection heat transfer in the air at the surface of the model cookie. This problem was also modeled as 2-d jet impinging on the cylindrical geometry. The details of the geometry and the computational mesh for z/d =3 and cylinder of diameter of 1 cm are shown in **Figure 3.13.**

For this set up also, both local and average surface heat transfer coefficient were obtained using numerical simulation. Simulations were carried out for three different cylindrical geometries, i.e., cylinder diameter of 1 cm, 1.5 cm and 2 cm at for four different values of maximum jet centerline velocity (U_{max}),

i.e., 22, 29, 36 and 42 m/s. These velocities were chosen to exactly match the jet flow conditions in the experimental set up.

Comparison of numerical simulation with experimental measurements for cylindrical hot dog geometry

Experiments for measurement of average surface heat transfer coefficient were carried out using aluminum model cylinders of same dimensions as used in numerical simulation at two levels of maximum jet velocity of 22 and 42 m/s. Average surface heat transfer coefficient obtained using numerical simulation was compared with experimentally measured average heat transfer coefficient. Experiments were also performed on real hot dogs. In these experiments hot dog center temperature vs. time was measured at 42 m/s at two levels of temperature i.e. 65 °C, 149 °C. Numerical simulation was carried under same set of experimental conditions using thermophysical properties of real hot dog to simulate the rise of center temperature as a function of time. Simulation was carried out as a conjugate heat transfer problem as described above for the prediction of surface heat transfer coefficient. Details of thermophysical properties of model aluminum cylinders/ cookies, model food system and real hot dogs are provided in **Table 3.2.**

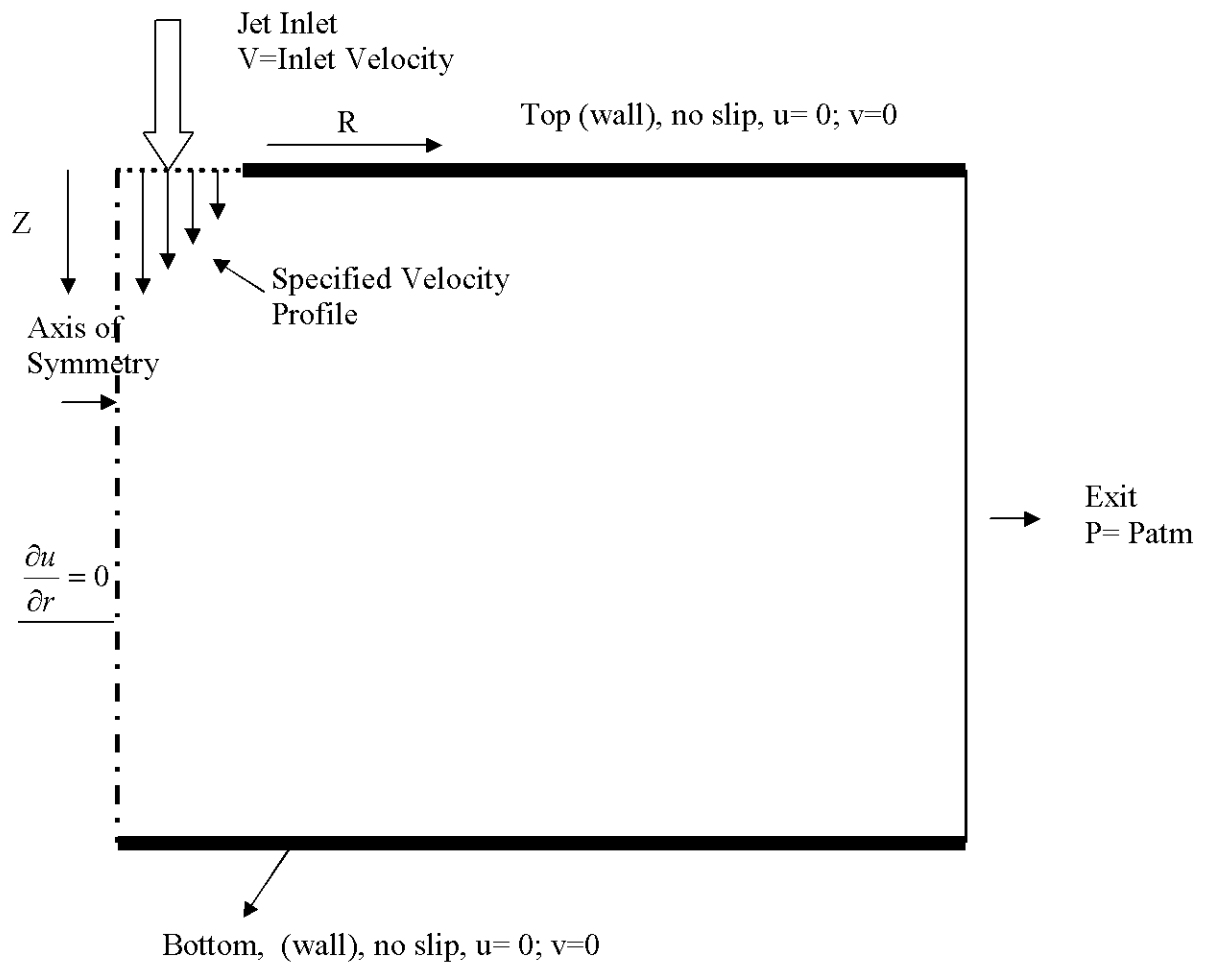Jet Inlet

Wall

Line of
symmetry

Open outlet

Half cylinder

Wall
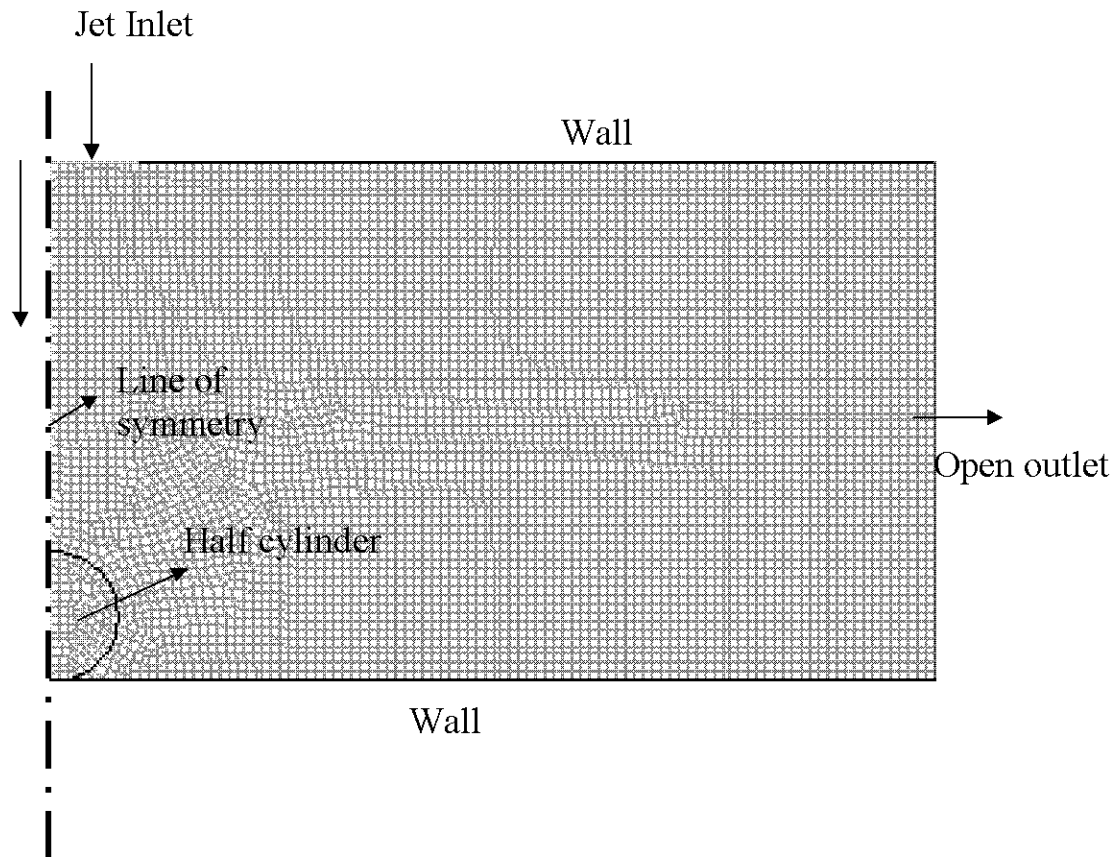
Figure 3.13

**Details of geometry and boundary conditions for numerical
simulations of a single jet impinging on a model cylinder at z/d =3**

Table 3.2

List of thermophysical properties of model cylinder/cookie, representative food material and real hot dogs

Material	Density (kg/m^3)	Cp (Specific Heat) J/kgK	Thermal Conductivity W/mK
Aluminum	2719	871	202.4 (Ozisik, 1993)
Hypothetical Food Material	1000	3500	0.5 (Choi and Okos, 1985)
Real Hot Dogs	1200	3300	0.4 (Choi and Okos, 1985)

Mathematical Modeling of Baking Process

In this study, in-depth analysis of mathematical modeling of a baking process was carried out. To develop a comprehensive understanding of the role of various transport processes during baking, mathematical models were developed. These baking models are derived from initial work carried by Zanoni et al. (1994), and were modified to include transport terms for vapor transport and to improve coupling of heat and mass transfer processes during baking. The overall aim of this modeling process is to evaluate the predictions of temperature and moisture content from various mathematical models with experimental observations. Based on these predictions, we can estimate the crust kinetics and thickness as a function of various parameters in design and operation of jet impingement baking.

Phenomenological Model of Crust and Crumb Based on Zanoni et al., (1993, 1994, 1995)

According to this phenomenological approach, baking is divided into two regions- Crust and Crumb. Crust is defined as a region in which temperature approaches the temperature of hot air, while crumb is a region in which temperature asymptotically approaches 100 °C. In this model, the transient distribution of temperature and moisture in the product during baking is determined by formation of an evaporation front at 100°C as shown schematically in **Figure 3.14**.

In early stages of baking (**Figure 3.14 a**), moisture loss from a food product is controlled by mass transfer coefficient at the surface. The crust starts to form at the surface when temperature of the top layer reaches 100°C. At that point, temperature remains at 100°C until moisture level drops to equilibrium moisture content M_e. After that the interface moves inside the product. On one side of the front is the crust where moisture is M_e and temperature asymptotically approaches the oven temperature. The crumb is defined where moisture is greater than M_e and temperature asymptotically tends to 100°C. Others have used a similar definition of crumb (Zitny, et al., 2002). The crust has much lower thermal conductivity as compared to the crumb. Thus, once the crust is formed, the transport problem is controlled by the rate at which heat can be transferred through the crust.

In Zanoni's model, it is assumed that moisture evaporating at the interface goes through the crust region without much resistance. According to this model, the rate of vapor formation and transport is controlled by a net rate of thermal flux within a control volume in a crust region. This implies that once a vapor is formed, it is transported out of food product. Hence, there is no resistance to vapor transport in a crust region. This model does not account for any pressure-associated flow of vapor in a food matrix (Darcy's law formulation). Thus, there is no coupling of pressure driven flow with heat and mass transfer associated diffusion of moisture in a food matrix. Further this model does not consider the effect of moisture migration due to temperature gradients (soret effect) during a baking process. In this model, a simple diffusion process controls the moisture

transport in a crumb region. This diffusive process is expected to have a small contribution to the total moisture efflux as compared to vapor transport during a phase change process in the crust region. Thus, in Zanoni's model there is a very limited coupling of heat and mass transport terms in simulating a baking process.

In this study we have made various modifications to this model. In a major modification to this phenomenological model, we have introduced a vapor transport term, which provides the rate of vapor generation and transport based on partial pressure of moisture content within a food matrix. In this model, vapor transport rate is mediated by rate of vapor diffusion, which is determined based on a gradient of partial vapor pressures at a given location within a food matrix. Introduction of this term overcomes limitations of the Zanoni's model where a baking process is predominantly controlled by thermal energy. Further we have also evaluated contribution of the Soret effect on diffusion of moisture within a food matrix to enhance coupling of heat and mass transfer processes.

Potato as a Model Food System

In this study we have used potato as a model food system to understand the transport processes during baking. For numerical simulation, thermo-physical properties of potato were used and numerical simulation results were validated using the experimental data obtained from potato slices. The reasons for selection of potato were as follows:

1. Potato is a homogeneous material with known physical properties (Heldman and Lund, 1992; Rao and Rizvi, 1995).

2. Potato can be shaped into desired geometrical shape and it maintains its shape reasonably intact during thermal processing at high moisture levels.

3. Potato is a representative of high moisture (~80% w.b.) food system.

4. Potato is consumed as high moisture baked product with crust.

5. Use of potato as a model system for baking also help in reducing the complexity of baking processes in cakes and bread where significant changes in volume are accompanied with a baking process. These changes can often lead to development of porous cavities within the food matrix, which can limit the assumptions of continuous physical properties with in a food matrix. However, this is also a simple system.

Development of Mathematical Models

In this section, the mathematical details of various models are presented:

Mathematical Model Based on Zanoni's Formulation of Heat and Mass Transport Equations (Zanoni et al., 1994)

Based on Zanoni's formulation the baking process can be divided into three stages.

Stage I (T< 100 °C): In this stage the temperature of a particular control volume is less than 100 °C i.e. T(i) < 100 °C. The heat and mass transport equations to model the baking process are:

$$\frac{\partial(\rho_p C_p T)}{\partial t} = \frac{\partial}{\partial r}(k_p \nabla T))$$

(3.13)

$$\frac{\partial(\rho X)}{\partial t} = \frac{\partial}{\partial r}(D\rho \nabla X)$$

(3.14)

where ρ is density (kg m^{-3}), C_p is heat capacity (Jkg^{-1}K^{-1}), T is temperature (K), t is time (s) ∇ is differential operator (m^{-1}), k_p is thermal conductivity of food (W m^{-1} K^{-1}). The above equation (3.13) with appropriate thermo-physical properties, will be used to obtain the temperature within the interior of food matrix for all conditions when temperature is less than 100 °C.

Similarly equation (3.14) is used to model the mass transport process within a food matrix. In equation (3.14) X is moisture content (kg water/kg solids) and D is the <u>effective moisture diffusivity</u> (m^{2}s^{-1}), which is a function of moisture content X and temperature T. The D describes the combined transport of moisture via various mechanisms such as molecular diffusion, capillary motion,

liquid diffusion through solid pores, Knudsen flow, vaporization-condensation sequence flow and hydrodynamic flow within the product matrix (Sablani et al., 2000). Even though more elegant theoretical models for transport of moisture in food systems are being developed (for example, Ashim Datta's group at Cornell University), use of D is very practical and convenient, as adopted by many researchers (Sabalani et al, 2000; Maroulis et al., 2001). As illustrated in equations (3.13) and (3.14), there is no coupling between heat and mass transport processes during stage 1 of the baking process based on Zanoni's model.

These heat and mass transfer equations within a food matrix will be solved along with appropriate boundary conditions for surface heat and mass transfer.

Stage II: When T =100 °C

In this stage the heat and mass transport equations based on Zanoni's baking model are:

$$\frac{\partial T}{\partial t} = 0 \tag{3.15}$$

$$\frac{\partial(\rho X)}{\partial t} = \frac{\partial}{\partial r}(D\rho\nabla X) - (\frac{\partial}{\partial r}(k_p\nabla T))/L \tag{3.16}$$

During a phase change process, Zanoni's model assumes that the temperature of a particular location will remain constant until the moisture content has been reduced below critical equilibrium moisture. This assumption leads to equation 3.15 for modeling heat transport process during a phase change state. For the mass transfer process, equation 3.16 represents the coupling between

heat and mass transport during a phase change process. In equation 3.16, the net flux of heat transfer within a control volume will be used for evaporation of moisture by providing the necessary latent heat for a phase transfer of water. Thus the rate of moisture evaporation is exclusively controlled by the rate of heat transfer within a control volume. This implies that Zanoni's model does not account for any resistance in vapor transport within a food matrix and its rate is independent of partial vapor pressure in a food matrix. This process leads to development of a crust region during a baking process as the moisture content drops below the equilibrium moisture content. Thus these assumptions in equation 3.15 and 3.16 lead to a constant temperature at a particular control volume. This also results in a rapid loss of moisture due to a phase transfer process. This model does not account for transport of vapor from a food matrix to a surrounding air.

IMPINGING JET
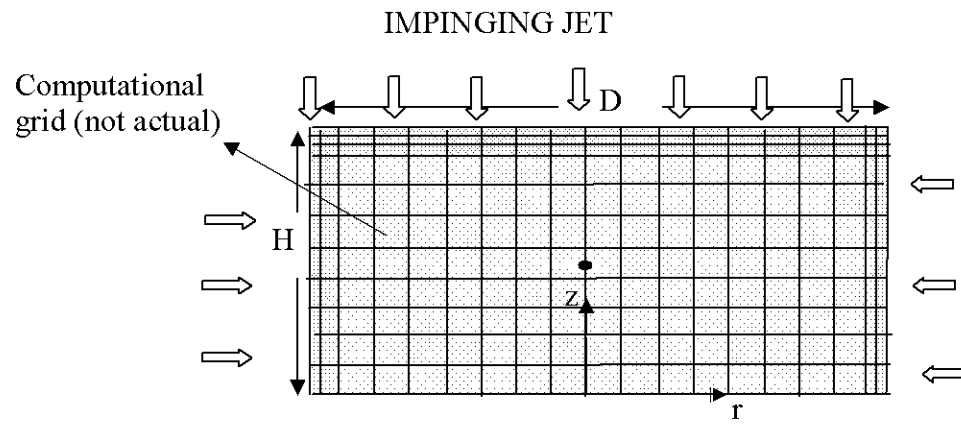
Figure 3.15

Schematic diagram showing top half of the food sample (not to scale) being baked in a Jet Impingement oven with jets from top and bottom

Stage III: When Temperature > 100 °C:

This represents the stage of baking when a crust region has been developed, the temperature at a particular control volume is greater than 100 °C and the moisture content is equal to the critical moisture content (M_e). During this stage the heat and mass transport process based on Zanoni's formulation can be modeled as:

$$\frac{\partial(\rho_p Cp_p T)}{\partial t} = \frac{\partial}{\partial r}(k_p \nabla T) \tag{3.17}$$

$$\frac{\partial(\rho X)}{\partial t} = 0 \tag{3.18}$$

Equations (3.17 and 3.18) represents rate of heat and mass transport respectively during a stage III of baking. In Zanoni's model, it is assumed that the heat conduction process equation determines rate of heat transfer within the food matrix and there is no change in moisture content within the crust region. This mathematical formulation does not have any coupling of heat and mass transport processes.

Modified Models of Heat and Mass Transfer during Baking

To address the limitations of various assumptions made in Zanoni's model, we developed two modified models. These modifications were aimed to provide a more realistic simulation of heat and mass transport processes during baking.

Modified Model 1: In this modified model, baking process is modeled based on the three stages as defined in Zanoni's model with modifications in vapor generation and transport rates within a food matrix. This modification also

changes the coupling between heat and mass transport equations during the three stages of baking. The modified model is discussed below.

Stage 1: When Temperature < 100 °C: In this stage the temperature of a particular control volume is less than 100 °C i.e. T(i) < 100 °C. The heat and mass transport equations to model the baking process are represented by equations 3.19 and 3.20 respectively:

$$\frac{\partial(\rho_p Cp_p T)}{\partial t} = \frac{\partial}{\partial r}((k_p \nabla T) - m_v * L) \qquad (3.19)$$

$$\frac{\partial(\rho X)}{\partial t} = \frac{\partial}{\partial r}((D\rho \nabla X) - m_v) \qquad (3.20)$$

The significant difference in these equations versus equations 3.13 and 3.14 in Zanoni's formulation is the introduction of m_v term in these modified equations, where m_v represents the vapor transport rate during baking. As shown in equations 3.19 and 3.20 this vapor transport rate term also couples the heat and mass transfer equations which were not coupled based on Zanoni's model.

The vapor transport rate is determined based on a following set of equations

$$m_v = -A \frac{\delta}{\mu} \frac{1}{RT} \frac{\partial p_v}{\partial r} \qquad (3.21)$$

$$p_v = a_w (X,T) * p_v^*(T) \qquad (3.22)$$

$$\frac{\partial p_v}{\partial r} = \frac{\partial p_v}{\partial X} * \frac{\partial X}{\partial r} = p_v^* * \frac{\partial a_w}{\partial X} * \frac{\partial X}{\partial r} \qquad (3.23)$$

$$m_v = -A * (\frac{\delta}{\mu} * \frac{p_v^*}{RT} (\frac{\partial a_w}{\partial X})(\frac{\partial X}{\partial r}) \qquad (3.24)$$

$$\frac{a_w}{X} = A * a_w^2 + B * a_w + C \qquad (3.25)$$

(3.21-3.25):

In this model, vapor transport rate is determined based on a gradient of vapor pressure (3.21). This approach has been used to model moisture transport during a drying operation (Dietl et al., 1998) Based on the fundamental relationships between vapor pressure, water activity and moisture content, the above equations can be transfromed to the form as represented in equation (3.23), which can be implemented in numerical discretization scheme based on conservation of mass and energy. All the terms in equation 3.23 can be either calculated or obtained from standard literature. To derive this equation (3.25) , following relationships among saturated vapor pressure, temperature, moisture content and water activity were used.

Since the vapor pressure in a given control volume is a function of water activity and saturated vapor pressure, we can calculate the gradient in vapor pressure in terms of gradient of water activity and saturated vapor pressure (equation (3.23)). The saturated vapor pressure can be calculated based on a known temperature within a control volume using a standard thermodynamic relationship between saturated vapor pressure and temperature. The gradient in water activity can then further be represented in terms of moisture gradient as shown in equation (3.23). Water activity at a particular moisture content can be calculated based on GAB equation as represented in equation (3.25). The terms δ/μ in equation (3.24) respresent the ratio of vapor diffusivity and vapor diffusion resisitance. In this study the ratio of δ/μ was obtained from the literature.

In this modifications, the mass transport rate is modeled using both liquid and vapor transport terms based on gradient in moisture content and gradient in partial vapor pressure respectively.

Stage II When Temperature = 100 °C

In this stage, the heat and mass transport equations are provided by:

$$\frac{\partial T}{\partial t} = 0 \qquad (3.26)$$

$$\frac{\partial (\rho X)}{\partial t} = \frac{\partial}{\partial r}(D\rho\nabla X - m_v)) \qquad (3.27)$$

Equation 3.26 represents the heat transport rate during a phase change process. This equation is identical to the equation proposed by Zanoni's model. Based on this equation temperature is maintained constant during a phase change process for a specified interval of time during which moisture is transported as described by equation 3.27. Equation 3.27 is significantly different from the mass transport rate equation proposed by Zanoni. In the modified equation, vapor flux is controlled by vapor transport rate m_v in contrast to Zanoni's model where vapor flux is entirely controlled by rate of heat transport within a control volume. Time period for this constant temperature phase is calculated based on time required to decrease the water activity in a given control volume below a value of 0.9. This criterion based on water activity in modified model is significantly different from the critical moisture content requirement in Zanoni's model. Water activity value of 0.9 was chosen to represent bound water content in a food matrix. The bound water content cannot be easily evaporated, as it is chemically associated with the food matrix. Thus the assumption in Zanoni's model where the entire water content within a food

matrix is a treated as free water content can be considered as an over-simplification of the complex interactions of water with food matrix. These assumptions in this modified model are an effort to develop realistic predictions of temperature and moisture content based on coupled heat and mass transport model.

Stage III: When Temparature > 100 °C

This represents the stage of baking when a crust region has developed after the temperature at a particular control volume is greater than 100 C and the water activity is lower than 0.9. The coupled heat and mass transport equations for this stage are:

Equations 3.28 and 3.29 represent the heat and mass transport rates in

$$\frac{\partial(\rho_p Cp_p T)}{\partial t} = \frac{\partial}{\partial r}(\ (k_p \nabla T) - m_v * L). \qquad (3.28)$$

$$\frac{\partial(\rho X)}{\partial t} = \frac{\partial}{\partial r}((D\rho \nabla X) - m_v) \qquad (3.29)$$

the crust region based on this modified model. These equations are significantly different from the analogous equations 3.17 and 3.18 formulated based on Zanoni's model. The first major difference is that the rate of moisture transport in the crust region is not zero, this indicates that as we continue to heat the food matrix to temperature above 100 °C, we are able to remove more of the bound water into vapor state. Further the heat transfer equation also has a coupling with the vapor transport term. These equations 3.28 and 3.29 are identical to the equations used in stage I of this modified model.

Based on above analysis the modified model addresses the following limitations of Zanoni's formulation:

- Zanoni's model is based on thermal driven flow of vapors within a food matrix at their boiling points with no contribution from vapor diffusion. In the modified model, we have included the vapor transport term derived from fundamental principles to account for this limitation.

- Zanoni's formulation also imposes no resistance to vapor movement once the temperature = boiling point. In the modified model, the rate of vapor movement is controlled by the gradient of vapor pressure, vapor diffusivity and the resistance in vapor diffusion. These terms account for the resistance to vapor movement. Specifically by changing the vapor resistance with crust development, we can reduce the rate of vapor movement within the food matrix.

- In Zanoni's formulation there is a limited coupling of heat and mass transfer rates. Heat and mass transport equations are coupled only during a phase change process. This is significantly different in case of modified baking model. In the modified model, we have improved the coupling of heat and mass transport terms during all stages of a baking process.

- Including water activity of food material in baking models will allow to model various phase changes in crust and crumb region during baking. The modified model links various thermophysical properties such as water activity, vapor pressure and moisture content to develop a significantly comprehensive model to study baking process.

Boundary Conditions:

Next section describes the mathematical details of the boundary conditions during a baking process.

<u>Surface heat flux boundary condition:</u>

$$k_p \frac{\partial T}{\partial n}\Big|_s = h\ (T_a - T_{ps}) - K_m H_v (P_{vs} - P_{va}) \tag{3.30}$$

Where T_a is air temperature (K), T_{ps} is surface temperature (K), n is the outward normal at the surface, h is surface heat transfer coefficient (W/m²K), K_m

$$\frac{\partial(\rho_p Cp_p T)}{\partial t} = \frac{\partial}{\partial r}(\ (k_p \nabla T) - m_v * L) \tag{3.31}$$

$$\frac{\partial(\rho X)}{\partial t} = \frac{\partial}{\partial r}((D\rho \nabla X) - m_v) \tag{3.32}$$

is surface mass transfer coefficient (kg water/m²sPa), H_v is latent heat of evaporation for water (J/kg), P_{vs} is vapor pressure at the product surface (Pa), P_{va} is vapor pressure in the air (Pa), a is air, s is food surface.

<u>Surface mass transfer boundary condition:</u>

$$-D\frac{\partial X}{\partial n}\Big|_s = K_m(P_{vs} - P_{va})/\rho \tag{3.33}$$

Where ρ is density of potato (kg/m³).

Vapor pressure of water in the oven (P_{va}) was assumed to be zero (dry air) and vapor pressure at the product surface (P_{vs}) was calculated using Antoine's law

assuming the surface was fully saturated. It is given as follows (Zanoni et al., 1995):

$$P_{vs} = 133.3 \exp\left[18.3036 - \frac{3816.44}{T_{ps} - 46.13}\right] \qquad (3.34)$$

Thermal Conductivity of potato (k_p):

Thermal conductivity (k_p) is a function of temperature and moisture of the food material. Prediction model based on composition and temperature, as proposed by Choi and Okos (1985), was used to predict changes in thermal conductivity during the baking process. The following correlation was obtained for potato assuming it has 78% of water and 19% starch and 3% protein.

$$k_p = 4.34 \times 10^{-2} + 3 \times 10^{-4} T - 9 \times 10^{-7} T^2$$
$$+ (5.7 \times 10^{-1} + 1.8 \times 10^{-3} T - 6.7 \times 10^{-6} T^2) M \qquad (3.35)$$

where k_p is thermal conductivity of potato (W/mK), T is temperature of the potato (°C) and M is moisture of the potato (%, wet basis).

Heat Capacity of potato (Cp):

Heat capacity (Cp) is a function of moisture and temperature of the food material. Various literature sources (Heldman and Lund, 1992; Wang and Brennan, 1993; Rao and Rizvi, 1995) give heat capacity data for foods. We obtained the following correlation for potato using the correlations given by Choi and Okos (1985). We assumed that potato has 78% of water and 19% starch and 3% protein.

$$Cp = 3.64 \times 10^{-1} + 4.2 \times 10^{-4}\,T - 1.2 \times 10^{-6}\,T^2$$
$$+ (4.1762 - 9 \times 10^{-5}\,T + 5.5 \times 10^{-6}\,T^2)\ M \qquad (3.36)$$

where Cp is heat capacity of potato (kJ/kgK), T is temperature (K), M is moisture content (%, wet basis)

Effective Mass Diffusivity (D):

It is well known that food materials exhibit variable moisture diffusivity during processing. Diffusivity of moisture in food materials is a function of moisture and temperature. As moisture level decreases, D decreases. Saravacos and Charm (1962), and Okos et al. (1992) have reported values of effective mass diffusivity, for potato. In many modeling studies the moisture diffusivity was assumed to be constant during processing, which is a limiting factor for accurate numerical prediction. We used the correlation given by Maroulis et al. (2001) as below:

$$D = \frac{1}{1+W}(D_o)\ \exp\left[-\frac{E_0}{R}\left(\frac{1}{T} - \frac{1}{Tr}\right)\right] + \frac{W}{1+W}(D_i)\ \exp\left[-\frac{E_i}{R}\left(\frac{1}{T} - \frac{1}{Tr}\right)\right] \quad (3.37)$$

Where W is moisture content (kg water/kg dry solids), D_o is diffusivity at W=0, D_i is diffusivity at W=∞, E_o and E_i are activation energies, T (°C) is temperature and Tr (°C) is reference temperature. For potato, the values are: D_o=4.31 $\times 10^{-10}$ m²/s, D_i=1.57 $\times 10^{-09}$ m²/s, E_o=76.9 kJ/mol, E_i=44.7 kJ/mol, R=8314.570 kJ/molK is the universal gas constant and Tr=60°C.

Latent Heat (H_v)-

Latent heat of evaporation is the amount of energy required to evaporate a unit amount of water. It is expected that as water activity decreases the latent heat

will increase. To model this increase the latent heat in calculated based on equations **(3.39-3.40)**. In this transition numerical value of moisture content > 0.43 corresponds to water activity value of 1.0, below this moisture content, the water activity decreases and results in increase in latent heat. This increase in latent heat during evaporation with decrease in water activity is due to increase in thermal energy required to release the bound water from the food matrix.

$$H_{\upsilon} = 2.339 * 10^6 \, J/kg \qquad\qquad \text{For W>0.43} \qquad (3.38)$$

$$H_{\upsilon} = \frac{2.4948 * 10^6}{100 * W} + 2.339 * 10^6 \, J/kg \qquad \text{For 0.01<W<0.43} \qquad (3.39)$$

Using this simple formulation we can account for the changes in the latent energy requirement.

In addition to these physical properties, we also studied the variation in vapor diffusivity with the development of crust. Since we did not find any suitable model to predict changes in vapor diffusivity with crust formation in the literature, we simply reduced its contribution in the crust layer by 10 fold to simulate an increase in vapor transport resistance. This allows us to estimate the effect of decreased vapor diffusion during baking of food materials.

Numerical Simulation of Heat and Mass transport in a One-dimensional Model of Baking

This section describes the details of the numerical discretization approach used to solve the coupled heat and mass during baking. We considered modeling the baking process based on a one-dimensional model of a food object to simplify the computational effort and to evaluate predictions of temperature – time and moisture-time profiles within the food matrix based on three different

models. One-dimensional models of object have been used to simulate problems in which one dimension of a 3-d object is particularly smaller (generally 10 fold difference in size) than the remaining two dimensions. Thus an object can be modeled can as a semi-infinite slab.

One Dimensional Model Based on Zanoni's Formulation

One-dimensional finite volume code was developed using MATLAB® (MATLAB® 6.1, Release 12.1, Mathworks Inc., Natick, MA) to solve the set of equations as described above. **Figure** 3.16 shows the computational domain for modeling the baking of a potato in which each domain represents the control volume. The total potato sample of 10 mm thickness was divided into 20 control volumes as shown in **Figure 3.16**.
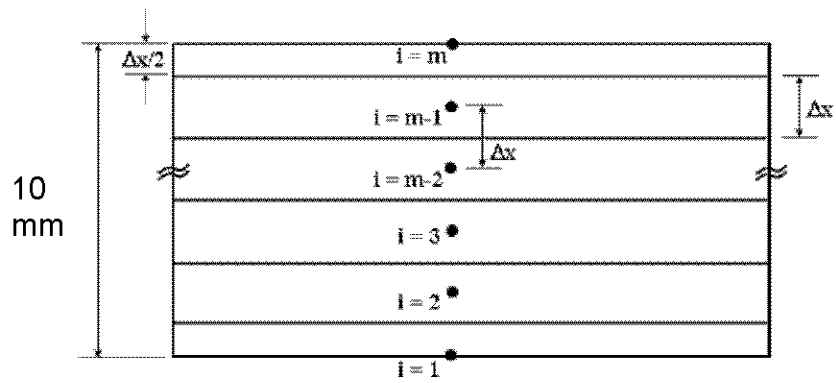
Figure 3.16

Computational grid for a 1-dimensional model of baking

The coupled heat and mass transport equations for these 20 finite volumes were solved using explicit scheme. The time step of 0.1 seconds was chosen to ensure numerical stability (Jaluria and Torrance, 1986), further the mesh size was varied to ensure independence of predicted temperature and moisture profiles for various grid spacings. The resulting coupled heat and mass transfer discretized equations are shown:

Top surface node:

Stage I: When temperature T (m, k)<100 °C. This represents early stages of baking process. Convective heat transfer from hot impinging air provides thermal energy to increase the temperature as well vapor pressure of moisture in the top surface node. The rate of convective heat transfer depends on surface heat transfer coefficient and difference in temperatures of surface node and hot air. Similarly rate of convective mass transfer depends on surface mass transfer coefficient and the difference in vapor pressure of top surface node and air. Based on this the discretized heat and mass transfer equations is:

$$\frac{\Delta x}{2} \rho \ Cp \ \frac{T_{m,k} - T_{m,k-1}}{\Delta t} = h(T_a - T_{m,k-1}) - k_p \frac{T_{m,k-1} - T_{m-1,k-1}}{\Delta x}$$
$$- K_m H_v (P_{vs} - P_{va}) \tag{3.40}$$

$$\frac{\Delta x}{2} \frac{W_{m,k} - W_{m,k-1}}{\Delta t} = D \ \frac{W_{m-1,k-1} - W_{m,k-1}}{\Delta x} - \frac{K_m}{\rho}(P_{vs} - P_{va}) \tag{3.41}$$

Stage II: When Temperature =100 °C. At this stage temperature of the top surface node reaches the evaporation temperature for water. Based on Zanoni's model, temperature of the particular node will remain constant while moisture content will continue to drop towards equilibrium moisture content during a phase

change process. The entire thermal energy provided by convective heat transfer process drives the moisture transport by contributing latent heat to the top surface node. Based on this the equations (3.41) and (3.42) are modified to represent the change in heat and mass transfer process during a phase change process. The modified equations are represented below:

$$\Delta x \rho \; Cp \frac{T_{m,k} - T_{m,k-1}}{\Delta t} = 0 \tag{3.42}$$

$$\frac{\Delta x}{2} \frac{W_{m,k} - W_{m,k-1}}{\Delta t} = D \frac{W_{m-1,k-1} - W_{m,k-1}}{\Delta x}$$
$$- \left[h(T_a - T_{m,k-1}) - k_p \frac{T_{m,k-1} - T_{m,k-1}}{\Delta x} \right] \bigg/ \rho \; H \tag{3.43}$$

Stage III: After moisture content of the top node has decreased below equilibrium moisture content, Zanoni's formulation assumes that there is no further loss of moisture content. This is due to absence of any driving force to further reduce the moisture. The entire thermal energy provided by the convective heat transfer contributes to an increase in temperature of the top surface node. Based on this the discretized heat and mass transfer equations are:

$$\frac{\Delta x}{2} \rho Cp \; \frac{T_{m,k} - T_{m,k-1}}{\Delta t} = h(T_a - T_{m,k-1}) - k_p \frac{T_{m,k-1} - T_{m-1,k-1}}{\Delta x} \tag{3.44}$$

$$\frac{\Delta x}{2} \frac{W_m - W_{m,k-1}}{\Delta t} = 0$$

Interior nodes:

Stage I: When Temperature < 100 °C. During this stage temperature of an interior node is controlled by the net flux of thermal energy from surrounding control volumes. Diffusion process controls the rate of moisture transport based on moisture gradient. There is no direct coupling of heat and mass transport terms during this stage except that physical properties e.g. thermal conductivity are a function of both temperature and moisture content. The following equations can describe thermal and mass transport processes:

$$\Delta x \rho \; Cp \; \frac{T_{i,k} - T_{i,k-1}}{\Delta t} = k_p \frac{T_{i+1,k-1} - 2T_{i,k-1} + T_{i-1,k-1}}{\Delta x} \qquad (3.45)$$

$$\Delta x \frac{W_{i,k} - W_{i,k-1}}{\Delta t} = D \frac{W_{i-1,k-1} - 2W_{i,k-1} + W_{i+1,k-1}}{\Delta x} \qquad (3.46)$$

Stage II: When Temperature=100 °C. During this stage temperature of an interior node reaches equal to the evaporation temperature of water. Based on Zanoni's formulation, during a phase change process, temperature is maintained constant a particular node and net flux of thermal energy within a particular control volume contributes towards the latent heat for evaporation of moisture. Temperature at the particular node is maintained at 100 °C until the moisture content drops below the equilibrium moisture content. This model does not take into account any resistance to vapor transport within the food matrix. Based on these assumptions the coupled heat and mass transport equations are:

$$\Delta x \rho \; Cp \; \frac{T_{i,k} - T_{i,k-1}}{\Delta t} = 0 \qquad (3.47)$$

$$\Delta x \frac{W_{i,k} - W_{i,k-1}}{\Delta t} = D \frac{W_{i-1,k-1} - 2W_{i,k-1} + W_{i+1,k-1}}{\Delta x}$$
$$- \left[k_p \frac{T_{i+1,k-1} - 2T_{i,k-1} + T_{i-1,k-1}}{\Delta x} \right] \bigg/ \rho \, H_V$$

(3.48)

Stage III: When Temperature > 100 °C. This represents the stage when temperature of a particular node is higher than the evaporation temperature of water and total moisture content in a given control volume is lower than the equilibrium moisture content. During this stage it is assumed that the rate of moisture transport is zero. This assumption is valid as above the evaporation temperature most of the free moisture content will be in a vapor state and Zanoni's model does not consider any resistance to vapor transport. As a result moisture content value remains constant at the equilibrium moisture content. The net flux of energy based on thermal conduction from adjacent control volumes results in increase of temperature at a particular node. The thermal and mass transport equations for this stage in the interior node are:

$$\Delta x \rho_p Cp_p \frac{T_{i,k} - T_{i,k-1}}{\Delta t} = k_p \frac{T_{i+1,k-1} - 2T_{i,k-1} + T_{i-1,k-1}}{\Delta x}$$

(3.48)

$$\Delta x \frac{W_{i,k} - W_{i,k-1}}{\Delta t} = 0$$

(3.49)

Bottom Surface Node (Insulated bottom or Symmetry Boundary Condition)

In our experimental studies, to overcome the effect of conduction from solid metallic surfaces during baking in jet impingement oven, the bottom of the oven

surface was insulated using wooden board. To simulate the same conditions in our model, we will assume insulated bottom surface area.

The mathematical representation of heat and mass transport equations for the bottom surface with insulating conditions are:

Stage I: When Temperature< 100 °C

The coupled heat and mass transport equations for the bottom surface are:

$$\frac{\Delta x}{2}\rho Cp \ \frac{T_{i,k}-T_{i,k-1}}{\Delta t} = -2*k_p \frac{T_{i,k-1}-T_{i-1,k-1}}{\Delta x} \tag{3.50}$$

$$\frac{\Delta x}{2}\frac{W_{i,k}-W_{i,k-1}}{\Delta t} = 2D\frac{W_{i-1,k-1}-W_{i,k-1}}{\Delta x} \tag{3.51}$$

Stage II: When Temperature =100 °C

$$\frac{\Delta x}{2}\rho Cp \ \frac{T_{i,k}-T_{i,k-1}}{\Delta t} = 0 \tag{3.52}$$

$$\frac{\Delta x}{2}\frac{W_{i,k}-W_{i,k-1}}{\Delta t} = 2D\frac{W_{i-1,k-1}-W_{i,k-1}}{\Delta x}$$
$$-\left[2k_p\frac{T_{i,k-1}-T_{i-1,k-1}}{\Delta x}\right]\Big/\rho Hv \tag{3.53}$$

Stage III: When Temperature> 100°C

$$\frac{\Delta x}{2}\rho Cp \ \frac{T_{i,k}-T_{i,k-1}}{\Delta t} = -2*k_p \frac{T_{i,k-1}-T_{i-1,k-1}}{\Delta x} \tag{3.54}$$

$$\frac{\Delta x}{2}\frac{W_{i,k}-W_{i,k-1}}{\Delta t} = 0 \tag{3.55}$$

Based on equations **(3.53) to (3.58)** the coupled heat and mass transport process during baking was modeled to simulate the temperature and moisture

profiles within the food matrix and predict the rate of crust formation during baking.

One Dimensional Model of Baking Based on Modified Baking Model I

In this section numerical discretization of coupled heat and mass transport equations based on the modified baking model I are discussed. This direct comparison among two models (Zanoni's and Modified baking model I) will help understand the significant differences in modeling transport processes based on these models.

Top surface boundary conditions in a 1-d baking model are same as in Zanoni's formulation so the numerical discretization of coupled heat and mass transport equations is identical for this model as well as Zanoni's formulation. The significant difference in these models is in modeling the moisture transport (Dietl et al., 1998) in interior nodes and its coupling with thermal transport. The numerical discretization for the interior nodes is discussed below:

Interior Nodes:

Stage I When Temperature <100 °C.

The coupled heat and mass transport equations are:

$$\Delta x \rho \, Cp \, \frac{T_{i,k} - T_{i,k-1}}{\Delta t} = k_p \frac{T_{i+1,k-1} - 2T_{i,k-1} + T_{i-1,k-1}}{\Delta x} - (m_{vap}(i,k-1) - m_{vap}(i-1,k-1)) * \frac{1}{\Delta x}$$

(3.56)

$$\Delta x \frac{W_{i,k} - W_{i,k-1}}{\Delta t} = D \frac{W_{i-1,k-1} - 2W_{i,k-1} + W_{i+1,k-1}}{\Delta x} - (m_{vap}(i,k-1) - m_{vap}(i-1,k-1)) / \rho$$

(3.57)

Where m_{vap} represents the rate of vapor transport (Dietl et al., 1998) at a particular control volume.

(3.58)

$$m_{vap} = -(\frac{\delta}{\mu} * \frac{p_v^*}{RT}(\frac{\partial a_w}{\partial X})(\frac{\partial X}{\partial r}))$$

Based on the above equation 3.61, to calculate the rate of vapor transport partial saturated vapor pressure (pv*) at a particular temperature, gradient of water activity with moisture content ($\frac{\partial a_w}{\partial X}$), and spatial gradient in moisture content ($\frac{\partial X}{\partial r}$) are required. Saturated vapor pressure can be calculated based on the thermodynamic relationship between vapor pressure and temperature. Based on GAB equation, we can estimate water activity as well as partial derivative of water activity with moisture content. The following equations illustrate the process of calculation of water activity as well gradient of water activity as a function of moisture content at a particular temperature. In these equations C1, C2 and C3 represents the three coefficient of the GAB equation, which is a quadratic equation to calculate the water activity.

GAB equation and calculation of water activity gradient with change in moisture content:

$$C1(i,k-1) = -17.19 + ((9.83*10^{\wedge}(-3))*(T(i,k-1)-273)) \tag{3.59}$$

$$C2(i,k-1) = (19.79 - 0.091*(T(i,k-1)-273)) - 1/(W(i,k-1)) \tag{3.60}$$

$$C3(i,k-1) = -1.69 + 0.095*(T(i,k-1)-273) \tag{3.61}$$

$$a_w(i,k-1) = (-C2(i,k-1) - sqrt(((C2(i,k-1)^{\wedge}2) - 4*C1(i,k-1)*C3(i,k-1)))/(2*C1(,k-1)) \tag{3.62}$$

$$C4(i,k-1) = ((2*C1(i,k-1)*aw(i,k-1) + C2(i,k-1))*W(i,k-1)*W(i,k-1)) \tag{3.63}$$

$$\partial a_w / \partial X = -aw(i,k-1)/C4(i,k-1) \tag{3.64}$$

Based on this we can calculate the rate of vapor transport by (Dietl et al., 1998):

$$m_{vap} = -(\frac{\delta}{\mu} * \frac{p_v^*}{RT}(\frac{\partial a_w}{\partial X})(\frac{W(i+1,k-1)-W(i,k-1)}{\Delta x}) \tag{3.65}$$

The inclusion of vapor transport term in this modified model represent a significant difference from Zanoni's approach in modeling heat and mass transport processes in interior nodes when the temperature is less than 100°C

Stage II: When Temperature=100°C, This represent the stage when temperature at a particular node is equivalent to the boiling temperature of water. In this modified model analogous to the Zanoni's formulation, we consider that during a phase change process rate of change of temperature within a particular control volume is zero, until the water activity of that particular node has decreased below 0.9. This assumption is to reflect that a phase change process at 100 °C can remove free moisture content, while removal of bound water requires higher levels of thermal energy. This concept of water activity in determining the time period for this phase change process is significantly

different from the Zanoni's model, in which it is assumed that moisture evaporates till its level drops below the equilibrium moisture content. Based on these assumptions the coupled heat and mass transport equations are:

$$\Delta x \rho \ Cp \ \frac{T_{i,k} - T_{i,k-1}}{\Delta t} = 0 \qquad (3.66)$$

$$\Delta x \frac{W_{i,k} - W_{i,k-1}}{\Delta t} = D \frac{W_{i-1,k-1} - 2W_{i,k-1} + W_{i+1,k-1}}{\Delta x} - (m_{vap}(i,k-1) - m_{vap}(i-1,k-1))/\rho \qquad (3.67)$$

Stage III: **When Temperature > 100°C** The coupled heat and mass transport equations for this stage of baking are:

$$\Delta x \rho \ Cp \ \frac{T_{i,k} - T_{i,k-1}}{\Delta t} = k_p \frac{T_{i+1,k-1} - 2T_{i,k-1} + T_{i-1,k-1}}{\Delta x} - (m_{vap}(i,k-1) - m_{vap}(i-1,k-1)) * \frac{1}{\Delta x} \qquad (3.68)$$

$$\Delta x \frac{W_{i,k} - W_{i,k-1}}{\Delta t} = D \frac{W_{i-1,k-1} - 2W_{i,k-1} + W_{i+1,k-1}}{\Delta x} - (m_{vap}(i,k-1) - m_{vap}(i-1,k-1))/\rho \qquad (3.69)$$

These equations are significantly different than the Zanoni's model. In Zanoni's model it is assumed that rate of moisture transport is zero after the moisture content in a particular control volume is equal to the equilibrium moisture content. According to modified baking model I, rate of moisture transport is not zero at temperature >100 °C. At temperatures higher than the boiling point, the bound moisture is evaporated with higher levels of latent heat.

Soret Effect

To improve coupling between heat and mass transport in Zanoni's model, we simulated the contribution of Soret effect during baking. Soret effect models the effect of temperature gradient on moisture diffusivity within a food matrix.

The following set of equations describes the additional transport terms, which were introduced to model Soret effect.

$$\Delta x \rho \; Cp \; \frac{T_{i,k}-T_{i,k-1}}{\Delta t} = k_p \frac{T_{i+1,k-1}-2T_{i,k-1}+T_{i-1,k-1}}{\Delta x} + \frac{\varepsilon \lambda D}{c_m} \frac{W_{i+1,k-1}-2W_{i,k-1}+W_{i-1,k-1}}{\Delta x} \qquad (3.70)$$

$$\Delta x \frac{W_{i,k}-W_{i,k-1}}{\Delta t} = D \frac{W_{i-1,k-1}-2W_{i,k-1}+W_{i+1,k-1}}{\Delta x} + \frac{D\delta}{c_m} \frac{T_{i+1,k-1}-2T_{i,k-1}+T_{i-1,k-1}}{\Delta x} \qquad (3.71)$$

In this set of equations:

ε=Ratio of vapor diffusion coefficient to water diffusion

δ=Thermogradient coefficient (1/K)

c_m = Specific moisture capacity

For the numerical simulation of a 1-d baking process with Soret effect modification in a Zanoni's model, the numerical values of ε, δ, c_m were 0.7, 0.015, 0.003 respectively selected to represent transport process in a starch (Ranjan et et al., 2002).

In the next section, numerical discretization approaches for a 2-d baking model discussed. A 2-d baking model is an extension of a 1-d model with radial co-ordinates to simulate baking of a cylindrical shape potato slice.

Two-dimensional Numerical Simulation of Baking Process

After development of a 1-d model to study baking process during jet impingement baking, the next step was to develop a 2-d axisymmetric model of heat and mass transfer in a cylindrical disk. This extension of a 1-d model to a 2-d axisymetric model will improve the simulation of a real food object and overcome some of the assumptions made in case of 1-d geometry. Further y

different boundary conditions on top surface as well as sides can be used to simulate jet impingement baking of a cylindrical disk. In this study a two-dimensional axisymmetric heat and mass transfer model was developed based on impinging hot air jets on the top surface with an insulating boundary condition at the bottom of a model food object (Figure 3.17).

Numerically discretized equations for the 2-D finite volume code were solved using MATLAB® (MATLAB® 6.1, Release 12.1, Mathworks Inc., Natick, MA). **Figure 3.17** shows the computational domain used to model the potato disk in which the domain was divided into 26*11 finite volumes. The number of control volumes within the computational domain was varied to verify that the grid independence of the predicted temperature and moisture profiles.
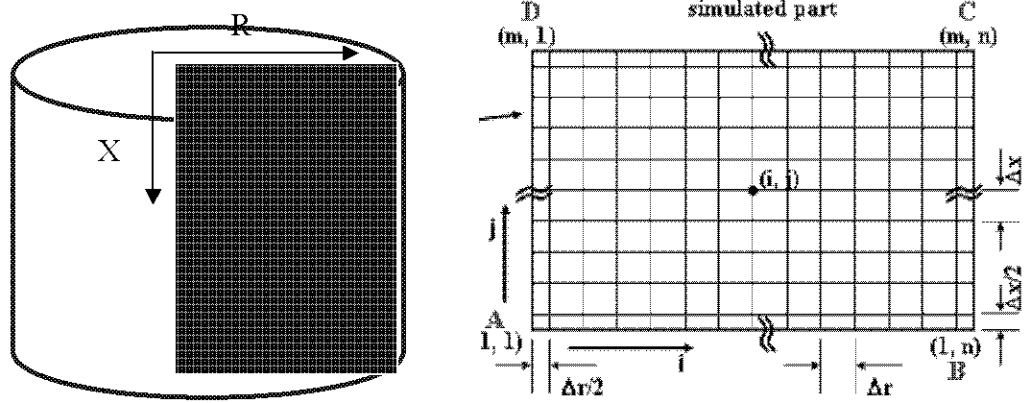
Figure 3.17

Schematic diagram showing the potato sample and computational domain

The mass and energy conservation equations for these 26*11 finite volumes were solved using explicit scheme with time step of 0.1 seconds to ensure numerical stability. Equations for numerical discretization of two-dimensional model are as follows:

To illustrate the differences among three models (Zanoni's model, Modified Baking Model I and II), the next section describes numerical discretization of coupled heat and mass transport equations at a interior node point. This detailed analysis will supplement the earlier descriptions of these models and clearly illustrate the differences in formulation and implementation of these three models.

4. Interior nodes:
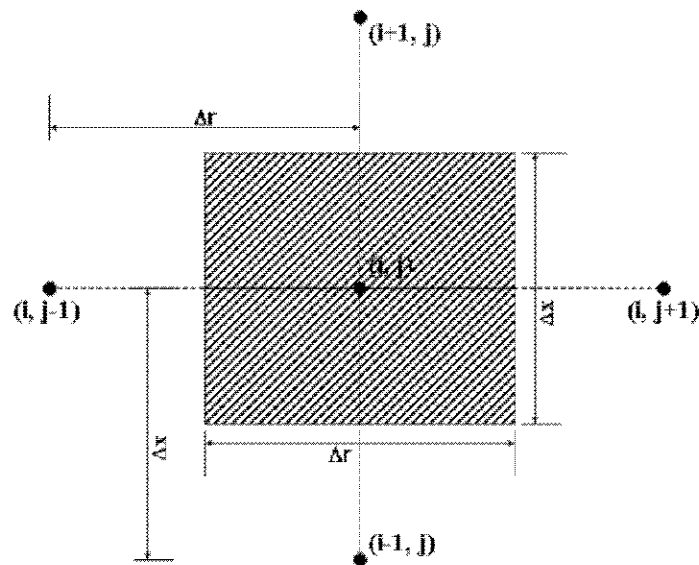
Figure 3.18: Control volume for interior nodes

Zanoni's Model

Similar to a 1-d model, thermal transport rate at an interior node of a 2-d axisymmetric geometry is controlled by heat conduction. Diffusion of moisture

content combined with rapid evaporation of water during a phase change process (when Temperature=100 °C) controls rate of mass transport at a particular interior node. Zanoni's model does not account for the resistance to vapor transport from a interior node to the surface of the food matrix. According to Zanoni's modes, the baking process can be divided into three stages.

Stage I- When Temperature< 100 °C: In this stage heat transfer rate is controlled by heat conduction, while the mass transport is controlled by moisture diffusion. There is very limited coupling of heat and mass transport equation in this stage of baking. The following set of equations represents rates of thermal and mass transport during this stage of baking.

$$
\pi(2j-3)\Delta r^2 \Delta x \rho Cp \frac{T_{i,j,k} - T_{i,j,k-1}}{\Delta t} =
$$
$$
+ \pi(2j-3)\Delta r^2 k_p \frac{T_{i+1,j,k-1} - T_{i,j,k-1}}{\Delta x} - \pi(2j-3)\Delta r^2 k_p \frac{T_{i,j,k-1} - T_{i-1,j,k-1}}{\Delta x}
$$
$$
+ \pi(2j-1)\Delta r \Delta x k_p \frac{T_{i,j+1,k-1} - T_{i,j,k-1}}{\Delta r} - \pi(2j-3)\Delta r \Delta x k_p \frac{T_{i,j,k-1} - T_{i,j-1,k-1}}{\Delta r} \tag{3.72}
$$

$$
\frac{\pi}{2}(2j-3)\Delta r^2 \Delta x \frac{W_{i,j,k} - W_{i,j,k-1}}{\Delta t} =
$$
$$
+ \pi(2j-3)\Delta r^2 D \frac{W_{i-1,j,k-1} - W_{i,j,k-1}}{\Delta x} - \pi(2j-3)\Delta r^2 D \frac{W_{i,j,k-1} - W_{i+1,j,k-1}}{\Delta x}
$$
$$
+ \pi(2j-3)\Delta r \Delta x D \frac{W_{i,j-1,k-1} - W_{i,j,k-1}}{\Delta r} - \pi(2j-1)\Delta r \Delta x D \frac{W_{i,j,k-1} - W_{i,j+1,k-1}}{\Delta r} \tag{3.73}
$$

Stage II: When Temperature =100 °C, During this stage of baking, temperature is maintained constant during a phase change process, while moisture content continues to drop until it becomes equal to the equilibrium moisture content. During this phase change process, net flux of thermal energy controls the rate of

vapor transport. This model does not consider any resistance to vapor transport within a food matrix. The coupled heat and mass transport equations for a particular interior node is described below:

$$\pi(2j-3)\Delta r^2 \Delta x \rho\ Cp\frac{T_{i,j,k}-T_{i,j,k-1}}{\Delta t}=0 \tag{3.74}$$

$$\pi(2j-3)\Delta r^2 \Delta x\frac{W_{i,j,k}-W_{i,j,k-1}}{\Delta t}=+\pi(2j-3)\Delta r^2 D\frac{W_{i-1,j,k-1}-W_{i,j,k-1}}{\Delta x}$$

$$-\pi(2j-3)\Delta r^2 D\frac{W_{i,j,k-1}-W_{i+1,j,k-1}}{\Delta x}+\pi(2j-3)\Delta r\Delta xD\frac{W_{i,j-1,k-1}-W_{i,j,k-1}}{\Delta r}$$

$$-\pi(2j-1)\Delta r\Delta xD\frac{W_{i,j,k-1}-W_{i,j+1,k-1}}{\Delta r} \tag{3.75}$$

$$-\left[\begin{array}{c}\pi(2j-3)\Delta r^2 k_p\dfrac{T_{i+1,j,k-1}-T_{i,j,k-1}}{\Delta x}-\pi(2j-3)\Delta r^2 k_p\dfrac{T_{i,j,k-1}-T_{i-1,j,k-1}}{\Delta x}\\[2mm]+\pi(2j-1)\Delta r\Delta xk_p\dfrac{T_{i,j+1,k-1}-T_{i,j,k-1}}{\Delta r}-\pi(2j-3)\Delta r\Delta xk_p\dfrac{T_{i,j,k-1}-T_{i,j-1,k-1}}{\Delta r}\end{array}\right]\Big/\rho\mathrm{H}_v$$

Stage III- When Temperature> 100 °C: During this stage, moisture content remains constant while temperature increases due to heat transfer by conduction. Since moisture content at this node point is equal to the equilibrium moisture content, there is no gradient for the moisture transport. Heat and mass transport equations are not coupled at this stage of baking according to Zanoni's model. Following set of equations describes heat and mass transport rates for this stage:

$$\pi(2j-3)\Delta r^2 \Delta x \rho Cp \frac{T_{i,j,k} - T_{i,j,k-1}}{\Delta t} =$$

$$+\pi(2j-3)\Delta r^2 k_p \frac{T_{i+1,j,k-1} - T_{i,j,k-1}}{\Delta x} - \pi(2j-3)\Delta r^2 k_p \frac{T_{i,j,k-1} - T_{i-1,j,k-1}}{\Delta x} \qquad (3.76)$$

$$+\pi(2j-1)\Delta r \Delta x k_p \frac{T_{i,j+1,k-1} - T_{i,j,k-1}}{\Delta r} - \pi(2j-3)\Delta r \Delta x k_p \frac{T_{i,j,k-1} - T_{i,j-1,k-1}}{\Delta r}$$

$$\pi(2j-3)\Delta r^2 \Delta x \frac{W_{i,j,k} - W_{i,j,k-1}}{\Delta t} = 0 \qquad (3.77)$$

Interior Node (Based on Modified Model I)

To understand differences among Zanoni's and Modified Baking Model I, numerical discretization of interior node points is presented in this section. In modified baking model I, we consider same stages of baking as proposed in Zanoni's model, but there are significant differences in calculation of mass transport rates. In modified baking model I, mass transport process combines water diffusion and vapor transport. The rate of vapor transport is based on a gradient of vapor pressure. Following set of equations describes the calculation for determination of vapor transport rate in modified baking model I:

$$m_{vap_{i,j,k-1}} = -(\frac{\delta}{\mu} * \frac{p_v^*}{RT}(\frac{\partial a_w}{\partial X}))((2 * W_{i,j,k-1} - W_{i+1,j,k-1} - W_{i-1,j,k-1}) / (\Delta x^2) \dots$$

$$+ (W_{i,j,k-1} - W_{i,j-1,k-1}) / (\Delta r^2)$$

$$+((2 * j - 1) / ((2 * j - 3) * \Delta r^2) * (W_{i,j,k-1} - W_{i,j+1,k-1}))) \qquad (3.78)$$

Stage I: When Temperature< 100°C, In this model the significant difference as compared with Zanoni's model is the vapor transport term. This term is not considered in Zanoni's model as a result mass transport rate is only controlled by a diffusion of moisture. Using the above equation (3.78), modified model I

introduces vapor transport rate in modeling mass transport process even when the temperature at a particular node is below 100 °C. The contribution from the vapor transport term can be significant especially as the temperature of interior nodes increases and approaches the boiling point. Further in this model, the vapor transport term also appears in the thermal transport rate equation to account for the latent heat of evaporation. This improves the coupling of heat and mass transport equations.

$$
\rho Cp \frac{T_{i,j,k} - T_{i,j,k-1}}{\Delta t} =
$$

$$
(+\pi(2j-3)\Delta r^2 k_p \frac{T_{i+1,j,k-1} - T_{i,j,k-1}}{\Delta x} - \pi(2j-3)\Delta r^2 k_p \frac{T_{i,j,k-1} - T_{i-1,j,k-1}}{\Delta x}
$$

$$
+ \pi(2j-1)\Delta r \Delta x k_p \frac{T_{i,j+1,k-1} - T_{i,j,k-1}}{\Delta r} - \pi(2j-3)\Delta r \Delta x k_p \frac{T_{i,j,k-1} - T_{i,j-1,k-1}}{\Delta r}) / (\pi(2j-3)\Delta r^2 \Delta x)
$$

$$
- m_{vapi,j,k-1} H_\upsilon \qquad\qquad (3.79)
$$

$$
\frac{W_{i,j,k} - W_{i,j,k-1}}{\Delta t} =
$$

$$
(+\pi(2j-3)\Delta r^2 D \frac{W_{i-1,j,k-1} - W_{i,j,k-1}}{\Delta x} - \pi(2j-3)\Delta r^2 D \frac{W_{i,j,k-1} - W_{i+1,j,k-1}}{\Delta x}
$$

$$
+ \pi(2j-3)\Delta r \Delta x D \frac{W_{i,j-1,k-1} - W_{i,j,k-1}}{\Delta r} - \pi(2j-1)\Delta r \Delta x D \frac{W_{i,j,k-1} - W_{i,j+1,k-1}}{\Delta r}) / (\pi(2j-3)\Delta r^2 \Delta x)
$$

$$
- m_{vapi,j,k-1} / \rho \qquad\qquad (3.80)
$$

Stage II: When Temperature=100 °C, Similar to the Zanoni's model the modified baking model I also considers three stages for baking. During a phase change state, temperature at a particular control volume is maintained constant at 100 °C, while moisture content continues to drops due to vapor transport as well as water diffusion. The moisture transport rate in this model considers a

resistance to vapor transport and calculates its rate of transport based on gradient of vapor pressure. This is significantly different from Zanoni's model. Zanoni's model does not consider any resistance to vapor transport and the rate of vapor transport is completely controlled by net flux of thermal energy at a particular control volume. Further in the modified baking model I, temperature is maintained constant only until its water activity drops below 0.9. This reflects that the modified model I takes into account differences in free and bound water, whereas in Zanoni's model there is no such difference in the total water content. As a result, temperature is maintained constant until water content drops to the level of equilibrium moisture content, which is significantly lower than the water activity level of 0.9.

$$\rho\, Cp\ \frac{T_{i,j,k} - T_{i,j,k-1}}{\Delta t}\ =\ 0 \qquad\qquad (3.81)$$

$$\frac{W_{i,j,k} - W_{i,j,k-1}}{\Delta t} =$$

$$(+\pi(2j-3)\Delta r^2 D\frac{W_{i-1,j,k-1} - W_{i,j,k-1}}{\Delta x} - \pi(2j-3)\Delta r^2 D\frac{W_{i,j,k-1} - W_{i+1,j,k-1}}{\Delta x}$$

$$+\pi(2j-3)\Delta r\Delta x D\frac{W_{i,j-1,k-1} - W_{i,j,k-1}}{\Delta r} - \pi(2j-1)\Delta r\Delta x D\frac{W_{i,j,k-1} - W_{i,j+1,k-1}}{\Delta r}) /(\pi(2j-3)\Delta r^2 \Delta x)$$

$$-\frac{m_{vapi,j,k-1}}{\rho} \qquad\qquad (3.82)$$

Stage III When Temperature> 100 °C: The modified baking model also has significant differences from the Zanoni's model in this stage of baking. Rate of moisture transport in the modified model I is nonzero as compared with Zanoni's model. Thus moisture transport model in this modified baking model I allows for

vaporization of bound water as temperature of a particular interior node rises above100°C

$$\rho Cp \frac{T_{i,j,k} - T_{i,j,k-1}}{\Delta t} =$$

$$(+\pi(2j-3)\Delta r^2 k_p \frac{T_{i+1,j,k-1} - T_{i,j,k-1}}{\Delta x} - \pi(2j-3)\Delta r^2 k_p \frac{T_{i,j,k-1} - T_{i-1,j,k-1}}{\Delta x}$$

$$+ \pi(2j-1)\Delta r \Delta x k_p \frac{T_{i,j+1,k-1} - T_{i,j,k-1}}{\Delta r} - \pi(2j-3)\Delta r \Delta x k_p \frac{T_{i,j,k-1} - T_{i,j-1,k-1}}{\Delta r}) / (\pi(2j-3)\Delta r^2 \Delta x)$$

$$-m_{vapi,j,k-1} H_v \qquad\qquad (3.83)$$

$$\frac{W_{i,j,k} - W_{i,j,k-1}}{\Delta t} =$$

$$(+\pi(2j-3)\Delta r^2 D \frac{W_{i-1,j,k-1} - W_{i,j,k-1}}{\Delta x} - \pi(2j-3)\Delta r^2 D \frac{W_{i,j,k-1} - W_{i+1,j,k-1}}{\Delta x}$$

$$+ \pi(2j-3)\Delta r \Delta x D \frac{W_{i,j-1,k-1} - W_{i,j,k-1}}{\Delta r} - \pi(2j-1)\Delta r \Delta x D \frac{W_{i,j,k-1} - W_{i,j+1,k-1}}{\Delta r}) / (\pi(2j-3)\Delta r^2 \Delta x)$$

$$- m_{vapi,j,k-1} / \rho \qquad\qquad (3.84)$$

Modified Baking Model II

In this modified model, there are significant differences as compared with Zanoni's model for baking as well the proposed modified baking model I. The first major difference is that the modified baking model II does not consider baking as a three state process. In this model, a baking process is determined by a single stage and thus a single set of equations to model all the conditions during baking. In addition the modified baking model II has all the same set of differences from Zanoni's model as discussed in comparison of modified baking model I and Zanoni's model. These differences are highlighted in numerical discretization scheme for interior nodes of a 2-d axis-symmetric geometry. The equations below clearly illustrate that modified baking model II is similar to

modified baking model I without any stages in baking. Thus it does not manually control the simulation process by maintaining temperature at a constant value during any particular stage of baking. In addition to interior nodes, the boundary conditions also a treated as a single step baking without any stages. The vapor transport process in case of boundary conditions is controlled by a gradient of vapor pressure and convective heat transfer coefficient.

Discretization at Interior Nodes (Modified Baking Model II):

$$\rho Cp \frac{T_{i,j,k} - T_{i,j,k-1}}{\Delta t} =$$

$$(+\pi(2j-3)\Delta r^2 k_p \frac{T_{i+1,j,k-1} - T_{i,j,k-1}}{\Delta x} - \pi(2j-3)\Delta r^2 k_p \frac{T_{i,j,k-1} - T_{i-1,j,k-1}}{\Delta x}$$

$$+ \pi(2j-1)\Delta r \Delta x k_p \frac{T_{i,j+1,k-1} - T_{i,j,k-1}}{\Delta r} - \pi(2j-3)\Delta r \Delta x k_p \frac{T_{i,j,k-1} - T_{i,j-1,k-1}}{\Delta r})/(\pi(2j-3)\Delta r^2 \Delta x)$$

$$- m_{vapi,j,k-1} H_v \qquad\qquad (3.85)$$

$$\frac{W_{i,j,k} - W_{i,j,k-1}}{\Delta t} =$$

$$(+\pi(2j-3)\Delta r^2 D \frac{W_{i-1,j,k-1} - W_{i,j,k-1}}{\Delta x} - \pi(2j-3)\Delta r^2 D \frac{W_{i,j,k-1} - W_{i+1,j,k-1}}{\Delta x}$$

$$+ \pi(2j-3)\Delta r \Delta x D \frac{W_{i,j-1,k-1} - W_{i,j,k-1}}{\Delta r} - \pi(2j-1)\Delta r \Delta x D \frac{W_{i,j,k-1} - W_{i,j+1,k-1}}{\Delta r})/(\pi(2j-3)\Delta r^2 \Delta x)$$

$$- m_{vapi,j,k-1}\Big/\rho \qquad\qquad (3.86)$$

Boundary Conditions:

In the next section, boundary conditions are described for Zanoni's baking model to illustrate the numerical details for the discretization scheme. Similar equations with modification in vapor transport terms as discussed above were also derived for baking model I and baking model II. In this section the representative

equations based on Zanoni's model are described to illustrate the process of 2-d axis-symmetric modeling of food system.

1. Location C

Stage I: When Temperature (T (m, n, k-1)) < 100 °C, Figure X shows the control volume for location C. During this stage convective heat and mass process controls the influx of thermal energy as well transport of moisture content from the surface to air respectively. The equations for coupled heat and mass transfer are :
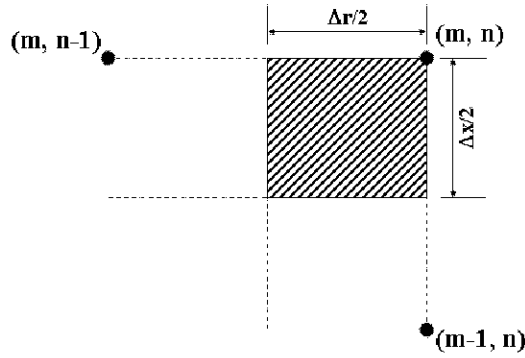
Figure 3.19 : Control volume for location C

$$\frac{\pi}{4}(2n-3)\Delta r^2 \Delta x \rho \; Cp \; \frac{T_{m,n,k}-T_{m,n,k-1}}{\Delta t} =$$

$$+\frac{\pi}{2}(2n-3)\Delta r^2 h(T_a - T_{m,n,k-1}) - \frac{\pi}{2}(2n-3)\Delta r^2 k_p \frac{T_{m,n,k-1}-T_{m-1,n,k-1}}{\Delta x}$$

$$+ \pi(n-1)\Delta r \Delta x h(T_a - T_{m,n,k-1}) - \frac{\pi}{2}(2n-3)\Delta r \Delta x k_p \frac{T_{m,n,k-1}-T_{m,n-1,k-1}}{\Delta r} \qquad (3.87)$$

$$-\frac{\pi}{2}(2n-3)\Delta r^2 K_m H_v (P_{vs} - P_{va}) - \pi(n-1)\Delta r \Delta x K_m H_v (P_{vs} - P_{va})$$

$$\frac{\pi}{4}(2n-3)\Delta r^2 \Delta x \frac{W_{m,n,k} - W_{m,n,k-1}}{\Delta t} =$$

$$+\frac{\pi}{2}(2n-3)\Delta r^2 D \frac{W_{m-1,n,k-1} - W_{m,n,k-1}}{\Delta x} - \frac{\pi}{2}(2n-3)\Delta r^2 \frac{K_m}{\rho}(P_{vs} - P_{va}) \qquad (3.88)$$

$$+\frac{\pi}{2}(2n-3)\Delta r \Delta x D \frac{W_{m,n-1,k-1} - W_{m,n,k-1}}{\Delta r} - \pi(n-1)\Delta r \Delta x \frac{K_m}{\rho}(P_{vs} - P_{va})$$

Stage II: When Temperature (T(m,n,k-1) =100 °C. This stage represents a phase change process. During a phase change process temperature at a particular node is maintained constant until moisture content is reduced to the level of equilibrium moisture content. Thus the net thermal flux within a control volume controls the rate of evaporation of water and hence controls the rate of moisture transport. The equations for heat and mass transport are:

$$\frac{\pi}{4}(2n-3)\Delta r^2 \Delta x \rho Cp \frac{T_{m,n,k} - T_{m,n,k-1}}{\Delta t} = 0 \qquad (3.89)$$

$$\frac{\pi}{4}(2n-3)\Delta r^2 \Delta x \frac{W_{m,n,k} - W_{m,n,k-1}}{\Delta t} =$$

$$+\frac{\pi}{2}(2n-3)\Delta r^2 D \frac{W_{m-1,n,k-1} - W_{m,n,k-1}}{\Delta x}$$

$$+\frac{\pi}{2}(2n-3)\Delta r \Delta x D \frac{W_{m,n-1,k-1} - W_{m,n,k-1}}{\Delta r}$$

$$-\begin{bmatrix} \frac{\pi}{2}(2n-3)\Delta r^2 h(T_a - T_{m,n,k-1}) \\[2mm] -\frac{\pi}{2}(2n-3)\Delta r^2 k_p \frac{T_{m,n,k-1} - T_{m-1,n,k-1}}{\Delta x} \\[2mm] +\pi(n-1)\Delta r \Delta x h(T_a - T_{m,n,k-1}) \\[2mm] -\frac{\pi}{2}(2n-3)\Delta r \Delta x k_p \frac{T_{m,n,k-1} - T_{m,n-1,k-1}}{\Delta r} \end{bmatrix} \Bigg/ \rho H_v \qquad (3.90)$$

Stage III: When Temperature > 100 °C, This represent the state when moisture content at a particular node position is at the level of equilibrium moisture

content, as a result there is a no gradient for the moisture transport process. Based on this assumption, the moisture content for this particular node stays constant, while temperature continues to increase based on influx of thermal energy by convective heat transfer. In this stage, top surface temperature approaches the temperature of hot air as baking is continued. The following equations were used to determine rates of heat and mass transport:

$$\frac{\pi}{4}(2n-3)\Delta r^2 \Delta x \rho C p \frac{T_{m,n,k} - T_{m,n,k-1}}{\Delta t} =$$

$$+ \frac{\pi}{2}(2n-3)\Delta r^2 h(T_a - T_{m,n,k-1}) - \frac{\pi}{2}(2n-3)\Delta r^2 k_p \frac{T_{m,n,k-1} - T_{m-1,n,k-1}}{\Delta x}$$

$$+ \pi(n-1)\Delta r \Delta x h(T_a - T_{m,n,k-1}) - \frac{\pi}{2}(2n-3)\Delta r \Delta x k_p \frac{T_{m,n,k-1} - T_{m,n-1,k-1}}{\Delta r}$$

(3.91)

$$\frac{\pi}{4}(2n-3)\Delta r^2 \Delta x \frac{W_{m,n,k} - W_{m,n,k-1}}{\Delta t} = 0$$

(3.92)

2. Left side of the disk along x-axis (BC line):
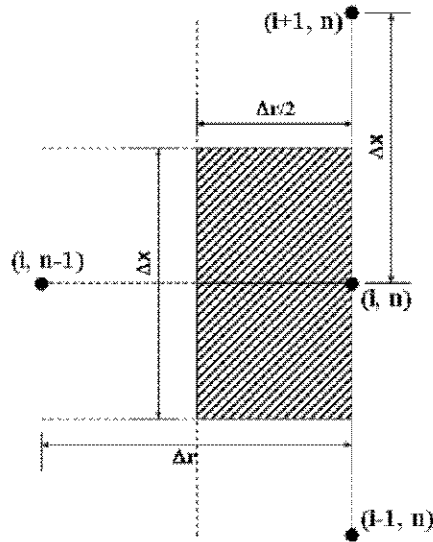
Figure 3.20: Control volume for left side of the disk along x-axis (Line BC)

This surface represents the lateral surface of a cylindrical disc and is exposed to convective heat transfer due to spreading of a jet layer around a cylinder after impinging on its top surface. Similar to the case of Point C, the baking process can be divided into three stages based on the temperature value at a particular node position

Stage I: When Temperature < 100 °C The following coupled heat and mass transfer equations were written to calculate temperature and moisture profile for this control volume (Fig. 3.19):

$$\frac{\pi}{2}(2n-3)\Delta r^2 \Delta x \rho Cp \frac{T_{i,n,k} - T_{i,n,k-1}}{\Delta t} =$$

$$+ \frac{\pi}{2}(2n-3)\Delta r^2 k_p \frac{T_{i+1,n,k-1} - T_{i,n,k-1}}{\Delta x} - \frac{\pi}{2}(2n-3)\Delta r^2 k_p \frac{T_{i,n,k-1} - T_{i-1,n,k-1}}{\Delta x}$$

$$+ 2\pi(n-1)\Delta r \Delta x h(T_a - T_{i,n,k-1}) - \pi(2n-3)\Delta r \Delta x k_p \frac{T_{i,n,k-1} - T_{i,n-1,k-1}}{\Delta r} \qquad (3.93)$$

$$- 2\pi(n-1)\Delta r \Delta x K_m H_v (P_{vs} - P_{va})$$

$$\frac{\pi}{2}(2n-3)\Delta r^2 \Delta x \frac{W_{i,n,k} - W_{i,n,k-1}}{\Delta t} =$$

$$+ \frac{\pi}{2}(2n-3)\Delta r^2 D \frac{W_{i-1,n,k-1} - W_{i,n,k-1}}{\Delta x} - \frac{\pi}{2}(2n-3)D \frac{W_{i,n,k-1} - W_{i+1,n,k-1}}{\Delta x} \qquad (3.94)$$

$$+ \pi(2n-3)\Delta r \Delta x D \frac{W_{i,n-1,k-1} - W_{i,n,k-1}}{\Delta r} - 2\pi(n-1)\Delta r \Delta x \frac{K_m}{\rho}(P_{vs} - P_{va})$$

Stage II When Temperature=100 °C, Similar to the case of location C, temperature is maintained constant during a phase change process until its moisture content becomes equal to the equilibrium moisture content. The following equations were written to calculate the temperature and moisture profile within this control volume:

$$\frac{\pi}{2}(2n-3)\Delta r^2 \Delta x \rho\ Cp\ \frac{T_{i,n,k}-T_{i,n,k-1}}{\Delta t}=0 \qquad (3.95)$$

$$\frac{\pi}{2}(2n-3)\Delta r^2 \Delta x \frac{W_{i,n,k}-W_{i,n,k-1}}{\Delta t}=$$

$$+\frac{\pi}{2}(2n-3)\Delta r^2 D\ \frac{W_{i-1,n,k-1}-W_{i,n,k-1}}{\Delta x}-\frac{\pi}{2}(2n-3)D\frac{W_{i,n,k-1}-W_{i+1,n,k-1}}{\Delta x}$$

$$+\pi(2n-3)\Delta r \Delta x D\ \frac{W_{i,n-1,k-1}-W_{i,n,k-1}}{\Delta r}$$

$$-\left[\begin{array}{l}\dfrac{\pi}{2}(2n-3)\Delta r^2 k_p\ \dfrac{T_{i+1,n,k-1}-T_{i,n,k-1}}{\Delta x}\\[2ex] -\dfrac{\pi}{2}(2n-3)\Delta r^2 k_p\ \dfrac{T_{i,n,k-1}-T_{i-1,n,k-1}}{\Delta x}\\[2ex] +2\pi(n-1)\Delta r \Delta x h(T_a-T_{i,n,k-1})\\[2ex] -\pi(2n-3)\Delta r \Delta x k_p\ \dfrac{T_{i,n,k-1}-T_{i,n-1,k-1}}{\Delta r}\end{array}\right]\Bigg/\rho\ H_v \qquad (3.96)$$

Stage III: When Temperature > 100 °C. When moisture reaches the equilibrium moisture content, temperature starts to increase, which is controlled by convective heat transfer and conduction heat transfer towards inside. Following equations were written to calculate temperature and moisture profile at this boundary condition:

$$\frac{\pi}{2}(2n-3)\Delta r^2 \Delta x \rho Cp\ \frac{T_{i,n,k}-T_{i,n,k-1}}{\Delta t}=$$

$$+\frac{\pi}{2}(2n-3)\Delta r^2 k_p\frac{T_{i+1,n,k-1}-T_{i,n,k-1}}{\Delta x}-\frac{\pi}{2}(2n-3)\Delta r^2 k_p\frac{T_{i,n,k-1}-T_{i-1,n,k-1}}{\Delta x} \qquad (3.97)$$

$$+2\pi(n-1)\Delta r \Delta x h(T_a-T_{i,n,k-1})-\pi(2n-3)\Delta r \Delta x k_p\frac{T_{i,n,k-1}-T_{i,n-1,k-1}}{\Delta r}$$

$$\frac{\pi}{2}(2n-3)\Delta r^2 \Delta x\ \frac{W_{i,n,k}-W_{i,n,k-1}}{\Delta t}=0 \qquad (3.98)$$

3. Top surface of the disk along radius (Line CD):
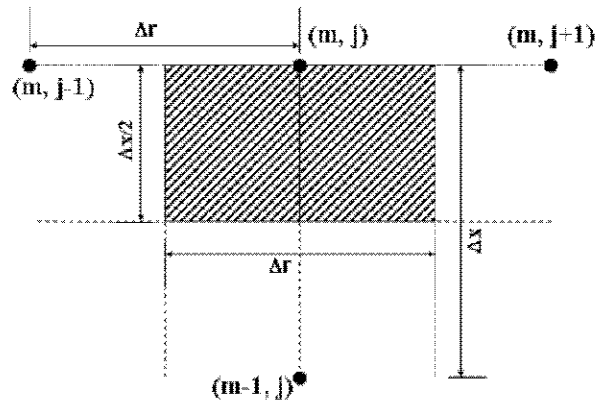
Figure 3.21: Control volume for top surface of the disk along radius (Line CD)

Line CD represents the top surface of a cylindrical disc on which hot air jet impinges. After impingement, the jet spreads in a radial direction along line CD. The thermal and mass transport processes in this control volume are directly affected by the convective heat and mass transfer coefficients. Similar to the previous case of line BC, the baking in this model can be divided into three stages.

Stage I: When Temperature< 100 °C Heat and mass transport equations for this stage along the top surface nodes are as follows:

$$\frac{\pi}{2}(2j-3)\Delta r^2 \Delta x \rho\, Cp \frac{T_{m,j,k} - T_{m,j,k-1}}{\Delta t} =$$

$$+ \pi(2j-3)\Delta r^2 h(T_a - T_{m,j,k-1}) - \pi(2j-3)\Delta r^2 k_p \frac{T_{m,j,k-1} - T_{m-1,j,k-1}}{\Delta x}$$

$$+ \frac{\pi}{2}(2j-1)\Delta r \Delta x k_p \frac{T_{m,j+1,k-1} - T_{m,j,k-1}}{\Delta r}$$

$$- \frac{\pi}{2}(2j-3)\Delta r \Delta x k_p \frac{T_{m,j,k-1} - T_{m,j-1,k-1}}{\Delta r}$$

$$- \pi(2j-3)\Delta r^2 K_m H_v (P_{vs} - P_{va})$$

(3.99)

$$\frac{\pi}{2}(2j-3)\Delta r^2 \Delta x \frac{W_{m,j,k} - W_{m,j,k-1}}{\Delta t} =$$

$$+ \pi(2j-3)\Delta r^2 D \frac{W_{m-1,j,k-1} - W_{m,j,k-1}}{\Delta x} - \pi(2j-3)\Delta r^2 \frac{K_m}{\rho}(P_{vs} - P_{va})$$

$$+ \frac{\pi}{2}(2j-3)\Delta r \Delta x D \frac{W_{m,j-1,k-1} - W_{m,j,k-1}}{\Delta r}$$

$$- \frac{\pi}{2}(2j-1)\Delta r \Delta x D \frac{W_{m,j,k-1} - W_{m,j+1,k-1}}{\Delta r}$$

(3.100)

Stage II: When Temperature= 100 °C, Following equations represents a phase change process during which temperature at this particular node is maintained at 100 °C, while its moisture content is reduced by a thermal driven evaporation of the moisture. This reduction in moisture content is allowed until it becomes equal to the equilibrium moisture content.

$$\frac{\pi}{2}(2j-3)\Delta r^2 \Delta x \rho\, Cp \frac{T_{m,j,k} - T_{m,j,k-1}}{\Delta t} = 0$$

(3.101)

$$\frac{\pi}{2}(2j-3)\Delta r^2 \Delta x \frac{W_{m,j,k} - W_{m,j,k-1}}{\Delta t} = \pi(2j-3)\Delta r^2 D \frac{W_{m-1,j,k-1} - W_{m,j,k-1}}{\Delta x}$$

$$+ \frac{\pi}{2}(2j-3)\Delta r \Delta x D \frac{W_{m,j-1,k-1} - W_{m,j,k-1}}{\Delta r} - \frac{\pi}{2}(2j-1)\Delta r \Delta x D \frac{W_{m,j,k-1} - W_{m,j+1,k-1}}{\Delta r}$$

$$- \left[\begin{array}{l} \pi(2j-3)\Delta r^2 h(T_a - T_{m,j,k-1}) \\ - \pi(2j-3)\Delta r^2 k_p \dfrac{T_{m,j,k-1} - T_{m-1,j,k-1}}{\Delta x} + \dfrac{\pi}{2}(2j-1)\Delta r \Delta x k_p \dfrac{T_{m,j+1,k-1} - T_{m,j,k-1}}{\Delta r} \\ - \dfrac{\pi}{2}(2j-3)\Delta r \Delta x k_p \dfrac{T_{m,j,k-1} - T_{m,j-1,k-1}}{\Delta r} \end{array} \right] \Big/ \rho H_v$$

(3.102)

Stage III: When Temperature > 100 °C. During this stage, as described earlier moisture content remains constant while temperature increases due to net flux of thermal energy by convection and this top surface node approaches the temperature of the oven as baking is continued. The following equations describe heat and mass transport rates for this stage:

$$\frac{\pi}{2}(2j-3)\Delta r^2 \Delta x \rho C p \frac{T_{m,j,k} - T_{m,j,k-1}}{\Delta t} =$$

$$+ \pi(2j-3)\Delta r^2 h(T_a - T_{m,j,k-1}) - \pi(2j-3)\Delta r^2 k_p \frac{T_{m,j,k-1} - T_{m-1,j,k-1}}{\Delta x}$$

$$+ \frac{\pi}{2}(2j-1)\Delta r \Delta x k_p \frac{T_{m,j+1,k-1} - T_{m,j,k-1}}{\Delta r} - \frac{\pi}{2}(2j-3)\Delta r \Delta x k_p \frac{T_{m,j,k-1} - T_{m,j-1,k-1}}{\Delta r}$$

(3.103)

$$\frac{\pi}{2}(2j-3)\Delta r^2 \Delta x \frac{W_{m,j,k} - W_{m,j,k-1}}{\Delta t} = 0$$

(3.104)

4. Right top corner of the disk (Location D):
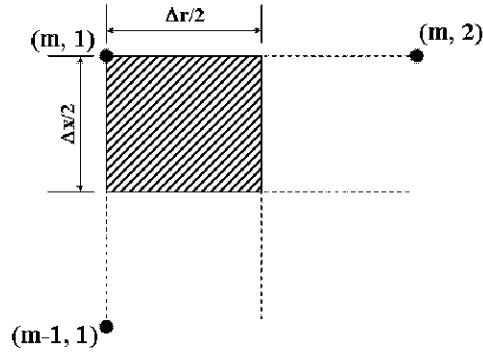
Figure 3.22: Control volume for right top corner of the disk (Location D)

This location represents the center of a top surface of a cylindrical disc. At this location impinging jet forms a stagnation point. Similar to the earlier case, baking process at this location can be divided into three stages.

Stage I- When Temperature< 100 °C: The following equations describe the heat and mass transport process during this stage.

$$
\frac{\pi}{8} \Delta r^2 \Delta x \rho C p \frac{T_{m,1,k} - T_{m,1,k-1}}{\Delta t} =
$$

$$
+ \frac{\pi}{4} \Delta r^2 h (T_a - T_{m,1,k-1}) - \frac{\pi}{4} \Delta r^2 k_p \frac{T_{m,1,k-1} - T_{m-1,1,k-1}}{\Delta x}
$$

$$
+ \frac{\pi}{2} \Delta r \Delta x k_p \frac{T_{m,2,k-1} - T_{m,1,k-1}}{\Delta r}
$$

$$
- \frac{\pi}{4} \Delta r^2 K_m H_v (P_{vs} - P_{va})
$$

(3.105)

$$
\frac{\pi}{8} \Delta r^2 \Delta x \frac{W_{m,1,k} - W_{m,1,k-1}}{\Delta t} =
$$

$$
+ \frac{\pi}{4} \Delta r^2 D \frac{W_{m-1,1,k-1} - W_{m,1,k-1}}{\Delta x} - \frac{\pi}{4} \Delta r^2 \frac{K_m}{\rho} (P_{vs} - P_{va})
$$

(3.106)

$$
- \frac{\pi}{2} \Delta r \Delta x D \frac{W_{m,1,k-1} - W_{m,2,k-1}}{\Delta r}
$$

Stage II: When Temperature= 100 °C The following equations describe rate of heat and mass transfer process during a phase change conditions at this specific location:

$$\frac{\pi}{8}\Delta r^2 \Delta x \rho_p Cp_p \frac{T_{m,1,k} - T_{m,1,k-1}}{\Delta t} = 0 \tag{3.107}$$

$$\frac{\pi}{8}\Delta r^2 \Delta x \frac{W_{m,1,k} - W_{m,1,k-1}}{\Delta t} =$$

$$+\frac{\pi}{4}\Delta r^2 D \frac{W_{m-1,1,k-1} - W_{m,1,k-1}}{\Delta x} - \frac{\pi}{2}\Delta r \Delta x D \frac{W_{m,1,k-1} - W_{m,2,k-1}}{\Delta r} \tag{3.108}$$

$$-\left[\begin{array}{c} \frac{\pi}{4}\Delta r^2 h(T_a - T_{m,1,k-1}) - \frac{\pi}{4}\Delta r^2 k_p \dfrac{T_{m,1,k-1} - T_{m-1,1,k-1}}{\Delta x} \\ +\frac{\pi}{2}\Delta r \Delta x k_p \dfrac{T_{m,2,k-1} - T_{m,1,k-1}}{\Delta r} \end{array}\right] \Bigg/ \rho H_v$$

Stage III: When Temperature > 100 °C. The following equations describe the heat and mass transport process during this stage. As in earlier cases, the rate of moisture transport is zero while the temperature rises due to net influx of thermal energy.

$$\frac{\pi}{8}\Delta r^2 \Delta x \rho\, Cp \frac{T_{m,1,k} - T_{m,1,k-1}}{\Delta t} =$$

$$+\frac{\pi}{4}\Delta r^2 h(T_a - T_{m,1,k-1}) - \frac{\pi}{4}\Delta r^2 k_p \frac{T_{m,1,k-1} - T_{m-1,1,k-1}}{\Delta x} \tag{3.109}$$

$$+\frac{\pi}{2}\Delta r \Delta x k_p \frac{T_{m,2,k-1} - T_{m,1,k-1}}{\Delta r}$$

$$\frac{\pi}{8}\Delta r^2 \Delta x \frac{W_{m,1,k} - W_{m,1,k-1}}{\Delta t} = 0 \tag{3.110}$$

<u>5. Right side of the disk along x-axis (line DA):</u>
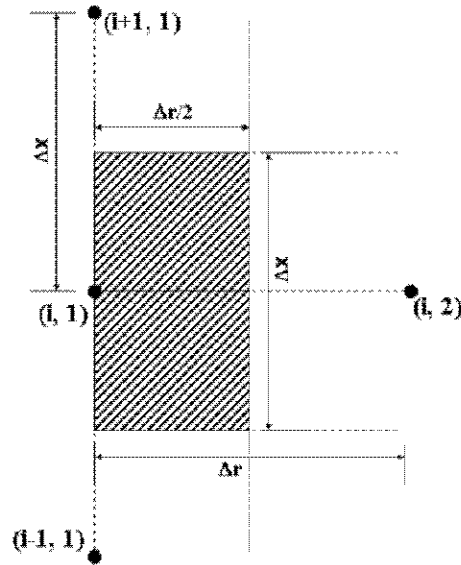
Figure 3.23: Control volume for right side of the disk along x-axis (Line DA)

This line DA represents the axis of symmetry for a cylindrical disk. The following coupled heat and mass transfer equations for this boundary condition during

Stage I, When Temperature < 100 °C are as follows

$$\frac{\pi}{4}\Delta r^2 \Delta x \rho\ Cp \frac{T_{i,1,k} - T_{i,1,k-1}}{\Delta t} =$$

$$+ \frac{\pi}{4}\Delta r^2 k_p \frac{T_{i+1,1,k-1} - T_{i,1,k-1}}{\Delta x} - \frac{\pi}{4}\Delta r^2 k_p \frac{T_{i,1,k-1} - T_{i-1,1,k-1}}{\Delta x} \qquad (3.111)$$

$$+ \pi\Delta r\Delta x k_p \frac{T_{i,2,k-1} - T_{i,1,k-1}}{\Delta r}$$

$$\frac{\pi}{4}\Delta r^2 \Delta x \frac{W_{i,1,k} - W_{i,1,k-1}}{\Delta t} =$$

$$+ \frac{\pi}{4}\Delta r^2 D \frac{W_{i-1,1,k-1} - W_{i,1,k-1}}{\Delta x} - \frac{\pi}{4}\Delta r^2 D \frac{W_{i,1,k-1} - W_{i+1,1,k-1}}{\Delta x} \qquad (3.112)$$

$$- \pi\Delta r\Delta x D \frac{W_{i,1,k-1} - W_{i,2,k-1}}{\Delta r}$$

During Stage II: When Temperature=100 °C

$$\frac{\pi}{4}\Delta r^2\Delta x\rho Cp\frac{T_{i,1,k}-T_{i,1,k-1}}{\Delta t}=0 \qquad (3.113)$$

$$\frac{\pi}{4}\Delta r^2\Delta x\frac{W_{i,1,k}-W_{i,1,k-1}}{\Delta t}=+\frac{\pi}{4}\Delta r^2 D\frac{W_{i-1,1,k-1}-W_{i,1,k-1}}{\Delta x}$$

$$-\frac{\pi}{4}\Delta r^2 D\frac{W_{i,1,k-1}-W_{i+1,1,k-1}}{\Delta x}-\pi\Delta r\Delta x D\frac{W_{i,1,k-1}-W_{i,2,k-1}}{\Delta r} \qquad (3.114)$$

$$-\left[\begin{array}{c}\frac{\pi}{4}\Delta r^2 k_p\frac{T_{i+1,1,k-1}-T_{i,1,k-1}}{\Delta x}-\frac{\pi}{4}\Delta r^2 k_p\frac{T_{i,1,k-1}-T_{i-1,1,k-1}}{\Delta x}\\ +\pi\Delta r\Delta x k_p\frac{T_{i,2,k-1}-T_{i,1,k-1}}{\Delta r}\end{array}\right]\Bigg/\rho H_v$$

When Temperature> 100 °C, Following equations were used to simulate the heat and mass transfer process along the axis of symmetry for this stage of baking

$$\frac{\pi}{4}\Delta r^2\Delta x\rho Cp\frac{T_{i,1,k}-T_{i,1,k-1}}{\Delta t}=$$

$$+\frac{\pi}{4}\Delta r^2 k_p\frac{T_{i+1,1,k-1}-T_{i,1,k-1}}{\Delta x}-\frac{\pi}{4}\Delta r^2 k_p\frac{T_{i,1,k-1}-T_{i-1,1,k-1}}{\Delta x} \qquad (3.115)$$

$$+\pi\Delta r\Delta x k_p\frac{T_{i,2,k-1}-T_{i,1,k-1}}{\Delta r}$$

$$\frac{\pi}{4}\Delta r^2\Delta x\frac{W_{i,1,k}-W_{i,1,k-1}}{\Delta t}=0 \qquad (3.116)$$

6. Left bottom corner of the disk (Location B):

To model this boundary condition at the bottom corner of the cylindrical disk, the following heat and mass transfer equations were used in

Stage I, When Temperature< 100 °C:
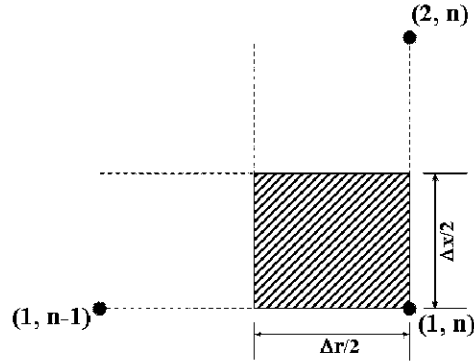
Figure 3.24: Control volume for left bottom corner of the cookie (Location B)

$$\frac{\pi}{4}\Delta r^2 \Delta x \rho Cp \frac{T_{1,n,k} - T_{1,n,k-1}}{\Delta t} =$$

$$+ \frac{\pi}{2}(2n-3)\Delta r^2 k_p \frac{T_{2,n,k-1} - T_{1,n,k-1}}{\Delta x}$$

$$+ \pi(\text{n}-1)\Delta r \Delta x \text{h} \ (\text{T}_a - \text{T}_{1,n,k\text{-}1}) - \frac{\pi}{2}(2n-3)\Delta r \Delta x k_p \frac{T_{1,n,k-1} - T_{1,n-1,k-1}}{\Delta r} \tag{3.117}$$

$$- \pi(n-1)\Delta r \Delta x K_m H_v (P_{vs} - P_{va})$$

$$\frac{\pi}{4}\Delta r^2 \Delta x \frac{W_{1,n,k} - W_{1,n,k-1}}{\Delta t} =$$

$$+ \frac{\pi}{2}(2n-3)\Delta r^2 D \frac{W_{1,n,k-1} - W_{2,n,k-1}}{\Delta x} \tag{3.118}$$

$$+ \frac{\pi}{2}(2n-3)\Delta r \Delta x D \ \frac{W_{1,n-1,k-1} - W_{1,n,k-1}}{\Delta r} - \pi(n-1)\Delta r \Delta x \frac{K_m}{\rho}(P_{vs} - P_{va})$$

Stage II, When Temperature=100 °C

$$\frac{\pi}{4}\Delta r^2 \Delta x \rho Cp \frac{T_{1,n,k} - T_{1,n,k-1}}{\Delta t} = 0 \tag{3.119}$$

$$\frac{\pi}{4}\Delta r^2 \Delta x \frac{W_{1,n,k} - W_{1,n,k-1}}{\Delta t} =$$

$$+\frac{\pi}{2}(2n-3)\Delta r^2 D \frac{W_{1,n,k-1} - W_{2,n,k-1}}{\Delta x}$$

$$+\frac{\pi}{2}(2n-3)\Delta r \Delta x D \frac{W_{1,n-1,k-1} - W_{1,n,k-1}}{\Delta r}$$

$$-\left[\begin{array}{l}\frac{\pi}{2}(2n-3)\Delta r^2 k_p \dfrac{T_{2,n,k-1} - T_{1,n,k-1}}{\Delta x} \\ +\pi(n-1)\Delta r \Delta x h(T_a - T_{1,n,k-1}) - \dfrac{\pi}{2}(2n-3)\Delta r \Delta x k_p \dfrac{T_{1,n,k-1} - T_{1,n-1,k-1}}{\Delta r} \\ -\pi(n-1)\Delta r \Delta x K_m H_v (P_{vs} - P_{va})\end{array}\right] \Bigg/ \rho H_v \qquad (3.120)$$

Stage III- When Temperature> 100 °C:

$$\frac{\pi}{4}\Delta r^2 \Delta x \rho C p \frac{T_{1,n,k} - T_{1,n,k-1}}{\Delta t} =$$

$$+\frac{\pi}{2}(2n-3)\Delta r^2 k_p \frac{T_{2,n,k-1} - T_{1,n,k-1}}{\Delta x} \qquad (3.121)$$

$$+\pi(n-1)\Delta r \Delta x h(T_a - T_{1,n,k-1}) - \frac{\pi}{2}(2n-3)\Delta r \Delta x k_p \frac{T_{1,n,k-1} - T_{1,n-1,k-1}}{\Delta r}$$

$$\frac{\pi}{4}\Delta r^2 \Delta x \frac{W_{1,n,k} - W_{1,n,k-1}}{\Delta t} = 0 \qquad (3.122)$$

7. Insulating surface along the bottom of the cookie (Line BA):

Boundary condition along the insulating bottom surface is described below:

Stage I, When Temperature< 100°C
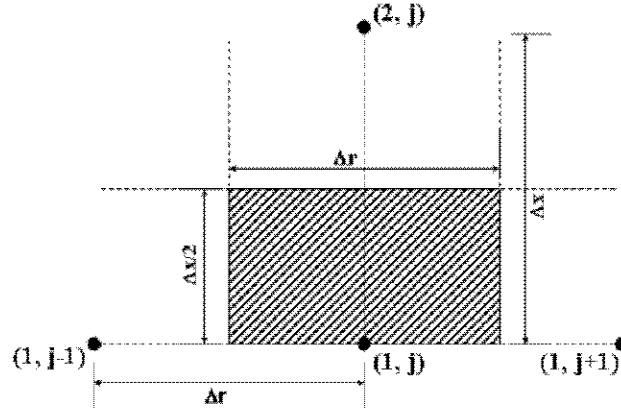
Figure 3.25: Control volume for insulating surface along the bottom of the cookie (Line BA)

$$\frac{\pi}{2}(2j-3)\Delta r^2 \Delta x \rho Cp \frac{T_{1,j,k} - T_{1,j,k-1}}{\Delta t} =$$

$$+ \pi(2j-3)\Delta r^2 k_p \frac{T_{2,j,k-1} - T_{1,j,k-1}}{\Delta x} \tag{3.123}$$

$$+ \frac{\pi}{2}(2j-1)\Delta r \Delta x k_p \frac{T_{1,j+1,k-1} - T_{1,j,k-1}}{\Delta r} - \frac{\pi}{2}(2j-3)\Delta r \Delta x k_p \frac{T_{1,j,k-1} - T_{1,j-1,k-1}}{\Delta r}$$

$$\frac{\pi}{2}(2j-3)\Delta r^2 \Delta x \frac{W_{1,j,k} - W_{1,j,k-1}}{\Delta t} =$$

$$+ \pi(2j-3)\Delta r^2 D \frac{W_{1,j,k-1} - W_{2,j,k-1}}{\Delta x} \tag{3.124}$$

$$+ \frac{\pi}{2}(2j-3)\Delta r \Delta x D \frac{W_{1,j-1,k-1} - W_{1,j,k-1}}{\Delta r} - \frac{\pi}{2}(2j-1)\Delta r \Delta x D \frac{W_{1,j,k-1} - W_{1,j+1,k-1}}{\Delta r}$$

Stage II When Temperature= 100 °C Following equations were written to

calculate the temperature and moisture content:

$$\frac{\pi}{2}(2j-3)\Delta r^2 \Delta x \rho Cp \frac{T_{1,j,k} - T_{1,j,k-1}}{\Delta t} = 0 \tag{3.125}$$

$$\frac{\pi}{2}(2j-3)\Delta r^2 \Delta x \frac{W_{1,j,k}-W_{1,j,k-1}}{\Delta t} = \pi(2j-3)\Delta r^2 D \frac{W_{1,j,k-1}-W_{2,j,k-1}}{\Delta x}$$

$$+\frac{\pi}{2}(2j-3)\Delta r \Delta x D \frac{W_{1,j-1,k-1}-W_{1,j,k-1}}{\Delta r} - \frac{\pi}{2}(2j-1)\Delta r \Delta x D \frac{W_{1,j,k-1}-W_{1,j+1,k-1}}{\Delta r}$$

$$-\left[\begin{array}{l} \pi(2j-3)\Delta r^2 k_p \dfrac{T_{2,j,k-1}-T_{1,j,k-1}}{\Delta x} \\[2mm] +\dfrac{\pi}{2}(2j-1)\Delta r \Delta x k_p \dfrac{T_{1,j+1,k-1}-T_{1,j,k-1}}{\Delta r} \\[2mm] -\dfrac{\pi}{2}(2j-3)\Delta r \Delta x k_p \dfrac{T_{1,j,k-1}-T_{1,j-1,k-1}}{\Delta r} \end{array}\right] \Big/ \rho\, H_v$$

(3.126)

Stage III- When Temperature>100 °C

$$\frac{\pi}{2}(2j-3)\Delta r^2 \Delta x \rho_p Cp_p \frac{T_{1,j,k}-T_{1,j,k-1}}{\Delta t} = (2j-3)\Delta r^2 k_p \frac{T_{2,j,k-1}-T_{1,j,k-1}}{\Delta x}$$

$$+\frac{\pi}{2}(2j-1)\Delta r \Delta x k_p \frac{T_{1,j+1,k-1}-T_{1,j,k-1}}{\Delta r} - \frac{\pi}{2}(2j-3)\Delta r \Delta x k_p \frac{T_{1,j,k-1}-T_{1,j-1,k-1}}{\Delta r}$$

(3.127)

$$\frac{\pi}{2}(2j-3)\Delta r^2 \Delta x \frac{W_{1,j,k}-W_{1,j,k-1}}{\Delta t} = 0$$

(3.128)

<u>8. Extreme right corner of the cylindrical disk (Location A):</u>
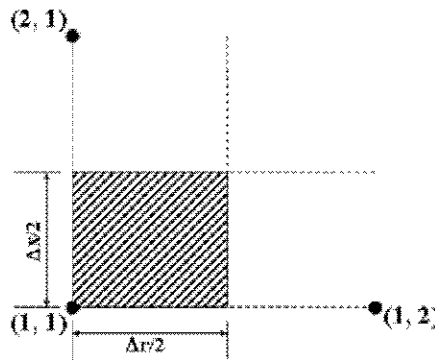
Figure 3.26: Control Volume for extreme right corner of the disk (Location A) Stage I When Temperature< 100 °C

$$\frac{\pi}{8}\Delta r^2 \Delta x \rho Cp \frac{T_{1,1,k} - T_{1,1,k-1}}{\Delta t} =$$

$$+\frac{\pi}{4}\Delta r^2 k_p \frac{T_{2,1,k-1} - T_{1,1,k-1}}{\Delta x} + \frac{\pi}{2}\Delta r \Delta x k_p \frac{T_{1,2,k-1} - T_{1,1,k-1}}{\Delta r} \qquad (3.129)$$

$$\frac{\pi}{8}\Delta r^2 \Delta x \frac{W_{1,1,k} - W_{1,1,k-1}}{\Delta t} =$$

$$-\frac{\pi}{4}\Delta r^2 D \frac{W_{1,1,k-1} - W_{2,1,k-1}}{\Delta x} - \frac{\pi}{2}\Delta r \Delta x D \frac{W_{1,1,k-1} - W_{1,2,k-1}}{\Delta r} \qquad (3.130)$$

Stage II- When Temperature=100°C:

$$\frac{\pi}{8}\Delta r^2 \Delta x \rho Cp \frac{T_{1,1,k} - T_{1,1,k-1}}{\Delta t} = 0 \qquad (3.131)$$

$$\frac{\pi}{8}\Delta r^2 \Delta x \frac{W_{1,1,k} - W_{1,1,k-1}}{\Delta t} =$$

$$-\frac{\pi}{4}\Delta r^2 D \frac{W_{1,1,k-1} - W_{2,1,k-1}}{\Delta x} - \frac{\pi}{2}\Delta r \Delta x D \frac{W_{1,1,k-1} - W_{1,2,k-1}}{\Delta r}$$

$$-\left[\frac{\pi}{4}\Delta r^2 k_p \frac{T_{2,1,k-1} - T_{1,1,k-1}}{\Delta x} + \frac{\pi}{2}\Delta r \Delta x k_p \frac{T_{1,2,k-1} - T_{1,1,k-1}}{\Delta r}\right] \Big/ \rho H_v \qquad (3.132)$$

Stage III- When Temperature> 100°C

$$\frac{\pi}{8}\Delta r^2 \Delta x \rho Cp \frac{T_{1,1,k} - T_{1,1,k-1}}{\Delta t} =$$

$$-\frac{\pi}{4}\Delta r^2 k_p \frac{T_{2,1,k-1} - T_{1,1,k-1}}{\Delta x} + \frac{\pi}{2}\Delta r \Delta x k_p \frac{T_{1,2,k-1} - T_{1,1,k-1}}{\Delta r} \qquad (3.133)$$

$$\frac{\pi}{8}\Delta r^2 \Delta x \frac{W_{1,1,k} - W_{1,1,k-1}}{\Delta t} = 0 \qquad (3.134)$$

Thermophysical Properties

To begin with, simulations were carried using constant thermophysical properties of potato which are given in **Table 3.3**.

Table 3.3: Input values for numerical simulation

Specific heat of potato (Cp_p)	3631.63 J/kgK	(Choi and Okos, 1985)
Effective diffusivity (D_{eff})	1.4×10^{-9} m^2/s	(Maroulis et al. 2001)
Average heat transfer coefficient (h)	220 W/m^{2}K	(our data)
Latent heat of evaporation for water (H_v)	2.33×10^6 J/kg water	(Zanoni et al., 1994)
Thermal conductivity of potato (k_p)	0.5269 W/mK	(Choi and Okos, 1986)
Convective mass transfer coefficient (K_m)	6×10^{-9} kg water/m^{2}sPa	(Zanoni et al., 1994)
Bulk density of potato (ρ_p)	1074.21 kg/m^3	(Choi and Okos, 1985)
Density of potato solids (ρ_{sp})	230.280 kg/m^3	(Choi and Okos, 1985)

CHAPTER 4

Results

The results are presented according to the objectives.

Objective 1

To carry out numerical simulation of conjugate thermal transport during jet impingement baking and validate it using experimental data

To carry out numerical simulation of conjugate heat transport, measurements of jet inlet velocity and inlet temperature were required. In this study, experiments were also conducted to measure average surface and local heat transfer coefficients. These measurements were made to characterize rate of thermal transport for the pilot scale experimental jet impingement unit. These experimental results were also used for validation of numerical simulation results. The first part of this section describes the experimental results for following measurements:

Experimental Measurements

(a) Maximum jet velocity

(b) Measurement of average top surface heat transfer coefficient

(c) Measurement of local maximum in surface heat transfer coefficient

Maximum Jet Velocity

Results for variation of the maximum jet velocity with plenum pressure for the three different jets (Jets # 7, 8 and 9 as shown in Figure 3.2) under different conditions of temperature are shown in **Figure 4.1**. Velocity was measured using

a pitot tube at 20 mm from the jet tube ends. The results showed an expected non-linear increase in velocity with an increase in jet air pressure. The results also indicated a small increase in velocity with an increase in jet air temperature for a fixed pressure. This trend was expected as density of air decreases with an increase in temperature. The theoretical relationship between jet velocity U, plenum pressure and density is given by $:(U = \sqrt{\dfrac{2\Delta P}{\rho(T)}})$. Results of velocity measurement experiments using the pitot tube indicated a fair amount of uniformity in the maximum velocity under different jets at same conditions of temperature and pressure. The velocity values ranged from 18 m/s to 44 m/s as the plenum pressure was changed from 250 Pa to 1050 Pa. The experimentally determined value of maximum velocity was used to calculate the Reynolds number. The range of the Reynolds number value based on jet tube inside diameter (17.8 mm) was 12,000-35,000, which indicated that the flow was turbulent. Based on literature, a round jet with the Reynolds number greater than 2500 is generally considered to be turbulent (Gardon and Akfirat, 1965).
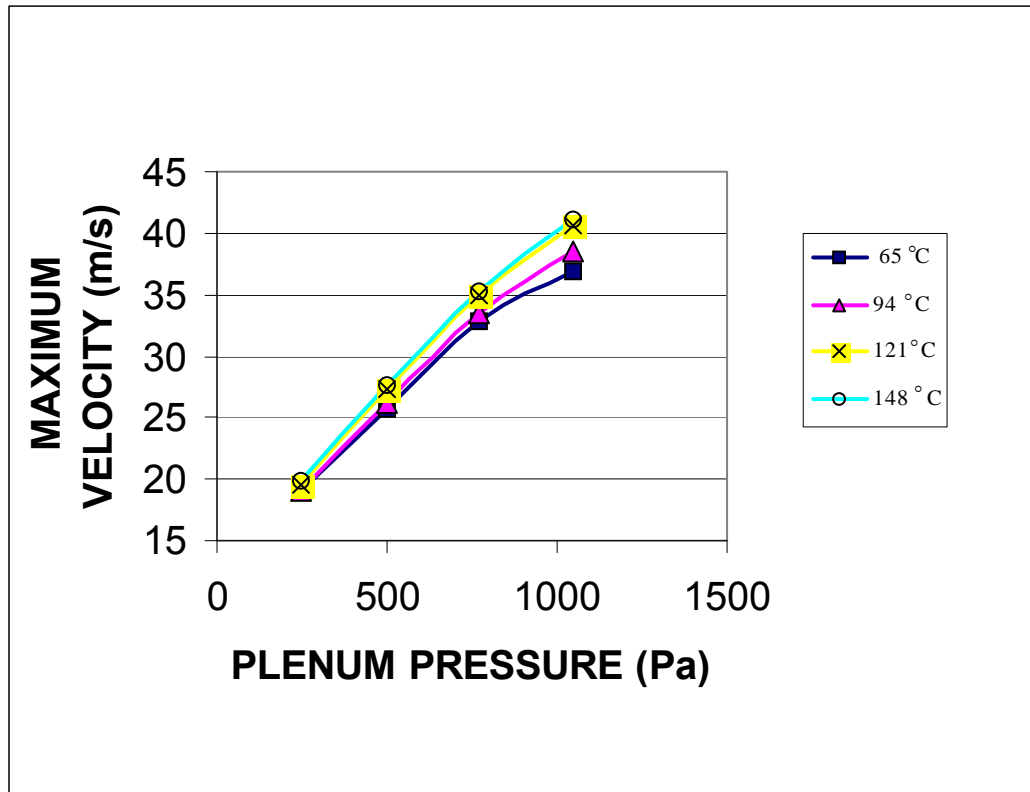
Figure 4.1

Variation of maximum jet velocity (measured using pitot tube) versus plenum pressure chamber at different temperatures

Measurement of Average Top Surface Heat Transfer Coefficient

Experiments for measurement of top surface average heat transfer coefficient were carried out at two levels of jet velocity (22 and 42 m/s), and at two levels of jet air temperature (65 °C and 150 °C). The experiments were carried out using a model cookie shaped object placed in a cavity of a wooden plate. The wooden plate was designed with a cut out to insulate sides of the model cookie shaped object such that only top surface of the model cookie is exposed to jet. Details of experimental designs are discussed in the experimental research methods section (Chapter 3). Results for surface heat transfer coefficient are shown in **Table 4.1**. The results show an expected increase in surface heat transfer coefficient with an increase in jet impingement velocity. Further, results show no significant effect of temperature of hot air impinging jet on average surface heat transfer coefficient.

The next step was to measure local surface heat transfer maxima. To design experiments for measurement of local surface heat transfer maxima and to analyze experimental results, an error range in measurement of local surface heat transfer coefficient was estimated based on a theoretical analysis. The following section presents the analysis for error estimation.

Table 4.1

**Average top surface heat transfer coefficient for a model cookie system
obtained at different plenum pressure and temperature**

Temperature (°C)	Plenum pressure (Pa)	Top surface average heat transfer coefficient with side areas covered $(W/m^2K)*$
65	250 (22 m/s)	117
65	1050 (42 m/s)	165
150	250 (22 m/s)	126
150	1050 (42 m/s)	180

* Typical Error = ± 15%

Estimation of Error in Measurement of the Local Maximum in Heat Transfer Coefficient

Error in measurement of local maximum in heat transfer coefficient "h max" will depend on a percent error in measurement of heat flux gage output and a percent error in measurement of temperature using T- type thermocouples. Total error can be represented in form of the following equation.

$$\Delta h/h = \Delta q/q + \Delta (\Delta T)/ (\Delta T) \qquad (4.1)$$

Δq represents the error in recording heat flux gage output using DAS1800 HR board. For 0-10 V output range, the Δq value is estimated to be 45 mV as supplied by the manufacturer (Keithley Metrabyte, OH). Error in determination of temperature is 1 $^{\circ}$C per 100 $^{\circ}$C range for the T type thermocouples (Omega Engineering catalog). For experiments with oven air temperatures below 100 $^{\circ}$C, the maximum error in recording cookie surface and air temperature will be a sum of the errors for each thermocouple (sum of the errors of both thermocouples-thermocouple for hot air jets and the thermocouple for the surface temperature of the heat flux gage). So the total error in temperature difference measurement in this case could be as high as 2 $^{\circ}$C. Based on this analysis it was established that error in measurement of temperature is a major contributor to the total error in determination of local heat transfer coefficient. As model cylindrical disc heats up, temperature difference between the hot air jets and the surface temperature of the heat flux gage decreases. The contribution of error term in measurement

of local heat transfer maximum increases as (ΔT) decreases (eqn. 4.1). Based on this approach the error in temperature measurement becomes 20 % when the temperature difference is about 10 ^{o}C, which lead to a total estimated error of 20.9% in measurement of heat transfer coefficient (h). Based on this analysis, it was determined that measurement of local surface heat transfer maximum with an impinging jet at 65 ^{o}C would result in significant error as the total range of increase in temperature from room temperature (25 ^{o}C) to 65 ^{o}C is small. Beyond a model cookie temperature of ~50 ^{o}C, the magnitude of error would increase significantly above the acceptable level. Based on this estimate, experiments were designed to measure local heat transfer maxima using impinging jet at temperature of 150 ^{o}C at different levels of impinging jet velocity (22, 29, 36 and 42 m/s).

Local Maximum in Heat Transfer Coefficient for Cookie Shaped Objects

Results for variation of local maximum in the heat transfer coefficient as a function of impinging jet velocity are presented in **Figure 4.2**. The results demonstrate that local maximum surface heat transfer coefficient increases with an increase in jet velocity (plenum pressure). As discussed in the previous section, error in measurement of local heat transfer coefficient is a function of temperature difference between a heat flux gage and a hot impinging air. As the temperature difference decreases the error in measurement of local surface heat transfer maxima increases. It was estimated that maximum error was in the range of ~ 20 % for a 10°C difference in temperature between a heat flux gage

and an impinging jet. Based on this estimate, to represent the worst-case scenario, error bars with 20% error range are shown in **Figure 4.2**. To establish statistical significance of change in local heat transfer coefficient as a function of impinging jet velocity, a single factor ANOVA (Analysis of Variance) was carried out. Result of the statistical analysis is shown in **Table 4.2.** For ANOVA, triplicate repeat values of local heat transfer at four different jet velocities were paired in groups of two jet velocities and a single factor ANOVA analysis was conduced with a confidence interval (alpha=0.05) of 95%. The results show that for differences larger than 14 m/s in jet velocity, a significant difference ($P<0.05$) in local heat transfer coefficient was observed for all groups of jet velocities.

Figure **4.3** compares local surface heat transfer maximum with measurements of average top surface heat transfer coefficient as a function of impinging jet velocity. The results show that the local maximum heat transfer coefficient is higher than the average top surface heat transfer coefficient measured under same experimental conditions. To establish statistical significance of difference between local maxima and average heat transfer coefficient, a single factor ANOVA (Analysis of Variance) using triplicate repeat values for each group was carried out. Statistical analysis is summarized in **Table 4.3**. Results clearly show that the local heat transfer coefficient values are significantly different from the average top surface heat transfer coefficient values. Together, these results indicate that jet impingement system will have some degree of non-uniformity in distribution of surface heat transfer coefficient

along the surface of cookie shaped model geometry. This can potentially have implications for uniformity of baking.
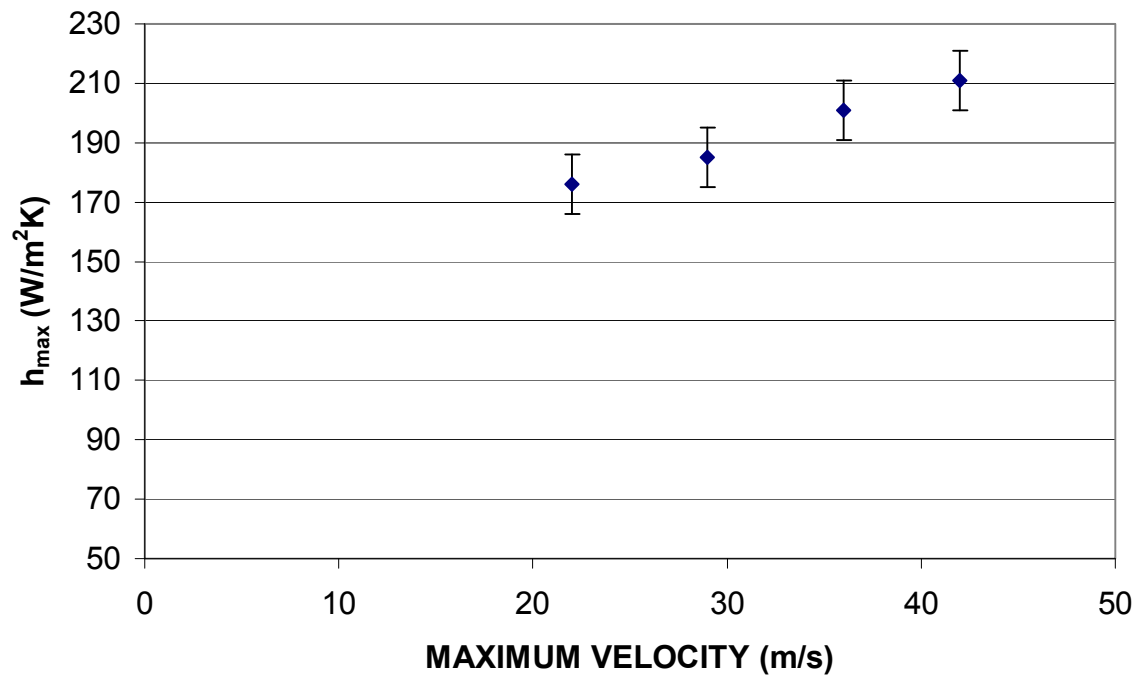
Figure 4.2

Variation of local maximum heat transfer coefficient with velocity for 50 mm diameter cookie placed under jet # 7 at 150 ^{o}C

Table 4.2

ANOVA analysis for local heat transfer coefficient at different jet velocities

Comparison pairs	Alpha=0.05		
	p value	Significant difference	
Local h values			
Vel=22, 42 m/s	0.013901	Yes	
Vel=22,36m/s	0.022191	Yes	
Vel=22,29m/s	0.184275	No	
Vel=29,42m/s	0.01886	Yes	
Vel=29,36m/s	0.033428	Yes	
Vel=36,42m/s	0.142982	No	
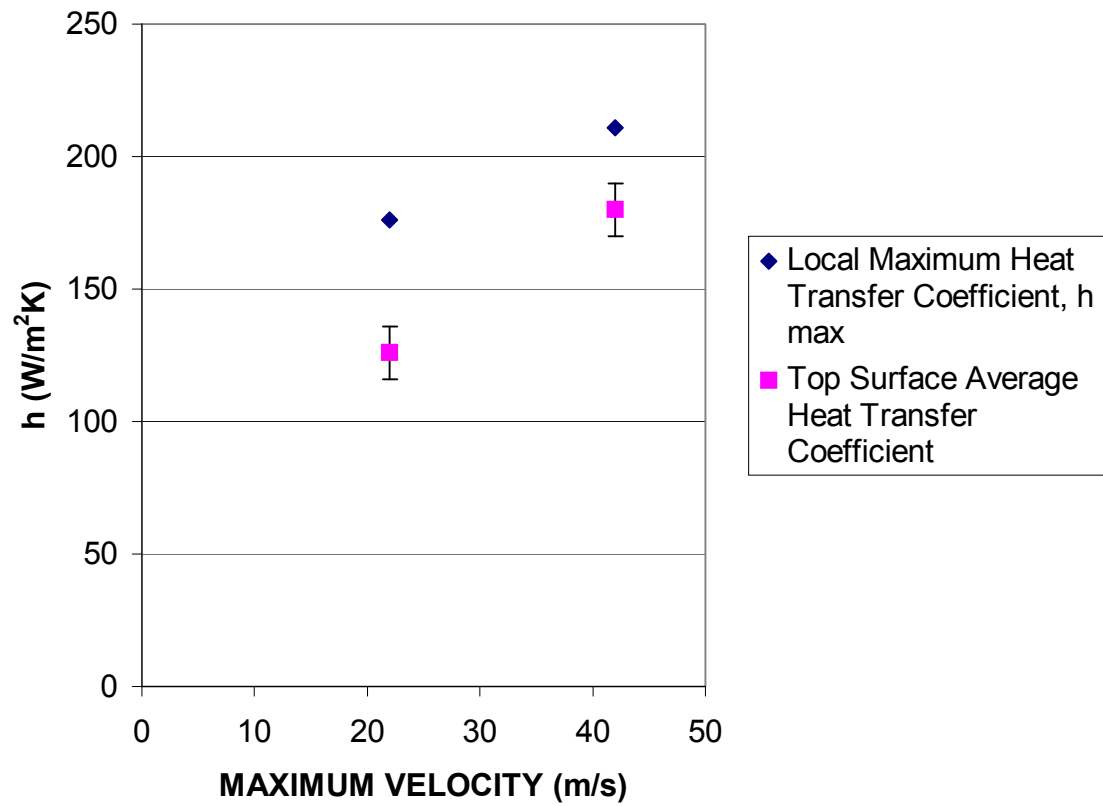
Figure 4.3

**Comparison of local maximum heat transfer coefficient (h max)
with average heat transfer coefficient for a cookie shaped objects
with side areas covered
(only top surface exposed) under jet # 7 at 150 ^{o}C**

Table 4.3

**ANOVA analysis for comparison of local and average heat
transfer coefficient at two levels of jet velocity with alpha =0.05**

Jet Velocity	Avg. h (W/m²K)	Local hmax (W/m²K)	p Value	Significant Difference
Inlet Velocity =22 m/s	126	176	0.006329	Yes
Inlet Velocity= 42m/s	181	211	0.006322	Yes

Numerical Simulation and Comparison with Experimental Results

Objective 1a: Numerical Simulation of Flow Field

Contours of velocity magnitude obtained using numerical simulation of flow field as described in the methods section for an isothermal impinging jet on a flat plate at z/d =5 are shown in **Figure 4.4**. The results indicate formation of a potential core in the initial region of a jet flow. As the jet develops further, results show narrowing of the potential core region. This is in full agreement with the studies carried by Gardon and Akfirat, (1965) and Martin, (1977).

Further, to validate the numerical simulation results, velocity contours obtained using numerical simulation were compared with the results of experimental study for a single impinging jet carried by Marcoft et al., (1999). In this experimental study velocity measurement were made using a LDA (Laser Doppler Anemometry) system on a jet impingement oven with a z/d spacing of 5. Velocity field was mapped at discrete plains at specific z positions. Velocity values at specific z positions (72% and 11.11% height from the impinging plate of the total nozzle to plate spacing in a z/d =5 geometry) obtained from the numerical simulation were compared with experimentally measured velocities at the same z position. **Figure 4.5 (a, b)** compares numerically predicted axial velocity of an impinging jet as a function of radial distance with experimentally measured jet velocity at two z levels (z positions, i.e. 72%, 11.11%) respectively. The results indicate a good agreement between the numerical predictions of the

flow field and the experimentally obtained impinging jet velocities at different stages (different z positions) of an impinging jet.

V_{max}=25m/s
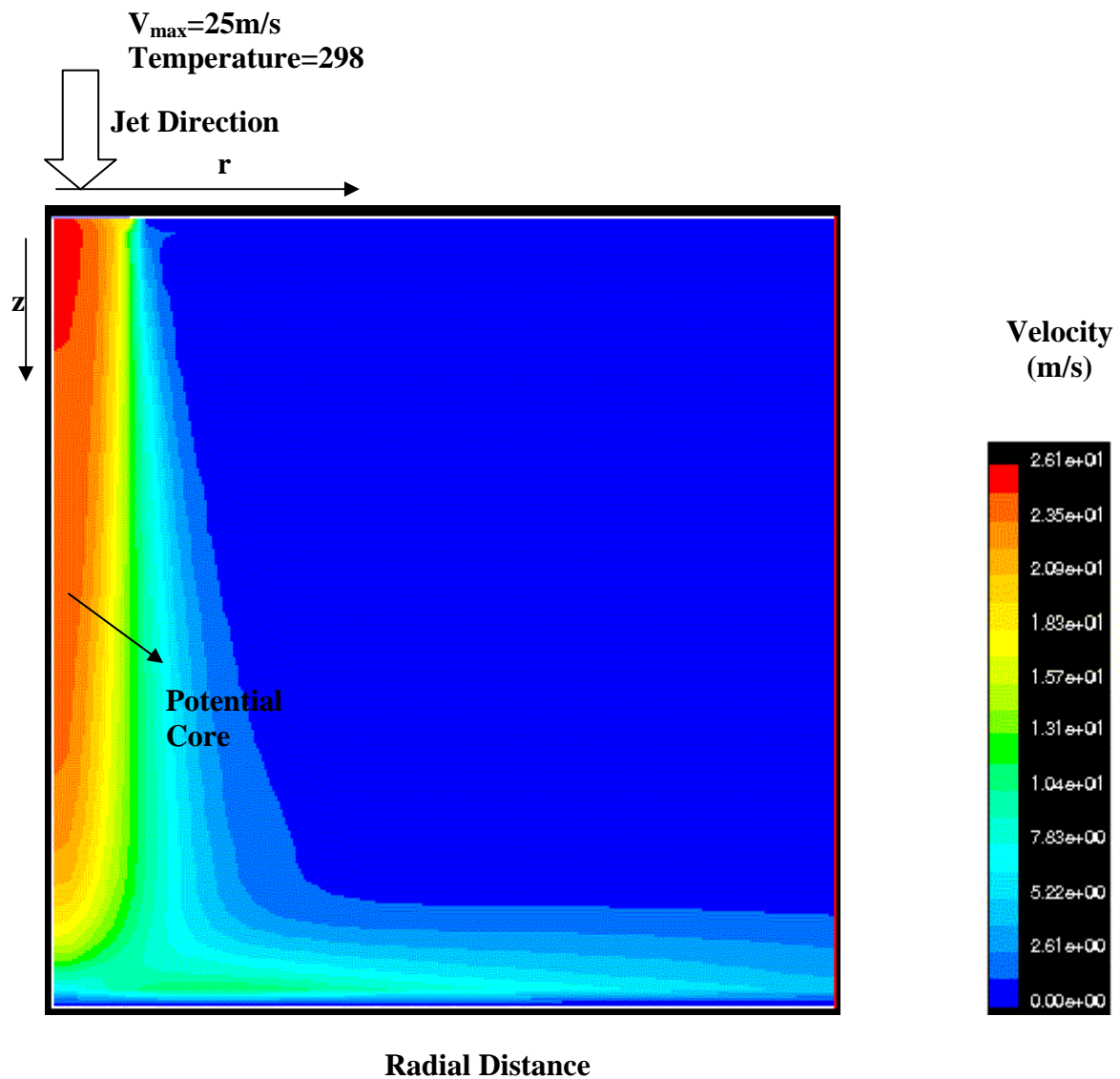
Figure 4.4

**Isothermal velocity (Total Velocity) contours of an axi-symmetric jet
impinging on a target plate at z/d=5 at maximum jet velocity of 25 m/s, and jet
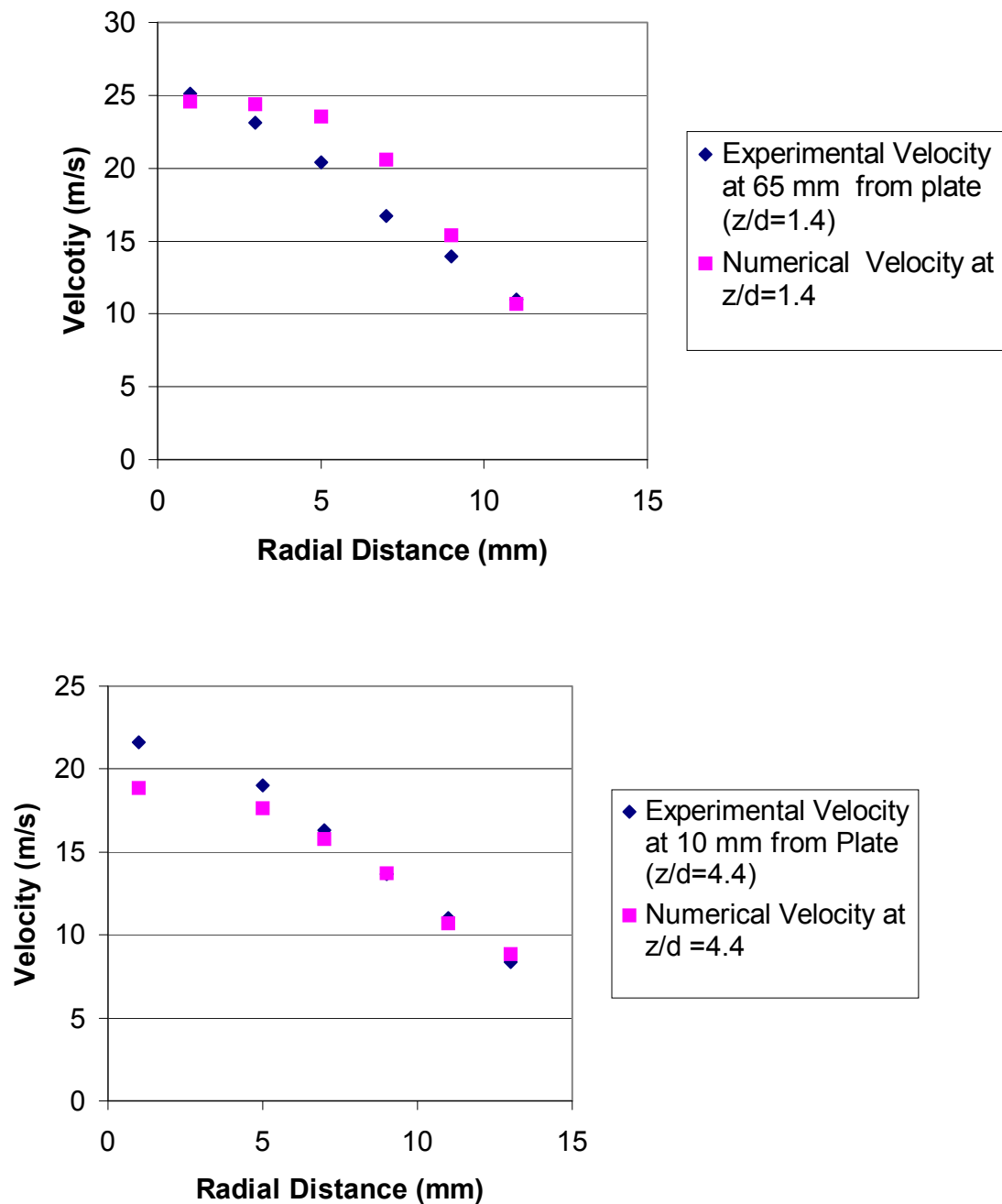inlet temperature of 298 K**

Figure 4.5

Comparison of the numerically obtained axial velocity with experimental axial velocity data (Marcoft et al, 1999) as a function of radial distance at various z/d positions (a) z/d= 1.4 (65 mm from the target plate), (b) z/d = 4.4 (10 mm from the plate)

Object 1(b)

To numerically predict the conjugate heat transfer between a turbulent hot air jet and a model food object and its experimental validation

Numerical Simulation of an Impinging Jet on Model Cookie Shape Geometry

Isovelocity (total) contours and isotherms obtained from numerical simulation of a single jet impinging on a cookie are shown in **Figures 4.6, 4.7 and 4.8** at time t = 200 s. Velocity contours in **Figure 4.6** clearly demonstrate presence of potential core along the centerline of the jet and the stagnation point at the center of an impinging jet. These results are in agreement with the results reported by Gardon and Akfirat (1965), Martin (1977), and Heather et al (1999).

Figure 4.7 shows isotherms for heating of a model cookie with the thermophysical properties of aluminum. The result shows uniform temperature in the aluminum cookie. When a model cookie with thermophysical properties typical of a food material is used in this simulation, result shows of substantial temperature gradients within the cookie (**Figure 4.8)**. This difference in the response of a model aluminum cookie and a model food cookie is expected due to significant internal resistance to heat transfer for a food cookie as compared to an aluminum cookie. As shown by Nitin and Karwe (2001), the Biot number Bi (= hH/k_{cookie}) for an aluminum cookie during jet impingement is much smaller than 0.1, which represents negligible internal resistance to heat transfer, whereas the Bi value for a real cookie is usually much greater than 0.1.

Based on this simulation, we calculated the surface heat transfer coefficient for a model cookie object. Variation of surface heat transfer coefficient along the model cookie surface obtained from numerical simulation at different values of nozzle-to- plate spacing (z/d= 2, 3, 5) are shown in **Figures 4.9, 4.10, and 4.11** respectively. The results show the radial variation of surface heat transfer coefficient along the top surface of the model cookie at four different jet velocities (i.e. 10, 20, 30, 40 m/s). This variation of surface heat transfer coefficient was same at t = 20, 50, 100, 200, 400 s. Variation of top surface heat transfer coefficient values shows the existence of local maximum at the stagnation point for the case of z/d= 2 and 3 at all four jet velocities. These results are in agreement with the results reported by Martin (1977) and Huber & Viskanta (1994a, 1994b). In case of z/d =5, the local maximum was observed at stagnation point for the jet velocities of 10 and 20 m/s. For the case of jet maximum velocities of 30 and 40 m/s, the maximum in heat transfer was slightly off center (away from the stagnation point). This shift in local maximum can be explained by radial acceleration of an impinging jet after impinging near the stagnation point combined with a decrease in jet centerline velocity due to increased entrainment at higher values of z/d. As a result the local maximum in heat transfer coefficient is slightly off center.

For a fixed z/d position, magnitude of the heat transfer coefficient increased with an increase in jet air velocity, as expected. The local and surface average heat transfer coefficient values also increased with a decrease in z/d

value (Lytle and Webb, 1994). Thus higher rates of heat transfer can be obtained by bringing the jets closer to the object.
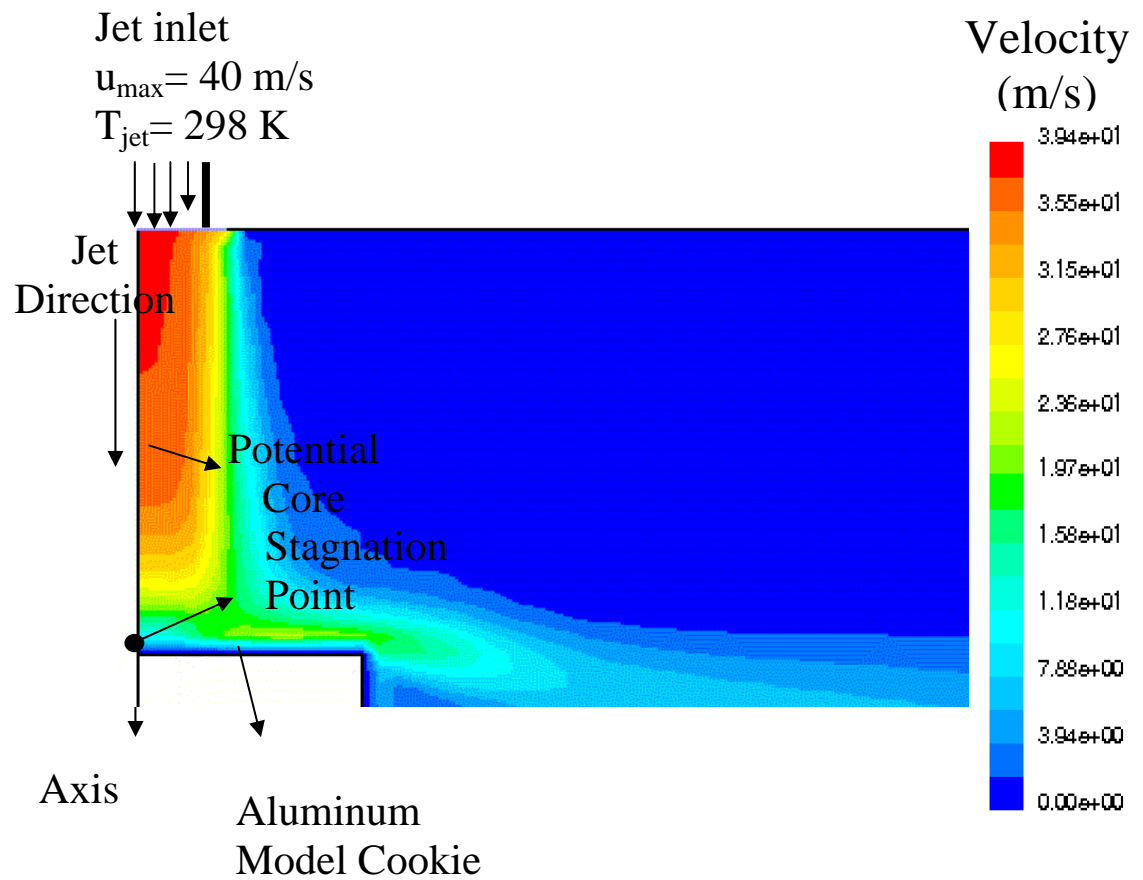
Figure 4.6

Contour plot of total velocity in a turbulent impinging jet at z/d= 3

Jet inlet
u_{max}= 10 m/s
T_{jet}= 450 K

Temperature
(K)

model aluminum cookie

4.50e+02
4.47e+02
4.43e+02
4.40e+02
4.37e+02
4.33e+02
4.30e+02
4.27e+02
4.23e+02
4.20e+02
4.16e+02
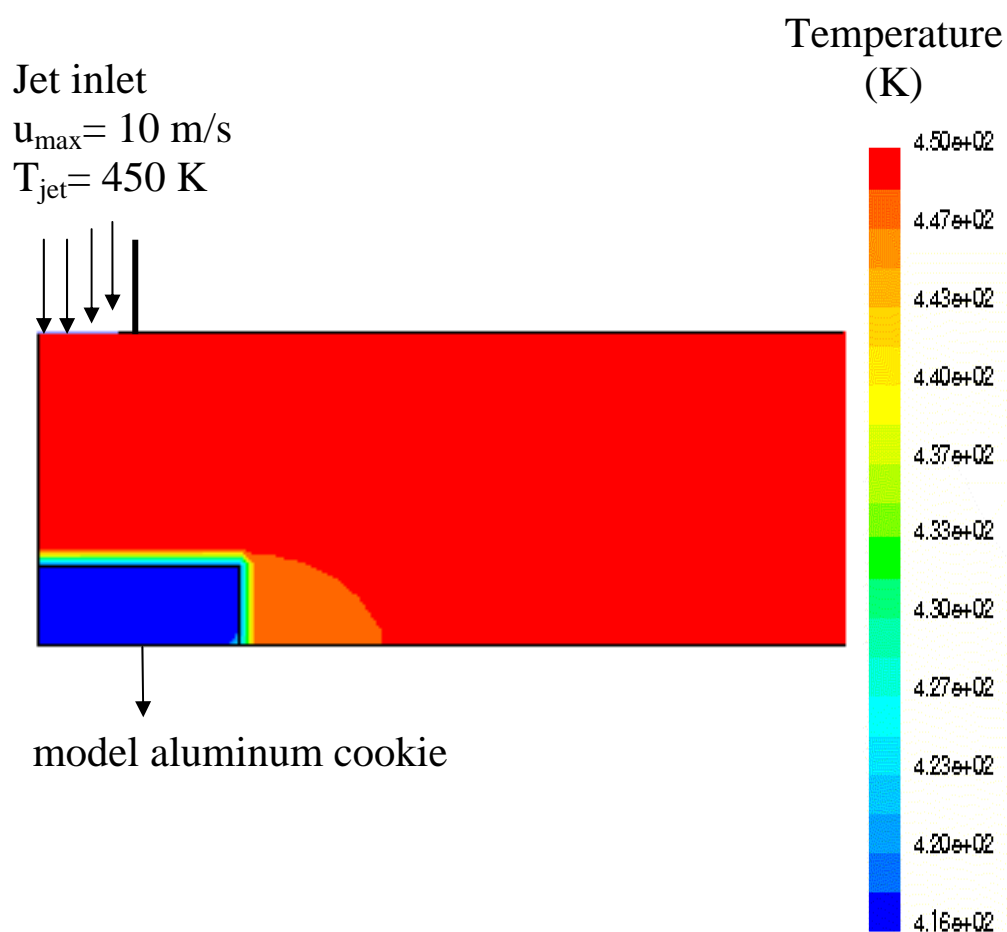
Figure 4.7

Isotherms in air and in aluminum model cookie placed under a hot air impinging jet at z/d=2 and maximum jet velocity of 10m/s

Jet inlet
u_{max}=10 m/s
T_{jet}=450 K

Temperature (K)

4.50e+02

4.38e+02

4.25e+02

4.13e+02

4.00e+02

3.88e+02

3.75e+02

3.63e+02

3.50e+02

3.38e+02

3.25e+02

Cookie made of food material

Figure 4.8

**Isotherms in air and in a cookie made up of representative food
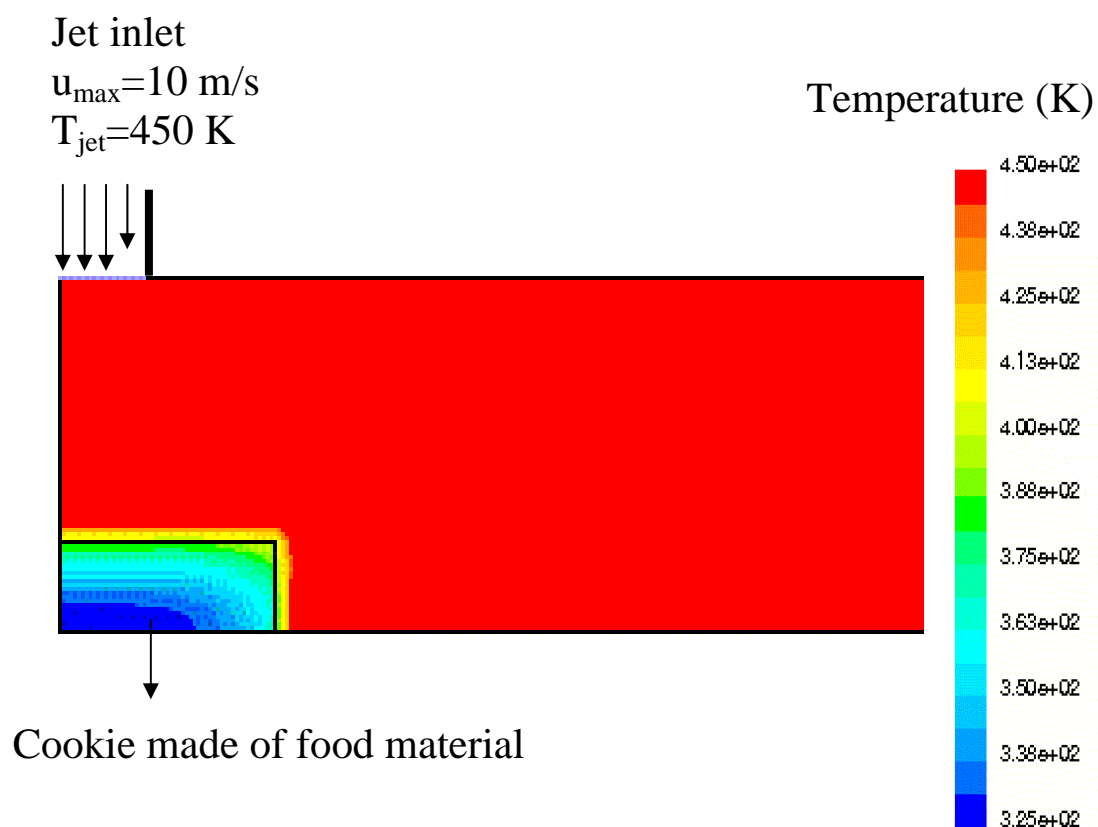material placed under a hot air impinging jet at z/d=2 and
maximum jet velocity of 10m/s**

Figure 4.9

Variation of local surface heat transfer coefficient as a function of position on top surface of cookie at different jet inlet velocities for z/d =2, T_{jet}=450K

Figure 4.10

Variation of local surface heat Transfer coefficient as a function of position on top surface of cookie at different jet inlet velocities for z/d =3, T_{jet}=450K

Figure 4.11

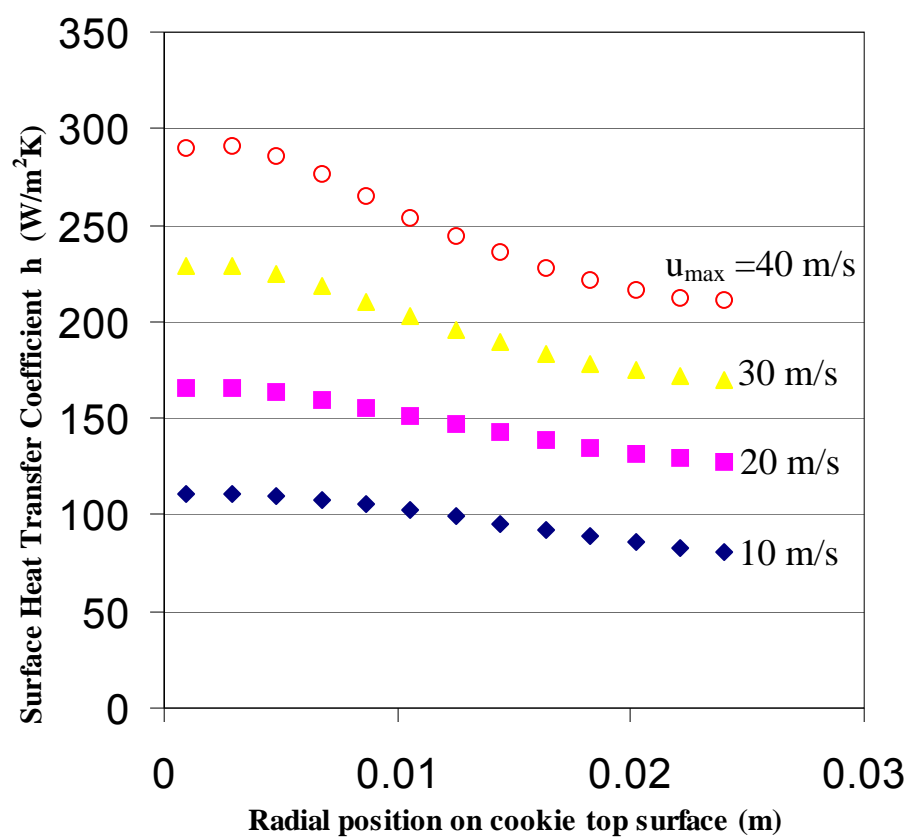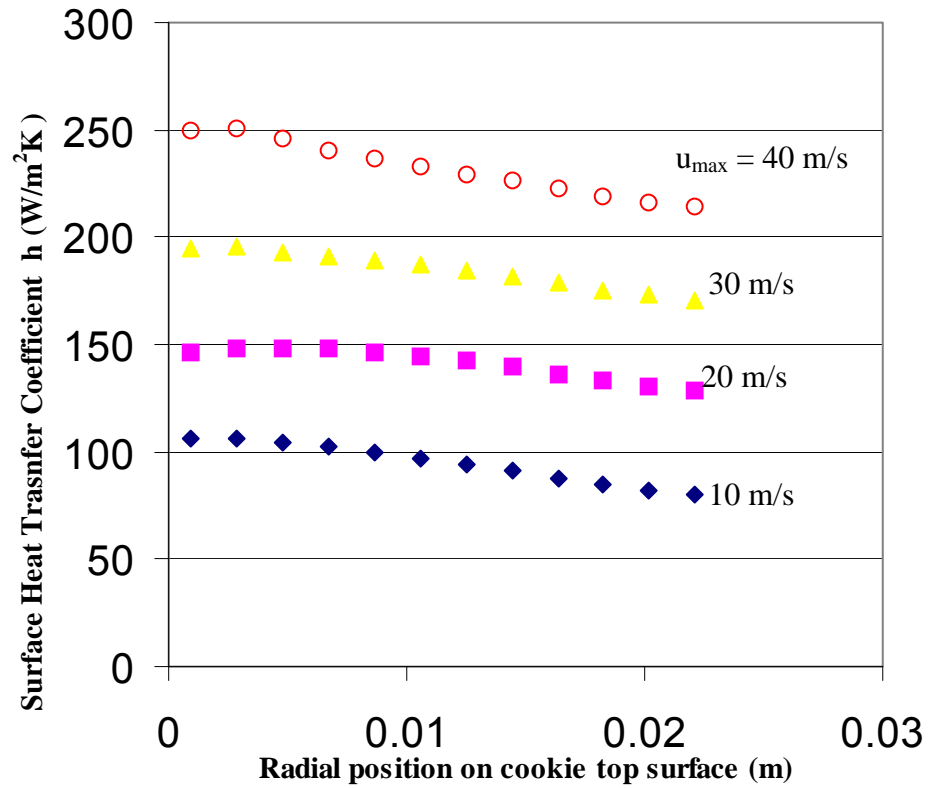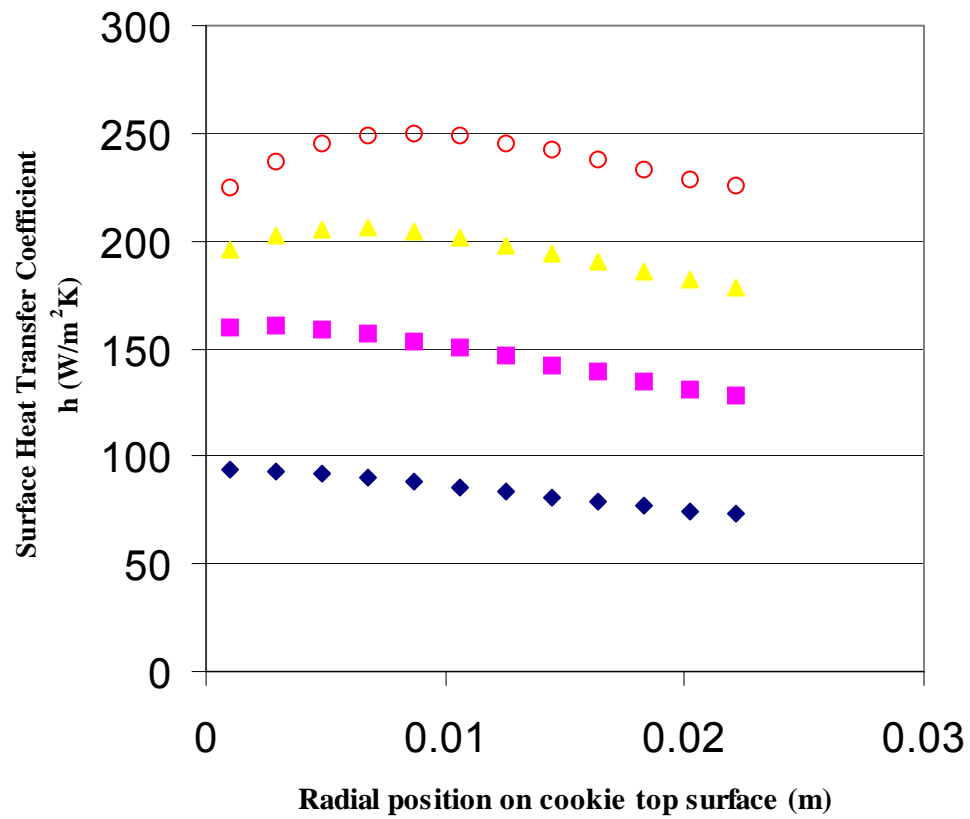**Variation of local surface heat transfer coefficient as a function of position on top surface of cookie at different jet inlet velocities for z/d =5, T_{jet}=450K**

Comparison of Numerically Predicted Surface Heat Transfer with Experimental Measurements

Local Heat Transfer Coefficient

Comparison of experimental data of local heat transfer coefficient at a stagnation point, with numerically determined values with and without heat flux gage modification at z/d=3 are shown in **Figure 4.12 (a and b)**. Experimental measurements provided the local average heat transfer coefficient over the area of the heat flux gage (10mm x 8 mm). To numerically calculate average heat transfer coefficient over the same area as the heat flux gage, numerically predicted local heat transfer coefficient values were averaged for 5 mm radial distance from the axis of symmetry. Results show that the numerical predicted values of local heat transfer coefficient are in agreement with the experimental measurements (within $\pm$ 15 %).

Results of numerical approach, simulating the effect of attachment of heat flux gage on the surface of a model cookie (for this simulation we modeled the effect of difference in thermal conductivity of heat flux gage and a model cookie), show a better agreement with the experimental data as compared to the results without the heat flux gage. The details of the error estimation using heat flux gage are discussed in Nitin (2001). These deviations can be partially attributed due to difference in the thermal conductivity of the aluminum model cookie and that of the heat flux gage (Deo and Karwe, 1998), due to the bonding cement, etc.

Average Surface Heat Transfer Coefficient

Comparison of experimentally measured average surface heat transfer coefficient results with the numerical simulation is shown in **Figure 4.13**. Results demonstrate a good agreement (within ± 15 %) between experimentally measured average heat transfer coefficient and numerically predicted results. Details of the error analysis for average heat transfer measurements are discussed in Nitin and Karwe, (2001).

To validate that the surface heat transfer coefficient values measured using aluminum disks indeed represent the heat transfer coefficient values for a real cookie (neglecting any mass transfer), numerical simulations were carried out using thermophysical properties of aluminum and a food material. Radial variation of the surface heat transfer coefficient obtained for two model materials (aluminum and food) are shown in **Figure 4.14.** The results demonstrate that surface heat transfer coefficient values for an aluminum cookie and a real food material cookie were the same (**Fig. 4.14a**), although the surface temperature values for the two cookies were vastly different (**Fig. 4.14b**). This validates the theoretical prediction that surface heat transfer coefficient is independent of the thermophysical properties of a product.
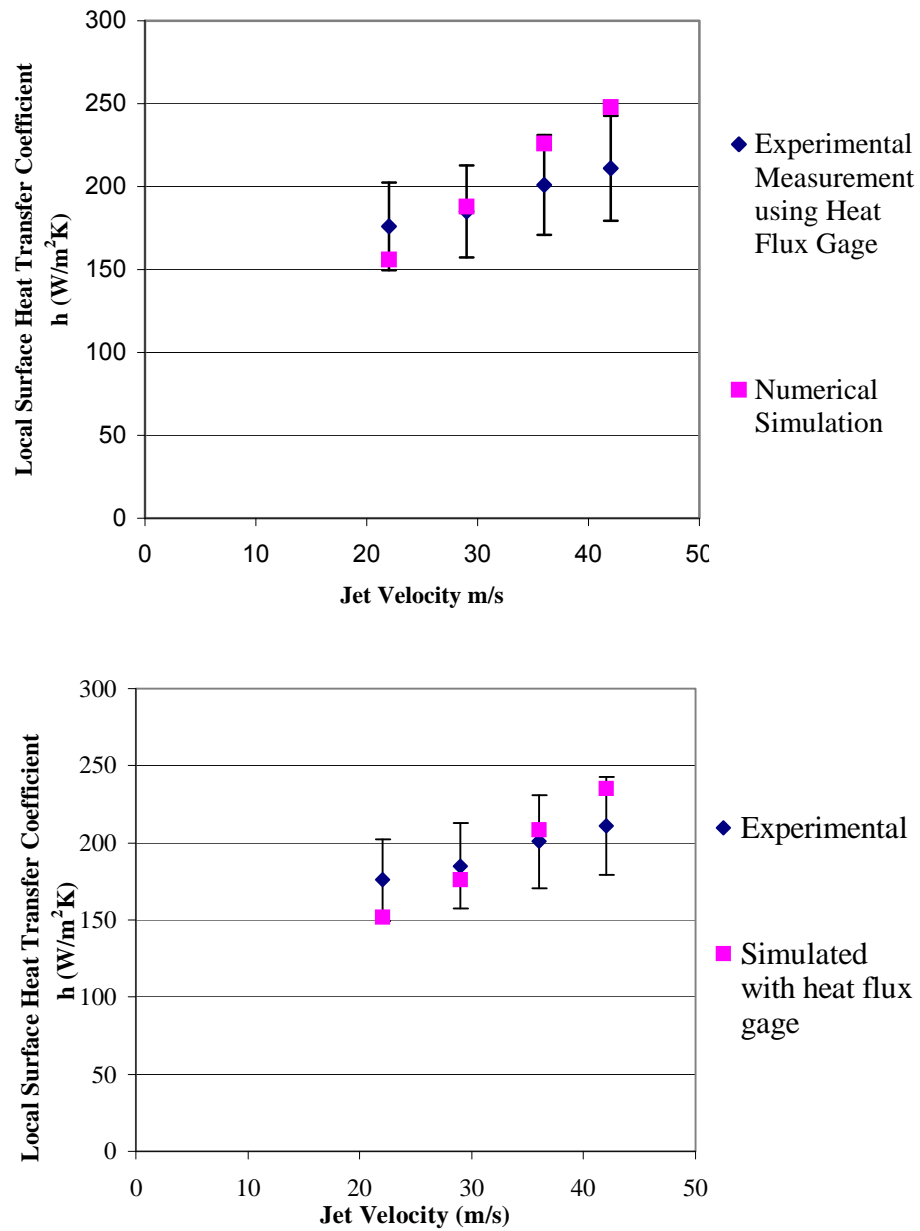
Figure 4.12

**Comparison of experimentally measured local average
heat transfer coefficient around stagnation point using heat flux gage with
results of numerical simulation (a) without heat flux gage; (b) with
heat flux gage at different jet inlet velocities and T_{jet}=450 K**
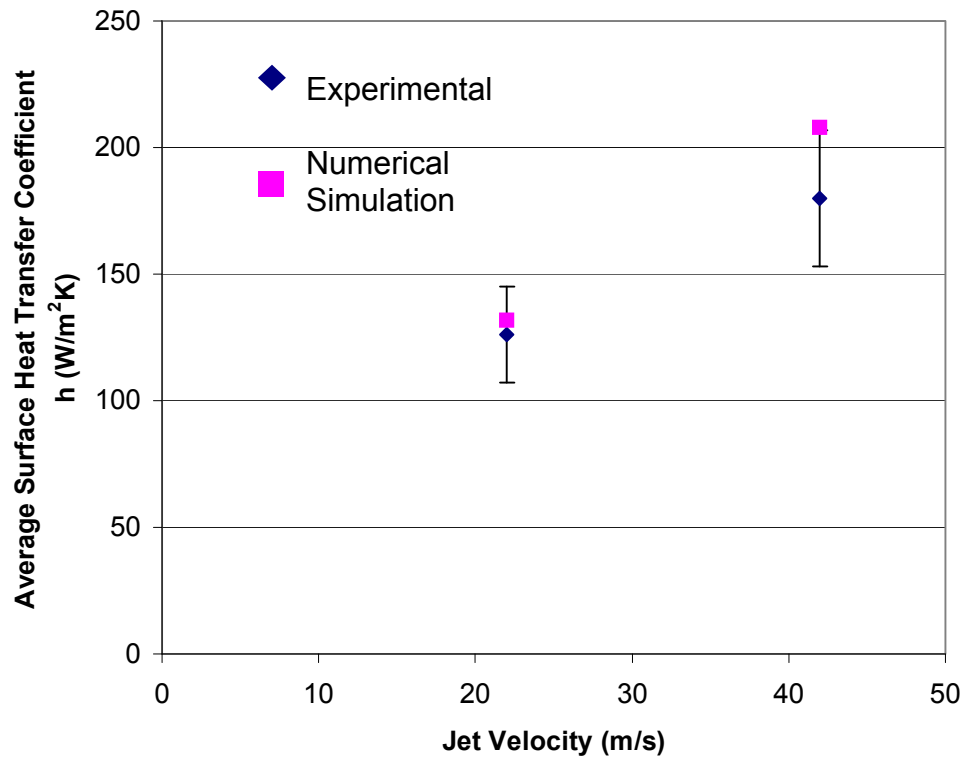
Figure 4.13

Comparison of experimentally measured average surface heat transfer coefficient with results of numerical simulation at different jet inlet velocities and T_{jet}=450 K

(a)
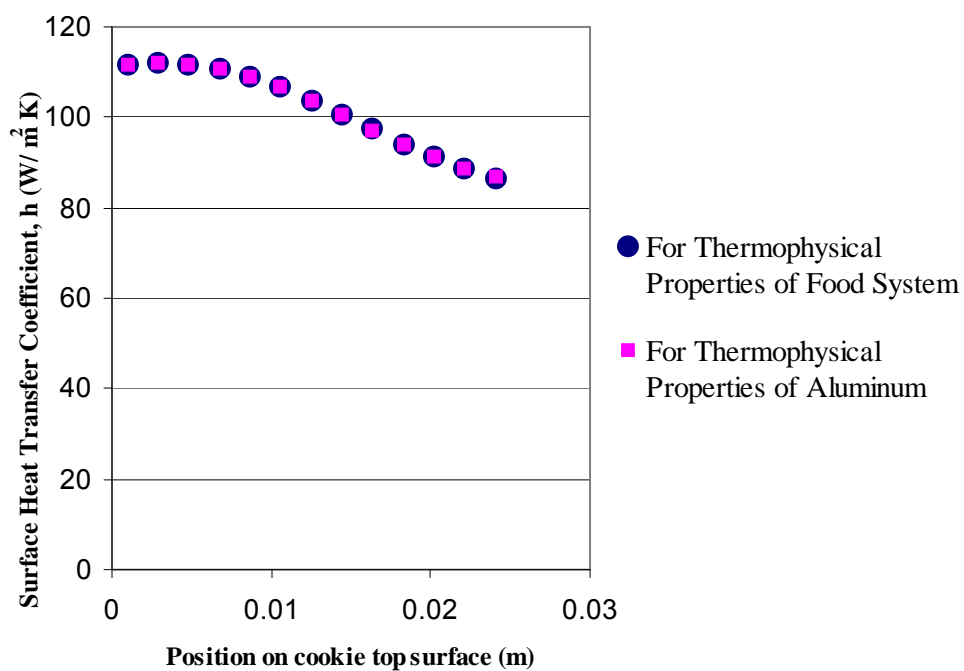
(b)

Figure 4.14

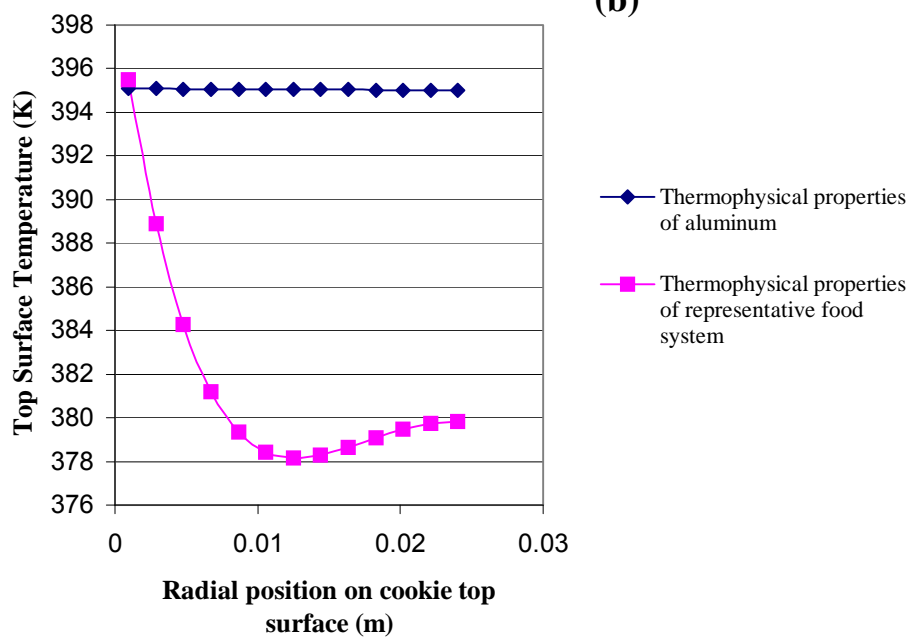**Numerical Simulation of Jet Impinging on a Model Cylindrical Object
Numerically obtained (a) variation of local surface heat transfer coefficient
and (b) surface temperature, for cookies with thermophysical
properties of aluminum and typical food material**

Isovelocity contours of an impinging jet on a model cylindrical object of 1 cm diameter for the case of z/d =3 are shown in **Figure 4.15**. Similar isovelocity contours for 1.5 cm and 2 cm diameter model cylinders are shown in **Figures 4.16, and 4.17**. Simulation results show that flow field of an impinging jet for a curved geometry is quite different in many regards as compared to a model cookie. The thickness of stagnation domain is narrower as compared to a model cookie system shown in **Figure 4.6**. The other major difference is the expected separation of flow near the bottom of the model cylinder, suggesting non-uniform heat transfer rates along the curved surface of cylinder. Comparison of isovelocity contours shown in **Figures 4.15, 4.16, 4.17** indicate no significant changes in the overall flow profile with changes in diameter, indicating similar trends in surface heat transfer variation for different cylindrical geometries.

Numerically obtained average surface heat transfer coefficients for model cylindrical geometry of diameter 1 cm, 1.5 cm and 2 cm as a function of impinging jet velocity are shown in **Figure 4.18**. The results show an increase in average heat transfer coefficient with an increase in jet velocity as expected. Comparison among different cylindrical geometries shows no significant difference in surface heat transfer coefficient for 1 cm and 1.5 cm diameter cylinders. Numerically obtained average surface heat transfer coefficient for 2 cm cylinder was only slightly higher than 1 cm and 1.5 cm diameter cylinders, at all jet velocity values. This trend is supported by very similar flow profile for all three geometries under same conditions of jet inlet velocity.

Results for variation of local surface heat transfer coefficient along the cylindrical surface are shown in **Figure 4.19 (a), (b), and (c)** for three different cylindrical geometries with diameters of 1 cm, 1.5 cm, and 2 cm respectively. The results show a significant variation of local heat transfer coefficient along the cylindrical surface as compared to results with model cookie system. In **Figure 4.19 (a), (b) and (c)** the distance (x coordinates) represents the projection of the curved surface on axial coordinate (axis of symmetry). The maximum in local surface heat transfer coefficient was observed at stagnation point for all three geometries. In all cases, we observed a drop in local heat transfer coefficient along the surface of a model cylinder, with a sharper drop along the bottom edge of the cylinder. This result is in agreement with the results obtained from the isovelocity contours indicating a separation region towards the bottom edge of the curved geometry. This implies that the surface heat transfer coefficient can have large variations for a cylindrical hotdog shaped geometry. This variation may lead to non-uniform heating/ baking of the food material.
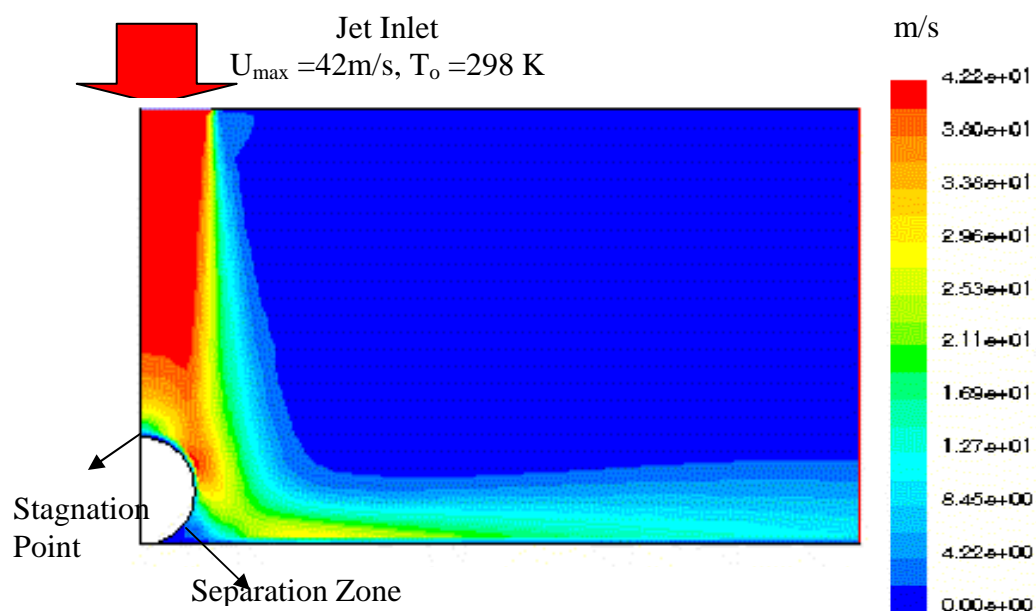
Figure 4.15

Isovelocity contours of an impinging jet on a 1 cm diameter cylinder
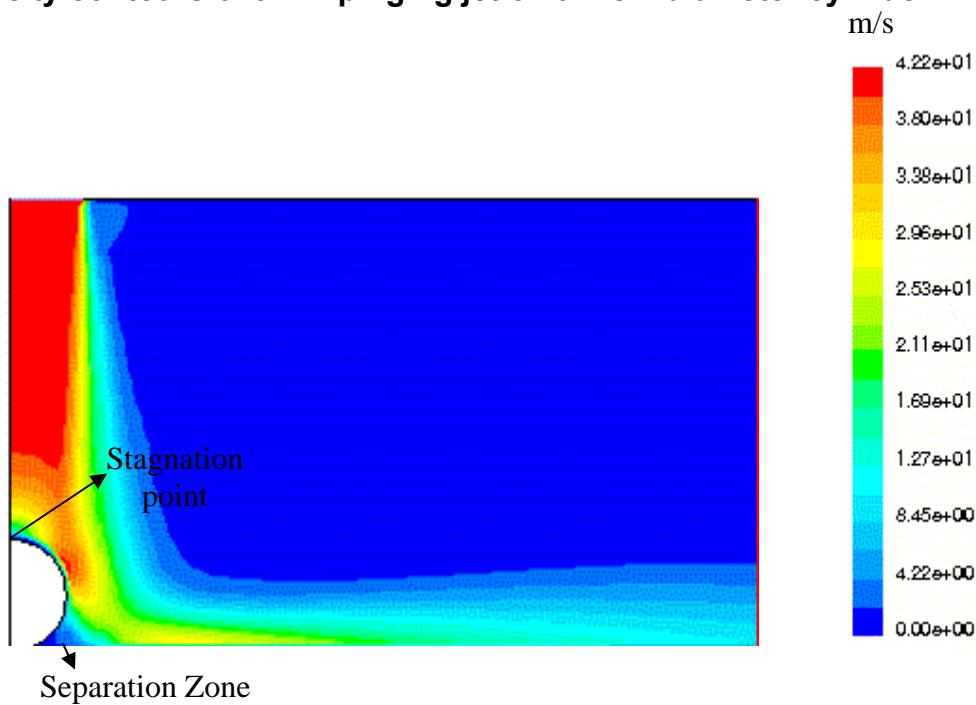
Figure 4.16

Isovelocity contours of an impinging jet on a 1.5 cm diameter cylinder
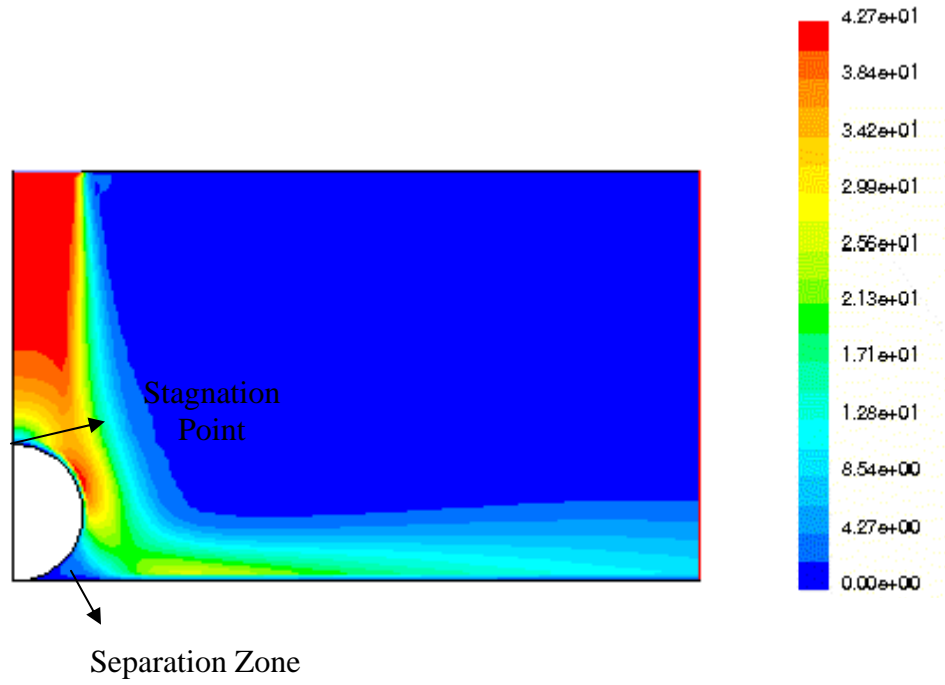
Figure 4.17

Isovelocity contours of an impinging jet on a 2 cm diameter cylinder
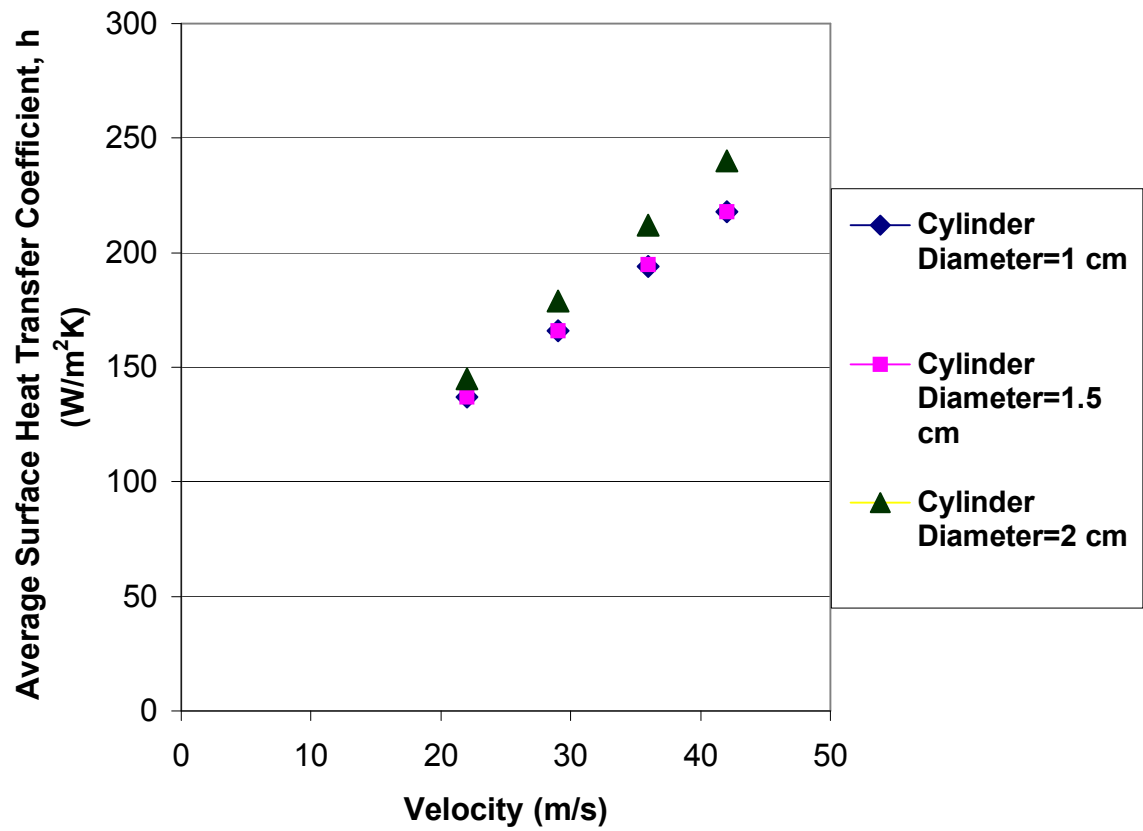
Figure 4.18

Variation of average surface heat transfer coefficient as a function of jet maximum velocity for three cylindrical diameters of 1 cm, 1.5 cm, 2 cm
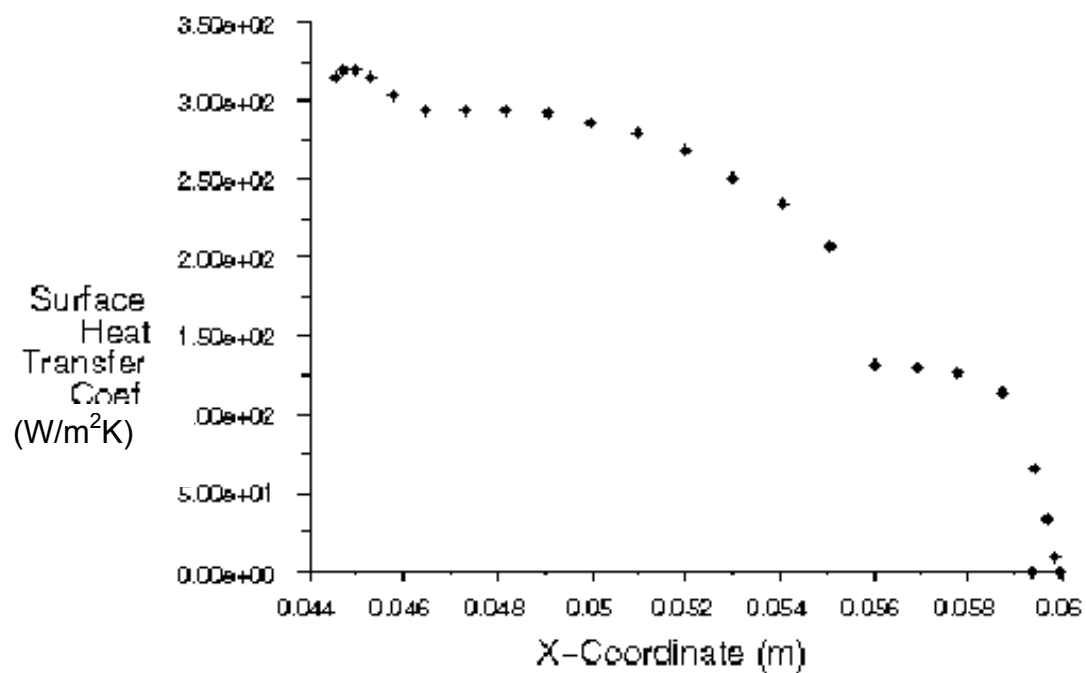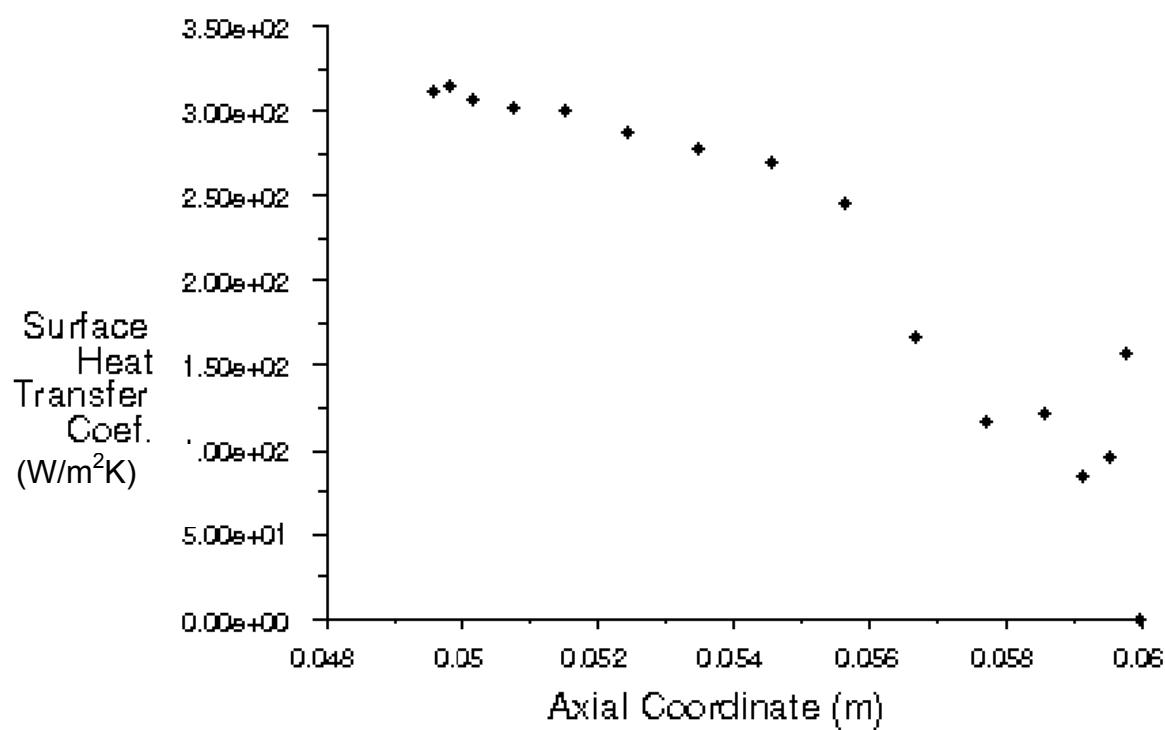
Continued Figure on next page
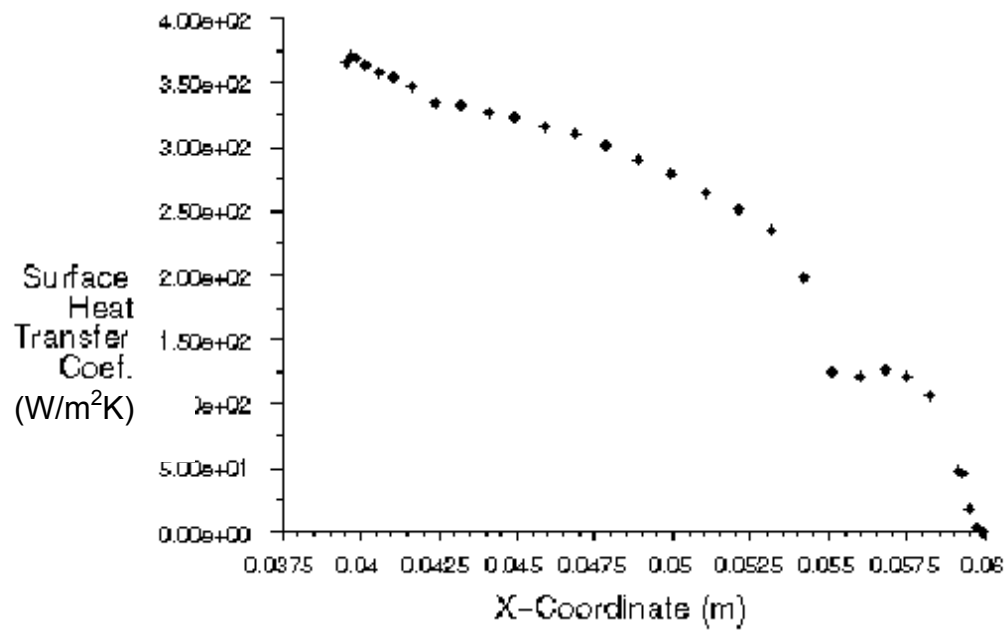
Figure 4.19

Variation of local surface heat transfer coefficient as a function of axial position for three cylindrical geometries of (a) 1 cm, (b) 1.5 cm and (c) 2 cm diameter

Comparison of Numerically Predicted Average Surface Heat Transfer Coefficient with Experimental Measurement

Results of average surface heat transfer coefficient predicted by numerical simulation for cylindrical geometry were compared with experimental results obtained using aluminum model cylinders (hot dog geometry) of different dimensions. Experimental study was carried out using the same experimental approach as described for the cookie shaped object. Comparison of the experimental results with numerical predicted values is shown in **Table 4.4**. Results show a good agreement between numerical prediction and experimental results. Numerical simulation results indicate an increase in surface heat transfer coefficient with an increase in the diameter of a model cylindrical geometry, which is expected as increase in diameter will tend to decrease the distance between an impinging jet and a target cylinder. This decrease in nozzle to target distance tends to increase both the local and average heat transfer coefficient as observed in case of a cookie shaped geometry. Similar trend was also observed in the local heat transfer coefficient for cylindrical geometry with an increase in diameter of a cylinder.

The other reason for an increase in average surface heat transfer coefficient is based on understanding that an increase in diameter will reduce the curvature of a cylindrical surface, resulting in more uniform surface heat transfer over a larger area. This trend was not observed in experimental data. It could have been due to some experimental error resulting from placement of this cylinder in an oven system or due to bad thermocouple contact, etc. Despite this

discrepancy in overall, numerical prediction results matches with experimental data within $\pm$ 20%, which is good as experimental system itself has an error range of $\pm$ 15 %.

Table 4.4

Comparison of numerically predicted average surface heat transfer coefficient with experimental data obtained for three cylindrical geometries of 1 cm, 1.5 cm and 2 cm diameter

Average Surface Heat Transfer Coefficient, h (W/m^{2}K)

	Velocity m/s	1 cm cylinder		1.5 cm cylinder		2 cm cylinder	
		Simu lation	Experi mental	Simu lation	Experi mental	Simul ation	Experime ntal
1	22	137	150	137	124	145	134
2	42	218	235	218	195	240	200

Comparison of Center Temperature For Real Food Material (Hot Dog) with Numerical Simulation of Conjugate Heat Transfer Problem in a Food Matrix with Impinging Jet

The aim of this study was to compare experimental measurements of center temperature in a real food system with numerical predicted results based on thermal transport modeling. In this study, we solved the conjugate heat transfer problem for a cylinder shaped food material (thermophysical properties of hot dog) with an impinging jet. In this numerical simulation, the thermophysical properties for a hot dog were used. They were: Cp (Specific heat)= 3300 J/kg, Density=1200 kg/m^3, and Thermal Conductivity =0.4 W/m K (Choi and Okos, 1985). The conjugate heat transfer was used to predict the center temperature of the hot dog based on conduction within the food matrix. Results of this simulation were compared with the experimental measurement of hot dog center temperature. Temperature time profiles for a real hot dog and that obtained from the numerical simulation based on conjugate heat transfer are shown in **Figures 4.20 and 4.21** at 65 °C and 100 °C jet inlet temperature respectively. Results indicate good agreement for the case when the jet air temperature was below 100 °C. For the case where jet air temperature was above 100 °C, the results indicate that the predicted temperature is higher than that observed experimentally. This is expected as in case of real food system, a part of thermal energy is used in evaporation and mass transfer processes. This indicates the importance of coupled heat and mass transfer processes to predict the temperature –time profiles in real food system.

Figure 4.20

Comparison of numerically predicted temperature time history at the center of model food with that of real food system for maximum jet temperature of 65 °C
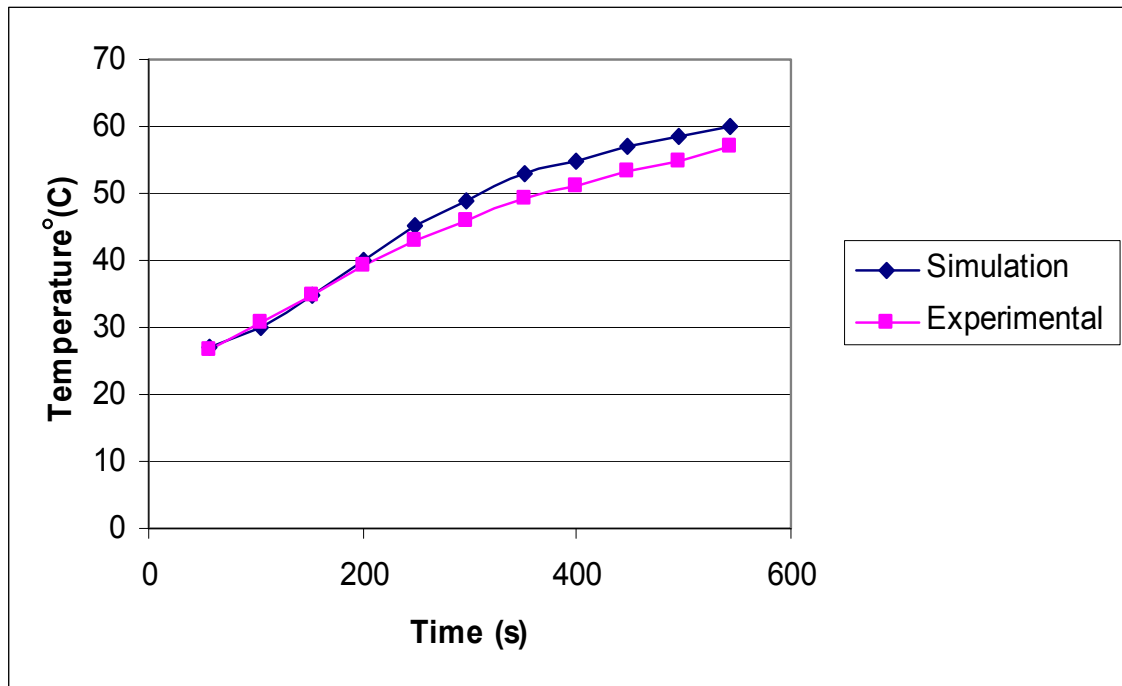
Figure 4.21

Comparison of numerically predicted temperature time history at the center of model food with that of real food system for maximum jet temperature of 150 ° C
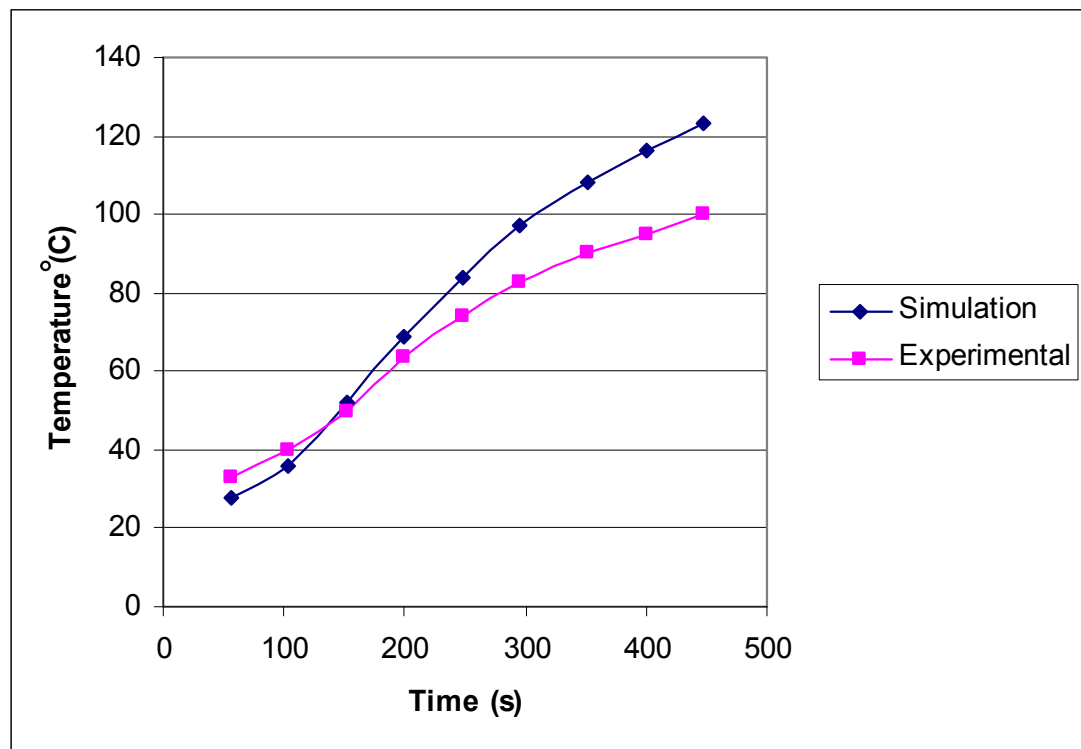
Objective 2

To develop mathematical models to numerically simulate the coupled heat and mass transport in a food product during baking and to validate them experimentally

Objective 2a: To model coupled heat and mass transport process in a 1-d model geometry based on three different phenomenological models to simulate baking process and compare the results with experimental measurements:

Comparison of Predicted Temperature-Time Profile

In the previous section (**Figures 4.20 and 4.21**), we concluded that the predicted temperature-time profile based on heat transfer model alone did not agree with the experimental observations in a model food especially when temperature > 100°C. To overcome this limitation, we developed coupled heat and mass transfer models to describe the baking process. The differences among these models are discussed in Chapter 3. In this specific objective, 1-d models of coupled heat and mass transfer processes were developed to simulate baking of a model cookie. This approach will provide a direct comparison of the predictions of all three models in a relatively simple geometry. For each of the model coupled heat and mass transfer equations were formulated using finite volume method based on conservation of mass and energy. These coupled equations were solved using explicit finite difference scheme. Cookie of 1 cm thickness was divided into 20 finite volume units (each slice of 0.05 cm). Mass

and energy conservation equations for these 20 units were solved using explicit formulation with a time step of 0.1 seconds.

Contour plots of the temperature-time profile of three baking models are shown in **Figure 4.22. Figure 4.22(a), (b), (c)** represent results based on Zanoni's model (Zanoni et al, 1993), modified baking model I and II respectively. The results represent temperature time history at different grid points on a 1-dimensional model grid.
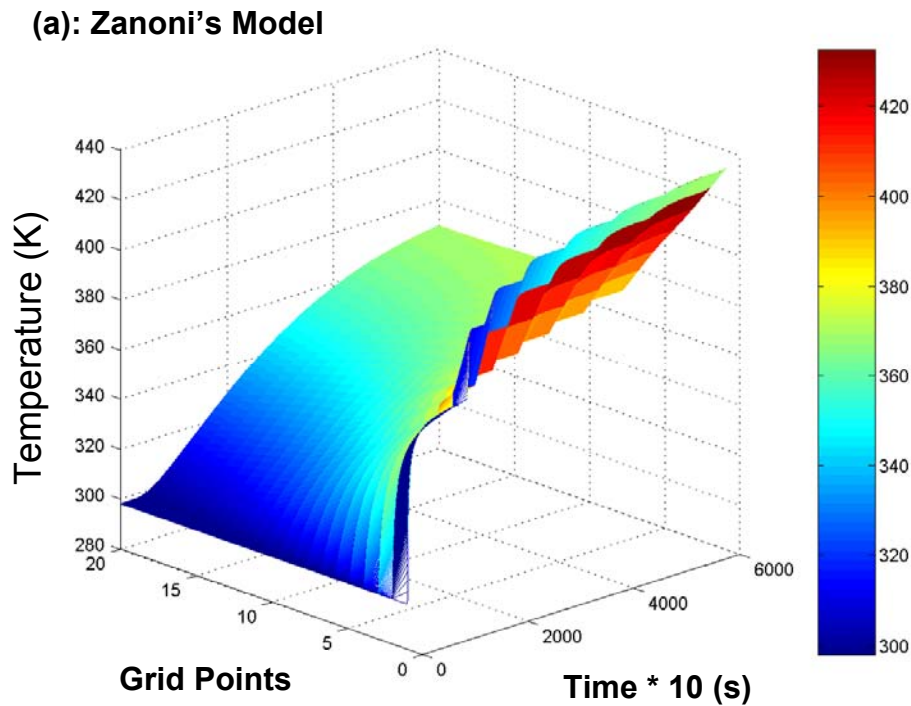
(a): Zanoni's Model

(b) Modified Baking Model I
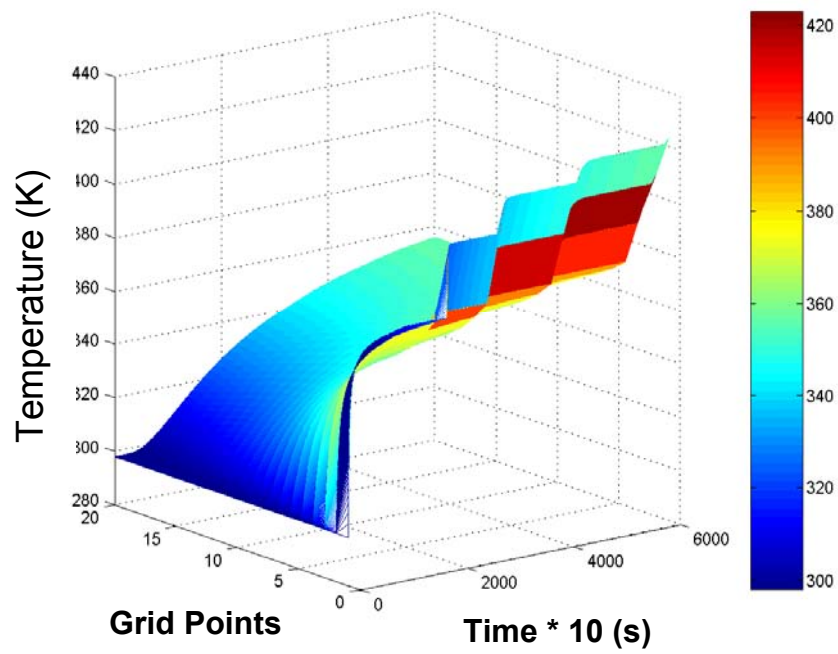
(c) Modified Baking Model II
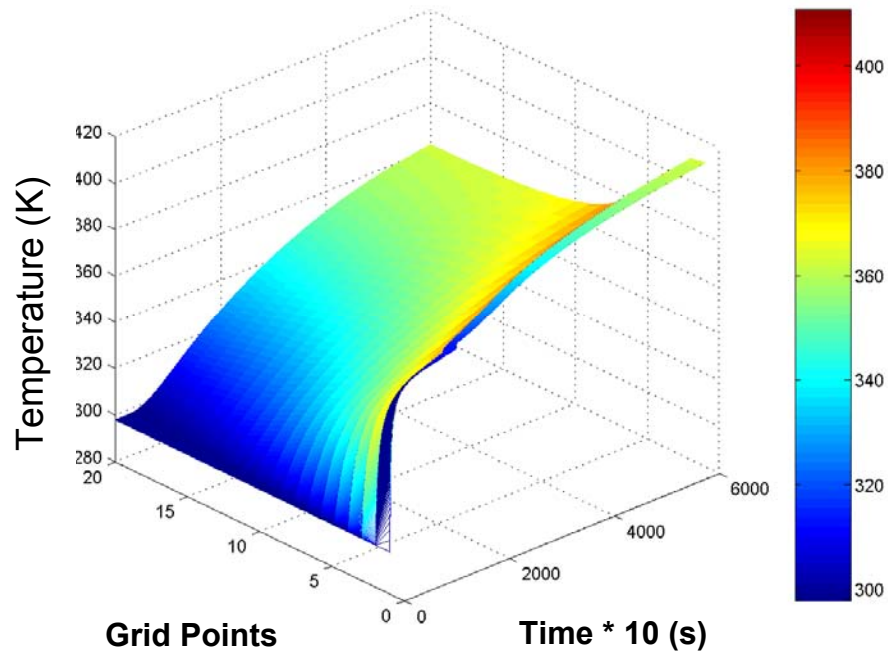
Figure 4.22

Contour plots of temperature-time profile predicted by three different baking models for a 1-d geometry. (a) Zanoni's Model; (b) Modified Baking Model I; (c) Modified Baking model II

Results based on all three models illustrate a rapid rise in the surface temperature of a cylindrical disk during baking, followed by a slower rise in temperature within a cylindrical disk. Comparison of the results among three baking models highlight significant differences in predicted temperature-time data. Results based on Zanoni's model and modified baking model I show a stepwise increase in the surface temperature as compared to a smooth continuous increase predicted by the modified baking model II. This stepwise increase in temperature is observed as a result of a phase change process at 100 °C, during which the temperature at that particular control volume is maintained constant until the moisture content in the control volume drops below a critical pre-determined value (e.g. equilibrium moisture content in Zanoni's model and drop in water activity below 1 in modified model I). This imposed condition during baking creates a stepwise increase in temperature-time profile. Since in case of modified baking model II, this condition is not used and the baking process is modeled based on using a same set of equations during all stages of baking, we do not observe a stepwise trend in a temperature-time profile.

In all three models, a similar rise in surface temperature is predicted, with significant differences among models in prediction of temperature gradients within a cylindrical disk. The contour plots show a steep gradient in temperature based on Zanoni's and modified baking model I as compared with modified baking model II. This steepness in temperature gradient with respect to time is

also caused by a stepwise rapid increase in surface temperature while the temperature of interior node rises slowly.

To further illustrate differences in these models, the above results are also represented using a 2-d plot of temperature-time profile at specific grid locations within a cylindrical disk. The direct comparison of these plots further validates the trends discussed above. The results (**Figure 4.23(a. b. c)**) clearly illustrate the differences in the temperature-time profile predicted by these three models.

(a) Zanoni's Model

Time * 0.02 (s)

(b) Modified Baking Model I

Time * 0.02 (s)
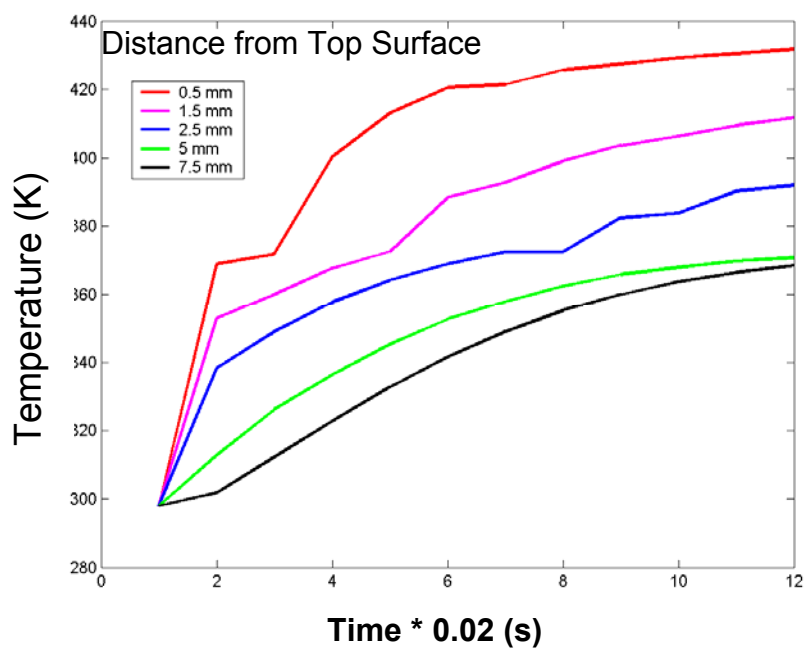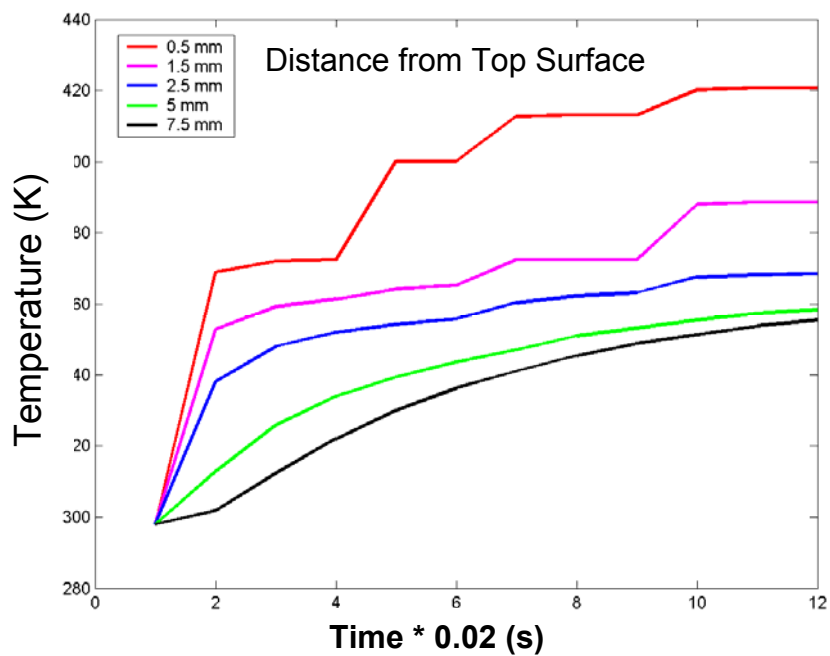
(c) Modified Baking Model II
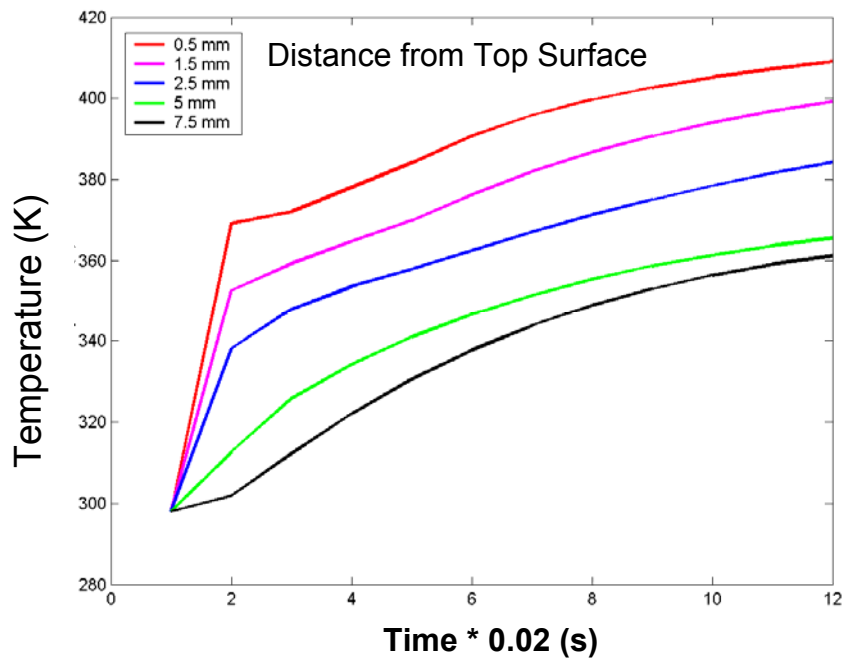
Figure 4.23

**Plot of temperature-time profile predicted by three different baking models
for a 1-d geometry at different depth locations
a) Zanoni's Model
b) Modified Baking Model I
c) Modified Baking model II**

Comparison of Predicted Moisture-Time Profile

Figure 4.24 (a, b, c) show contour plots of predicted moisture-time profile based on Zanoni's baking models, modified baking model I and modified baking model II, respectively. These predicted moisture profile illustrate significant differences among these three models. Based on Zanoni's model, baking process has a rapid evaporation of moisture content once the temperature becomes equal to the phase change temperature. This change results in a sharp drop in moisture content within a food matrix as illustrated by the contour plot in **Figure 4.24(a)**. This is expected, as Zanoni's model does not consider any resistance to vapor formation and transport within the food matrix. On the other hand, the moisture-time profiles predicted by modified baking model I and II have a gradual drop in moisture content within the food matrix **(Figures 4.24(b) and (c))** with increase in temperature (time of baking). This is due to the fact these modified models account for vapor transport rate in modeling loss of moisture from a food material during baking.

(a) Zanoni's Model

(b) Modified Baking Model I

(c) Modified Baking Model II

Moisture Content

Grid Points

Time * 10 (s)
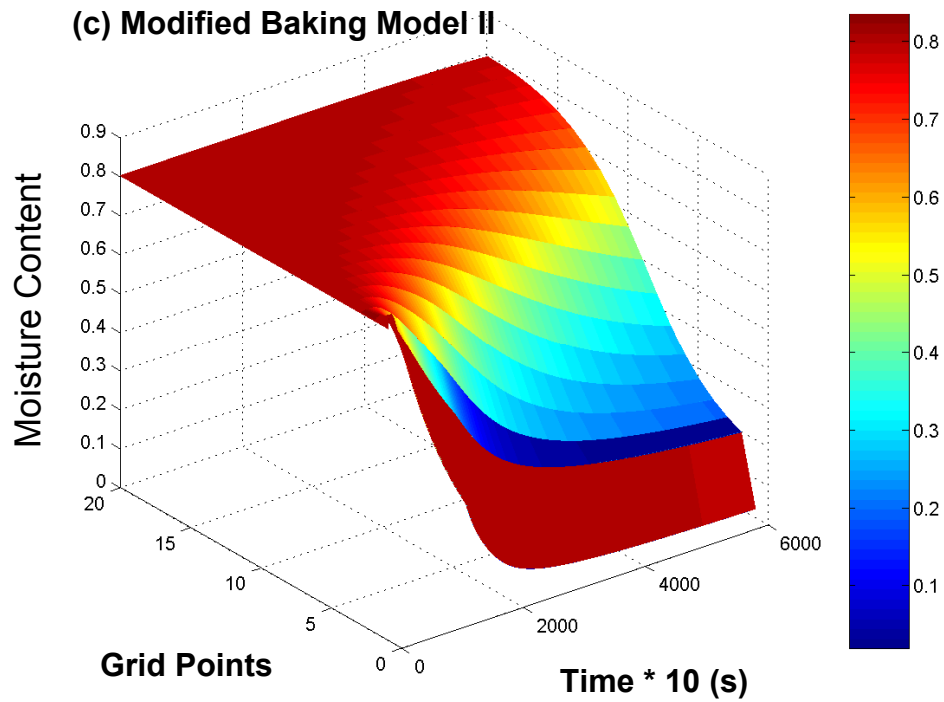
Figure 4.24

**Contour plots of moisture-time profile predicted by three different
baking models for a 1-d geometry
a) Zanoni's Model
b) Modified Baking Model I
c) Modified Baking model II**

To further illustrate the moisture-time history at discrete locations within the food matrix, **Figure 4.25** shows a 2-d plot of moisture content versus time. The results presented in this format clearly illustrate the differences in the moisture –time profiles predicted by Zanoni's model as compared with modified baking models. Based on these plots, the Zanoni's model predicts a much larger crust thickness (layer of material with moisture content less than the critical moisture content) as compared to predicted crust thickness based on modified models I and II. Further, Zanoni's model does not predict a significant drop in the moisture content at the center of the model food object as compared with modified models I and II. The rate of drop in moisture content due to vaporization in Zanoni's model is not affected by a decrease in water activity as the slope of moisture loss as function of time at a specified location is independent of the moisture level. In case of modified baking models I and II, a drop in rate of moisture loss is observed as the water content drops below a water activity of 1.

Figure 4.26 shows a plot of normalized average moisture content (ratio of moisture content (t) with respect to moisture content at t=0) as a function of time based on above discussed models. The plot clearly demonstrates more rapid loss of moisture content based on Zanoni's model as compared with modified model I and II. This is expected, as Zanoni's does not consider any resistance to vapor transport process.

(a) Zanoni's Model
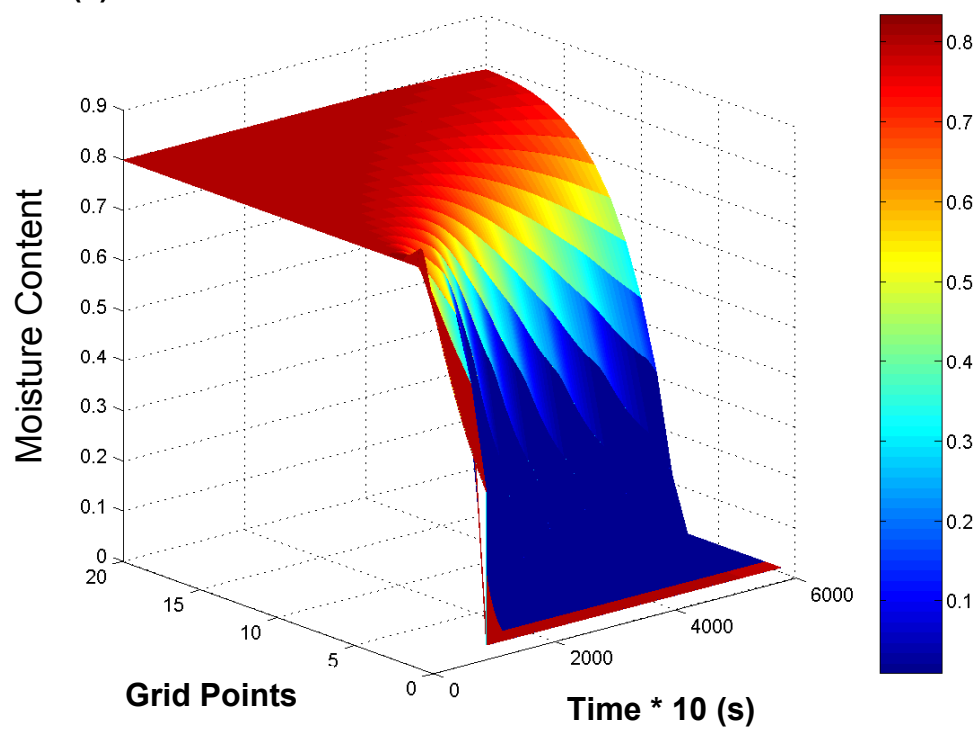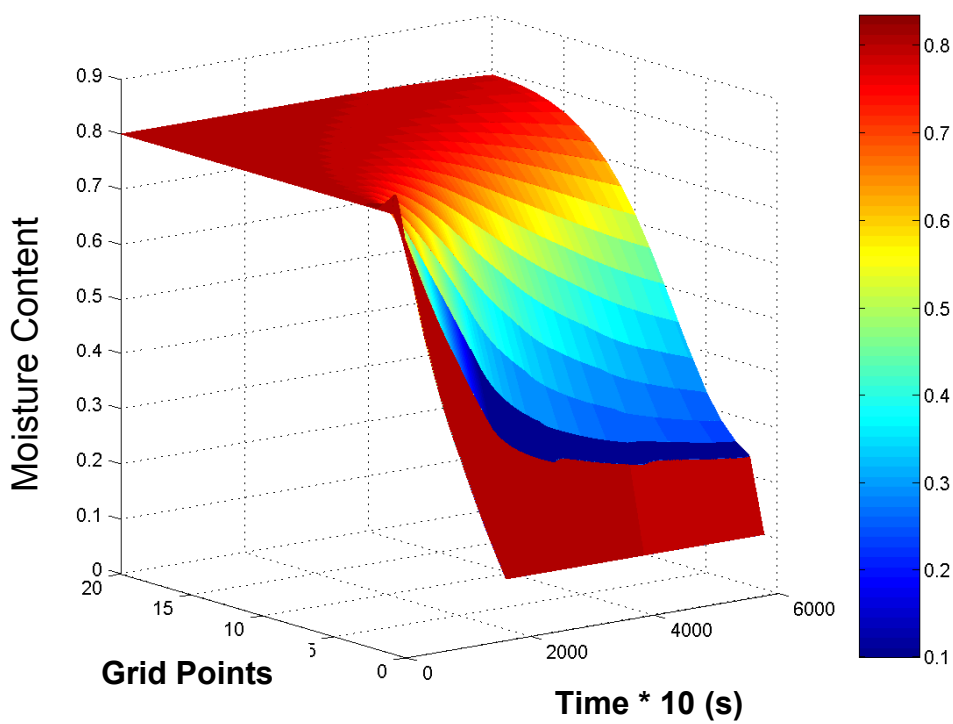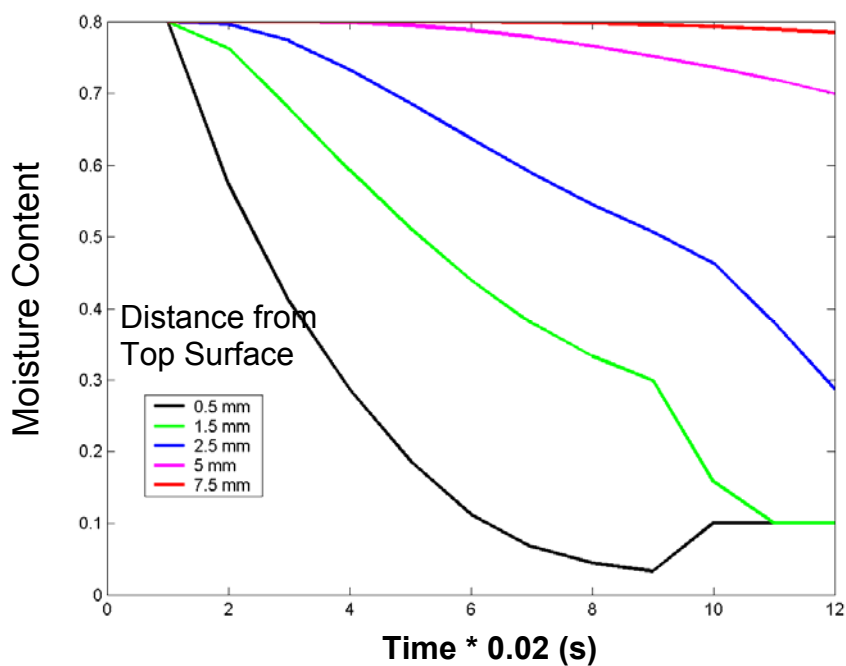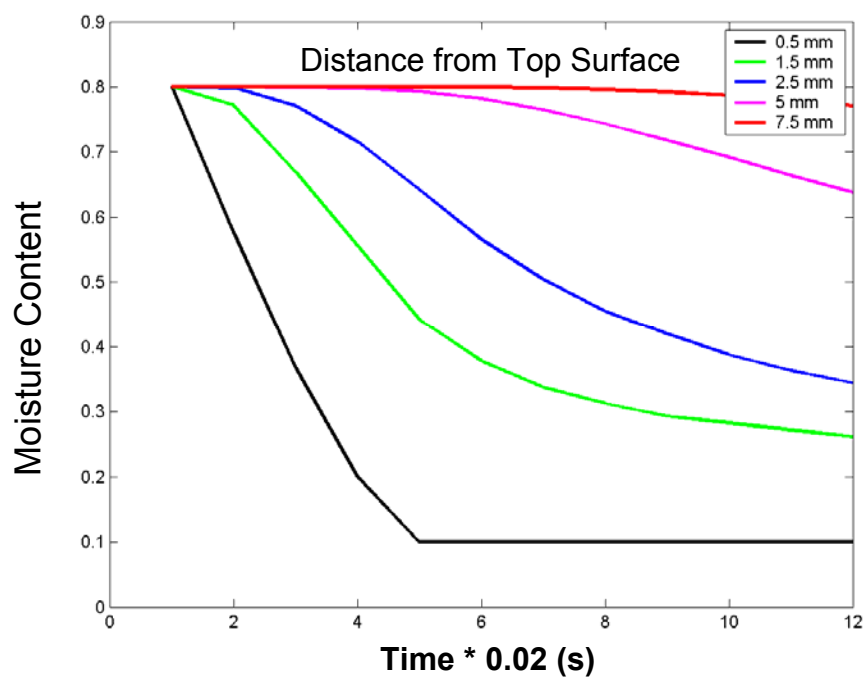

(b) Modified Baking Model I

(c) Modified Baking Model II
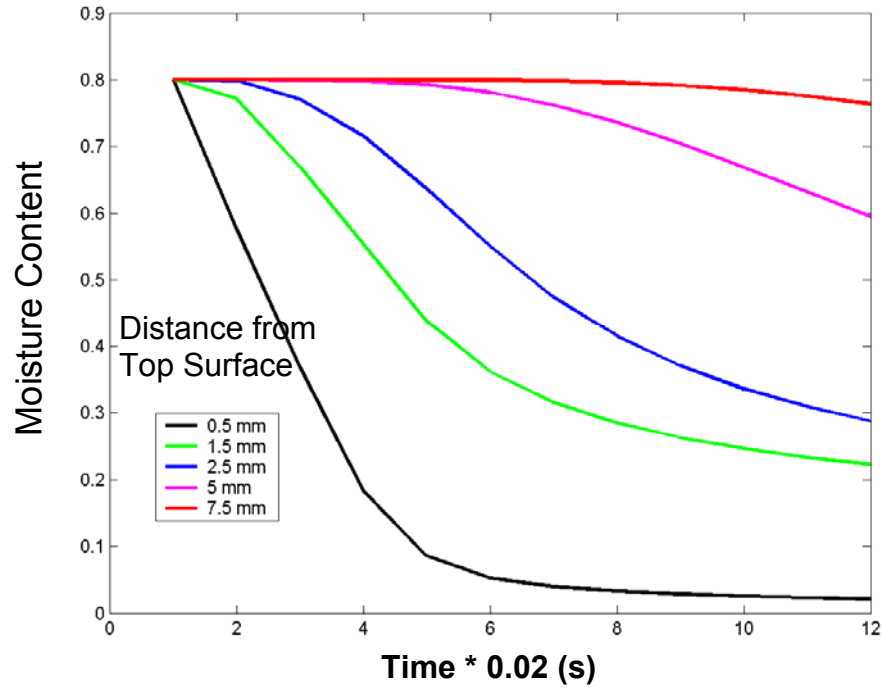
Figure 4.25

**Plot of moisture-time profile predicted by three different baking models for a 1-d geometry at different depth locations
(a) Zanoni's Model
(b) Modified Baking Model I
(c) Modified Baking model II**
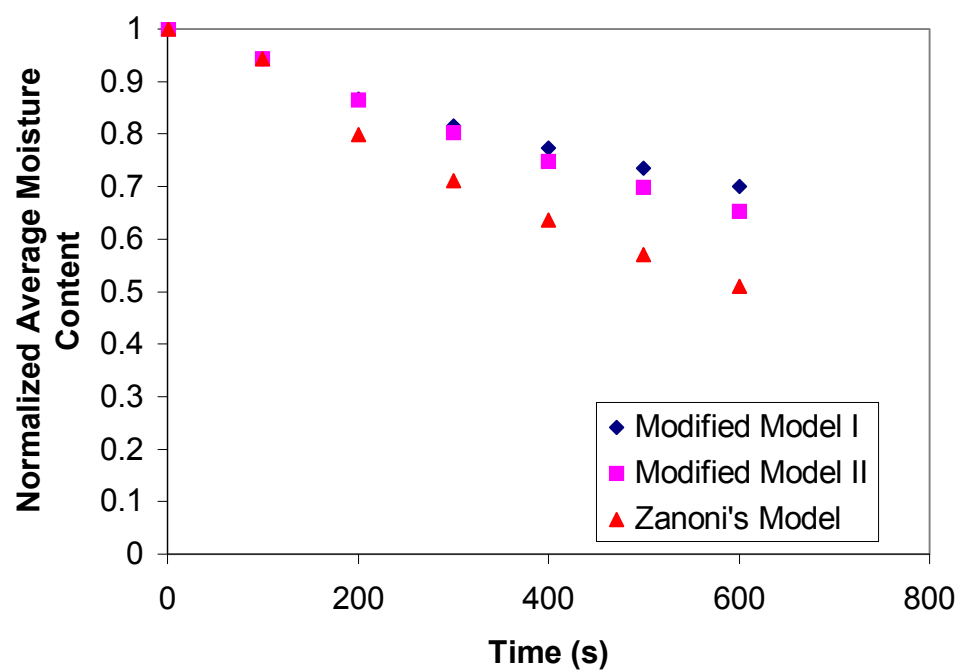
Figure 4.26

**Comparison of decrease in normalized average moisture
content of baked 1-d model geometry based on three
different baking models**

Soret Effect

To evaluate contribution of the Soret effect (thermo-diffusion) on predicted temperature and moisture profiles, we have compared results of modified Zanoni's model (Zanoni's model with addition transport terms to model thermo-diffusion process) with 1-d formulation of Zanoni's model. The details of this modification are discussed in Chapter 3. Results of predicted temperature and moisture profile are compared between Zanoni's and modified Zanoni's model. Comparison of predicted temperature profiles with (**Figure 4.27**) or without contribution (Zanoni's Model**; Figure 4.28**) of the Soret effect shows no significant difference. Similarly comparison of moisture profile with (**Figure 4.29**) and without (Zanoni's Model**; Figure 4.30**) contribution of the Soret effect shows no significant difference. These results indicate that contribution from thermodiffusion process is limited and it does not significantly effect the predicted temperature-moisture profile during baking. Thus for future simulation of baking process, thermo-diffusion transport was not considered.
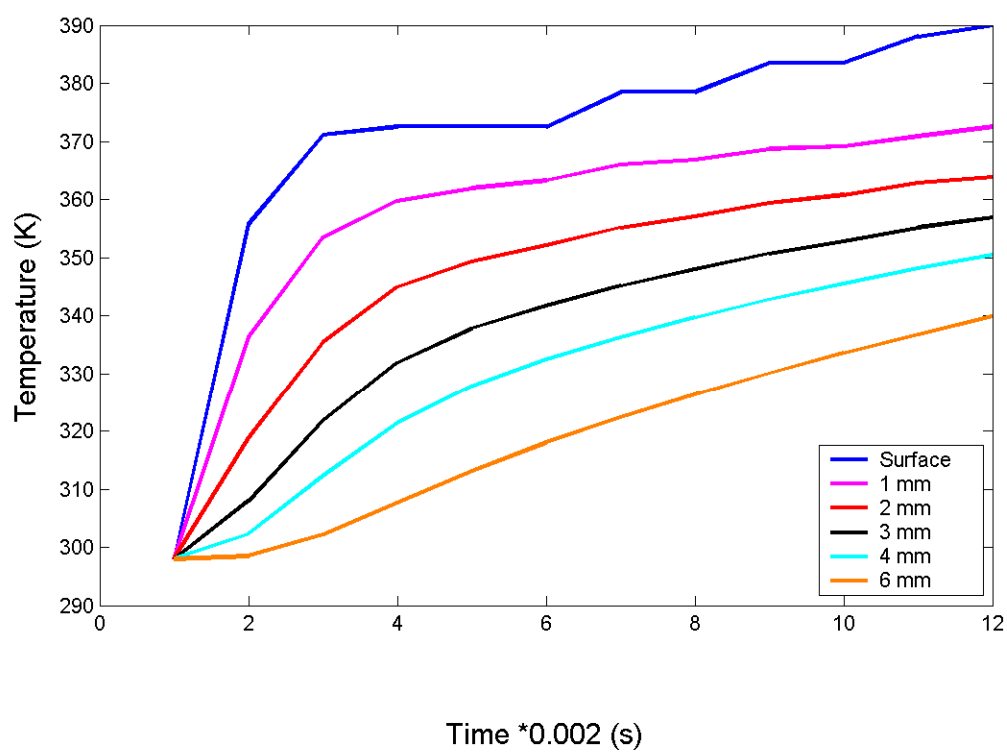
Figure 4.27

Predicted temperature-time profile based on modification of Zanoni's baking model with Soret effect
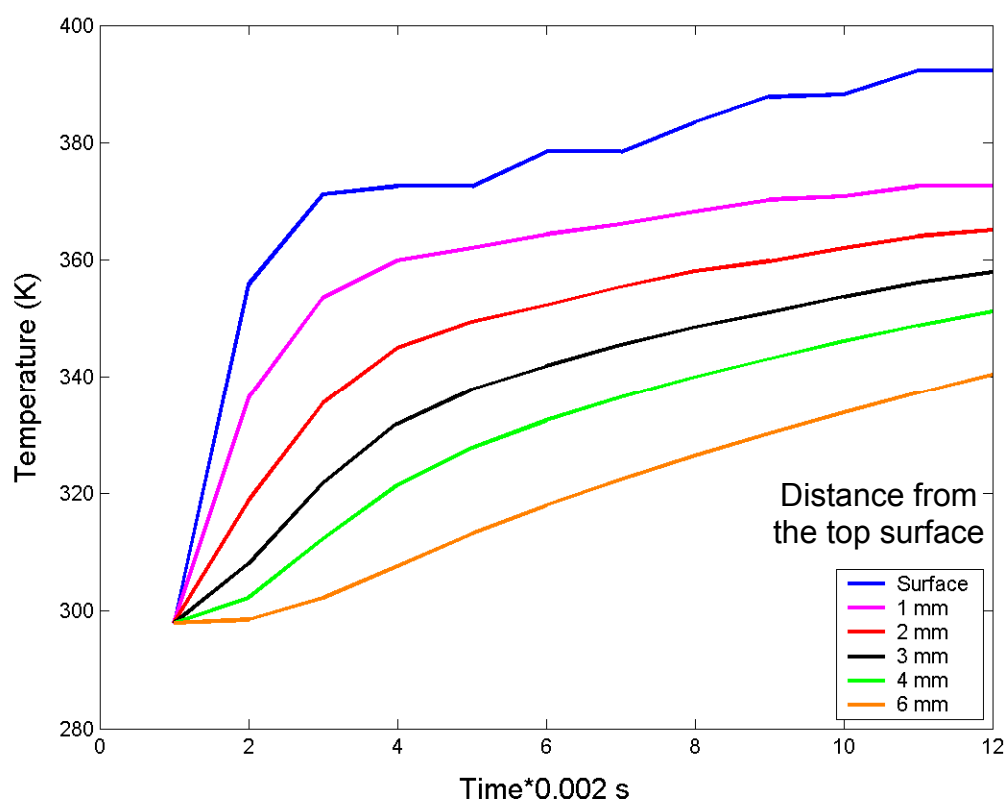
Figure 4.28

Predicted temperature-time profile based on Zanoni's Baking Model
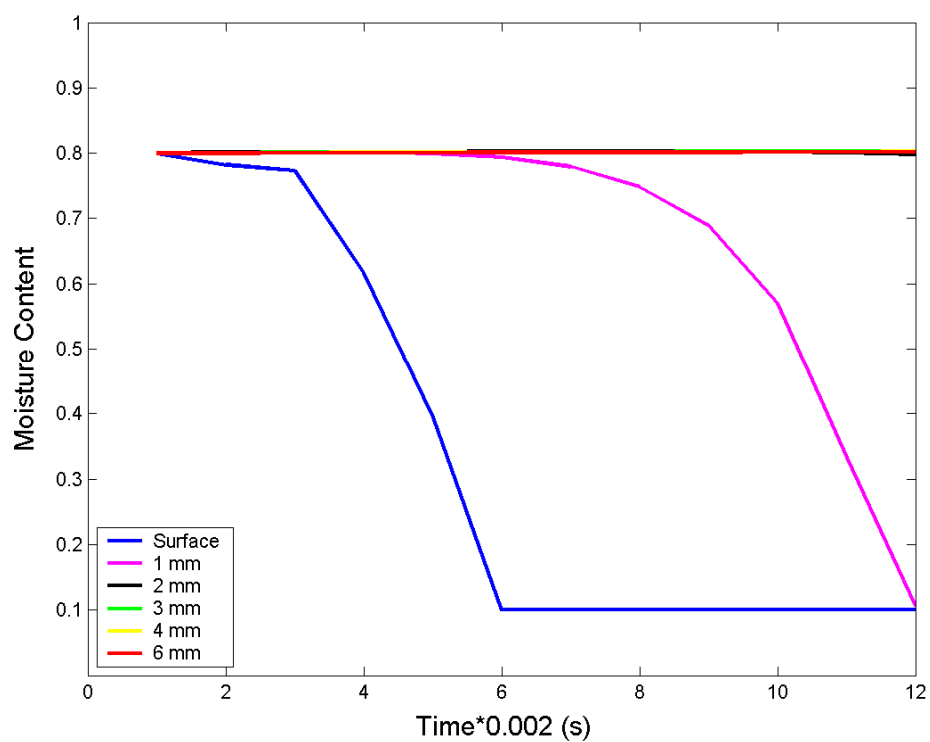
Figure 4.29

**Predicted moisture-time profile based on modification of Zanoni's
baking model with Soret effect**
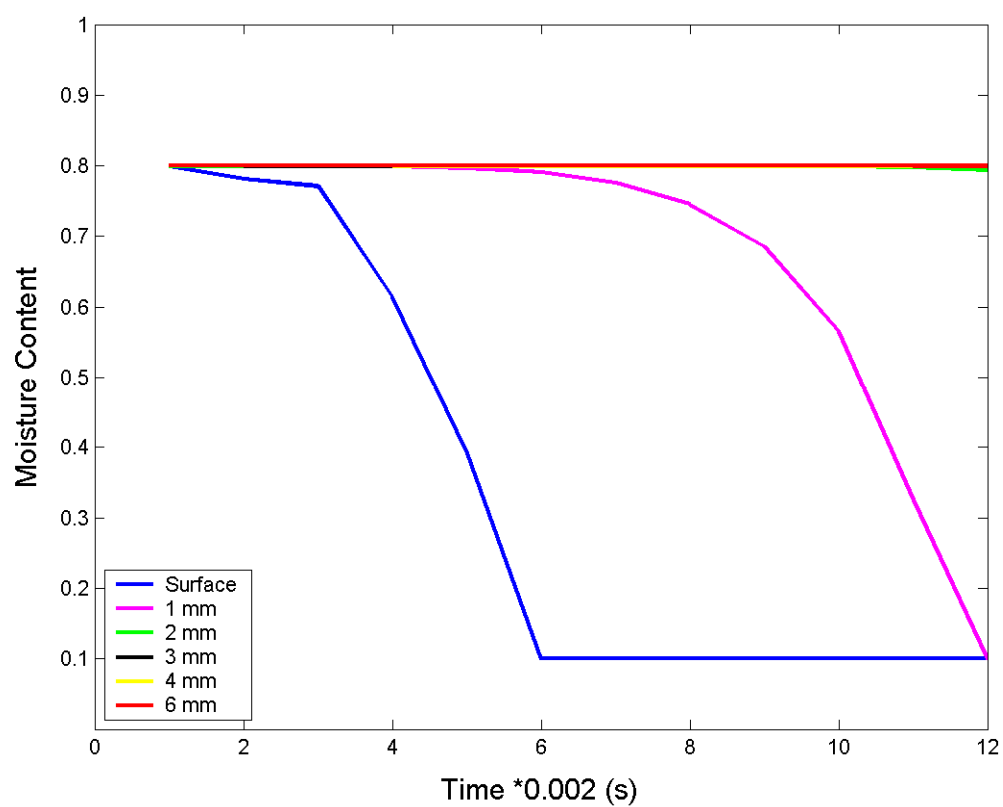
Figure 4.30

Predicted moisture-time profile based on Zanoni's Baking Model

Comparison of Numerically Predicted Temperature Profile with Experimental Measurements

Figure 4.31 compares numerically predicted temperature-time profile based on the above-discussed models (Zanoni, Modified Baking Model I and II) with the experimental measurement at the center of a 5 cm diameter potato disk with 1 cm thickness. The results demonstrates that based on 1-d approximation of this geometry, all of the above baking models under-predict the increase in temperature with time as compared with the experimental results. Earlier in **Figures 4.20 and 4.21**, the results demonstrated that modeling of baking process based on heat transfer alone, over-predicts the center temperature of a cylindrical hot dog as compared with experimental measurements. This is expected as the entire thermal energy is used for increasing the temperature of the food material with no contribution towards mass transport process including surface moisture evaporation and vapor transport within the food. In case of 1-d models based on both heat and mass transport, the numerical results predict lower temperature values as compared to experimental measurement. This suggests that 1-d approximation of cylindrical disk may not be a suitable approximation, as 1-d model does not account for the net energy transferred from the side surface of a cylindrical disk. This difference may account for under-predicting the center temperature based on these three models.
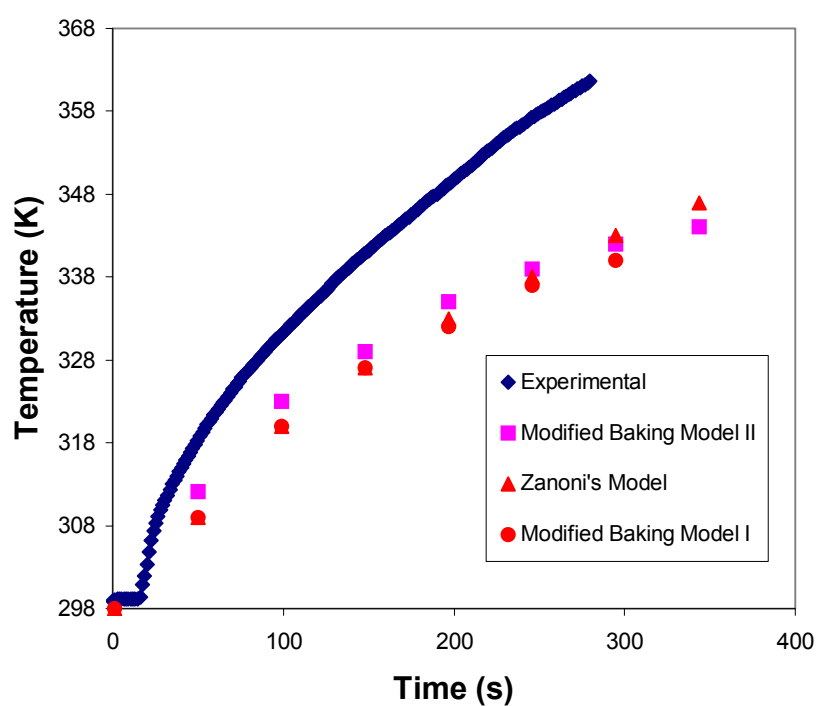
Figure 4.31

Comparison of the experimental data with the numerically predicted temperature values for the center point of a 1-D model geometry. The numerical data was predicted based on three different baking models

2-D Axisymmetric Models of Baking

To overcome some of the limitations associated with a 1-d approximation of a model cylindrical disk, the 1-d models of baking were extended to 2-d axisymmetric models. Details of the 2-d axisymmetric models are discussed in Chapter 3. Using 2-d axisymmetric grid geometry, numerically predicted temperature and moisture profiles were compared among three baking models. In addition the numerically predicted temperature profiles at a center point of a potato disk were compared with the experimental measurements.

Comparison of Temperature Profile Based on Three Baking Models

Figure 4.32 shows temperature contours within a cylindrical disk based on Zanoni's model at following specified intervals of time (1 min, 2 min, 5 mins and 10 mins.) As observed in case of 1-d model, the temperature at the surface increases rapidly. Top and side surface temperatures of a model cylindrical disc approaches the temperature of the oven, while center temperature rises slowly and approaches 100 °C (Phase change temperature or boiling point of water).

Figures 4.33 and 4.34 show the numerically predicted temperature contours based on modified model I and II respectively.

(a) 1 min

Temperature (K)

Radial Co-ordinate

(b) 2 min

Temperature (K)

Radial Co-ordinate

Figure 4.32 (a-b)

Numerically predicted temperature contours within a cylindrical disk (2-d axisymmetric disc) based on Zanoni's model at intervals of (a) 1 and (b) 2 minutes after baking

Figure 4.32 (c-d)

Numerically predicted temperature contours within a cylindrical disk (2-d axisymmetric disc) based on Zanoni's model at intervals of (a) 5 and (b) 10 minutes after baking

(b) 1 min

Temperature (K)

Radial Co-ordinate

(b) 2 min

Temperature (K)

Radial Co-ordinate

Figure 4.33 (a-b)

Numerically predicted temperature contours within a cylindrical disk (2-d axisymmetric disc) based on Modified Baking Model I at intervals of (a) 1 and (b) 2 minutes after baking
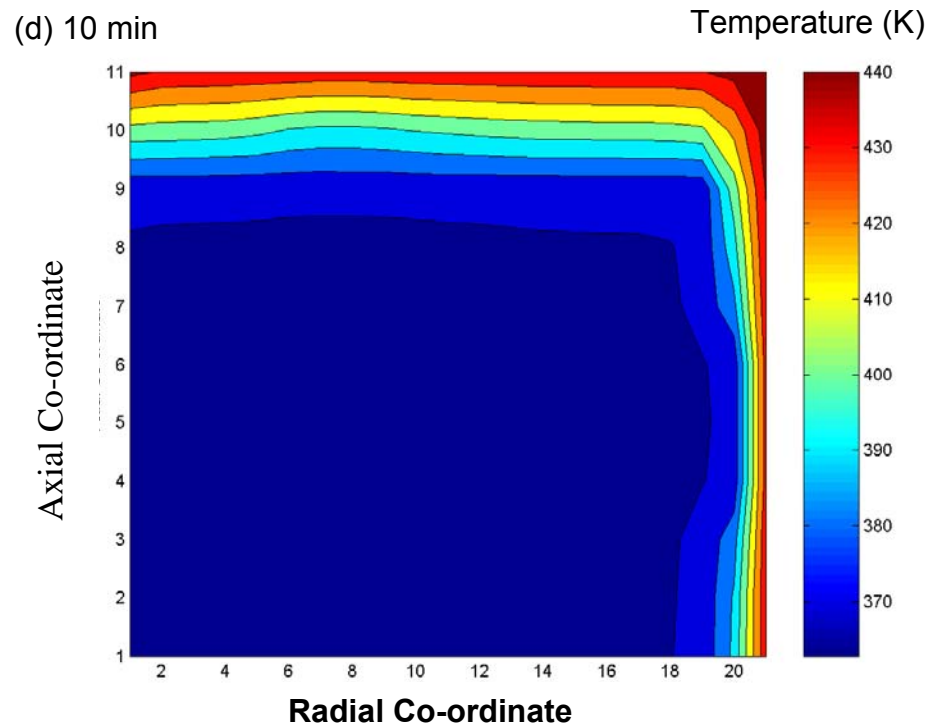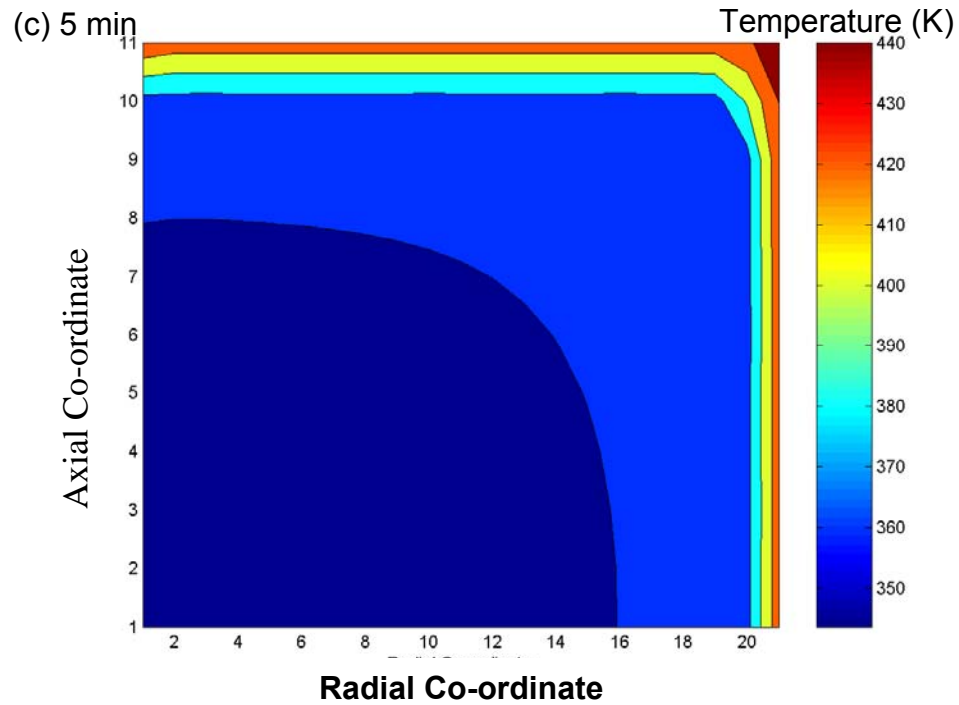
Figure 4.33 (c-d)

Numerically predicted temperature contours within a cylindrical disk (2-d axisymmetric disc) based on Modified Baking Model I at intervals of (c) 5 and (d) 10 minutes after baking
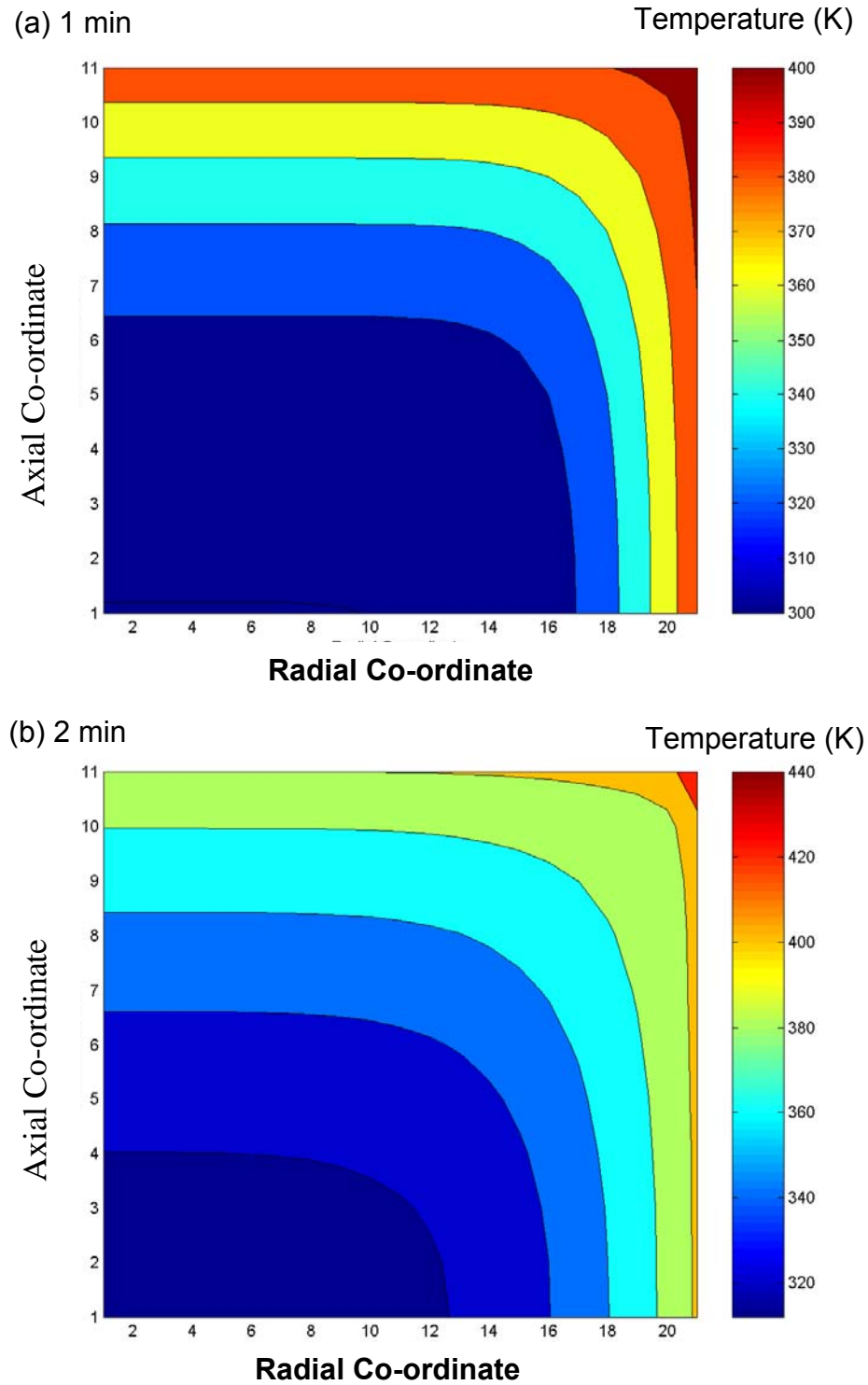
Figure 4.34 (a-b)

Numerically predicted temperature contours within a cylindrical disk (2-d axisymmetric disc) based on Modified Baking Model II at intervals of (a) 1 and (b) 2 minutes after baking

(c) 5 min

Temperature (K)

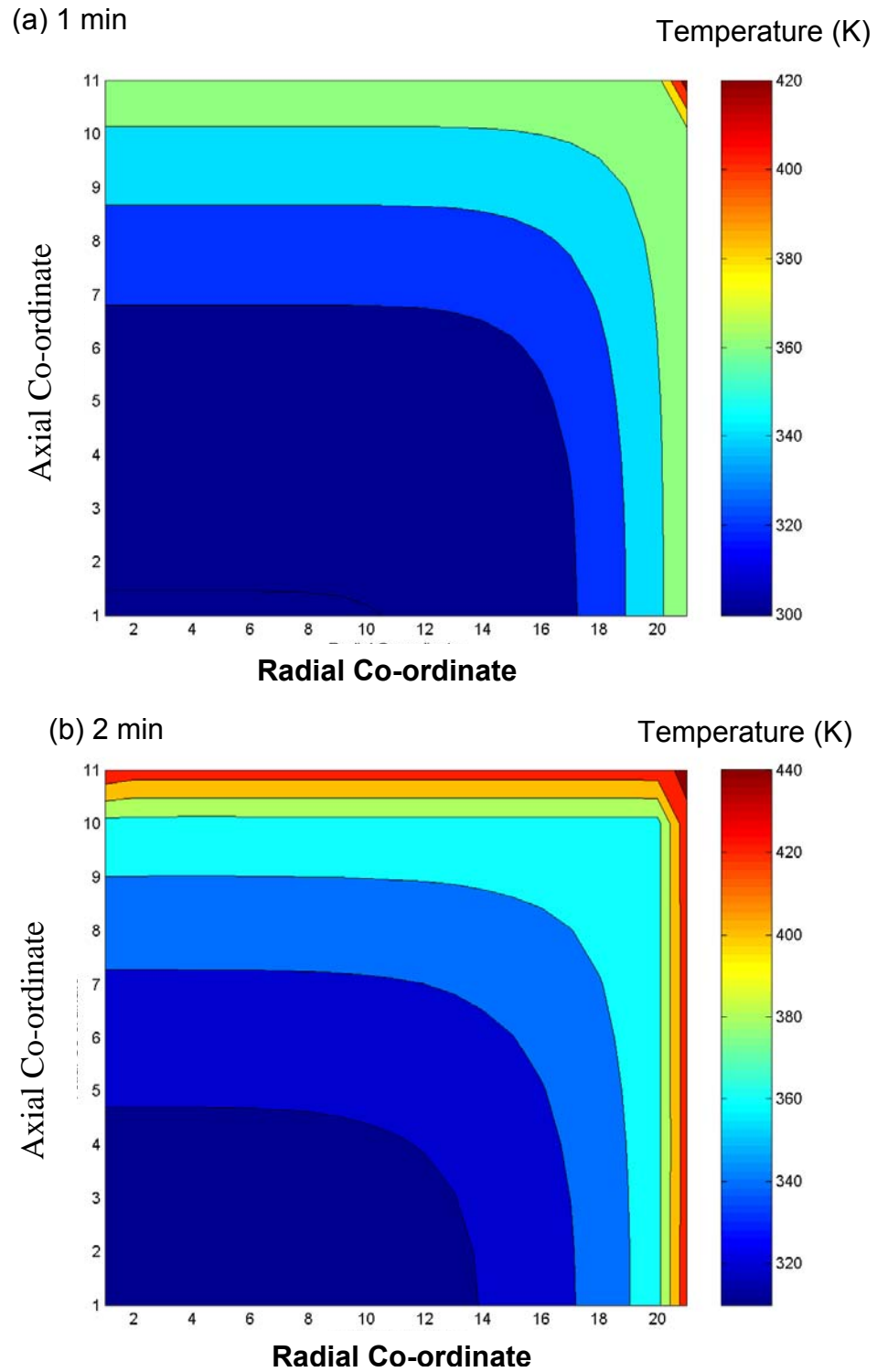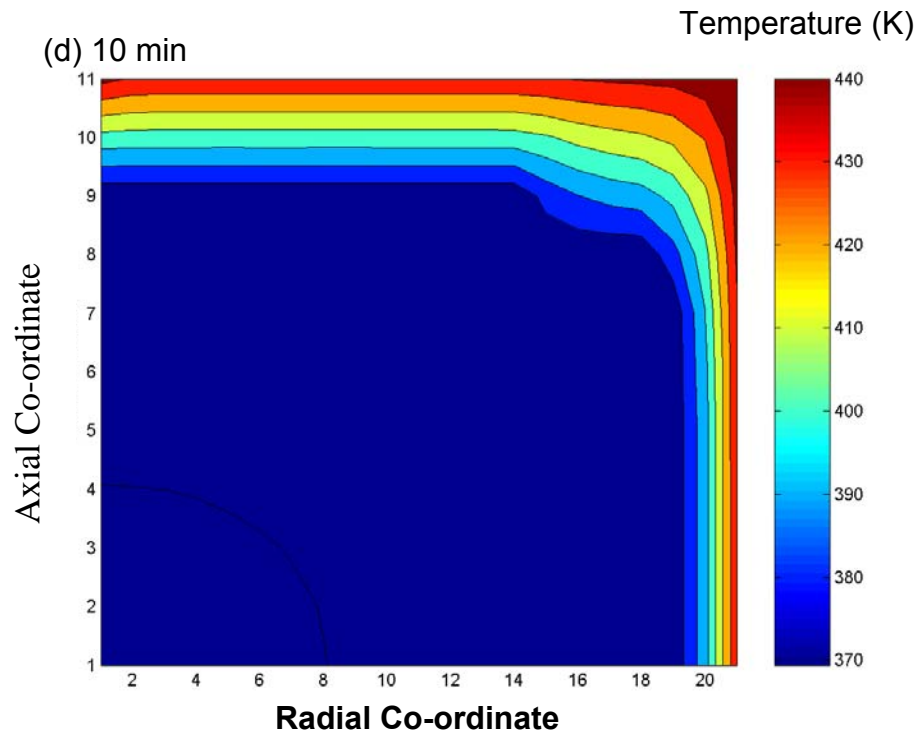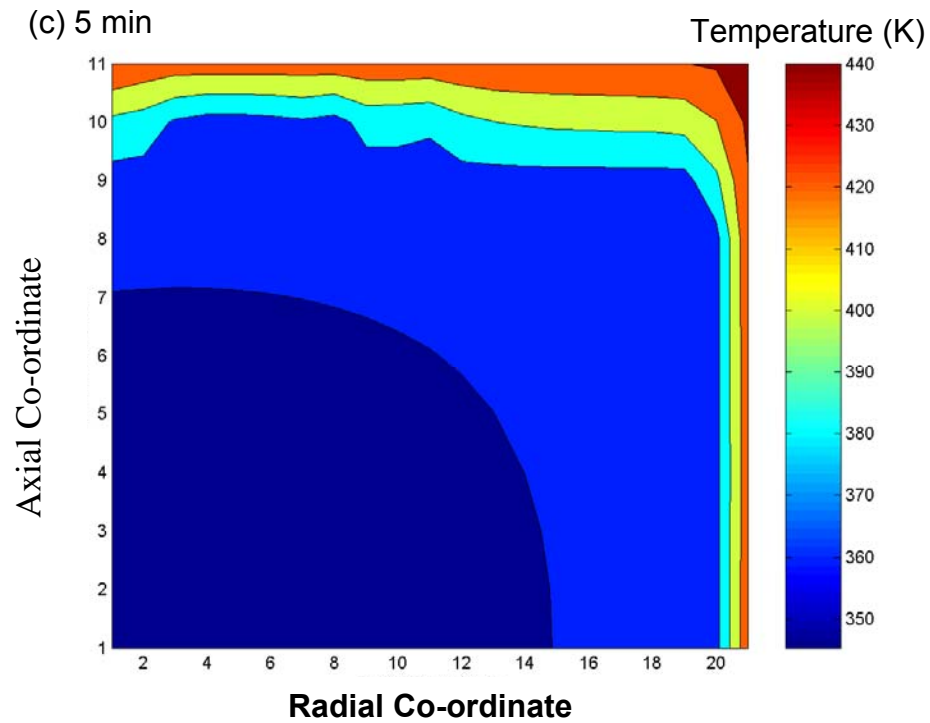**Radial Co-ordinate**

(d) 10 min

Temperature (K)

Radial Co-ordinate
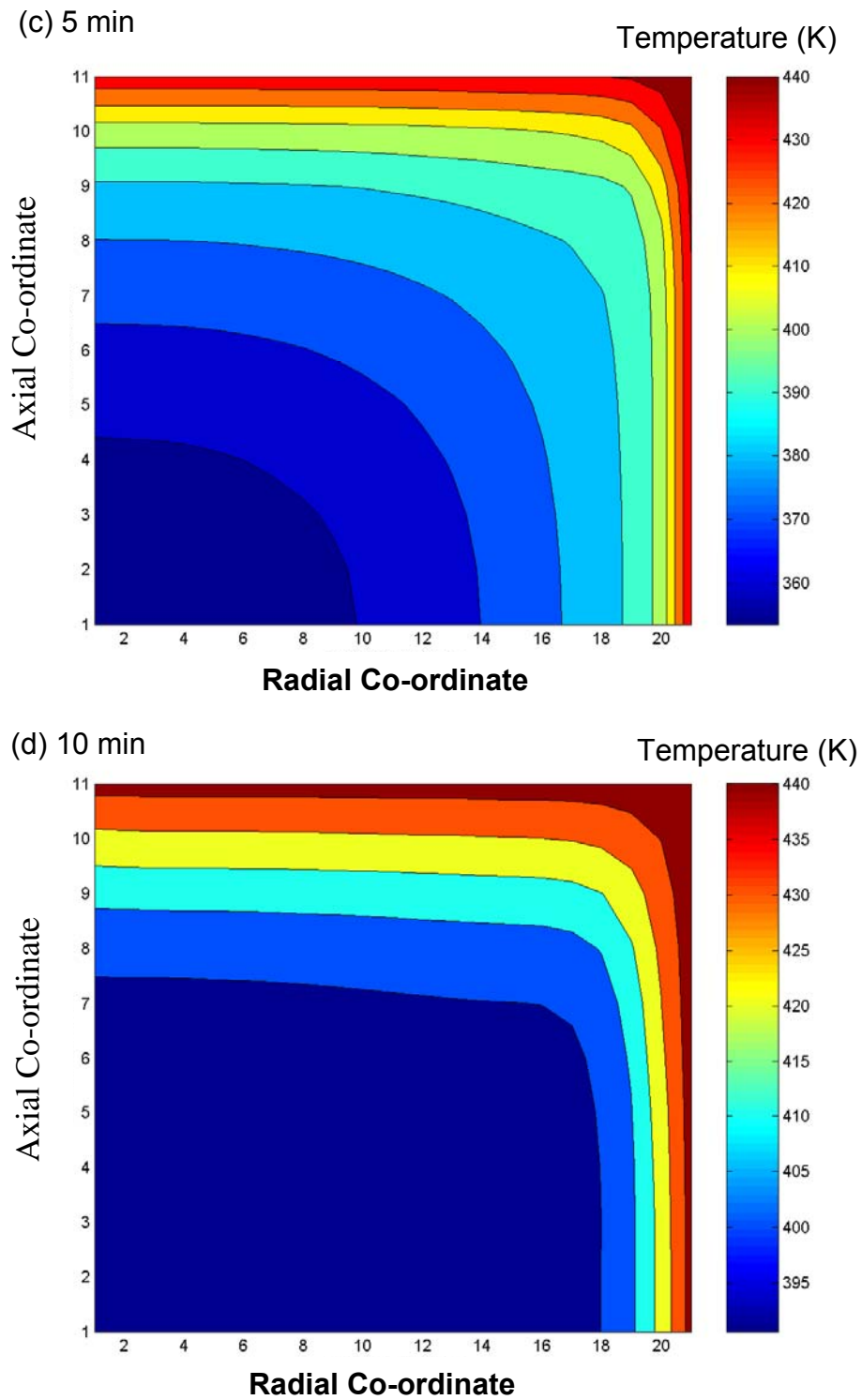
Figure 4.34 (c-d)

Numerically predicted temperature contours within a cylindrical disk (2-d axisymmetric disc) based on Modified Baking Model II at intervals of (a) 5 and (b) 10 minutes after baking

Based on comparison of results in **Figures 4.32, 4.33**, the contour shape of temperature distribution predicted by Zanoni's model and the modified baking model I are similar during the initial period of baking (temperature contours at 1 and 2 minute interval). After this initial interval of time, numerically predicted temperature based on Zanoni's model increases rapidly as compared with modified baking model I. This is expected as both these models are based on three stage baking process as discussed in Chapter 3 and have same set of boundary conditions. The difference in the temperature profile observed at 5 and 10 minutes interval of baking is due to the differences in vapor transport and coupling of heat and mass transport equations during a baking process.

Numerically predicted temperature contours based on modified baking model II (Figure 4.34) are significantly different from predictions based on Zanoni's (Figure 4.32) and modified baking model I (Figure 4.33). In numerically predicted temperature contours based on modified baking model II, the contour shape is smooth as compared with predicted contours based on Zanoni's and modified baking model I. This difference in the contour profiles can be explained on the basis of differences in numerical formulation of these three models. In case of Modified Baking Model II the baking process is modeled as a single continuous process as discussed in Chapter 3 as compared to a three step baking process. Despite these differences among models, the general trend of rapid increase in surface temperature, with a slower increase in temperature at the central core of a food material is predicted by all three models.

Comparison of moisture profile based on three baking models

Next we discuss the results of moisture profile within the food matrix. Comparison of numerically predicted moisture profile based on three different models (**Figures 4.35, 4.36 and 4.37)** clearly highlights differences among different baking models. Moisture contours predicted by Modified baking models I and II are distinct from the contour profiles predicted by Zanoni's baking model. Based on Zanoni's model, numerically predicted moisture contour show a sharp gradient within a food matrix in contrast with modified baking models. Based on these moisture contours, Zanoni's model provides a larger crust thickness as compared with modified baking models. This can be explained as Zanoni's model does not consider any resistance to vapor transport within the solid, thus rate of moisture loss as predicted by this model is higher than the numerical predicted results of modified baking models.

The trends observed with 2-D axisymmetric model are comparable with the results obtained from 1-D models. Similar to 1-D models, the numerical predicted results based on Zanoni's model have a shaper gradient in moisture content within the food matrix and also results in thicker crust formation.

(a) 1 min

Moisture Content

Radial Co-ordinate

Axial Co-ordinate

(b) 2 min

Moisture Content

Radial Co-ordinate

Axial Co-ordinate

Figure 4.35 (a-b)

Numerically predicted moisture contours within a cylindrical disk (2-d axisymmetric disc) based on Zanoni's model at intervals of (a) 1 and (b) 2 minutes after baking
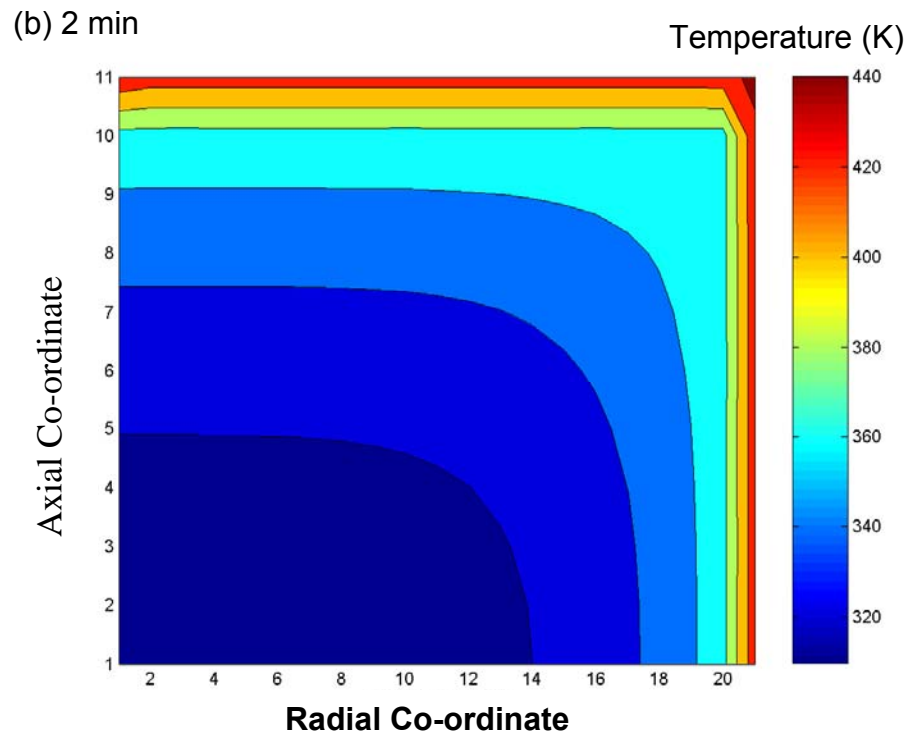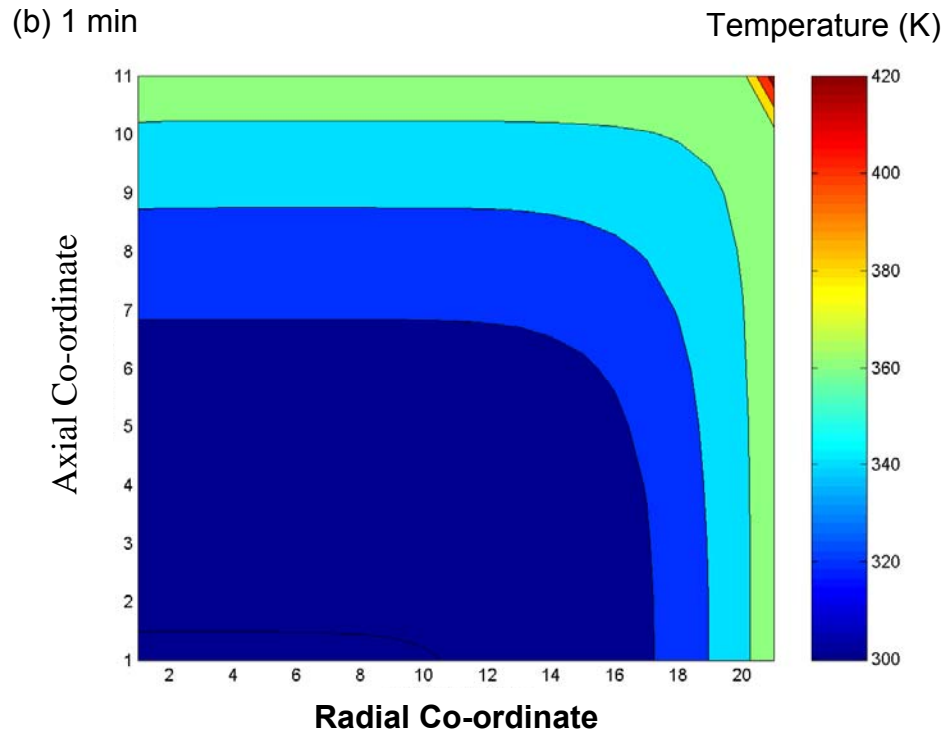
(c) 5 min   Moisture Content

Axial Co-ordinate

Radial Co-ordinate

(d) 10 min   Moisture Content

Axial Co-ordinate

Radial Co-ordinate
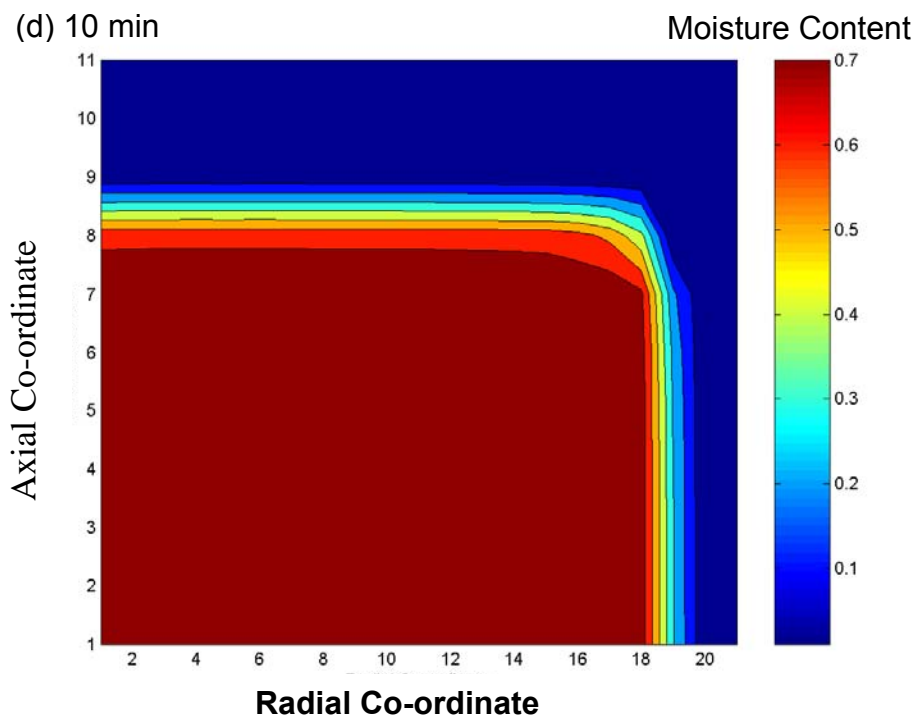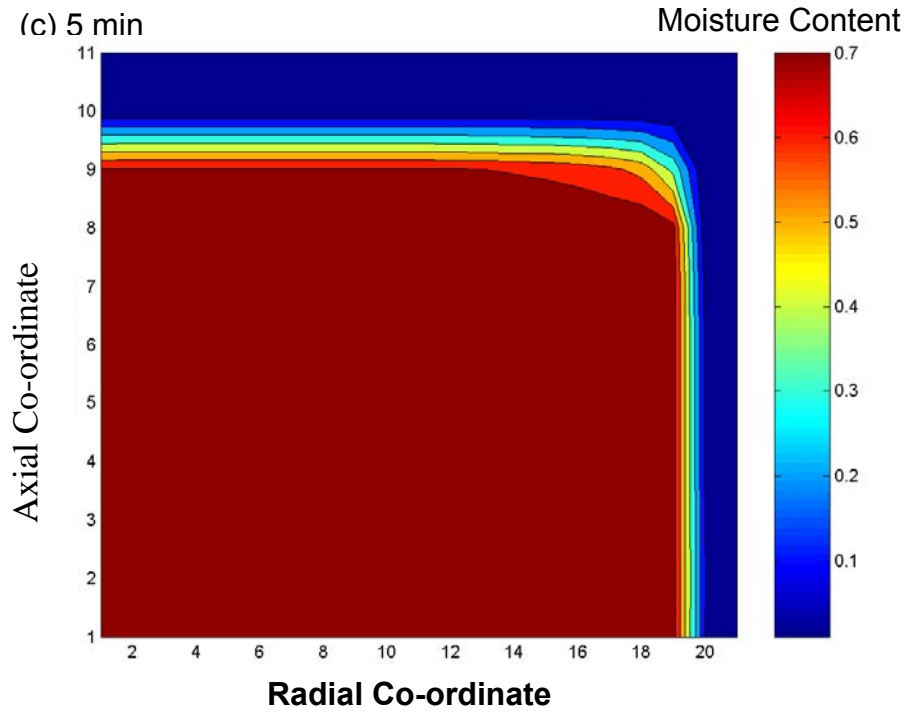
Figure 4.35 (c-d)

Numerically predicted moisture contours within a cylindrical disk (2-d axisymmetric disc) based on Zanoni's model at intervals of (a) 5 and (b) 10 minutes after baking
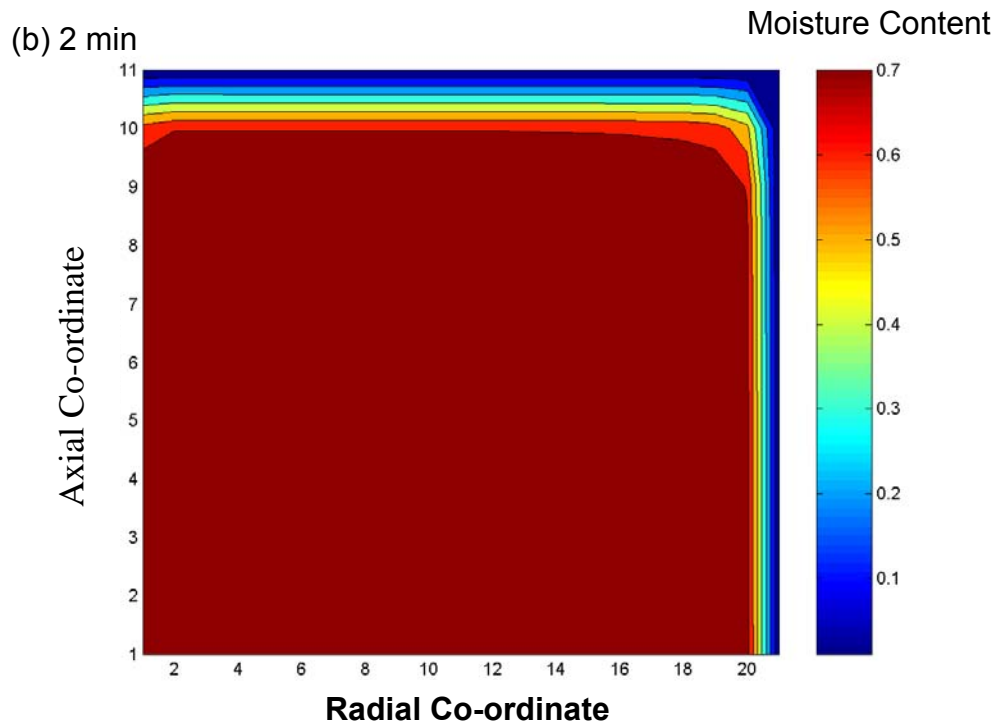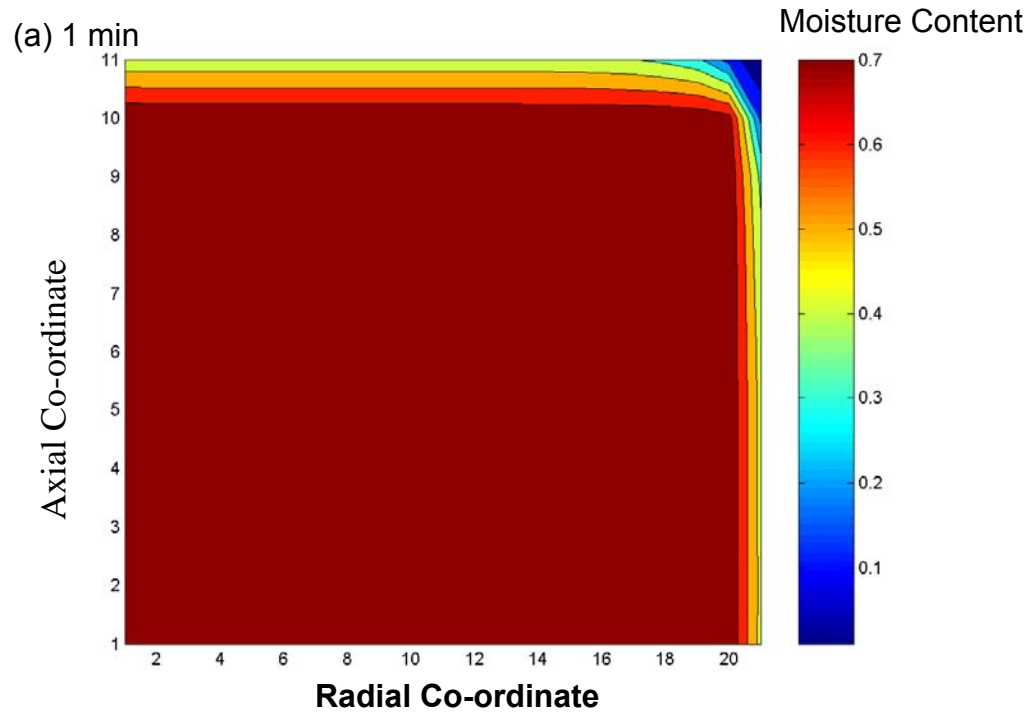
Figure 4.36 (a-b)

Numerically predicted moisture contours within a cylindrical disk (2-d axisymmetric disc) based on Modified Baking Model I at intervals of (a) 1 and (b) 2 minutes after baking

(c) 5 min — Moisture Content

(d) 10 min — Moisture Content
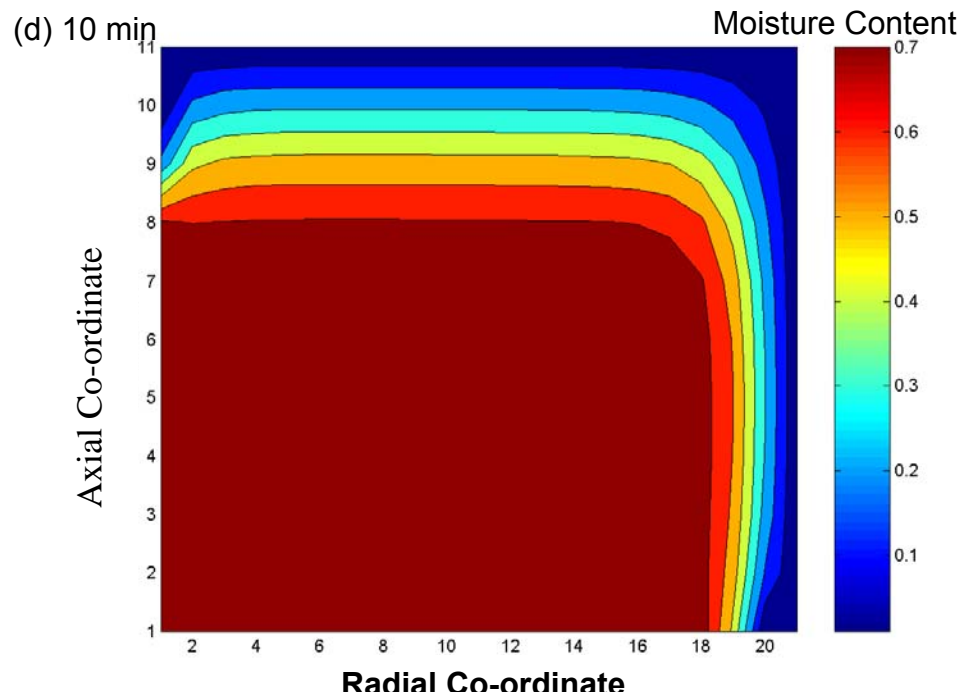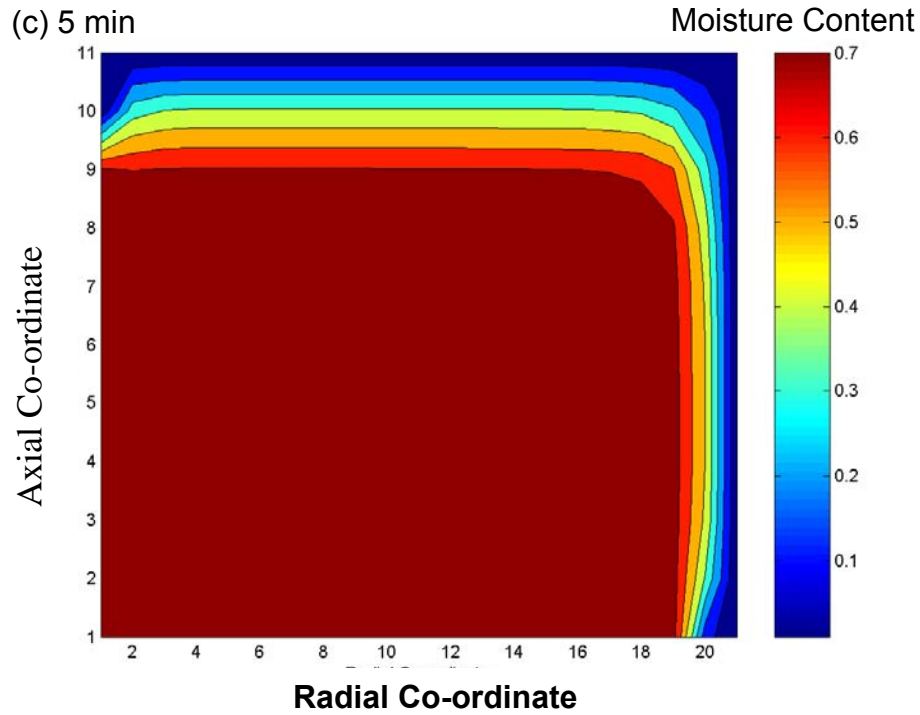
Figure 4.36 (c-d)

Numerically predicted moisture contours within a cylindrical disk (2-d axisymmetric disc) based on Modified Baking Model I at intervals of (c) 5 and (d) 10 minutes after baking

(a) 1 min

Moisture Content

Radial Co-ordinate

(b) 2 min

Moisture Content

Radial Co-ordinate
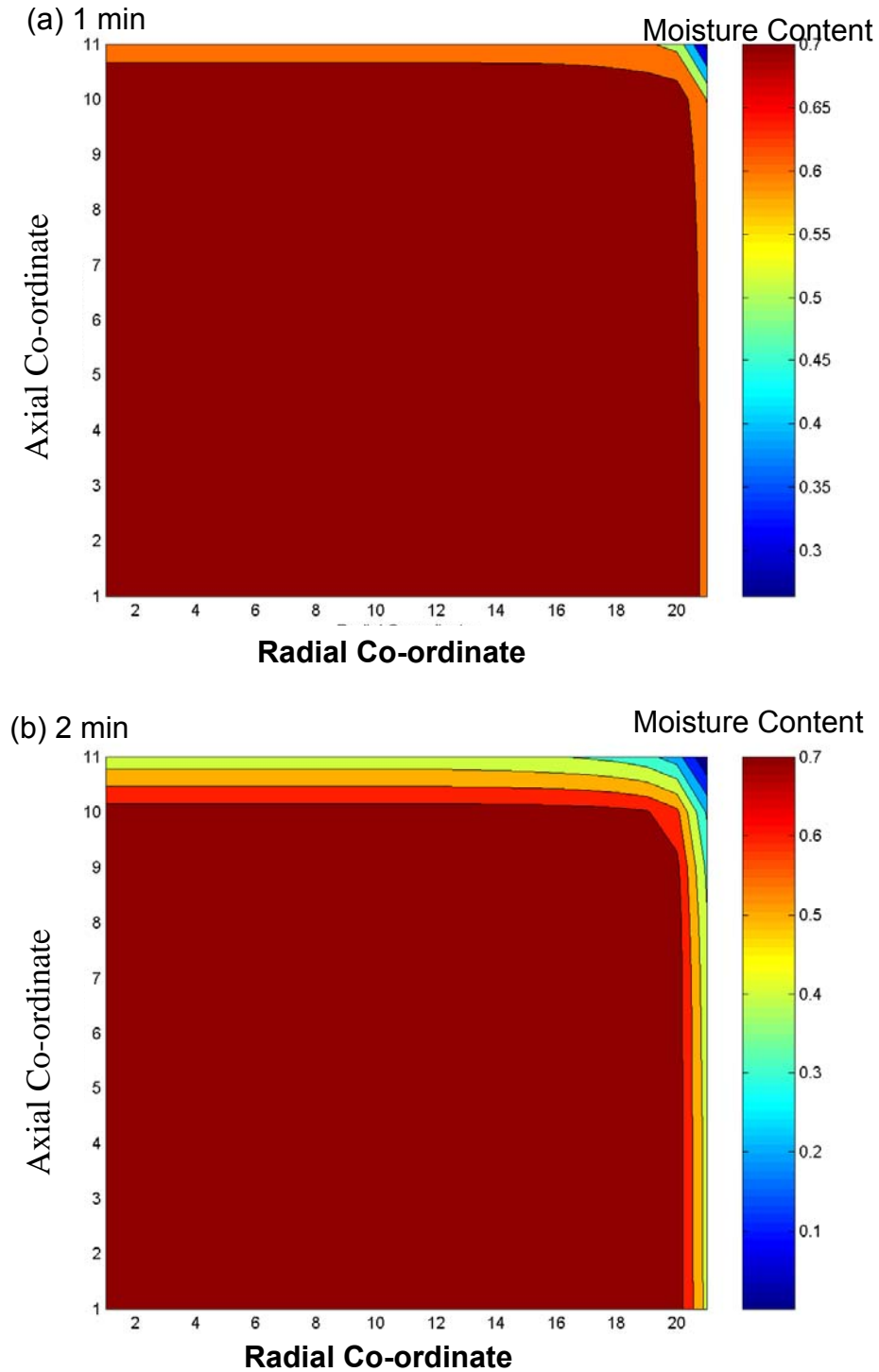
Figure 4.37 (a-b)

Numerically predicted moisture contours within a cylindrical disk (2-d axisymmetric disc) based on Modified Baking Model II at intervals of (a) 1 and (b) 2 minutes after baking

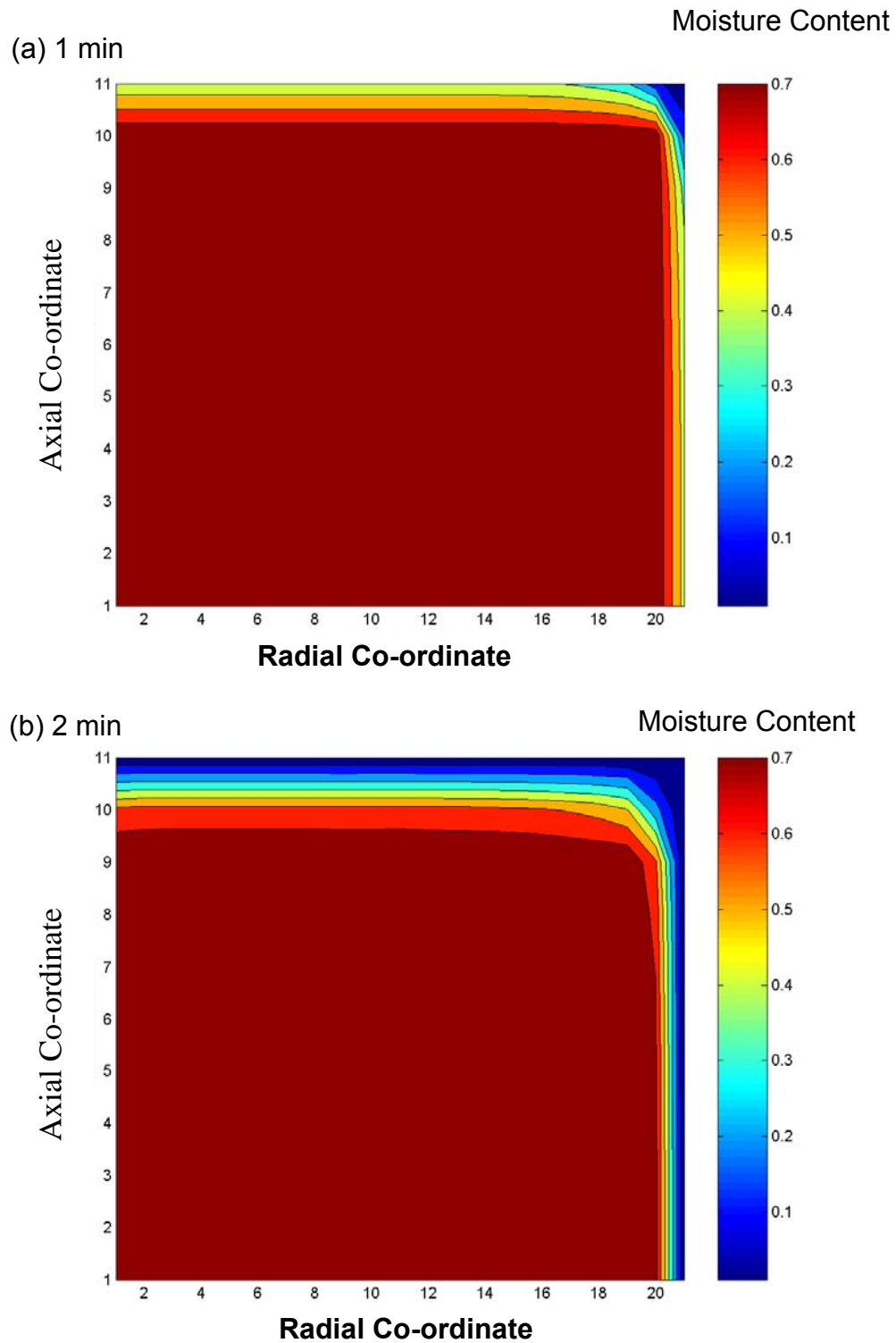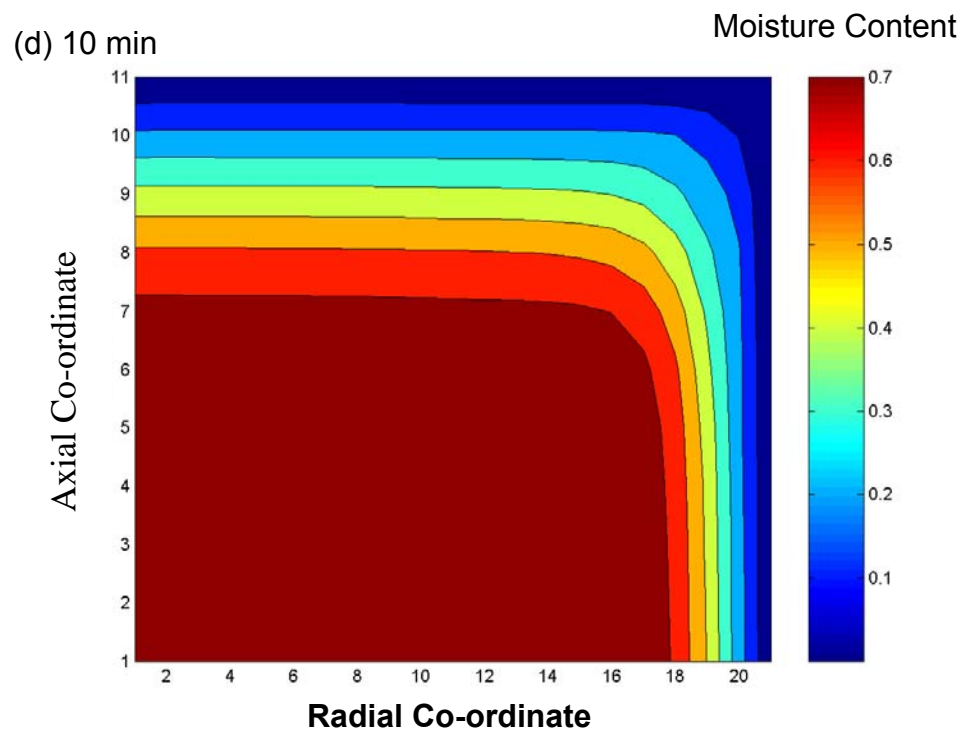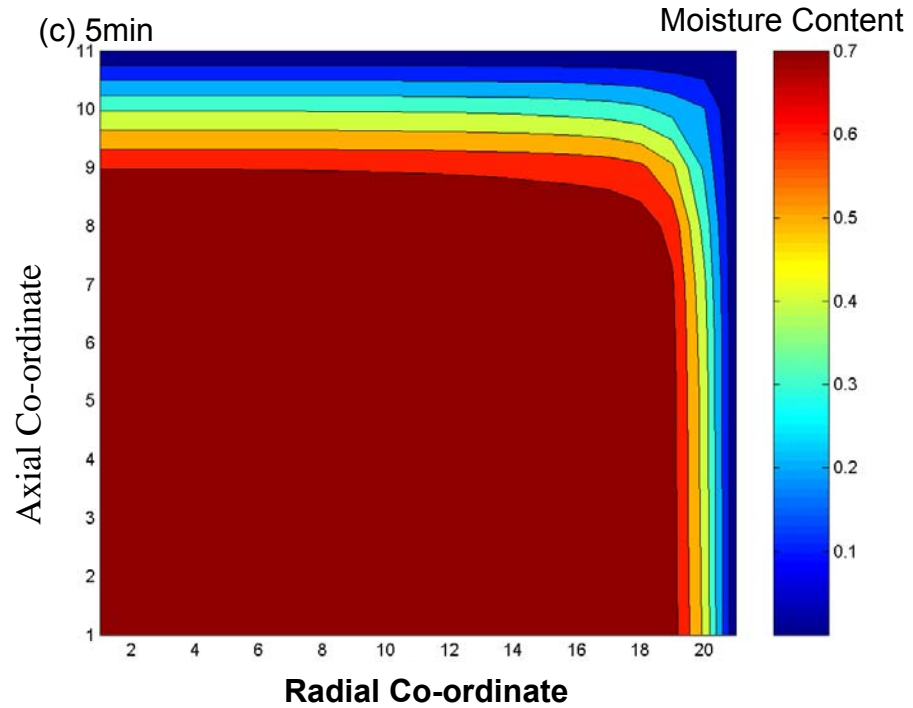**Figure 4.37 (c-d)**

Numerically predicted moisture contours within a cylindrical disk (2-d axisymmetric disc) based on Modified Baking Model II at intervals of (c) 5 and (d) 10 minutes after baking

Comparison of numerically predicted temperature with experimental results

In this section, results of numerically predicted temperature at the center of potato disc from three different baking models are compared with experimental measurements (**Figure 4.38**). Based on comparison among these three baking models, the modified baking model II predicts a higher temperature as compared with Zanoni's and modified baking model I. The differences between numerically predicted temperature among three baking models increases as the temperature approaches 100 °C. This is expected as baking process in Zanoni's and modified baking model I is divided into a three stage baking process in which temperature is constant at the phase change state (Temperature =100 °C) until moisture content drops below the critical moisture content. Similar trend was also observed for 1-d models of baking (**Figure 4.19**). Further comparison of the experimental results with numerically predicted results clearly demonstrate that overall trend predicted by three baking models is in agreement with the experimental results. Further analysis of the results clearly shows that numerically predicted temperature profile by modified baking model II shows better agreement with the experimental results. One of limitation of experimental set up with a potato based food material is difficulty in exact placement of thermocouples for measurement of center point temperature during baking. This is due to opaque nature of potato and also since potato is a soft material.
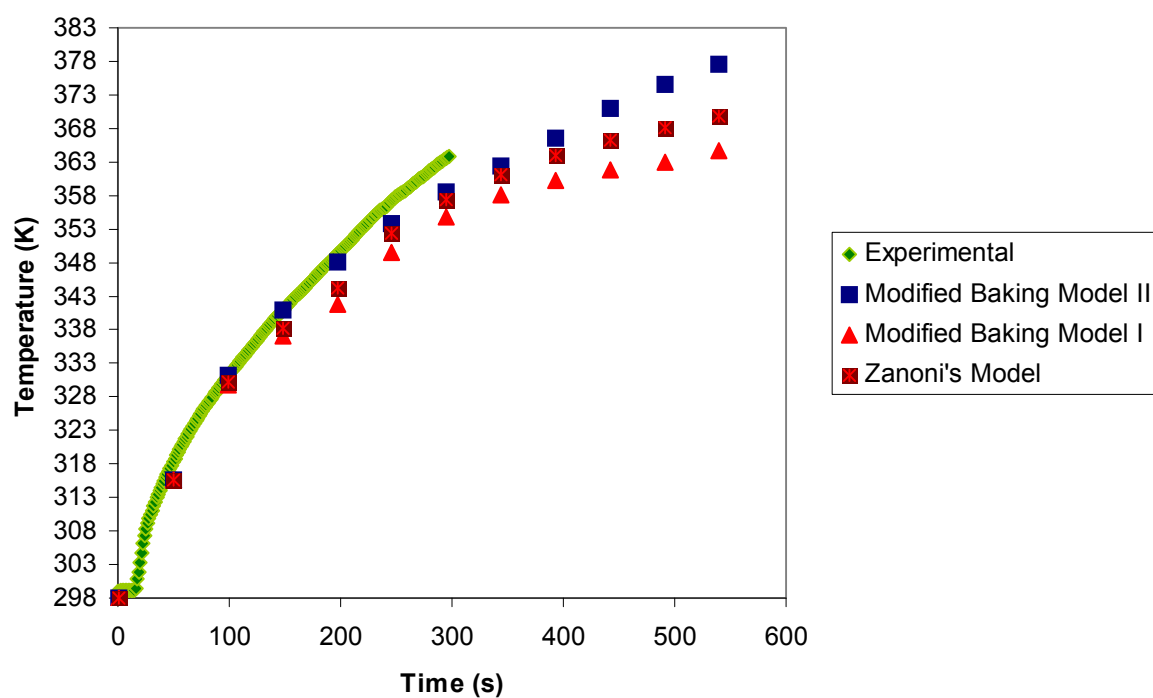
Figure 4.38

Comparison of numerically predicted temperature based on various baking models at the center of food material with experimental measurements

Further comparison of the results from a 2-D axisymmetric model with a 1-D baking model demonstrates that 2-D axisymmetric geometry provides a better model for baking of a potato disc as compared to an infinite rectangular slab. This result also validates our hypothesis that heat and mass transfer from side surface area of a cylindrical disc during jet impingement baking are significant.

CHAPTER 5

Conclusions and Future Work

Conclusions

Numerical Simulation of Conjugate Thermal Transport During Jet Impingement Baking and Validate It Using Experimental Data

The overall aim of this goal was to develop a numerical simulation based approach to model thermal transport during jet impingement baking. To model conjugate thermal transport, numerical simulation of flow field and its associated conjugate heat transfer was developed. Flow field numerical simulation results were compared with experimentally measured results of an impinging jet. To validate the results of numerical simulation, we have compared numerically predicted flow field with experimental measurements of jet axial velocity as a function of radial distance (along radial co-ordinate). Results of numerically simulation and experimental studies were compared at two different z positions, i.e. close to the jet nozzle (15 mm from the nozzle) and near the impinging surface (10 mm from the surface).

The results show that velocity profile predicted by numerical simulation was in agreement with the experimental data. Both numerical simulation and experimental results show a decrease in axial velocity along the radial co-ordinate with a maximum velocity at or near the centerline of an impinging jet.

The results also show a decrease in centerline jet axial velocity near an impinging surface as compared with jet velocity near the jet nozzle.

In a next step, numerical simulation approach was developed to model conjugate thermal transport using model food geometries. Based on this simulation, numerical values of heat transfer coefficient were predicted along the surface of a model cookie and a model cylindrical object. Local surface heat transfer coefficient (average over the area of the heat flux gage) and average surface heat transfer coefficient (average over the top surface area) were calculated based on predicted heat transfer coefficient values. Numerically predicted results show an increase in both local and average surface heat transfer coefficient with an increase in jet velocity and also with a decrease in z/d spacing (z/d=2, 3 and 5). This indicates that for a selected dimension of model geometry (cookies), a decrease in z/d spacing and an increase in jet velocity will provide a faster baking process.

The dimensions of selected product are important because optimal z/d position for a jet impingement baking process will depend on it. Variation in surface heat transfer coefficient along the surface also increased with a decrease in z/d spacing, indicating an increase in non-uniformity in surface heat transfer rates. Thus for a larger diameter product, the optimal z/d position may be achieved at a higher levels (z/d=3, or 5) as compared to a decrease in a nozzle to target spacing. Numerical simulation approach developed in this study can be used to determine optimal heat transfer rates for selected product geometry. This

approach can significantly overcome the limitations of empirical approaches currently used in many baking operations.

Comparison of predicted surface heat transfer coefficient for a model cookie and a cylindrical geometry (hot dog) highlights significant differences. Based on numerical simulations, a large variation in surface heat transfer is predicted for cylindrical geometry as compared to model cookie. These differences in predicted surface heat transfer coefficient indicate that a single jet impingement system can lead to a non-uniform heating of a stationary cylindrical shaped object in a jet impingement oven. This can be potentially reduced by using two impinging jets from opposite directions (top and bottom) or by rotating a cylindrical object along its axis.

Results of experimentally measured local surface heat transfer coefficient and average surface heat transfer coefficient were compared with numerically predicted values at a range of jet velocities (20 m/s to 40 m/s). Comparison of experimental results with numerically predicted values show agreement within the error range of measurement system. This approach validated the numerical simulation results and demonstrated that numerical approach can be effectively used for understanding thermal transport during jet impingement baking. Using numerical simulation, we predicted the variation in surface heat transfer coefficient for a model cookie and model cylindrical object.

Results of numerical simulation based on thermal transport model were compared with experimental measurements of temperature in a model food object. This comparison highlighted that based on thermal transport model only

(no mass transfer), the temperature- time data can be predicted for low jet temperature treatment (jet temperature= 60 °C). The results also highlighted that for high temperatures (jet temperatures> 100 °C), thermal transport is not adequate to predict the temperature-time profile during a baking process. This is expected as at higher temperatures, contribution from moisture transport process becomes significant along with thermal transport process. In summary, these results demonstrated that for effective simulation of baking process, modeling of both heat and mass transport process is required.

Development and Analysis of Baking Models

The next step after validation of numerical simulation of conjugate thermal transport during baking was to develop a baking model to simulate temperature and moisture profiles within a food matrix. The focus of this study was to understand significance of various transport processes for mathematical modeling of a baking process. In this study, we have analyzed three different formulations of coupled heat and mass transport models to simulate a baking process. These models significantly differ from each other based on modeling of vapor transport and a phase transition stage, i.e. transition from water to a vapor state during a baking process.

One of the models selected in this study was adapted from a phenomenological model developed by Zanoni et al., (1994). According to this model, during baking food material can be divided into two distinct zones (crust region and crumb region) with a moving evaporation front at the crust-crumb interface. This model is based on a three stage baking process determined by

the temperature at a selected location. To extend this phenomenological approach, we have proposed and evaluated two different baking models. Compared with Zanoni's models, these models specifically focus on vapor transport models and improved coupling of heat and mass transport terms at different stages of baking. Further in modified baking model II, baking process is modeled as a single stage process using the same numerical formulation at all temperature conditions.

To compare three different baking models, the predicted temperature and moisture profiles under same baking conditions were analyzed. Comparison of the results highlights significant differences in predicted temperature and moisture profiles. Zanoni's model predicted a larger crust thickness as compared to modified baking models. Based on Zanoni's model, a steep moisture gradient was predicted within the food matrix. The major contributing factor for this significant difference is a lack of vapor transport terms in Zanoni's model. Due to lack of resistance for vapor formation and transport in Zanoni's model, a rapid loss of moisture was predicted by Zanoni's model during a phase change process. Results clearly demonstrate the significance of vapor transport terms in baking models and also highlighted that moisture diffusion alone may not accurately predict the moisture profile in baked products.

To understand contribution of thermo-diffusion process during baking, we compared the predicted moisture and temperature profile of Zanoni's baking model with and without the Soret effect. Results of the comparison show that the Soret effect, i.e., diffusion of moisture due to temperature gradient does not have

a significant effect on moisture and temperature profile. Thus, the Soret effect has no significant effect in modeling of a baking process.

Comparison of temperature profile among three baking models shows significant differences between modified baking model II and Zanoni's and modified baking model I. In both Zanoni's and modified baking model I, we observed a step-wise rise in temperature as compared to a smooth increase in predicted temperature profile by modified baking model II. In Zanoni's and baking model I, baking is modeled as a three-step process. During a phase change step (T=100 °C), temperature at a local grid point is maintained constant, while moisture evaporates. In modified baking model II, baking process is modeled as a continuous process. This eliminates the hold step during a phase change process.

Comparison of three baking models highlight differences in coupling of heat and mass transport terms and vapor-moisture transport. In Zanoni's model, there is a very limited coupling of heat and mass transport rates during different stages of baking as compared to modified models. Based on the results, this lack of coupling results in a rapid rise of temperature and a loss of moisture in the crust region. In modified models II and I, improved coupling of heat and mass transport rates and additional vapor transport terms account for differences in predicted temperature-moisture profiles and thickness of crust region as compared with Zanoni's model.

Comparison between modified model I and II highlights the difference in formulation of a phase change step i.e. when temperature > 100 °C. The

presence of hold step during a phase change in modified model I accounts for a slow increase in center point temperature as compared to modified model II.

Comparisons of experimentally measured temperature results with numerically predicted results based on a 2-D axis-symmetric geometry clearly demonstrate that overall trend predicted by three baking models is in agreement with the experimental results. Further analysis of the results clearly shows that numerically predicted temperature profile by modified baking model II show a better agreement with the experimental results. Comparison of 2-D and 1-D numerically predicted results highlights significance of energy transport from the side surface area during a baking process.

Future Work

Based on the results of this research the below directions could be investigated to develop future research programs:

Experimental Measurements

1. **Experimental investigation of moisture distributions:** A technique should be developed to non-invasively measure moisture distribution within a sample. Method developed by Thorvaldsson and Skjoldebrand (1996), and Wahlby and Skjoldebrand uses fiber-optic NIR (Near Infrared Reflectance) measurement to measure changes in local water content within the food. NMR (Nuclear Magnetic Resonance) imaging is another technique that can be used to measure the moisture distribution. Based on these techniques nondestructive measurement of moisture distribution

within the samples can be achieved. In addition, these methods could be used to understand moisture transfer mechanisms as well as to estimate the moisture diffusion coefficients.

2. **Experimental measurement of thermophysical properties of food matrix during baking:** One of the significant challenges in modeling of a baking process is due to lack of dynamic measurements of thermophysical properties during baking. These include changes in resistance to moisture and thermal transport due to crust formation, changes in moisture diffusivity and vapor transport.

3. **Measurement of food structure changes during baking:** There is a lack of experimental measurements to characterize structural changes in a food matrix during baking. Baking is a complex process, which includes changes in volume, pore generation and various chemical changes effecting the structural properties. Experimental measurements in this area will improve fundamental understanding of baking and also aid in developing better phenomenological models.

Mathematical Modeling

4. **Integrated baking models to predict structural properties**: One of the limitations of the current models is lack of modeling of structural changes during baking including changes in porosity and volume. Mathematical modeling of these complex processes will aid in developing comprehensive models.

5. **Kinetic modeling of chemical changes during** - The current work can be extended to model chemical changes associated with baking process. Kinetic modeling of starch gelatinization and resulting browning process can be integrated to develop comprehensive models. These comprehensive models will increase utility of modeling for key attributes of a food product.

REFERENCES

1. Adrian RJ. 1991. Particle-imaging techniques for experimental fluid mechanics. Annual Review of Fluid Mechanics. 23:261-304.
2. Angioletti, M., Di Tommaso, R.M., Nino, E., Ruocco, G. 2003. Simultaneous visualization of flow field and evaluation of local heat transfer by transitional impinging jets. International Journal of Heat and Mass Transfer 46: 1703-1713.
3. Arpaci, VS., Larsen, PS. 1984. Convective Heat Transfer. Prentice Hall.
4. Barata, J.M.M. and Durao, D.F.G and Heitor, M.V. 1992. Velocity characteristics of multiple impinging jets through a cross flow. Journal of Fluids Engineering. 114:231-239.
5. Baughn, JW. 1995. Liquid crystal methods for studying turbulent heat transfer. International Journal of Heat and Fluid Flow. 16(5): 365-375.
6. Baughn JW, Shimizu S. 1989. Heat transfer measurements from a surface with uniform heat flux and an impinging jet, Journal of Heat Transfer. 111: 1096-1098.
7. Beckwith, TG, Marangoni, D. and Lienhard, JH. 1993. Mechanical Measurements, Addison-Wesley Publishing Company.
8. Behnia M., Parneix S., Shabany Y. 1999. Numerical study of heat transfer in a turbulent confined and unconfined impinging jets. International Journal of Heat and Fluid Flow. 20(1): 1-9.
9. Behrouzi P., McGuirk JJ. 1998. Laser Doppler velocimetry measurements of twin-jet impingement flow for validation of computational models. Optics and Lasers in Engineering. 30 (3): 265-277.
10. Broyart, B., and Trystram, T. 2002. Modleing heat and mass transfer during the continuous baking of biscuits. Journal of Food Engineering. 1: 47-57.
11. Borquez, R, Wolf W, Koller WD, Spieb, WEL. 1999. Impinging jet drying of pressed fish cake. Journal of Food Engineering. 40(1-2): 113-120.
12. Catalano GD, Chang KS, Mathis JA. 1989. Investigation of Turbulent jet impingement in a confined cross-flow. AIAA Journal 27(11): 1530-1535.
13. Chen G, Douglas WJM. 1995. Impingement drying of paper. Drying Technology. 13(5-7): 1331-1344.
14. Choi Y, Okos MR, 1985, Effect of temperature and composition on the thermal properties of foods, in Food Engineering and Process Applications, Le Mageur, M. and Jelen, P., Eds., Elseiver, London, 93-101.
15. Colucci, D.W. and Viskanta, R. 1996. Effect of nozzle geometry on local convective heat transfer to a confined impinging air jet. Experimental Thermal and Fluid Science. 13: 71-80.
16. Cornaro C, Fleischer AS, Goldstein RJ. 1999. Flow visualization of a round jet impinging on cylindrical surfaces. Experimental Thermal and Fluid Science. 20(2): 66-78.

17. Craft TJ, Iacovides H, Mostafa NA. : Modelling of three-dimensional jet array impingement and heat transfer on a concave surface. International Journal of Heat and Fluid Flow. 29 (3) : 687-702.

18. De Vries, U., Sluimer, P. and Bloskma, A.H. 1989. A quantitative model for heat transport in dough and crumb during baking. Cereal Science and Technology in Sweden. 174-188

19. De Vries, U., Velthuis, H., and Koster, K. 1995. Baking ovens and product quality: a computerm del. Fodd science and Technology Today. 9:232-234

20. Deo, I.S. and Karwe, M.V. 1998. Effect of dimensions and thermal properties of heat flux gage on local heat flux. Proceedings of ASME Heat Transfer. 5: 361-365.

21. Dietl, C., Edgar, RF., Viskanta, R. 1998. An efficient simulation of the heat and mass transfer processes during drying of a capillary porous, hygrosco materials. Intl. Journal of Heat and Mass Transfer. 41:3611-3625.

22. Donaldson CduP, Snedeker RS, Margolis DP. 1971. A Study of free jet impingement. Part 2. Free jet turbulent structure and impingement heat transfer, J Fluid Mechanics 45(3): 477-512.

23. Florscheutz, L.W., Truman, C.R., and Metzger, D.E. 1981. Streamwise flow and heat transfer distributions for jet array impingement with cross flow. Journal of Heat Transfer. 102:337-342.

24. Gardon R. and Akfirat J.C. 1964. Heat transfer characteristics of impinging two-dimensional air jets. ASME-HT-20l, 410-414.

25. Gardon R. and Akfirat J.C. 1965. The role of turbulence in determining the heat transfer characteristics of impinging jets. International Journal of Heat and Mass Transfer, 8: 1261-1272.

26. Gardon, R. and Cobonpue, J. 1962. Heat Transfer between a flat plate and jets of air impinging on it. International Developments in Heat Transfer, 454-60. ASME, New York.

27. Gardon R, Akfirat JC. 1966. Heat transfer characteristics of impinging two dimensional air jets. Journal of Heat Transfer. 88: 101-108.

28. Gogineni S, Visbal M, Shih C. 1999. Phase-resolved PIV measurements in a transitional plane wall jet: a numerical comparison. Experiments in Fluids. 27(2):126-136.

29. Goldstein, R.J. and Timmers, J.F. 1982. Visualization of heat transfer from arrays of impinging jets. International Journal of Heat and Mass Transfer. 25(12): 1857-1868.

30. Goldstein R.J. and Behbahni, A.I. 1982. Impingement of a circular jet with and without cross flow. International Journal of Heat and Mass Transfer. 25:1377-1382.

31. Goldstein RJ, Seol WS. 1991. Heat-transfer to a row of impinging circular air-jets including the effect of entrainment International Journal of Heat and Mass transfer. Volume: 34 Issue: 8 Pages: 2133-2147.

32. Hallback, M., Johansson, A.V., and Burden, A.D. 1996. The basics of turbulence modeling. Turbulence and Transition Modeling. 81-150. Kluwer Academic Publishers, London.

33. Heldman D.R. and Lund D.B., 1992. Handbook of Food Engineering. Marcel Dekker Inc. New York.

34. Hsiao FB, Sheu SS. 1996. Experimental studies on flow transition of a plane wall jet. Aeronautical Journal. 100(999):373-380.

35. Hu Z, Sun DW. 2000. CFD simulation of heat and moisture transfer for predicting cooling rate and weight loss of cooked ham during air-blast chilling process. Journal of Food Engineering. 46(3): 189-198.

36. Hu Z, Sun DW. 2001. Effect of fluctuation in inlet airflow temperature on CFD simulation of air blast chilling process. Journal of Food Engineering. 48(4): 311-316.

37. Huber, A.M. and Viskanta, R. 1994b. Heat transfer to a confined impinging array of jets with spent air exits. Journal of Heat Transfer. 116:570-576.

38. Huber A.M., and Viskanta, R. 1994a. Impingement heat transfer with a single rosette nozzle. Experimental Thermal and Fluid Science. 9: 320-329

39. Hollworth, B.R. and Berry, R.D. 1978. Heat transfer from arrays of impinging jets with large jet-to-jet spacing. Journal of Heat Transfer, 100:352-357.

40. Hoogendoorn, C.J. 1977. The effect of turbulence on heat transfer at a stagnation point. International Journal of Heat and Mass Transfer. 20: 1333-1338.

41. Icoz D, Sumnu G, Sahin S. 2004. Color and texture development during microwave and conventional baking of breads. International Journal of Food Properties Volume: 7 Issue: 2: 201-213.

42. Jaluria Y. and Torrance K., 1986. Computational Heat Transfer. Hemisphere Publishing Co. New York.

43. Jambunathan K, Lai E, Moss MA, Button BL. 1992. Review of heat transfer data for single circular jet impingement. International J Heat Fluid Flow 13(2): 106-115.

44. Jones, W. P., and Launder, B. E. 1972. The Prediction of Laminarization with a Two-Equation Model of Turbulence. Int. J. Heat Mass Transfer, Vol. 15, pp. 301-314.

45. Launder BE, Spalding DB. 1972. Mathematical models of turbulence. Academic Press, New York.

46. Lee J, Lee SJ. 2000. Effect of nozzle configuration on stagnation region heat transfer of axisymmetric jet impingement. International Journal of Heat and Mass Transfer. 43(18): 3497-3509.

47. Li A, Walker, CE. 1996. Cake baking in conventional, impingement and hybrid ovens. J Food Sci 61(1): 188-191, 197.

48. LujanAcosta J, Moreira RG, SeyedYagoobi J. 1997. Air-impingement drying of tortilla chips. Drying Technol 15(3-4): 881-897.

49. LujanAcosta J, Moreira RG, SeyedYagoobi J. 1997. Air-impingement drying of tortilla chips. Drying Technology, 15(3-4): 881-897.

50. Lytle, D., Webb, B. W. 1994. Air jet impingement heat transfer at low nozzle-plate spacings. International Journal of Heat and Mass Transfer. 37: 1687-1697.

51. Kaiser, V.A. 1974. Modeling and simulation of a multi-zone band oven. Food Technology. 28. 52-53.

52. Kataoka, K. Sahara, R., Ase, H., Mihata, I. 1987. Role of large-scale coherent structures in impinging jet heat transfer. Journal of Chemical Engineering. 20: 71-76.
53. Khan, A., Hirata, M.M., Kasagi, N. and Nishiwati, N. 1982. Heat transfer augmentation in an axisymmetric impinging jet. International Heat Transfer Conference. 3: 363-368.
54. Marcroft HE, Chandrasekaran M, Karwe MV. 1999. Flow field in a hot air jet impingement oven- Part II. Multiple impingement jets. J Food Proc Preservation. 23(3): 2335-248.
55. Marcroft HE, Karwe MV. 1999. Flow field in a hot air jet impingement oven- Part I. A single impinging jet. J Food Proc Preservation. 23(3): 217-233.
56. Martin H. 1977. Heat and mass transfer between impinging gas jets and solid surfaces. Adv Heat Transfer. 13(1): 1-60.
57. Maroulis Z.B., Saravacos G.D., Panagiotou N.M., and Krokida M.K, 2001. Moisture diffusivity data compilation for foodstuffs: effect of material moisture content and temperature. International Journal of Food Properties, 4(2): 225-237.
58. Mesbah, M., Baughn, J. W. and Yap, C. W. 1996. The effect of curvature on the local heat transfer to an impinging jet on a hemispherically concave surface. Proceedings of the Ninth International Symposium on Transport Phenomena in Thermal-Fluids.
59. Metzger, D.E. and Korstad, R.J. 1972. Effects of cross flow on impingement heat transfer. Journal of Engg. Power. 94: 35-42.
60. Mirade, P. S., Kondjoyan, A. and Daudin, J. D. 2002. Three-dimensional CFD calculations for designing large food chillers. Computers and Electronics in Agriculture. 34(1-3):67-88.
61. Moreira RG. 2001. Impingement drying of foods using hot air and superheated steam. J of Food Eng 49(4): 291-295.
62. Morris GK, Garimella SV, Amano RS. 1996. Prediction of jet impingement heat transfer using a hybrid wall treatment with different turbulent prandtl number functions. Journal of Heat Transfer-Transactions of ASME. 118(3): 562-569.
63. Nakabe, K., Fornalik, E., Eschenbacher, J. F., Yamamoto, Y., Ohta, T. and Suzuki, K. 2001. Interactions of longitudinal vortices generated by twin inclined jets and enhancement of impingement heat transfer. International Journal of Heat and Fluid Flow. 22(3): 287-292.
64. Nitin, N. 2001. Measurement of heat transfer coefficient for cookie shaped objects in a hot air jet impingement oven. MS Thesis, Rutgers University.
65. Nitin N, Karwe MV. 2001. Heat transfer coefficient for cookie shaped objects in a hot air jet impingement oven. J Food Proc Eng. 24(1): 51-69.
66. Okos M., Narsimhan Singh R.K., and Weitnauer A.C., 1992. Food Dehydration. In Handbook of Food Engineering edited by D.R. Heldman and D.B. Lund, Chapter 10, pp. 437-562, Marcel Dekker Inc., New York.
67. Ovadia DZ, Walker CE. 1998. Impingement in food processing. Food Technol. 52(4): 46-50.
68. Ozisik, M.N. 1993. Heat Conduction, Wiley Inter-Science. NY.

69. Park TS, Sung HJ. 2001. Development of a near –wall turbulence model and application to jet impingement heat transfer. 22(1) 10-18.
70. Patankar, S. V. 1980. Numerical heat transfer and fluid flow. Hemisphere Pub. Corp. WA. p197.
71. Polat S, Huang B, Majumdar AB, Douglas WJM. 1989. Numerical flow and heat transfer under impinging jets: A review, in: C. L. Tien (Ed.), Ann Rev Numerical Fluid Mechanics Heat Transfer, Washington, DC, Vol. 2: 157-197.
72. Popiel, C. O. and Tras, O. 1991. Visualization of a free and impinging round jet. Experimental Thermal and Fluid Science. 4(3): 253-264.
73. Rao M.A. and Rizvi S.S.H., 1995. Engineering properties of foods. Marcel Dekker Inc., New York.
74. Ranjan R., Irudayaraj J., Mahaffy J., 2002. Modeling simultaneous heat and mass transfer using a control volume approach. Numerical Heat Transfer B, 41(5): 463-474.
75. Sablani S., Rahman, S., and Al-Habsi N., 2000. Moisture diffusivity in foods – an overview. in drying technology in agriculture and food sciences. Edited by A.S. Mujumdar, Science Publishers, Inc., Enfield, New Hampshire, Chapter 2.
76. Sarkar A., 2002. Study of heat transfer under impinging jets for freeze-thaw conditions. [ms thesis]. Davis, Calif.: University of California, Davis. 104p. Available from: Library University of California.
77. Sarkar A. and Singh R.P., 2003. Spatial variation of convective heat transfer coefficient in air impingement applications. Journal of Food Science, 68(3): 910-916.
78. Saripalli, K.R., 1983. Visualization of multijet impingement flow. AIAA Journal, 21(4): 483-484.
79. Savoye, I., Trystram, G., Brunet, P. and Marchin, F., 1992. Heat and mass transfer dynamic modeling of an indirect biscuit baking tunnel- oven, Part I: Modeling and principles. Journal of Food Engineering. 16. 173-196.
80. Saravacos G.D. and Charm, S.E., 1962. A study of the mechanism of fruit and vegetable dehydration. Food Technology, 16:78-81.
81. Schlichting, H., 1979. Boundary-layer theory. 7th ed. New York : McGraw-Hill, p.817.
82. Seyedein S., Hasan M., Mujumdar A., 1994. Modeling of a single confined turbulent slot jet impingement using various kappa-epsilon turbulence models. Applied Mathematical Modelling. 18(10):526-537.
83. Smith D. P., 1975. Cooking Apparatus. U.S. Patent # 3,884,213
84. Sparrow E.M. and Lovell B.J., 1980. Heat transfer characteristics of an obliquely impinging circular jet. Journal of Heat Transfer. 102: 202-209.
85. Sugiyama, Y. and Usami Y., 1979. Experiments on flow in and around jets directed normal to a cross flow. Bulletin JSME. 22:1736-1745.
86. Sumnu G, Sahin S, Sevimli M., 2005. Microwave, infrared and infrared-microwave combination baking of cakes Journal of Food Engineering. Volume: 71 Issue: 2 Pages: 150-155.

87. Verboven, P., Scheerlinck, N., De Baerdemaeker, J., Nicolai, B.M., 2000a. Computational fluid dynamics modelling and validation of the isothermal flow in a forced convection oven. Journal of Food Engineering. 43 (1): 41-53.

88. Verboven, P., Scheerlinck, N., De Baerdemaeker, J., Nicolai, B.M., 2000b. Computational fluid dynamics modelling and validation of the temperature distribution in a forced convection oven. Journal of Food Engineering. 43 (2): 61-74.

89. Viskanta, R. 1993. Heat transfer to impinging isothermal gas and flame jets. Experimental Thermal and Fluid Science. 6: 111-134.

90. Wahlby, U., Skjoldebrand, C., and Junker, E. 2000. Impact of impingement on cooking time and food quality. Journal of Food Engineering. 43(3): 179-187.

91. Walker C.E. 1987. Impingement oven technology - Part I Principles. AIB Research Department Technical Bulletin, Volume XI, Issue 11, November

92. Walker C.E. and Sparman A.B., 1989. Impingement Oven Technology- Part II: Applications and Future. AIB, Research Department, Technical Bulletin, Volume XI, Issue 11.

93. Walker C.E. and Li A., 1993. Impingement oven technology-Part III: Combining impingement with microwave (Hybrid Oven). AIB, Research Department, Technical Bulletin, Volume XV, Issue.

94. Wang N. and Brennan J.G., 1993. The influence of moisture content and temperature on specific heat of potato measured by differential scanning calorimetry. Journal of Food Engineering, 19(3): 303-310.

95. Westknemper, J. C. 1961. On the error in plug in type calorimeters caused by surface temperature mismatch. Journal of Aeronautical Sciences. 28(11): 907-908.

96. Yin Y. and Walker, C.E., 1995. A quality comparison of breads baked by conventional versus nonconventional ovens: a review. J. Sci. Food Agriculture. 67:283-291.

97. Zanoni, B., Peri, C., and Pierucci, S. 1993. A study of bread-baking process. I: A phenomenological model. Journal of Food Engineering. 19. 389-398.

98. Zanoni, B. and Pierucci, S., and Peri, C. 1994. Study of the bread baking process. II: Mathematical Modeling. Journal of Food Engineering. 23. 321-336.

99. Zanoni, B., Peri C., and Bruno, D. 1995. Modeling of starch gelatinization kinetics of bread crumb during baking. Lebesnmittel-Wissenschaft und-Technologie. 28. 604-609.

100. Zitny R., Sestak J., Tsiapouris A., and Linke, L., 2002. Modeling of thermal pressure forming of starch based materials. Journal of Food Engineering, 52:375-385.

101. Zuckerman, H. and Miltz, J. 1998. Temperature profiles in dough heated with a susceptor in the microwave oven. Journal of Food Processing and Preservation. 22:53-65.

Curriculum Vita

NITIN NITIN

EDUCATION:

Rutgers, State University of New Jersey, NJ
Ph.D. Food Engineering (September, 2001- January, 2009)

Georgia Institute of Technology, GA
U.A. Whitaker School of Biomedical Engineering
Ph.D. Bioengineering (September, 2001- May, 2005)

Georgia Institute of Technology, GA
Dupree School of Management
Graduate Certificate in Management of Technology (September, 2002- May, 2005)

Rutgers, State University of New Jersey, NJ
Master of Science in Food Engineering (September, 1998- April, 2001)

Panjab University, India
B.S. Chemical Engineering (August, 1994 - July, 1998)

REFERRED JOURNAL PUBLICATIONS:

1. **N. Nitin** and M.V. Karwe, "Heat transfer coefficient for disk shaped object in jet impingement", Journal of Food Process Engineering, 24(1) 2001

2. **N. Nitin** and M.V. Karwe, "Numerical simulation and experimental investigation of conjugate heat transfer between a turbulent hot air jet and model geometry", Journal of Food Science, 69(2), 2004

3. A. Sarkar, **N. Nitin**, M.V. Karwe, and R.P. Singh, "Fluid flow and heat transfer in air jet impingement in food processing," Journal of Food Science, 69(4), 2004

4. **N. Nitin**, P. Santangelo, G. Kim, S. Nie and G. Bao, "Peptide linked molecular beacons for efficient delivery and rapid mRNA detection in living cells", Nucleic Acids Research, E58, 2004

5. **N. Nitin**, L.E.W. LaConte, O. Xurkiya, X. Hu, and G. Bao, "Development of functionalized superparamagnetic iron oxide nanoparticles for intracellular molecular imaging applications using MRI", Journal of Biological Inorganic Chemistry, June 2004

6. P. Santangelo, **N. Nitin** and G. Bao, "Direct imaging of co-localization of K-Ras and GAPDH mRNA with Mitochondria, and ER in living cells", Journal of Biomedical Optics, 10(4), 2005

7. L. LaConte, **N. Nitin** and G. Bao, "Magnetic Nanoparticle Probes for MR imaging", Materials Today, 2005

8. P. Santangelo, **N. Nitin,** L. LaConte, A. Wollums, and G. Bao, "Live-cell characterization and analysis of a clinical isolate of bovine respiratory syncytial virus, using molecular beacons", Journal of Virology, 80(2), 2006

9. **N. Nitin**, Gadiraju RP, Karwe MV, "Conjugate heat transfer associated with a turbulent hot air jet impinging on a cylindrical object ", Journal of Food Process Engineering 29 (4): 386-399, 2006

10. P. Santangelo, **N. Nitin** and G. Bao, "Nanostructured probes for RNA detection in living cells", Annals of Biomedical Engineering, 34(1), 2006

11. J. Aaron, **N. Nitin** et al., "Plasmon resonance coupling of metal nanoparticles for molecular imaging of carcinogenesis *in vivo*", Journal of Biomedical Optics, 12(3), 2007

12. Leslie LaConte, **N. Nitin** et al.," Coating thickness of magnetic iron oxide nanoparticles directly affects R_2 relaxivity", Journal of Magnetic Resonance Imaging, 1634-41, 26(6), Dec., 2007

13. **N. Nitin***, D. Javier* and Rebecca Richards-Kortum, "Widefield and high-resolution reflectance imaging of gold and silver nanospheres." Journal of Biomedical Optics, 12(5):051505, 2007 (* Equal Contributions)

14. **N. Nitin**, D. Javier and Rebecca Richards-Kortum, "Oligonucleotide coated metallic nanoparticles as a flexible platform for molecular imaging agents", Bioconjugate Chemistry, 2090-6, 18(6), Dec., 2007

15. D L Nida, **N. Nitin**, W W Yu, V L Colvin and R Richards-Kortum, "Photostability of quantum dots with amphiphilic polymer-based passivation strategies", Nanotechnology, 19:035701, 2008

16. D. Javier*, **N. Nitin***, D. Robyler and Rebecca Richards-Kortum, "Metal-based nanorods as molecule-specific contrast agents for reflectance imaging in 3D tissues," Journal of Nanophotonics, Vol. 2, 023506, 2008. (* Equal Contributions)

17. Javier DJ, **Nitin N**, Levy M, Ellington A, Richards-Kortum R., "Aptamer-Targeted Gold Nanoparticles As Molecular-Specific Contrast Agents for Reflectance Imaging". Bioconjugate Chemistry, May, 2008.

18. **N. Nitin**, A. Carlson, T. Muldoon, A. El-Naggar, A. Gillenwater, R. Richards-Kortum, "Molecular imaging of glucose uptake in oral neoplasia following topical application of fluorescently labeled deoxy-glucose", (Accepted -International Journal of Cancer Research)

19. **N. Nitin**, P. Santangelo and G. Bao, "Targeted Delivery and detection of nuclear RNA in living cells using peptide linked molecular beacons" Bioconjugate Chemistry, Oct., 2008.

20. **N. Nitin**, A. El-Naggar, A. Gillenwater, R. Richards-Kortum, ""Widefield and high-resolution optical molecular imaging of EGFR expression to improve detection of oral neoplasia", (Under review by Oral Oncology)